NANOSTRUCTURED MATERIALS FOR ELECTROCHEMICAL ENERGY STORAGE

Thesis submitted to the University of Kerala for the award of the

Degree of **Doctor of Philosophy** in **Physics** under the Faculty of Science

By

Anjana P M

Materials Science and Technology Division

CSIR- National Institute for Interdisciplinary Science and Technology

Research Centre, University of Kerala

Thiruvananthapuram-695 019, Kerala, India

2023

DECLARATION

I hereby declare that the Ph.D. thesis entitled "**Nanostructured materials for electrochemical energy storage**" is an independent work carried out by me at the Materials Science and Technology Division of the National Institute for Interdisciplinary Science and Technology (CSIR), Thiruvananthapuram, under the supervision of **Dr. Rakhi R. B** and it has not been submitted anywhere else for any other degree, diploma or title of the University or any other institution. I also declare that plagiarism checking has been effected using the software URUKUND (OURIGINAL) approved by the UGC/University and no plagiarism is found in the thesis.

Thiruvananthapuram **Anjana P. M**

June, 2023

राष्ट्रीय अंतर्विषयी विज्ञान तथा प्रौद्योगिकी संस्थान
NATIONAL INSTITUTE FOR INTERDISCIPLINARY SCIENCE AND TECHNOLOGY
वैज्ञानिक तथा औद्योगिक अनुसंधान परिषद्
Council of Scientific and Industrial Research
इंडस्ट्रियल एस्टेट पी ओ, पाप्पनमकोड, तिरुवनंतपुरम, भारत – 695 019
Industrial Estate P O, Pappanamcode, Thiruvananthapuram, India – 695 019

डॉ. राखी आर.बी
प्रिंसिपल वैज्ञानिक
सामग्री विज्ञान और प्रौद्योगिकी प्रभाग

Dr. Rakhi R.B
Principal Scientist
Materials Science and Technology Division

CERTIFICATE

This is to certify that the work embodied in the thesis entitled "**Nanostructured materials for electrochemical energy storage**" has been carried out by **Anjana P. M** under my supervision and guidance at the Materials Science and Technology Division of the National Institute for Interdisciplinary Science and Technology (CSIR), Thiruvananthapuram, and it has not been submitted anywhere else for any other degree, diploma or title of the University or any other institution. It is also certified that plagiarism checking has been effected using the software URUKUND (OURIGINAL) approved by the UGC/University and that no plagiarism is found in the thesis.

Dr. Rakhi R.B

(Thesis Supervisor)

Thiruvananthapuram

June, 2023

ACKNOWLEDGEMENTS

I would like to take this opportunity to convey my sincere gratitude to a number of people for their support, love, encouragement, and guidance throughout my journey.

With great pleasure, I would like to express my sincere gratitude to **Dr. Rakhi R. B**. and **Dr. S. R. Sarath Kumar**, my thesis supervisors, for suggesting the research problem and for their guidance, vast knowledge, tender care, ongoing encouragement, and inspiration, leading to the successful completion of this work.

I would like to express my sincere thanks to **Dr. C. Anandharamakrishnan** and **Dr. Ajayaghosh**, present and former directors of the CSIR-National Institute for Interdisciplinary Science and Technology (CSIR), Thiruvananthapuram, for providing the necessary facilities for my research.

I want to express my gratitude to **Dr. V. Biju, Dr. Sibi K. S., Dr. Subodh G.,** and **Dr. I. Hubert Joe**, present and former HODs of the Department of Physics, University of Kerala, for all the help and support.

I would like to express my sincere thanks to **Dr. Ananthakumar S., Dr. Ravi M.,** and **Dr. Savithri S**., present and former HODs of the Materials Science and Technology Division of the National Institute for Interdisciplinary Science and Technology (CSIR), Thiruvananthapuram, for all the help and support.

I would like to express my sincere thanks to **Dr. Narayanan Unni, Dr. Sujatha Devi, Dr. Suraj Soman, Dr. Adarsh Ashok, Dr. Rajan T P D, Dr. Hareesh U S, Dr. Surendran K P**, and all other scientists of the Materials Science and Technology Division, and Chemical Sciences and Technology Division of the National Institute for Interdisciplinary Science and Technology (CSIR) for all the help and support extended to me.

I would like to thank **Dr. Bindu M. R**., M.Phil. research supervisor, **Ms. Haritha A.H., Mr. Anoop, Mrs. Mini,** and **Mr. Adarsh** for general help, **Mr. Kiran Mohan, Mr. Peer Mohammad, Mr. Harish Raj, Mrs. Dhanya,** and **Mrs. Aswathi** for general characterization techniques.

I express my sincere thanks to my group members, **Dr. Manuraj Mohan, Mrs. Haritha V. S., Mr. Visakh V. Mohan, Mrs. Shilpa R., Ms. Sophy Mariam Varghese,** and **Ms. Aparna S. M**., for their help and support. I also thank our M.Sc. Project students, **Ms. Ruparanjini, Ms. Sahana, Ms. Ganga, Ms. Krishnapriya, Mr. Alias M.,** and **Ms. Anakha**, for their help.

I owe **Mr. Rishad Baig** a huge debt of gratitude for his constant support during my research journey.

I would like to thank **Ms. Ramees Jebin, Ms. Sruthi, Mrs. Surya, Ms. Arsha N, Ms. Arsha M. S., Ms. Akhila Murali J., Mr. Mahesh A., Dr. Sariga C. Lal,** and all other research scholars of Department of Physics, University of Kerala and CSIR-NIIST for their help.

I owe my in-depth gratitude to **my parents S Padmaja and K Mohanachandran, brother Adarsh, husband Sreenath, daughter Aaradhya, parents-in-law,** and **all my relatives** for their support and encouragement. I would also like to extend my thanks and appreciation to all my teachers for their help and blessings.

I sincerely thank the Department of Science and Technology (DST), Government of India, for the financial support.

I am grateful to God Almighty for His abundant blessings in my life, especially at the toughest times.

Anjana. P. M

CONTENTS

Chapter 2

Chapter 3

Chapter 4

Chapter 5

Chapter 6

Chapter 7

LIST OF TABLES

LIST OF FIGURES

ABBREVIATIONS

EDL	Electric Double Layer
ES	Electrochemical Supercapacitor
C_{sp}	Specific Capacitance
EDLC	Electric Double Layer Capacitor
CV	Cyclic Voltammetry
GCD	Galvanostatic Charge-Discharge
EIS	Electrochemical Impedance Spectroscopy
Rs	Series Resistance
Rct	Charge -Transfer Resistance
W	Warburg Diffusion
BTM	Binary Transition Metal
rGO	Reduced Graphene Oxide
CNT	Carbon Nano Tube
PVDF	Polyvinylidene fluoride
PTFE	Polytetrafluoroethylene
PANI	Polyaniline
CC	Carbon Cloth
NF	Nickel Foam

SHE	Standard Hydrogen Electrode
CBD	Chemical Bath Deposition
XRD	X-ray diffraction
FTIR	Fourier Transform Infrared spectroscopy
XPS	X-ray photoelectron spectroscopy
BET	Brunauer-Emmett-Teller
BJH	Barret-Joyner-Halenda
SEM	Scanning Electron Microscopy
TEM	Transmission Electron Microscopy
SAED	Selected Area Electron Diffraction
EDX	Energy Dispersive X-ray

PREFACE

To reduce the serious issues of environmental pollution caused by greenhouse gases emitted via the combustion of fossil fuels, and to cater to the ever-increasing energy requirements, the modern world is moving rapidly towards renewable energy conversion and storage technologies. Supercapacitors are electrochemical energy storage devices with an eco-friendly nature, characterized by rapid charge/discharge rate, increased power density, low cost, and long cyclic life. Nowadays, supercapacitors are successfully applied in hybrid electric vehicles, electronic devices, volatile memory backups in personal computers, and uninterruptible power supplies. However, the low energy density of supercapacitors is a major drawback that limits their widespread use. According to the individual mechanism of charge storage, supercapacitors can be divided into electric double-layer capacitors (EDLCs) and pseudocapacitors or Faradaic battery-type supercapacitors. In EDLCs, carbonaceous electrode materials are used and the charge storage process is purely electrostatic in nature, bringing in high power density. In contrast, transition metal oxide or hydroxide-based materials are used in pseudocapacitors, and the storage mechanism is due to the fast Faradaic redox reaction taking place at the electrode surface, resulting in higher energy density values than EDLCs. However, the lower electrical conductivity of transition metal oxides and hydroxides inhibits the ion diffusion rate, resulting in a poor capacitance value and cyclic performance. Therefore, producing an excellent active electrode material with increased electrical conductivity and good nanostructure is necessary to elevate the electrochemical properties of the supercapacitors.

Recently, Mn-Co based binary transition metal oxides/hydroxides, sulfides, selenides, and their nanocomposites have attained superior interest as electrode materials in the electrochemical energy storage industry, due to their diverse physicochemical properties. The incorporation of two different metals provides excellent capacitive behavior and rate properties for binary transition metal-based systems. The measurable oxidation states, the tunable surface morphology, high electrical conductivity, simple and scalable preparation methods, low cost, and eco-friendly nature provide great demand for these materials. The capacitive performance of the binary transition metals can be further improved by

developing unique morphologies that promote greater interaction between the electrolytes and the active materials.

The thesis is divided into seven Chapters. The first chapter gives a brief introduction to supercapacitors, focusing on the structure and storage mechanisms as well as their applications. The chapter also covers the different electrochemical characterization techniques and how they can be used to estimate the various performance parameters involved in supercapacitor research. The chapter also discusses the challenges and opportunities in the field of supercapacitor research. An introduction to Mn-Co-based binary nanostructures and a literature review on their application as promising electrode materials in supercapacitors are also included in this chapter.

Chapter 2 of the thesis deals with the layer-by-layer growth of $Mn(OH)_2/Co(OH)_2$ nanoparticles over different current collectors for supercapacitor application. The symmetric supercapacitor fabricated by the $Mn(OH)_2/Co(OH)_2$/CC (CC being carbon cloth) and $Mn(OH)_2/Co(OH)_2$/NF (NF being nickel foam) -based electrodes respectively exhibit a maximum specific capacitance of 385 F g^{-1} and 400 F g^{-1} at 5 mV s^{-1}. Furthermore, the supercapacitor electrodes exhibit remarkable cyclic stability. The $Mn(OH)_2/Co(OH)_2$/CC electrode delivers 94% and $Mn(OH)_2/Co(OH)_2$/NF electrode delivers 95% capacitance retention at 2 A g^{-1} after 6000 continuous galvanostatic charge-discharge (GCD) cycles. The superior electrochemical performance of $Mn(OH)_2/Co(OH)_2$/NF electrode is due to the highly porous structure that provides a large area for active material growth, excellent mechanical strength, and good electrical conductivity.

Chapter 3 deals with the fabrication and performance studies of a symmetric supercapacitor based on $MnCo_2O_4$ nanoneedle grown over NF substrate. The symmetric supercapacitor with the binder-free $MnCo_2O_4$ electrodes exhibits a maximum specific capacitance of 420 F g^{-1} at 5 mV s^{-1}. At a specific power of 1 kW kg^{-1}, the supercapacitor device based on $MnCo_2O_4$ nanoneedle delivers a specific energy of 39 W h kg^{-1}. The electrode also offers outstanding cyclic stability retaining 96% of its initial discharge capacitance after 10000 continuous GCD cycles, at a constant high current density of 5 A g^{-1}.

In Chapter 4, we report $MnCo_2S_4$ nanoflowers directly grown over Ni foam for high-performance supercapacitor application. A symmetric supercapacitor assembled using $MnCo_2S_4$ nanoflower electrodes delivers a specific capacitance of 1243 F g^{-1} at 1 A g^{-1} along with a cyclic performance of 97% and a coulombic efficiency of 98% at 5 A g^{-1} after 10000 GCD cycles. Furthermore, at a specific power of 1 kW kg^{-1}, the $MnCo_2S_4$ nanoflower-based symmetric supercapacitor exhibits superior performance with an increased specific energy of 170 W h kg^{-1}.

Chapter 5 deals with the fabrication and performance studies of symmetric supercapacitors based on $MnCoSe_2$ nanoneedle on a three-dimensional NF substrate, by a simple hydrothermal method. The as-prepared nanocomposites are studied using routine and electrochemical characterization techniques. The $MnCoSe_2$ nanoneedle-based supercapacitor electrode exhibits an enhanced specific capacitance of 384 F g^{-1} at 1 A g^{-1}. At a specific power of 1 kW kg^{-1}, $MnCoSe_2$ nanoneedle-based supercapacitor device gives a specific energy of 53 W h kg^{-1} with superior cyclic stability of 95% retention at the end of 10000 GCD cycles at 5 A g^{-1}.

In Chapter 6, we discuss an asymmetric supercapacitor device (ASC) fabricated using $MnCo_2S_4$ nanoflower as the positive electrode and rGO as the negative electrode. The $MnCo_2S_4$ nanoflower//rGO ASC device exhibited a large gravimetric specific capacitance of 162 F g^{-1} at 1 A g^{-1} and a remarkable cyclic performance of 99% at 5 A g^{-1} along with a high coulombic efficiency of 99.5% after 10000 cycles. The ASC device delivered a gravimetric energy density of 73 W h kg^{-1}, at a gravimetric power density of 151 W kg^{-1}, indicating the great potential of $MnCo_2S_4$ nanoflower electrode for electrochemical energy storage.

The summary of the entire thesis is included in Chapter 7, which also discusses the future scope of the work.

Chapter 1

An Introduction to Supercapacitors

1.1. Outline of the chapter

In order to meet the needs of the consumer electronics and electric vehicle markets, energy storage systems that provide superior performance are essential. Supercapacitors, with their higher power densities, fast charge-discharge rates, excellent cycle stabilities than batteries, and higher energy densities than conventional dielectric capacitors, offer a promising approach to satisfy the increasing power demands of energy storage systems in the 21st century. The selection of stable and high-performance electrode materials is an essential aspect of the design of a supercapacitor. Manganese and Cobalt-based binary transition metal-based hydroxides, oxides, sulfides, and selenides have attained significant research interest in electrochemical energy storage applications due to their diverse physicochemical properties such as the presence of various oxidation states, tunable surface morphologies, high electrical conductivity, availability of simple and scalable preparation methods, low cost, and eco-friendly nature. The present chapter focuses on the different types of supercapacitors, the distinct energy storage mechanisms, and the significance of binary transition metals Mn-Co based hydroxides, oxides, sulfides, and selenides in energy storage applications.

1.2. Introduction

It is not easy to imagine modern society without electronic gadgets such as smartphones, tablet PCs, and laptops. The increasing proliferation of these gadgets also demands the development of environmentally benign, high-efficiency portable electrochemical energy storage devices (ESD) that power not just the electronic circuits but also electric vehicles, in the pursuit of high efficiency, zero-emission transportation systems. Supercapacitors have become popular electrochemical energy storage devices that make portability tenable thanks to their greater power density, rate capability, and high cycle life. The two prime aspects of an energy storage device are specific energy (Wh Kg^{-1}) and specific power (W Kg^{-1}). Specific energy is the amount of energy stored per unit mass of the device or active material in the device. On the other hand, specific power is the speed at which the energy is released per unit weight of the device or active material. Seldom does the energy storage devices compromise either with specific power or specific energy.

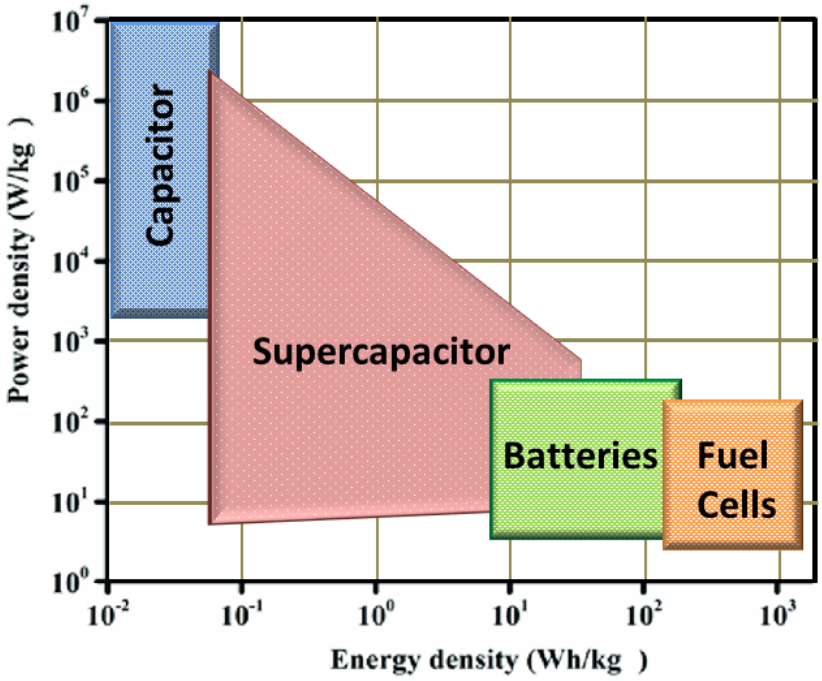

Figure 1.1. Ragone plot of various energy storage and conversion devices

Figure 1.1 represents the Ragone plot of the energy and power density of various energy storage devices. Although batteries have cemented their position as prominent electrochemical ESDs which power all electronic devices, they take hours to charge due to low power density and possess a shorter lifetime which is inadequate for the fast-moving technical world. Also, battery produces hazardous waste substances as by-

products which add difficulties in device recycling. The supercapacitor bridges the gap between conventional capacitors and batteries with its excellent electrochemical performance. This prompted a renewed research interest towards supercapacitors which have been known for the high specific power, stability, safety operation, economy and eco-friendly nature (Halper et al. 2006).

1.3. Capacitor to Supercapacitor

Capacitor is the fundamental passive two terminal component in an electrical circuit that stores energy electrostatically in the electric field. Based on the choice of electrode and electrolyte, the capacitors can be classified into three major categories: electrostatic capacitor, electrolytic capacitor and supercapacitor which are explained below in detail.

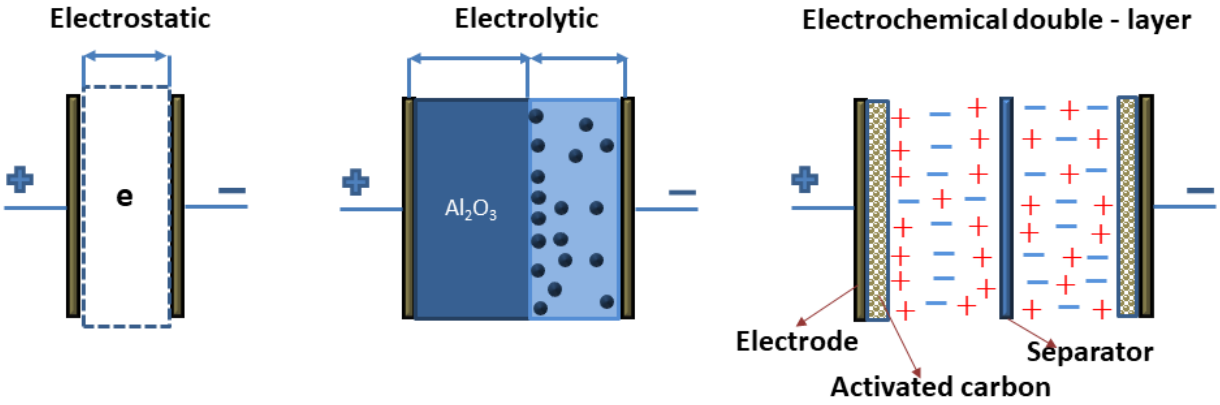

Figure 1.2. Schematic representation of electrostatic capacitor, electrolytic capacitor and supercapacitor

1.3.1. Electrostatic Capacitor

The electrostatic capacitor consists of two parallel metallic conductors (copper or aluminium) and in order to prevent electrical contact between them, a dielectric (air, glass, paper, mica, polymer film or ceramic) is interposed. The electrodes are polarized by the applied voltage which causes the migration of positive and negative charges towards the surface of electrodes of opposite polarity. As a result, when the two metal plates are charged, a capacitor connected in a circuit will act as a voltage source and current will flow until a complete charge balance is achieved.

The operating voltage and life time of the electrostatic capacitor is very high. The capacitance of conventional capacitor is calculated using the following Equation (1.1),

$$C = \varepsilon_0 \, \varepsilon_r \, \frac{A}{D} \qquad (1.1)$$

Where 'C' is the electrostatic capacity (μF), 'A' is the surface area of each electrode (m^2 g^{-1}), 'D' is the distance between the two electrodes (m), ε_0 is the dielectric constant of free space (F m^{-1}), and ε_r is the dielectric constant of the insulating material between the two electrodes. The capacitance yield of this capacitor ranges from 0.1 μF to 1 μF with an operating voltage range of 50 to 400 V. The capacitance value of electrostatic capacitor can be upgraded by expanding the surface area of electrodes, increasing the dielectric constant of the interposed material and decreasing the distance between the two electrodes.

1.3.2. Electrolytic Capacitor

The next generation of capacitive devices is the electrolytic capacitor which yields a maximum capacitance in the range of 0.1 μF to 10 μF with a voltage profile of 25 V to 50 V. Electrolytic capacitors can also be called as aluminium capacitors which consist of an electrolytic paper containing boric acid solution and two pieces of aluminium foil. A thin layer of aluminium oxide with the thickness between 1.3 nm and 1.5 nm acts as the dielectric of the device. This thin layer is obtained by etching and oxidizing one of the aluminium foils. The aluminium foil with insulating oxide layer acts as anode while the liquid electrolyte and second foil acts as cathode.

Although electrolytic capacitor exhibits better energy performance in comparison with electrostatic capacitor, it still could not able to achieve a large series capacitance value due to the difficulty in reducing the thickness of the dielectric medium below 1 nm. Before the evolution of supercapacitor, aluminium electrolytic capacitor was widely used in a variety of applications such as automobiles, aircraft, space vehicles, computers, monitors, motherboards of personal computers and other electronics (Kim et al. 2015).

1.3.3. Supercapacitor

Supercapacitor is the third-generation capacitive device which is the hybridization of electrochemical double layer capacitor (EDLC) and pseudocapacitor. The working of supercapacitor relies on the capture and release of energy by nanoscopic charge separation at the interface between electrode and electrolyte. It has the potential to deliver higher specific energy than conventional electrostatic capacitor and exhibits higher

specific power as well. The physical assembly of a supercapacitor is similar to that of the battery which is composed of vital components such as high surface area electrodes (anode and cathode) immersed in an electrolyte, thin and porous ion permeable membrane (separator) that electrically isolates the two electrodes and a current collector to conduct the flow of electrons between the active material and the external power source. In spite of the above-mentioned components, the perfect nanoscale architecture of electrode material with high surface area and porosity results in the technical advancement of electrochemical performance and offers a great potential to supercapacitor to overcome the shortcomings of batteries and conventional capacitors. The fundamental charge storage technique of supercapacitor includes the following phenomena in chronological order such as:

- Polarization of electrodes by applied voltage,
- Diffusion of electrolytic ion through the separator,
- Attraction of ions towards its oppositely polarized electrode (negative ions towards positively polarized electrode and positive ions towards negatively polarized electrode),
- Adsorption and intercalation of ions on the electrode/electrolyte interface,
- Finally, accumulation of charges in double layer fashion at the electrode/electrolyte interface due to electrostatic charge attraction and fast reversible Faradaic reaction.

The charges in the inner surface of the electrode are balanced by the accumulation of counter ions in the electrolyte which results in electric neutrality. The penetration of ions into double layer caused by the structure of active electrode material gives rise to pseudocapacitance. The electron flow in the supercapacitor continues until the potential difference between the two electrodes becomes equal to the applied voltage and thus the supercapacitor gets charged. During discharge process, the electron starts migrating from electron rich sites to electron deficient sites. The stability and efficiency of the material is determined by the constant rate of charging and discharging over a long period of time ($>10^5$ cycles). Supercapacitors establish an increased specific capacitance and energy density by a factor of 100,000 or even greater than that of regular capacitors. This could be achieved by the incorporation of electrochemically active material on the electrode surface with 1000 times high surface area, nanoscale dielectric distance and additional pseudocapacitance by fast reversible Faradaic reactions (González et al. 2016).

1.4. History of Supercapacitors

In 1879, Helmholtz predicted the fundamental phenomena of double layer formation in the supercapacitor at electrode/electrolyte interface. Subsequently, there was a sudden increase in the capacitor industry through various researches. In 1957, Howard Becker of General Electric (GE), developed the first activated carbon based electric double layer capacitor and patented their development. But GE did not follow this evolution. In 1970, Standard Oil Company of Ohio, Japan (SOHIO) constructed a carbon-based electrolytic capacitor. In 1978, the Nippon Electric Company (NEC) marketed aqueous electrolyte capacitors as electrochemical supercapacitors. They commercialized electric double layer capacitors for computer backup memory. In the late 20^{th} century, many companies started the manufacturing of supercapacitor to increase the business. Pinnacle Research Institute (PRI) in 1982 established supercapacitor having low internal resistance for portable energy storage. They widely used these for military applications. In 1992, Maxwell technologies gained all the studies done by PRI on supercapacitor. They developed their own supercapacitor in the name of "BOOST CAPS". Supercapacitors with large specific energy were still difficult at that period and no important progress happened in the area of active electrode materials. In 1999, B E Conway launched a new storage mechanism established as pseudo capacitance with the electrode material RuO_2. The experiments on supercapacitors again started after recognizing their importance in hybrid electric vehicles. This led to the production of new pseudocapacitive materials with 10-100 times higher energy density than the double layer capacitor. This renewed research interest paved the way to high performance supercapacitors commercially available in present market (Kim et al. 2015).

1.5. Classification of Supercapacitors

Based on the underlying energy storage mechanism, supercapacitors can be broadly classified into three types: Electrochemical double layer capacitors (EDLCs), Pseudocapacitors or Faradaic capacitors (FC's) and hybrid capacitors which are described in a detailed manner below.

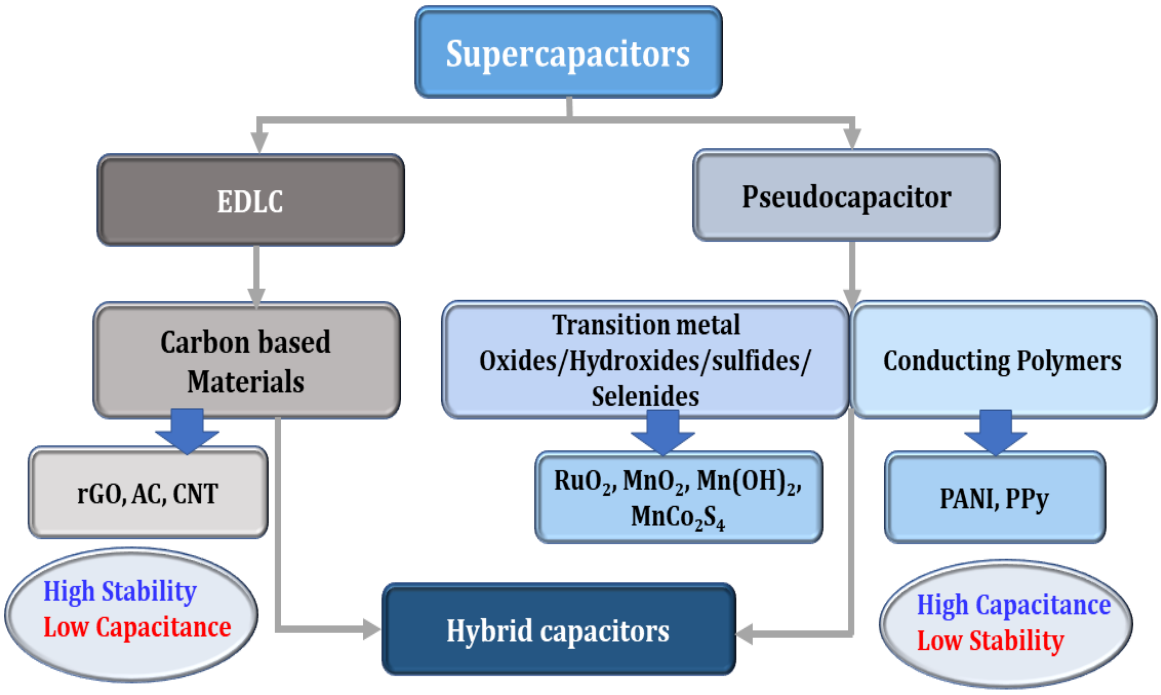

Figure 1.3. Classification of supercapacitors based on the storage mechanism

1.5.1. Electrochemical Double Layer Capacitor

An EDLC is defined by the double layer structure which is formed spontaneously due to the organization of charges at the interface of the electrode and the electrolyte. An EDLC is regarded as the simplest and most commercially available supercapacitor which stores energy physically by electrostatic charge adsorption, and in which no Faradaic process occurs. In the physical electrostatic processes, the formation and relaxation of the electric double layer occurs in a very short range of time, on the order of $\sim 10^{-8}$ s, which is smaller than that of redox reactions. For pseudocapacitance this time scale is in the range of 10^{-2}–10^{-4} s. Also, the concentration and size of electrolytic ions determine the effective thickness of the electric double layer which ranges from 5−10 Å. EDLCs possess higher energy density than conventional dielectric capacitors because of their several orders of magnitude higher effective surface area and the nanoscale charge separation distance.

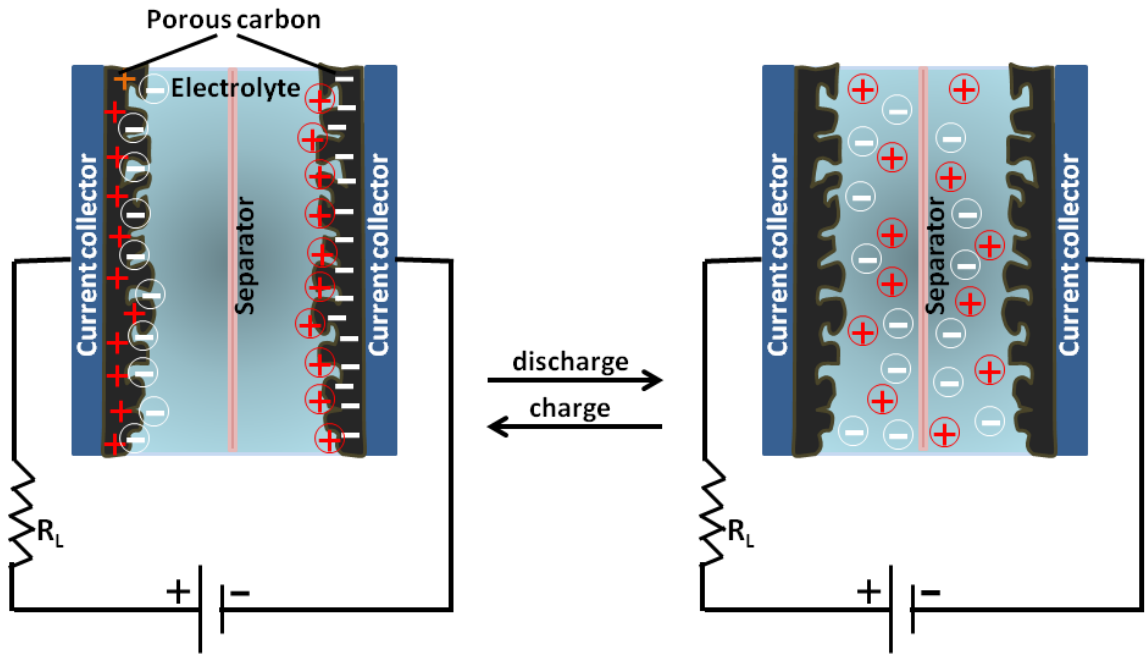

Figure 1.4. Schematic representation of charge storage mechanism in EDLC

During charging process, cations migrate towards the negative electrode while anions move towards the positive electrode forming the double-layer in the interface of electrode and electrolyte and on the other hand, the reverse processes can take place when the system is forced to discharge which is shown in the **Figure 1.4**. Though the technology of EDLC is very simple and shows better electrochemical performance, it also presents some drawbacks. The assembly of dried carbon materials having high specific area on current collector requires a foreign agent called binder. The metallic current collector is coated with the wet mixture of carbon powder and binder. Although the procedure is simple and cheap, it exhibits three major disadvantages such as increase in material resistivity, risk of material loss and electrode malfunction. Thus, there is a need to develop new strategies to improve the electrochemical performance, lifetime and reliability of supercapacitor (Halper et al. 2006; Sharma and Bhatti 2010).

1.5.1.1. EDLC Model

The electric double layer structure is the formation of two parallel layers of charge in which one layer is on the surface itself while the other layer is oppositely charged near the surface. As shown in the **Figure 1.5** there are three important models which explain the double layer structure of EDLCs: Helmholtz model, Gouy and Chapman model and Stern model.

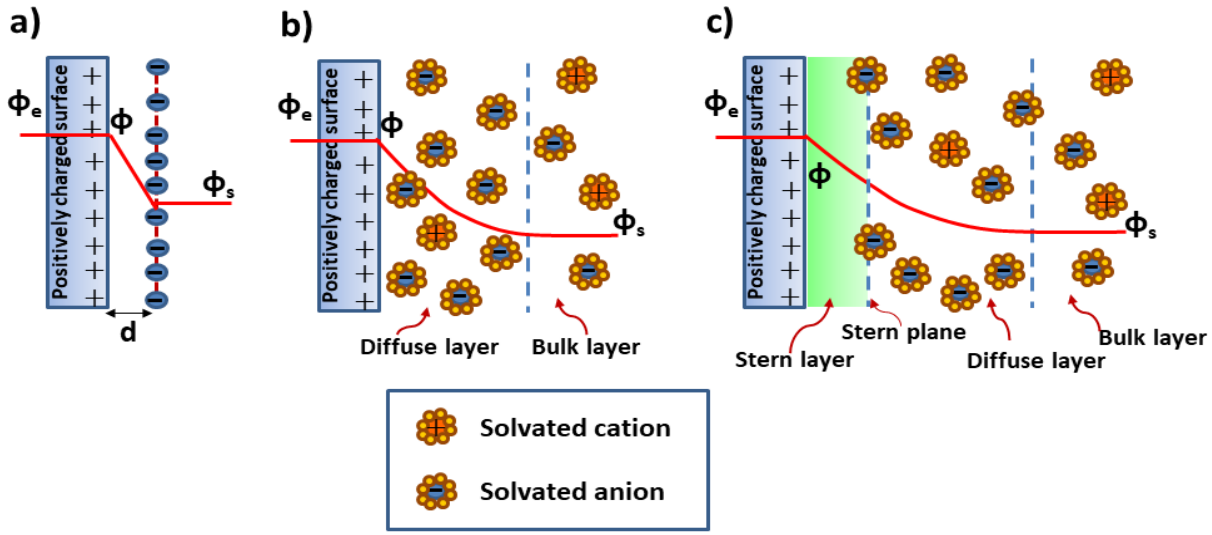

Figure 1.5. Models of the electrical double layer at a positively charged Surface. (a) Helmholtz model, (b) Gouy and chapman model and (c) the Stern model

The Helmholtz Model is the simplest possible model. It postulates that ions (anions and cations) occupy a plane located at a distance, d, from the electrode surface. The electrical double layer, according to the Helmholtz model, behaves as a parallel plate capacitor. According to Gouy- Chapman model, ions are considered to be point charges. There is no chemical adsorption occurring in the contacts between ions or between ions and the electrode; instead, they are solely electrostatic. In 1924 Stern observed that neither Helmholtz model nor Gouy-Chapman model could adequately explain the properties of double layer and so he discussed the merits and demerits of both the models. Finally, he introduced two regions of ion distribution – the inner region called the compact layer or Stern layer and the outer region called diffusive layer. The Stern layer occurs near the surface of the particle, and the diffuse layer occurs next to the Stern layer (in between the Stern layer and the bulk). According to the Gouy-Chapman-Stern Model, the capacitance of the double layer, $C_{dl,}$ can be expressed by the following Equation (1.2):

$$\frac{1}{C_{dl}} = \frac{1}{C_H} + \frac{1}{C_{diff}} \qquad (1.2)$$

Where, C_H is the capacitance of the compact layer from the Helmholtz model and C_{diff} is the capacitance of the Gouy-Chapman diffusion region.

The factors such as electrode material, electrode surface, accessibility to the electrode surface and electric field across the electrode determines the capacitance of EDL. The chemical affinity between the adsorbed ions and electrode surface and the type of

electrolyte ions also greatly affects the capacitance of EDL (González et al. 2016; Halper et al. 2006; Xie et al. 2020).

1.5.2. Pseudocapacitor

The energy storage mechanism in a pseudocapacitor is based on Faradaic redox reaction depending upon the electrode potential, as illustrated in the **Figure 1.6**. Simultaneously there is formation of electric double layer along with Faradaic process that occurs at the surface of active electrode material exposed to electrolyte.

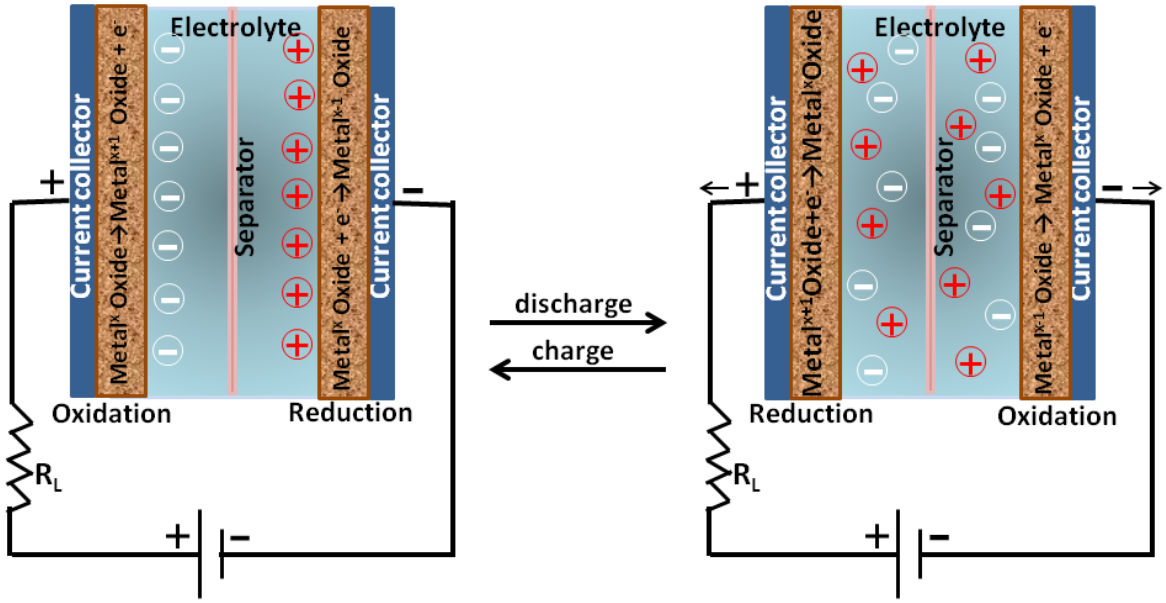

Figure 1.6. Schematic of charge-discharge process in Faradaic capacitor

There are three prime pseudocapacitive features, as illustrated in the **Figure 1.7** These are underpotential deposition, redox pseudocapacitance and intercalation pseudocapacitance which have been obtained as a result of various Faradaic mechanisms. The redox mechanisms are explained below:

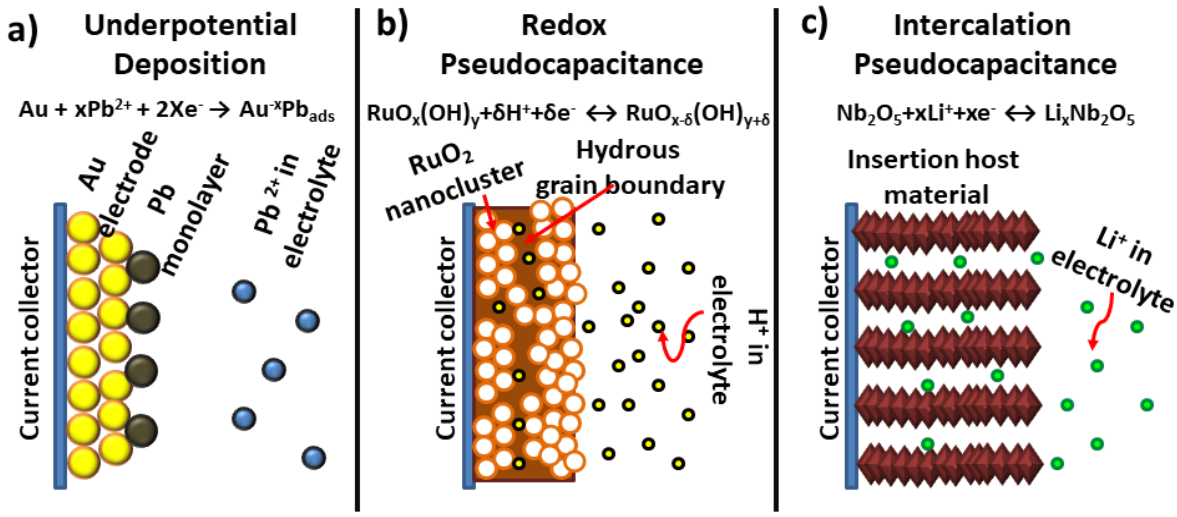

Figure 1.7. Schematic of three prime redox mechanisms which give rise to pseudocapacitance

(a) **Underpotential deposition:** This refers to the formation of a monolayer by the adsorption of metal ions at the surface of different metals above their redox potential (**Figure 1.7 (a)**). The best example is the Langmuir-type electrosorption of H on a noble metal substrate such as Pt, Rh, and Ru.

(b) **Redox pseudocapacitance:** This involves the electrochemical ion adsorption onto or near the surface of the electrode with fast Faradaic charge transfer (**Figure 1.7 (b)**). The electrochemically active materials such as metal oxides and conducting polymers are best suited for redox pseudocapacitance, and are currently under extensive research.

(c) **Intercalation pseudocapacitance:** This occurs due to the intercalation of ions into active redox electrode materials, accompanied by fast Faradaic charge transfer with no crystallographic phase separation (e.g. intercalation of Li ion on Nb_2O_5, as in **Figure 1.7 (c)**).

1.5.3. Hybrid Capacitor

Hybrid electrochemical capacitors have attracted significant attention in recent years due to their improved specific energy without altering the specific power. The high specific capacitance of hybrid supercapacitors is composed of electric double layer capacitance stored by porous carbon materials and the pseudocapacitance stored by metal oxide or conducting polymer (**Figure 1.8**). The hybrid supercapacitors enhance the electrochemical performance by combining the advantage of the EDLCs and the

pesudocapacitors, all the while overcoming most of their disadvantages (Chen et al. 2017b). The formation of hybrid system is based on the combination of different capacitive materials with the uniqueness of certain capacitive characteristics. Based on the mechanical design of electrode material, hybrid capacitors are classified into three categories: composite hybrids, asymmetric hybrids and battery-type hybrids.

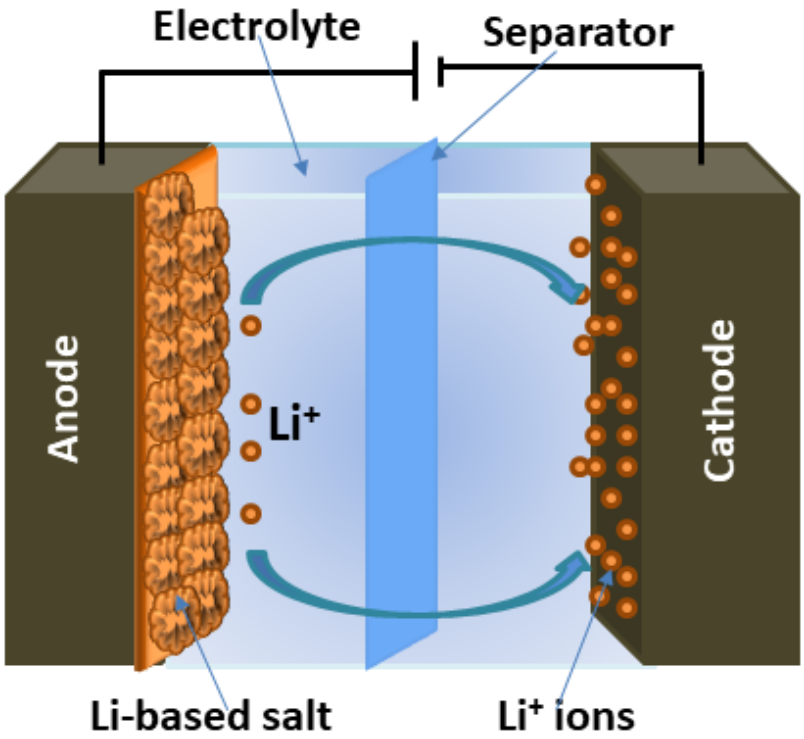

Figure 1.8. Schematic diagram of a hybrid capacitor

1.6. Electrode Material

The electrochemical performance of supercapacitors relies on factors such as properties of electrode materials used, electrolyte and voltage range. However, the research is widely focused on the development of new electrode materials that will yield better electrochemical performances. The electrodes must be established with the following features such as high surface area per unit volume and mass, good conductivity, long-term chemical stability, high corrosion resistance, environment friendly, high temperature stability and low-cost materials. The amount of capacitance, due EDLC and pseudocapacitive behaviour, stored per unit voltage in a supercapacitor is predominantly a function of the electrode surface area. Therefore, supercapacitor electrodes are typically made of electrochemically active porous materials with high surface area. Additionally,

the ability of the electrode material to perform Faradaic charge transfers enhances the total capacitance.

1.6.1. EDLC Electrodes

The most widely used electrode materials for EDLCs are carbon-based materials ranging from commercial activated carbons (ACs), carbon aerogels, and carbon nanomaterials such as carbon nanotubes (CNTs) and graphene. Among them, ACs are highly preferred in the commercially available supercapacitors due to their low cost, high availability, excellent electrical conductivity, stable electrochemical response and environmental compatibility. The nanoporous nature of carbon materials can be classified into three categories such as microporous (< 2 nm), mesoporous (2-50 nm) and macroporous (> 50 nm). The porous nature of the electrodes helps maximize the surface area and provides short distance between electrode and electrolyte. Thus, the high surface area promotes the capacitance value of EDLCs to 300-550 F g^{-1}. However, experimentally, the pure carbon-based capacitor has achieved a specific capacitance of ∼100−250 F g^{-1} only, due to finite conductivity and unavailability of all active sites.

1.6.2. Pseudocapacitor Electrodes

When compared to EDLC mechanism, the additional Faradaic process occurring in the electrode can result in significant increase in the specific capacitance of specifically designed redox capacitors. Thus, selecting best Faradaic electrode material with multiple oxidation states becomes important in order to facilitate fast reversible oxidation and reduction during the charging and discharging processes. The most widely used electrode materials for pseudocapacitor includes metal oxides (such as RuO_2) and conducting polymers (such as Polyaniline). Ruthenium oxide has been thoroughly investigated and specific capacitances up to 900 Fg^{-1} were reported. However, its high price and toxicity prohibits the commercial use of RuO_2 in supercapacitors. Now a days MnO_2 is highly preferred as an electrode material for supercapacitors because of its high electrochemical performance, low cost and eco friendliness (Wang et al. 2015a). Also, conducting polymers such as Polyaniline (PANI) possess high doping level and high electroactivity and shows a high specific capacitance of 400-500 F g^{-1} in acidic medium. However, the poor cyclic life and volume expansion of metal oxides and conducting polymers have limited their commercialization (Wang et al. 2012). Recently, extensive research has been

focused towards binary transition metal hydroxide, oxide, sulfide, and selenide based electrode materials, especially Mn-Co based hydroxides, oxides, sulfides, and selenides as electrode material for supercapacitors (Hsu et al. 2021; Melkiyur et al. 2021; Zhu et al. 2021). These materials possess qualitative electrical conductivity, rich valence state, good mechanical and thermal stability, abundance, low cost, rich redox chemistry and environmental friendliness. In addition, these materials always exhibit the pseudocapacitive behaviour which greatly upgrades the electrochemical activity of the device.

1.6.3. Hybrid Capacitor Electrodes

Based on the electrode materials, the hybrid electrodes are classified into three types: composite hybrids, asymmetric hybrids and battery-type hybrids. In composite hybrid capacitor, the EDLC part is played by carbon materials thereby providing a greater surface area and capacitive double layer to enhance the electrochemical activity, whereas the other part is played by combining carbon-based materials with either metal oxide or conducting polymer materials and include both physical and chemical charge storage mechanisms. Several research works were carried out using carbon nanotubes and polypyrrole as composite electrodes (Raicopol et al. 2013). So many other combinations are also available as composite electrodes. For example in 2013, Kim *et al*. developed a new hybrid capacitor using anatase TiO_2 and reduced graphene oxide composite as anode and activated carbon as cathode (Kim et al. 2013). The asymmetric hybrid capacitors employ both Faradaic and non-Faradaic processes by incorporating an EDLC type electrode material with a pseudocapacitive type electrode material (Muzaffar et al. 2019). Recently Xu *et al*. designed an asymmetric supercapacitor where $MnCo_2O_4$ nanorod arrays on three-dimensional Ni foam (PMCN@NF) acts as positive electrode and reduced graphene oxide (rGO) acts as negative electrode (Xu et al. 2018). Elshahawy *et al*. constructed an asymmetric supercapacitor where $MnCo_2S_4$ on carbon cloth acts as the positive electrode and a (Porous Carbon Polyhedron) PCP/rGO hydrogel acts as the negative electrode (Elshahawy et al. 2017b). Asymmetric hybrid supercapacitors show better cyclic stability and exhibits higher energy density and power density than EDLCs. The third type of hybrid capacitor contains both battery type electrode material and supercapacitor electrode which provides higher energy density than supercapacitor and higher power density than those of batteries. The battery-type hybrids have a big potential

to bridge the gap between the normal supercapacitors and batteries, if they can combine the specific power, short charge time, cycle life as well as reversibility of supercapacitors and higher energy density of batteries (Muzaffar et al. 2019).

1.7. Electrolytes

Besides the highly tuned nanostructured electrode material, the electrolyte which resides between the two electrodes and separator also determines the electrochemical performance of a supercapacitor. The electrolyte defines the supreme parameters of supercapacitor performance such as maximum and optimal operating voltage that influences its energy capacity, device total resistance that can vary power density, device life time, toxicity and the level of encapsulation required for supercapacitor cell (**Figure 1.9**). Therefore, the selection of suitable electrolyte for supercapacitor requires the following features such as high electrochemical stability, low toxicity, good electric conductance, high ionic concentration, purity, wide voltage window, low volatility and flammability and low cost. The manipulation of supercapacitor electrolyte to enlarge the cell voltage (V) can effectively increase the energy density as seen from the equation $E = \frac{1}{2}CV^2$ .The equation reveals that the energy density is proportional to the square of cell voltage and hence widening the potential window of an electrolyte solution would be efficient in terms of energy density enhancement. Along with the property of the electrolyte potential window, the interaction between the electrolyte and the electrode materials also plays a key role in the ES performance. For instance, the matching of electrolyte ion size and the pore size of active electrode material has a profound influence on the achievable specific capacitance (Zhong et al. 2015). Other factors such as the viscosity, boiling point and freezing point of the electrolytes can also largely affect the thermal stability and thereby the operating temperature of supercapacitors. It is noteworthy that the aging and failure of supercapacitors are highly dependent on the electrochemical decomposition of electrolytes. Interestingly, the evolution of some new types of supercapacitors such as flexible or solid- state supercapacitors and micro supercapacitors are highly dependent on new electrolytes. The liquid electrolyte used in supercapacitors can be classified into three types: Aqueous electrolyte, Organic electrolyte and Ionic liquid electrolyte.

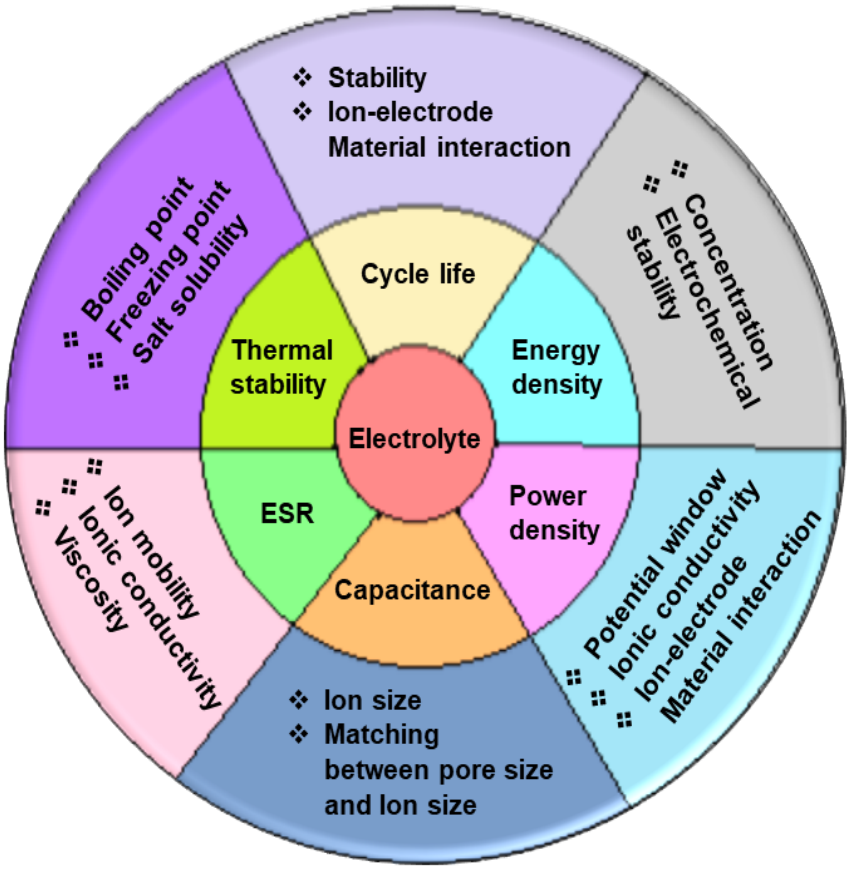

Figure 1.9. Schematic diagram on the effects of the electrolyte on the ES performance

1.7.1. Aqueous Electrolyte

Aqueous electrolytes are the most basic type of electrolytes which are made by dissolving inorganic salt or compound in deionised water. KOH, KCl, H_2SO_4 and Na_2SO_4 are the commonly used aqueous electrolytes, and they have the advantage of high ionic concentration and low resistance in comparison with organic electrolytes. The ionic conductivity of aqueous electrolyte highly relies on the temperature, pressure and molar concentration of the salts in deionised water. Therefore, aqueous electrolyte with high molar concentration can exhibit high ionic conductivity which will significantly enhance the power density of the supercapacitor and reduce the device resistance. Furthermore, the aqueous electrolyte can be prepared and utilized without complex preparation conditions, while the organic electrolytes require stringently controlled preparation processes to make them into ultra-pure electrolytes. According to the literature survey, the most widely used aqueous alkaline electrolyte is potassium hydroxide (KOH). Among various electrolytes,

KOH is mostly preffered because of its high ionic conductivity (0.6 cm^{-1} for 6 M at 25 °C), low temperature activation, simplified fabrication and assembly process and high yield. KOH electrolyte is suitable for EDLCs, pseudocapacitors and hybridcapacitors. However, aqueous electrolytes have three main disadvantages. Firstly, the aqueous electrolyte based supercapacitor exhibits minimum operating voltage of 1.23 V due to the electrolysis of water. Secondly, the aqueous electrolyte requires proper encapsulation in order to prevent evaporation which will otherwise lead to a very short life time of the device. Finally, a solution holder-like filter paper separator is required for aqueous electrolytes based supercapacitor design, which increases the total thickness of the supercapacitor and develops difficulty for the device encapsulation design (Pal et al. 2019; Zhong et al. 2015).

1.7.2. Organic Electrolyte

Although extensive research is highly focused on the aqueous electrolyte based ESs, organic electrolyte-based ESs are currently dominating the commercial market owing to their high operation potential window typically in the range of 2.5 to 2.8 V. The wide potential window can provide significant enhancement in both energy density and power density of ES. Typical organic electrolyte for EDLCs in commercial market consists of conductive salts such as tetraethylammonium tetrafluoroborate ($TEABF_4$) dissolved in acetonitrile (AC) or propylene carbonate (PC) solvent. Nevertheless, most organic electrolytes have drawbacks of higher cost, a smaller specific capacitance, a lower conductivity, and safety concerns related to the flammability, volatility and toxicity. Also, organic electrolyte undergoes complicated purification process in a strictly controlled environment to remove any residual impurities that can lead to serious self-discharge issues and large performance degradation. Recently studies have been made to investigate the relationship between nanostructured activated carbon and its capacitive performance in different electrolytes. The results indicated that the specific capacitance value of activated carbon is higher in aqueous electrolytes (100-300 Fg^{-1}) than in organic electrolytes (50-150 Fg^{-1}). This is due to the fact that the effective size of the electrolyte ions in organic solutions is much larger when compared with those in water. Also, organic electrolytes show higher resistivity than aqueous electrolytes because of their large ion size, which need a higher pore size in the electrode. Moreover, the chemical

affinity between electrode surface and organic electrolyte influences the wettability of the electrode (Pal et al. 2019).

1.7.3. Ionic Liquid Electrolyte

Ionic liquids (IL's) are a class of organic salts composed solely of ions (cations and anions) with melting points below 100 □C. IL's possess desirable electrolyte properties such as high ionic conductivity, low vapour pressure, non-flammability, wide potential window and high thermal stability. The presence of a large asymmetric cation and an organic or an inorganic anion leads to the special combination of certain anions and cations which contributes to a low melting point. Imidazolium, pyrrolidinium, ammonium, sulfonium, phosphonium cation are the most commonly used ionic liquid based electrolyte in supercapacitors. Tetrafluoroborate (BF_4^-), hexafluorophosphate (PF_6^-), dicynamide (DCA^-), bis (trifluoromethanesulfonyl) imide ($TFSI^-$), bis (fluorosulfonyl) imide (FSI^-) are some of the IL anionic electrolytes. Higher ionic conductivity is provided by imidazolium based IL's where as larger potential window is provided by pyrrolidinium based IL's. Unfortunately, there are several main drawbacks with most IL's based electrolytes such as high cost and high viscosity which can limit their practical use in supercapacitors. Recently, Dong Zhou et al developed an IL based supercapacitor where 1-ethyl-3-methylimidazolium tetrafluoroborate (EMIM BF4) was used as the electrolyte and carbon nanosheets acted as electrode material. As a result, a specific capacitance of 147 F g^{-1} and a high energy density of 98 kW kg^{-1} were obtained along with good cycling life stability (10% loss after 10000 cycles) (Pal et al. 2019; Zhong et al. 2015).

1.8. Separator

Separator is an ion permeable membrane which electrically isolates the two electrodes in an electrochemical cell and prevents short circuit. It is usually made up of thin and highly porous films on membranes. Some common examples are cellulose, polymer membrane, glass fibre, ceramic, polyester, mica etc. Recently graphene oxide(GO) films and egg shell are used as separators. Herein, we use commercially available polymer membrane called celgard separator as the ion permeable membrane between two active electrodes. The polymer membrane looks like a smooth white sheet which can be altered into desired shape and size with respect to the device (Xu et al. 2021). The factors such as chemical

stability, thickness, porosity, poresize distribution, permeability, mechanical strength, wettability, thermal stability and surface morphology of separators have a great effect on supercapacitor performance.

1.9. Binder

Binder provides a firm contact between the active electrode material and the current collector through its adhesive nature. The most commonly used binders are,

- PVDF (Polyvinylidene fluoride) and
- PTFE (Polytetrafluoroethylene)

The property and content of binders highly influence the performance of the electrodes as well as supercapacitors. PTFE is hydrophobic in nature, and hence it may retard the ion penetration and change the nature of electrode as hydrophobic. A minium addition of polyvinylpyrrolidone(PVP- 3%) into PTFE binder increases the wettability and performance of the electrode material. There are other binding agents such as PVP (polyvinylpyrrolidone), PEDOT (poly(3,4- ethylenedioxythiophene)), PANI (polyaniline) which are analyzed and explored as alternate binders for supercapacitor electrodes.

1.10. Electrochemical Analysis

The as-prepared electrode material is subjected to necessary electrochemical analysis to identify its suitability as the electrode material for supercapacitor. The major electrochemical techniques are:

- Cyclic Voltammetry (CV)
- Galvanostatic Charge-Discharge (GCD)
- Electrochemical Impedance Spectroscopy (EIS)

The function and graphical representation of each technique gives important characteristics of the electrode material. Two different types of configurations are used for performing the electrochemical analysis; viz. two-electrode and three-electrode configuration.

In the two-electrode configuration, the applied potential is measured between the working and counter electrodes, and the resulting current is measured in either the working or

counter electrode lead. In the three-electrode configuration, the basic electrodes used are working electrode, counter electrode and reference electrode.

1.10.1. Types of electrodes

1.10.1.1 Working electrode: The working electrode carries out the electrochemical event of interest. The prepared electrode material for the experiment plays the role as working electrode. The voltage of this electrode is varied and corresponding current vs. voltage value is plotted. The working electrode material changes according to the experiment. Different materials will provide different potential windows. Some common examples of working electrode materials are gold, platinum, carbon etc.

1.10.1.2 Counter electrode: The counter electrode acts as a cathode i.e.; it conducts the electrons from the working electrode and completes the circuit. Most commonly used counter electrodes are graphite and platinum.

1.10.1.3 Reference electrode: A reference electrode has a well-defined and stable equilibrium potential. It is used as a reference point against which the potential of other electrodes can be measured in an electrochemical cell. Some common reference electrodes used in aqueous media include the saturated calomel electrode (SCE), standard hydrogen electrode (SHE), and the Ag/AgCl electrode.

The combination of these electrodes in different ways forms the two- and three-electrode configurations (Simon and Gogotsi 2008b; Simon et al. 2014).

1.10.2 Two-Electrode Configuration

This method is also called as device method, which calculates the total specific capacitance of the device and measures the total cell voltage. A typical symmetric two-electrode configuration consists of cathode and anode current collectors coated with the same active material. The current collectors are coated with active electrode materials using different deposition techniques such as drop casting, printing, spin coating etc. The two electrodes are isolated via a porous separator to avoid electrical contact. The two electrodes and separator assembly are immersed in an appropriate electrolyte solution based on the application and nature of the electrode materials. The separator permits the flow of ionic current between the electrodes, and it hinders the flow of electronic current,

preventing the internal discharging of the cell. The whole electrode electrolyte assembly of the capacitor is put together into a metal case which can be tightly sealed to prevent from outside contact (Stoller and Ruoff 2010).

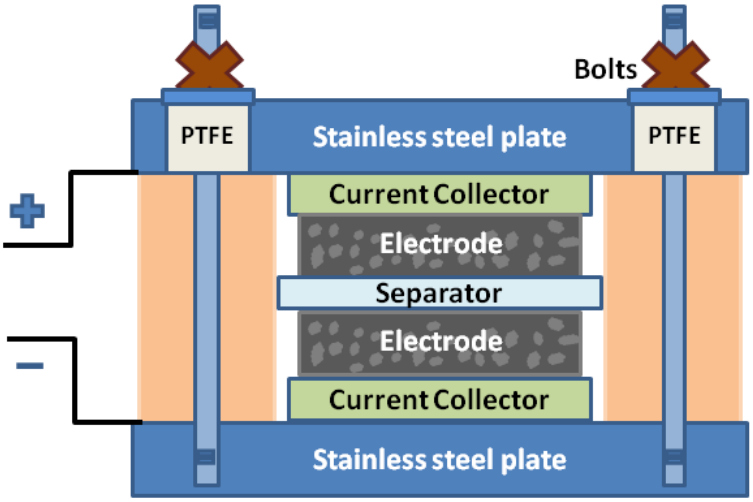

Figure 1.10. Schematic of two-electrode test cell configuration

1.10.3 Three-Electrode Configuration

Three-electrode configuration is a half-cell measurement where the specific capacitance and voltage of the electrode material is only obtained. Here the counter and reference electrodes are isolated from each other. A potential difference is maintained between the reference and working electrode. Only the potential differences of working electrode are calculated and the counter electrode is voltage independent (Stoller and Ruoff 2010).

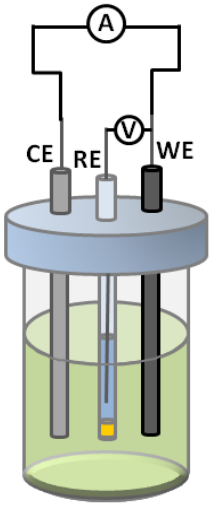

Figure 1.11. Schematic of three-electrode configuration

1.10.4 Electrochemical Characterization Techniques

1.10.4.1 Cyclic Voltammetry

Cyclic voltammetry (CV) is the first experiment performed in an electrochemical study of a compound, biological material, or an electrode surface. The effectiveness of CV results from its capability to rapidly record the redox behaviour over a wide potential range. In this technique, a linear voltage ramp is applied to the electrode (or a device) within a set voltage range to measure the resulting current. A CV test is carried out by applying a positive (charging) voltage sweep, dV/dt (scan rate) in a specific voltage range and then reversing (discharging) the voltage sweep polarity immediately after the maximum voltage is achieved whilst measuring the current flow.

A typical CV curve recorded in a three-electrode configuration is given in **Figure 1.12**. The important parameters of a cyclic voltammogram are anodic peak potential (E_{pa}), cathodic peak potential (E_{pc}), anodic peak current (i_{pa}), and cathodic peak current (i_{pc}). There are three regions in both the forward and backward scanning directions. These regions are capacitive current, Faradaic current and oxidation current.

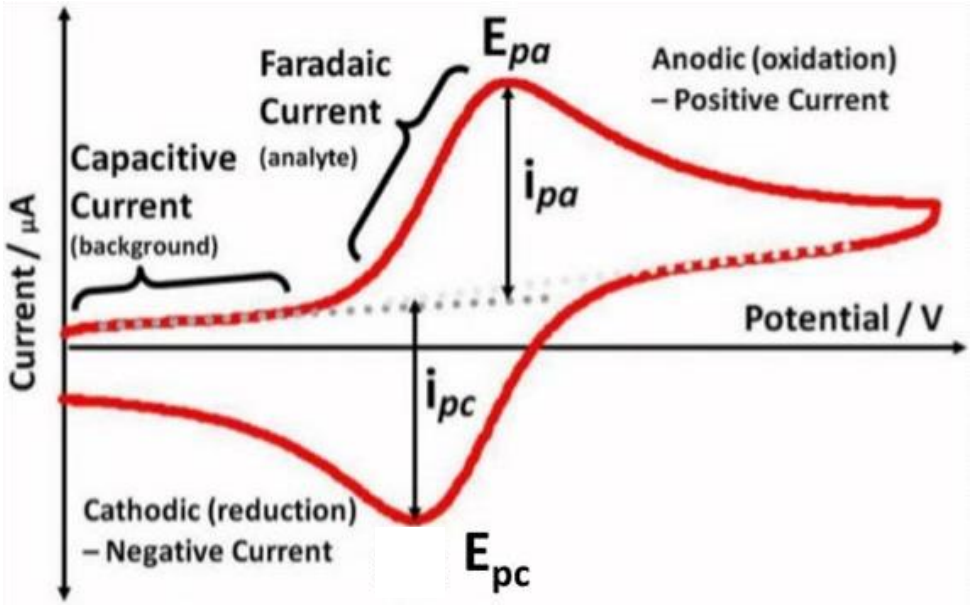

Figure 1.12. A typical CV recorded for a three electrode configuration (Adapted from the reference (Khan et al. 2018))

The Specific capacitance (C_{SP}) from a CV in a three-electrode system is calculated using,

$$C_{sp} = \frac{A}{2(FVm)} \quad (1.3)$$

where A is the area under the curve, F is the scan rate, V is the voltage window, and m is the mass of the active material per electrode.

An ideal CV curve of the supercapacitor in two-electrode configuration gives a rectangular shape, but in real cases, EDLCs exhibit a deformed rectangular shaped CV (**Figure 1.13**), whereas in the case of pseudocapacitive-type materials, oxidation and reduction peaks can be observed due to Faradaic reactions (**Figure 1.13).**
The specific capacitance (C_{SP}) from a CV in a two-electrode system is calculated using,

$$C_{sp} = \frac{A}{(FVm)} \quad (1.4)$$

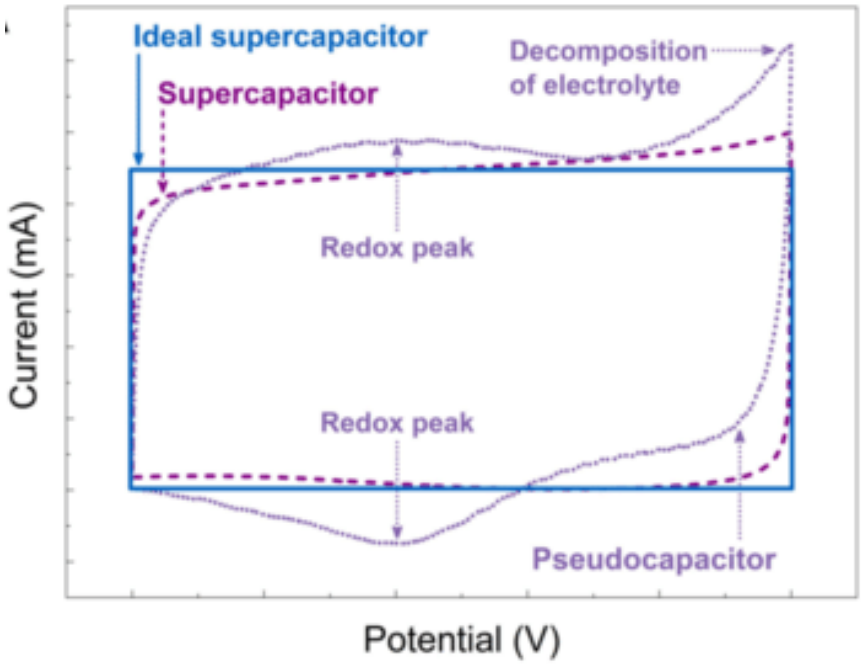

Figure 1.13. Cyclic voltammetry curves of (blue line) ideal capacitor, (dashed line) EDLC, and (dotted line) pseudocapacitive materials (Adapted from the reference (Castro-Gutiérrez et al. 2020))

1.10.4.2 Galvanostatic Charge - Discharge (GCD)

Galvanostatic charge - discharge (GCD) is the most popular technique used to calculate the specific capacitance and cycling stability of electrodes or devices. The principle of GCD is to measure the voltage with respect to time simultaneously when applying a constant current to an electrode or a device between two pre-set voltage limits. As the voltage changes linearly with time, perfect triangular-shaped curves are obtained. Exact triangular curves cannot be obtained in a pseudocapacitor because of Faradaic behaviour. The initial line of the discharge curve is due to voltage drop or IR drop which is caused by equivalent series resistance (ESR). The different shapes of the GCD curve obtained for EDLC and pseudocapacitors are illustrated in **Figure 1.14.** From the figure, EDLC materials exhibit linear charge-discharge curves, while pseudocapacitor deviates from linear behavior due to the redox reactions that take place in the electrodes.

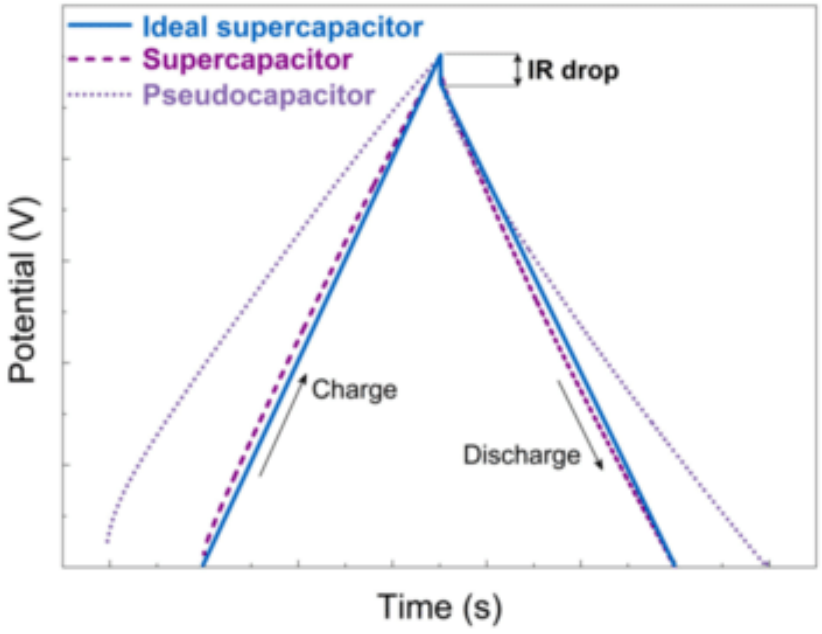

Figure 1.14. GCD curves of (blue line) ideal capacitor, (dashed line) EDLC, and (dotted line) pseudocapacitive materials (adapted from the reference (Castro-Gutiérrez et al. 2020))

The equation to find specific capacitance (C_{SP}) from slope of the discharge curve in the three-electrode system is given by,

$$C_{sp} = \frac{i}{m\left(\Delta v/\Delta t\right)} \quad (1.5)$$

where i is the average cathodic current, $\Delta v/\Delta t$ is the slope of the discharge curve and m is the mass of active material in single electrode.

The equation to find specific capacitance (C_{SP}) from slope of the discharge curve in the two-electrode system is given by,

$$C_{sp} = \frac{2i}{m\left(\Delta v/\Delta t\right)} \quad (1.6)$$

1.10.4.3 Electrochemical Impedance Spectroscopy (EIS)

EIS is the electrochemical study of a device in terms of a wide range of frequencies. In general, the term impedance means the total effective resistance of the electrical circuit caused by the combined effect of ohmic resistance, capacitance, and reactance. Similarly, in EIS, the resultant impedance caused by solution resistance, charge transfer resistance, electrochemical double-layer capacitance, and reactance due to adsorption and diffusion is calculated. Herein, a small amplitude (5 to 10 mV) alternative current over the frequency range of 0.01 Hz to 100 kHz is applied to the device. The EIS graph is plotted between real impedance (Z′) and imaginary impedance (Z").

The X-intercept point of the impedance spectra at the highest frequency side gives the equivalent series resistance (ESR) of the supercapacitor test cell which denotes the solution resistance of the electrolyte represented as R_s (**Figure 1.15**). The semicircle at the high frequency side is related to the charge transfer resistance that occurs due to the electronic resistance within the electrode materials. The vertical line at the lower frequency indicates ideal capacitive behavior. The line at the low frequency region makes a 45^o angle with the real axis, the Warburg line, and is a result of the frequency dependence of ion diffusion at the electrolyte- electrode interface.

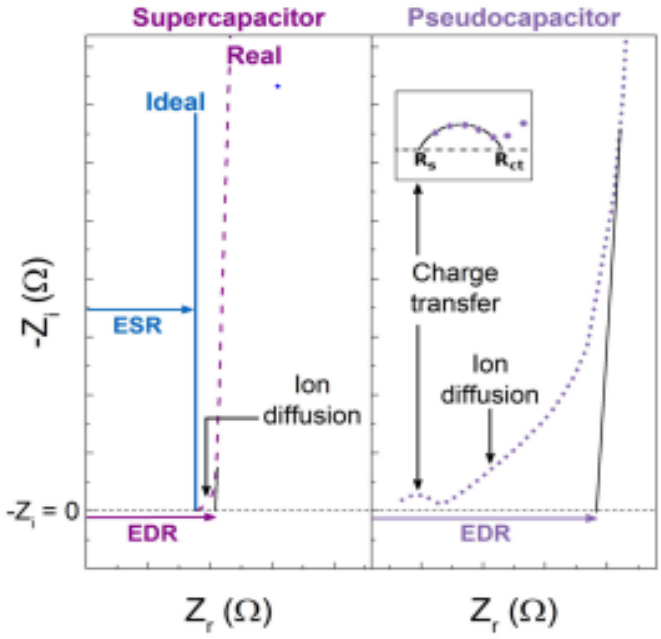

Figure 1.15. Nyquist plot of an ideal capacitor (blue line), EDLC (dashed line), and pseudocapacitor (dotted line) (adapted from the reference (Castro-Gutiérrez et al. 2020))

1.10.5 Specific energy and Specific power

Evaluating specific energy and specific power values are very crucial parameters for the supercapacitor for its practical applications.

The specific energy and specific power values can be measured by the following equations

$$E = \frac{1}{2} C_{sp} V^2 \qquad (1.7)$$

$$P = \frac{E}{\Delta t} \qquad (1.8)$$

where C_{sp} is the specific capacitance, V is the operating potential window and Δt is the discharging time.

The value of C_{sp} depends on the electrode materials used and V depends on the nature of electrolyte used. As observed from the equation (1.7), the specific energy of the supercapacitors can be increased either by selecting appropriate electrode materials or by choosing better electrolytes which can provide large voltage windows. The present thesis

work mainly focuses on the increasing in the C_{sp} values to enhance the specific energy. The relation connecting the specific capacitance and the nature of the electrode materials, are explained using the basic equation for the capacitance of a capacitor. The equation for the capacitance can be denoted as

$$C = \frac{\varepsilon A}{d} \tag{1.9}$$

where ε is the permittivity, A is the area of the electrode, and d is the separation between the two electrodes

Hence, to increase C, one must either improve the area of the electrodes or reduce the separation between the electrodes. For enhancing the surface area of the supercapacitor electrodes, the finest way is to select nanomaterials that have high surface to volume ratios. Among the different types of nanomaterials, binary transition metal hydroxides, oxides, sulfides, and selenides are highly promising for supercapacitor applications.

1.11 Binary transition metal (BTM)-based nanomaterials

Binary transition metal (BTM)-based nanomaterials including binary transition metal hydroxides such as $Co(OH)_2$/$Ni(OH)_2$ (Sari et al. 2022), CuCo-LDH (Kumar et al. 2021), $Mn(OH)_2$/$Co(OH)_2$ (Anjana et al. 2021) etc., binary transition metal oxides (BTMOs) such as $NiCo_2O_4$ (Wu et al. 2014), $MnFe_2O_4$ (Sharifi et al. 2021), $CoFe_2O_4$ (Sankar et al. 2015), $MnCo_2O_4$ (Akhtar et al. 2016) etc., binary transition metal sulfides such as $NiCo_2S_4$ (Shinde et al. 2019), $NiFe_2S_4$ (Atram et al. 2021), $MnCo_2S_4$ (Nguyet et al. 2022) etc., and binary transition metal selenides such as, Ni-Co-selenide (Jiang et al. 2022), MnCo-selenide (Miao et al. 2019) etc., are currently of great interest for the supercapacitor devices because of their environment-friendly nature, unique size effects, and substantially enhanced kinetics. Among the different BTMs, Mn and Co based binary systems are of great demand because of their cost-effectiveness, high theoretical capacitance, synergy of both transition metal, and the presence of variable valence states (Gonçalves et al. 2021; Rendale et al. 2022). The thesis deals with the application of Mn-Co based hydroxides, oxides, sulfides, and selenides as the electrode materials for supercapacitors.

1.12 Mn-Co-based nanomaterials

Mn-Co-based nanomaterials are highly attractive materials for various optoelectronics, nanoelectronics, and electrochemical sensing applications. The research interest in Mn-Co-based nanomaterials is in high demand because these materials are characterized by their eco-friendliness, greater specific capacitance, enlarge operating voltage, large active sites, and increased stability. Moreover, Co has a higher oxidation potential, and Mn is able to deliver more electrons. so the binary Mn-Co based nanostructure has good electronic conductivity (Gonçalves et al. 2021).

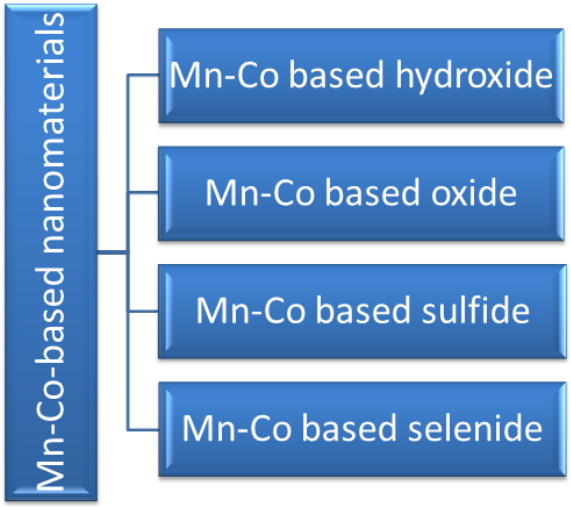

Figure 1.16. Different types of Mn-Co-based nanomaterials

1.12.1 $Mn(OH)_2/Co(OH)_2$

$Mn(OH)_2$ and $Co(OH)_2$ have been extensively studied as pseudo-capacitive electrode materials for the past several years because of their low price, eco-friendliness, easy preparation method, and superior capacitive performance. Generally, hexagonal $Mn(OH)_2$ and $Co(OH)_2$ were utilized as supercapacitor electrodes due to their outstanding electrochemical performance (Maile et al. 2018). The hexagonal $Mn(OH)_2$ is a layered brucite crystal. Each layer consists of edge-sharing $Mn(II)(OH)_6$ octahedron and neighboring layers are attached by van der Waal forces (Yan et al. 2014). Cobalt hydroxides mainly crystallize in two polymorphs, α-$Co(OH)_2$, and β-$Co(OH)_2$. β-$Co(OH)_2$ is a stoichiometric phase of the composition $Co(OH)_2$ with brucite-like structure and contain a hexagonal packing of hydroxyl ions with Co(II) occupying alternate rows of octahedral sites. On the other hand, α-$Co(OH)_2$ are reported to be isostructural with hydrotalcite-like compounds that consist of positively charged $Co(OH)_{2-x}$ layers and

charge balancing anions (e.g., CO_3^{2-}, Cl^-, NO_3^-, etc.) in the interlayer. β-$Co(OH)_2$ has recently attracted increasing attention due to its high specific capacitance. Hence the β-forms are theoretically expected to exhibit superior electrochemical activity as compared to the α-form. Thus, the β-$Co(OH)_2$ may be a more promising electrode material.

1.12.2 Spinel $MnCo_2O_4$

The spinel oxides of the type AB_2O_4 (where A and B are transition metals) are widely employed as electrode materials in lithium-ion batteries, catalysts, and magnetic materials (Akhtar et al. 2016). In particular, the spinel $MnCo_2O_4$ is widely used in various applications, especially for energy conversion and storage, due to its properties such as, low cost, high redox performance, different valence state, and eco-friendly nature. The $MnCo_2O_4$ has two types of spinel structures: the normal and inverse spinel (Hua et al. 2019). The unit cell of spinel $MnCo_2O_4$ consists of 8 Mn atoms, 16 Co atoms, and 32 O atoms. In normal spinel unit cell, there are 8 Mn atoms taking the tetrahedral (8a) sites, while 16 Co atoms taking the octahedral (16d) sites. On the other hand, in the inverse spinel, all the tetrahedral (8a) sites are occupied by 8 Co atoms while the octahedral (16d) sites are occupied by the rest 8 Co atoms and 8 Mn atoms. It is reported that the inverse spinel structure is more stable than the normal spinel structure (Li et al. 2015b).

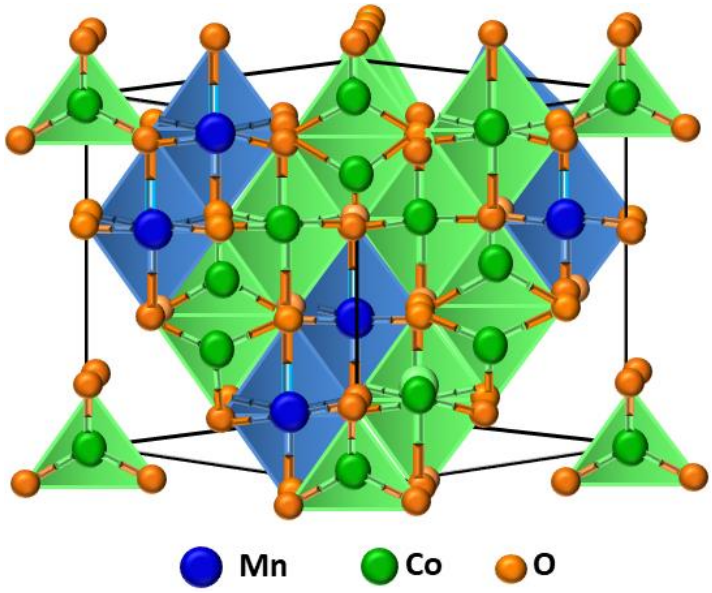

Figure 1.17. The atomic structure of the stable $MnCo_2O_4$ inverse spinel structure. The largest green, middle sized blue and smallest red spheres are Mn, Co and O atoms, respectively.

1.12.3 $MnCo_2S_4$

$MnCo_2S_4$ has been considered to be an outstanding electrode material in electrochemical energy storage arears because of the oxidation efficiency obtained from cobalt element and a lot of electrons/ions obtained from manganese element. In addition, binary sulfide-based material shows high conductivities than their oxide-based counterparts and exhibit superior electrochemical performance. The primitive and super-cells of $MnCo_2S_4$ are respectively shown in **Figure 1.18 (a)** and **(b)**, where the Mn atoms occupy the tetrahedral sites and the Co atoms occupy the octahedral sites.

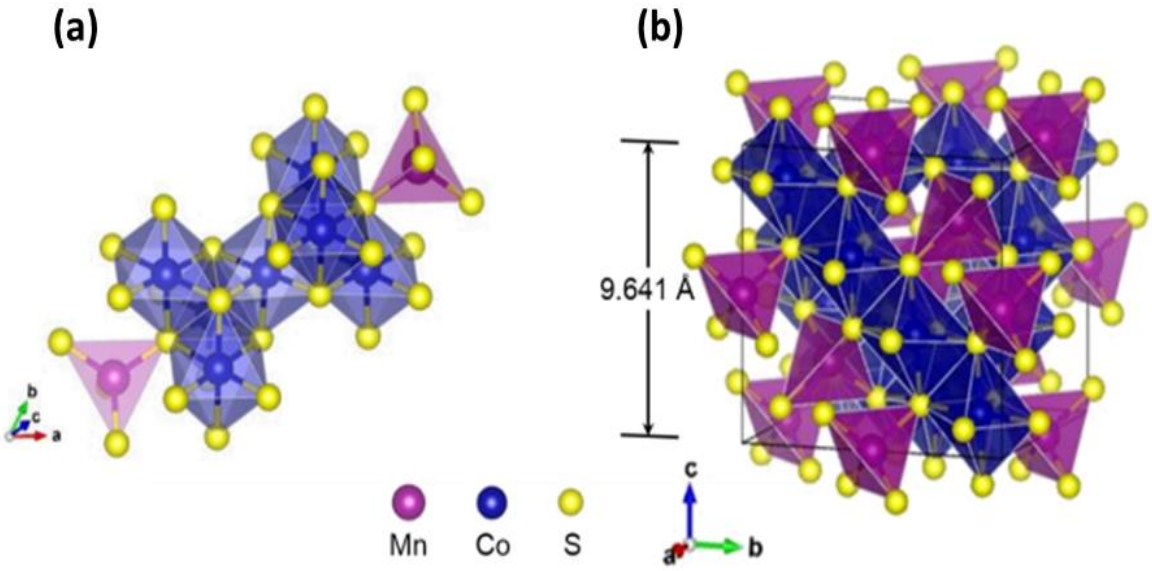

Figure 1.18. The schematic of $MnCo_2S_4$ (a) primitive- and (b) super-cells. (Adapted from the reference (Sadighi et al. 2018))

1.12.4 MnCo-selenides

MnCo-based selenides deliver superior electrochemical stability, better electronic conductivity, and greater electrochemical activity and hence can be considered as excellent electrode materials for supercapacitors. Selenium (Se) is a Group VI element which is situated with oxygen (O) and sulfur (S) elements. Hence it is clear that Se element also provides lower ionization energy, outstanding metallic property, and better conductivity.

1.13 Synthetic strategies of Mn-Co based nanomaterials

1.13.1 Microwave-assisted method

The microwave-assisted method is broadly used to prepare Mn-Co based nanomaterials as a fast synthetic method. The microwave-assisted method has the benefit of heat control in the synthesis of binary metal-based nanomaterials, whose growth is highly sensitive to the reaction conditions. In addition, microwave-assisted methods can overcome side reactions and deliver fast kinetics of crystallization. For the one-pot synthesis of different bimetallic oxide nanoparticles and nanostructures such as, $NiCo_2O_4$, $MnCo_2O_4$, and $ZnFe_2O_4$, we can utilize microwave-assisted method (Akhtar et al. 2016). The microwave-assisted method has many advantages, such as a large reaction rate, fast volumetric heating, low reaction time and greater yield of products, compared to other traditional heating techniques. Sannasi *et al*. synthesized flake like $MnCo_2O_4$ via simple microwave-assisted method with superior supercapacitive performance (Sannasi and Subbian 2019). Nissinen et al. used the same method to produce spinel $MnCo_2O_4$ for catalytic studies (Nissinen et al. 2003). However, it is difficult to control the morphology and phase of binary transition metal (BTM)-based nanomaterials in microwave-assisted synthesis. Therefore, more effective techniques are needed to crystallize nanomaterials with controllable phase and morphology.

1.13.2 Electrodeposition method

The electrodeposition technique is broadly used to produce Mn-Co based nanomaterial coatings. Compared with other preparation methods, the electrodeposition technique includes only one synthesis step in the entire experimental procedure. The electrodeposition is based on the principle of electrochemical redox reactions. When an electric current passes through a metal salt solution, the metal is deposited at the cathode side. At the cathode side, all other reactions depend on the choice of the anion, the deposition potential, and the pH of the solution (Sadighi et al. 2018). Sadighi *et al*. used the electrodeposition technique to produce $MnCo_2S_4$ nanosheets grown on carbon paper (MCS/CP) for application in Li-O_2 batteries (Sadighi et al. 2018). Sahoo *et al*. reported a simple one-step electrodeposition technique for the fabrication of spinel

$MnCo_2O_4$ nanosheet arrays on indium doped tin oxide (ITO) coated glass substrates for the supercapacitor device application (Sahoo et al. 2015b). However, it is very difficult to scale up the production, which remains the major problem with this method.

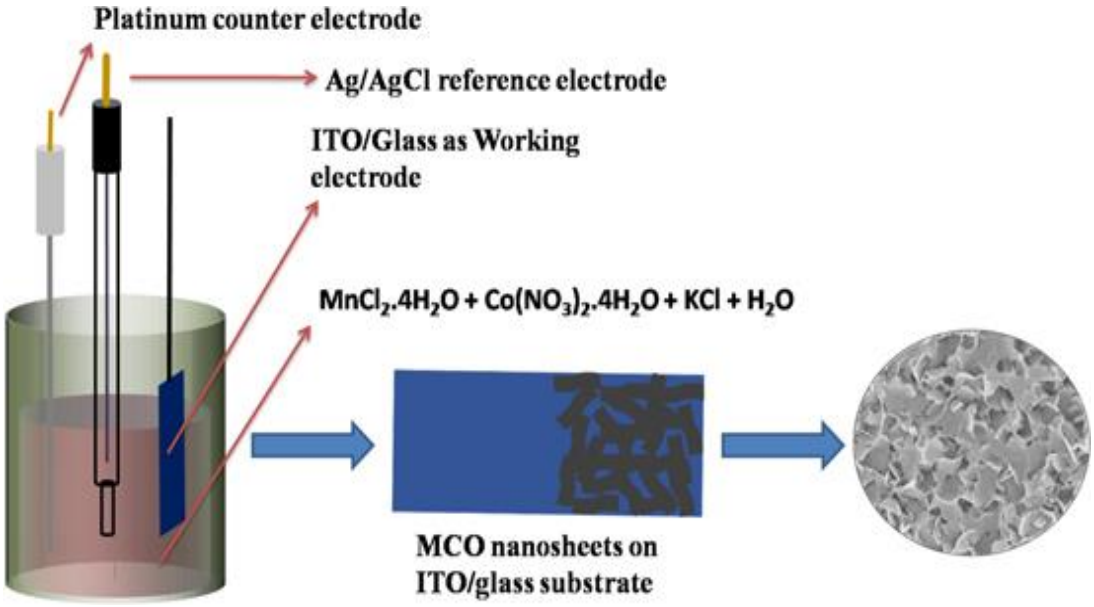

Figure 1.19. Schematic diagram of the electrodeposition process of spinel $MnCo_2O_4$ nanosheet (Adapted from the reference(Sahoo et al. 2015b)).

1.13.3 Chemical bath deposition (CBD)

Chemical Bath Deposition (CBD) is considered a simple method. The CBD technique consists of the controlled precipitation of a desired compound from the solution on the appropriate substrate. This technique needs a vessel to carry the aqueous chemical solution and the substrate on which deposition is to be achieved. In addition, a stirring mechanism and a constant temperature bath are also required for proper working. The rate of the chemical reaction is controlled by a number of parameters, such as the concentration of the precursor, the pH of the solution, and the solution temperature. The CBD technique can be conducted both in acidic and alkaline solutions.

1.13.4 Hydrothermal/Solvothermal method

The hydrothermal/solvothermal technique is one of the most common methods for synthesizing Mn-Co based nanomaterials. Hydrothermal and solvothermal methods are similar, except for the difference in the solution. The former uses water as the solvent for

the reacting chemicals, whereas the latter uses solvents other than water. Under high temperature and high pressure, the materials dissolve and recrystallize with the help of solvents. In general, a temperature higher than 100 ^{o}C is selected to obtain the pressure of vapor saturation, and by using a closed system, an autogenous pressure will be generated. Other experimental components, such as the amount of liquid and dissolved salts, also have an important effect on the final products (Lee et al. 2021). Also, the hydrothermal/solvothermal technique is known as a low-cost synthetic method for the preparation of transition metal-based nanomaterials. The method has many advantages, such as the usage of nontoxic chemicals, high purity of the sample, simple procedure, and highly crystalline particles (Jiang et al. 2022). Lee *et al*. reported the fabrication of mesoporous $MnCo_2S_4$ directly grown on porous Ni foam by a simple hydrothermal method for high-performance supercapacitors (Lee et al. 2021). Miao *et al*. used the hydrothermal method to produce urchin-like MnCo-selenide on nickel foam for energy storage applications (Miao et al. 2019). Saravanakumar et al. used this method to fabricate $MnCo_2O_4$ nanospheres for the superior supercapacitor application (Saravanakumar et al. 2019).

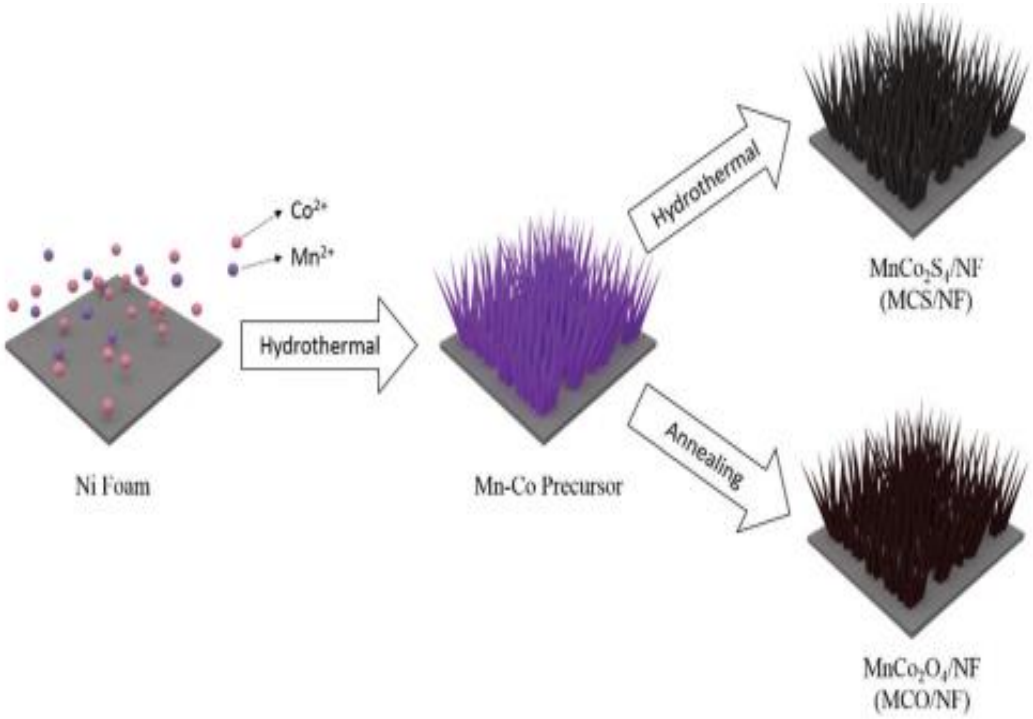

Figure 1.20. Schematic illustration of fabrication of nanostructured $MnCo_2S_4$ and $MnCo_2O_4$ grown uniformly on a Ni foam (Adapted from the reference(Hsu et al. 2021)).

1.14 Objectives of the thesis

Employing an efficient, cost-effective, and eco-friendly electrode material with superior electrochemical activity for supercapacitor applications is the main objective of the present work. The focus of this thesis is on the synthesis and analysis of the structural and electrochemical performance of Mn-Co-based nanomaterials for supercapacitor applications. The Mn-Co-based hydroxides/oxides/sulfides, and selenides having different morphologies were prepared, and their electrochemical properties were studied via a symmetric two-electrode configuration. The major objectives of the thesis are:

- Synthesis of $Mn(OH)_2/Co(OH)_2$ nanostructures via a simple chemical bath deposition method (CBD) for use as a cost effective electrode for supercapacitor applications
- Fabrication and performance studies of symmetric supercapacitors based on spinel $MnCo_2O_4$ based electrode materials
- Synthesis and characterization of nanostructures and fabrication of a symmetric supercapacitor based on $MnCo_2S_4$ cathodes
- Evaluation of the electrochemical performance of a $MnCoSe_2$ based system in symmetric two-electrode configuration
- Fabrication and performance studies of an asymmetric supercapacitor based on a $MnCo_2S_4$ cathode and rGO anode

Chapter 2

Layer-by-layer growth of $Mn(OH)_2/Co(OH)_2$ nanoparticles over different current collectors for supercapacitor application

2.1. Outline of the chapter

Transition metal hydroxides have emerged as highly promising electrode materials for supercapacitor applications owing to the rapid redox reactions between transition metal ions and OH^- ions. The present chapter deals with the synthesis of binary metal hydroxide ($Mn(OH)_2/Co(OH)_2$) nanoparticles over two different substrates, viz. carbon cloth ($Mn(OH)_2/Co(OH)_2$/CC) and nickel foam ($Mn(OH)_2/Co(OH)_2$/NF) by a simple and affordable chemical bath deposition method. Symmetric supercapacitor devices have been fabricated using $Mn(OH)_2/(Co(OH)_2$ nanoparticles and the electrochemical performance analysis in two electrode configurations indicates that at 5 mV s^{-1}, the $Mn(OH)_2/Co(OH)_2$/CC electrode exhibits a specific capacitance of 385 F g^{-1}, and the $Mn(OH)_2/Co(OH)_2$/NF electrode gives 400 F g^{-1}. At a specific power of 1 kW kg^{-1}, the supercapacitor based on $Mn(OH)_2/Co(OH)_2$/CC and $Mn(OH)_2/Co(OH)_2$/NF electrodes respectively gives a specific energy of 27 W h kg^{-1} and 29 W h kg^{-1}. The outstanding electrochemical performance of the $Mn(OH)_2/Co(OH)_2$/NF electrode is because of the high porosity that provides a large active surface area for electrochemical reaction, good electrical conductivity, and excellent mechanical strength.

2.2. Introduction

Supercapacitors have received tremendous attention as advanced high-performance energy storage systems because of their ultra-high specific power and exceptional storage properties compared to contemporary gadgets (Rakhi et al. 2016a; Rakhi et al. 2016b; Xiao et al. 2020a). However, the energy densities of supercapacitors still need to be constantly improved to cater to the stringent requirements of emerging commercial applications (Xiao et al. 2020a). Therefore, advanced supercapacitor electrode materials with enhanced energy density must be developed without compromising the power density and long life (Barik et al. 2020; Wang et al. 2020a). The supercapacitor can be broadly classified into electric double-layer capacitors and pseudocapacitors in terms of charge storage mechanism. EDLC electrodes are mainly fabricated using carbon derivatives (activated carbon, carbon nanotubes, graphene, etc.), and pseudocapacitor electrodes are fabricated using conductive polymers, and transition metal oxides (TMOs)/hydroxides (Wang et al. 2020b).

Among the different transition metal hydroxides, $Mn(OH)_2$, and $Co(OH)_2$ have been broadly investigated as efficient pseudocapacitive materials because of their high specific capacitance, increased energy density, eco-friendly nature, fast ion transport rate, and extended cyclic stability (Anandan et al. 2013; Su et al. 2019; Wang et al. 2014; Wang et al. 2020a; Yu et al. 2017). The electrochemical performance of these transition metal hydroxides is widely reported in the three-electrode configuration. Hexagonal $Mn(OH)_2$ nanoplates developed by Yan et al. demonstrated 116.1 F g^{-1} specific capacitance at 1 A g^{-1} (Yan et al. 2014). Anandan et al. reported a high specific capacitance of 127 F g^{-1} at 0.5 m A cm^{-2} for $Mn(OH)_2$ nanoparticles prepared using a simple sonochemical method (Anandan et al. 2013). Yan et al. published a specific capacitance of 240.2 F g^{-1} at 1 A g^{-1} for nanosheet $Mn(OH)_2$ thin films (Yan et al. 2014). $Co(OH)_2$ demonstrates excellent electrochemical activity in alkaline electrolytes, Salunkhe et al. developed $Co(OH)_2$ rods grown over nickel foam with a greater specific capacitance value of 1116 F g^{-1} at 2 A g^{-1} for $Co(OH)_2$ rods grown over nickel foam (Salunkhe et al. 2014). Aghazadeh et al. reported a high specific capacitance of 881 F g^{-1} at 5 mV s^{-1} for β-$Co(OH)_2$ nanosheets (Aghazadeh and Ganjali 2017). Yang et al. fabricated $Co(OH)_2$ over carbonized melamine foam via the electrochemical deposition method, as a supercapacitor electrode, and reported a specific capacitance of 284.71 F g^{-1} at 5 mV s^{-1} (Yang et al. 2019). Zhao

et al. reported a high specific capacitance of 1915.88 F g^{-1} at 1 A g^{-1} for Mn doped $Co(OH)_2$ nanosheet material (Zhao et al. 2020). Recently, Bai et al. reported cobalt manganese hydroxide-based electrode materials with nanowire-like morphology (CoMn-HW) and nanosheet-like morphology (CoMn-HS) which delivers a specific capacitance of 528 F g^{-1} and 485 F g^{-1} at current density 1 A g^{-1} for CoMn-HW and CoMn-HS respectively (Bai et al. 2020). The combined effect of metal hydroxides of manganese and cobalt will greatly enhance the charge-discharge characteristics and cycle life of the electrode (Bai et al. 2020; Reghu Nath et al. 2019; Sheng et al. 2019). All these measurements were carried out in a three-electrode configuration.

$Mn(OH)_2/Co(OH)_2$ nanocomposite can be a promising supercapacitor electrode material. In the present study, we report the direct growth of $Mn(OH)_2/Co(OH)_2$ nanocomposite over a conductive carbon cloth substrate for the fabrication of binder-free supercapacitor electrodes. The high electrical conductivity of flexible carbon fabric substrate is characterized by its high values of surface area and porosity (He et al. 2013). Besides, the fabric holds itself upon rough folding/twisting, making it a reliable flexible substrate (Yu et al. 2013). The direct deposition of the active materials over the current collector helps in reducing the contact impedance between the current collector electrode substrate and the active material, simplifying the electrode fabrication process (Chen et al. 2017a; Gomez and Kalu 2013; Li et al. 2016; Wang et al. 2016). Symmetric supercapacitors are fabricated using the as-prepared nanocomposite electrodes in 2 M KOH electrolyte, and the electrochemical performances are evaluated in a two-electrode configuration. Two-electrode configuration measurements give more reliable results to real test cell applications compared to the three-electrode measurement (Khomenko et al. 2005; Stoller and Ruoff 2010). The incorporation of $Mn(OH)_2/Co(OH)_2$ nanocomposite into carbon cloth without using a binder will increase the conductivity of the electrode and electrode-electrolyte accessibility. In addition, as a comparison, we study the direct growth of $Mn(OH)_2/Co(OH)_2$ nanocomposite over a conductive 3D nickel foam substrate as electrodes for supercapacitors. The result shows that $Mn(OH)_2/Co(OH)_2$ nanocomposite over nickel foam delivers superior performance than that grown over carbon cloth. The nickel foam substrate with an open porous structure contains a large electroactive surface area and can access a greater number of electrolyte ions for the electrochemical reaction (Han et al. 2018; Mola et al. 2021; Su et al. 2019).

2.3. Experimental Section

2.3.1. Synthesis of $Mn(OH)_2/Co(OH)_2$ nanoparticles over carbon cloth substrate

$Mn(OH)_2/Co(OH)_2$ nanocomposite was grown directly over the flexible free-standing carbon fabric substrate by following a simple two-step chemical bath deposition (CBD) process. The direct deposition of $Co(OH)_2$ nanoparticles over a flexible carbon cloth substrate by a CBD technique was performed in a beaker under an ambient atmosphere. In a typical procedure, a rectangular piece of carbon cloth (7302003, Fuel Cell Store) substrate of area 2 cm^2 was immersed in a chemical bath containing 0.1 M $CoCl_2.6H_2O$ in 10 ml of DI water under constant magnetic stirring. NH_4OH solution (5wt %) was slowly added into the above solution mixture until the pH reached 9, which was observed using a pH meter. The reaction mixture was stirred vigorously for another 3 h at room temperature. The resulting solution was kept without stirring for 1h and the $Co(OH)_2$ nanoparticle deposited carbon substrate was taken out. $Mn(OH)_2$ nanoparticles were further deposited over the same carbon substrate, the surface of which is already coated with $Co(OH)_2$ nanoparticles by repeating the CBD technique. The substrate was immersed in a chemical bath containing 0.1 M $MnCl_2.6H_2O$ in 10 ml of DI water and the solution pH was adjusted to 9 by the careful addition of NH_4OH solution (5wt %). The reaction mixture was subjected to magnetic stirring for 3 h and then allowed to rest for 1h, before taking out the binary hydroxide nanoparticles coated carbon substrate. The obtained Mn $(OH)_2/Co(OH)_2$ nanocomposite-coated carbon substrate was washed multiple times with DI water and dried at 60 ^oC for 1 h in air. Prior to the deposition of the nanomaterials, the carbon cloth substrate used in the present study was cleaned by rinsing with water and ethanol and dried. After each step of deposition, the mass loading of the samples was calculated from the weight of the carbon cloth substrates before and after the deposition using a microbalance (XP26, METTLER TOLEDO). The schematic of the preparation of the $Mn(OH)_2/Co(OH)_2$ nanocomposite over the carbon fabric is illustrated in **Figure 2.1**.

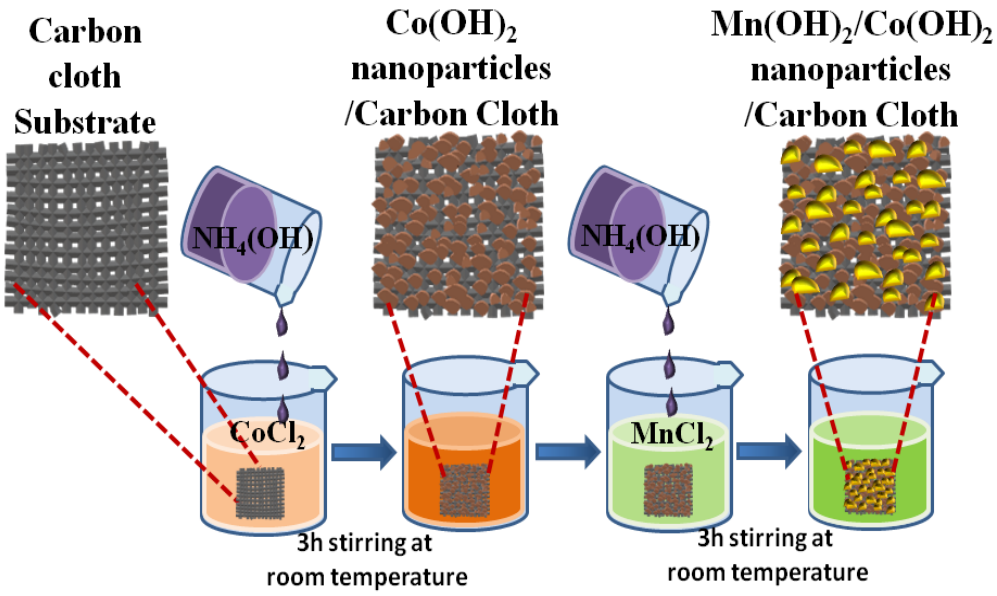

Figure 2.1. The schematic of the preparation of carbon cloth supported $Mn(OH)_2/Co(OH)_2$ nanoparticles electrode.

2.3.2. General characterization

The as-prepared $Mn(OH)_2/Co(OH)_2$ nanoparticles were characterized using a powder X-ray diffraction system (X-ray diffractometer, Philip's X'pert Pro) equipped with Cu Kα radiation (λ= 0.15406 nm). Fourier Transform Infrared spectroscopy (FTIR) measurements were carried out using Bruker spectrometer, Tensor 27. X-ray photoelectron spectroscopy (XPS) measurements of the samples were carried out using PHI 5000 Versa Probe II (purchased from ULVAC-PHI Inc., USA) equipped with micro-focused (200 µm, 15 KV) monochromatic Al-Kα X-Ray source (hν = 1486.6 eV). Brunauer-Emmett-Teller (BET) surface areas of the samples were determined using Micrometritics Tristar 3000 model surface area analyzer at 77 K. Prior to the BET measurements, the samples were degassed at 150˚C for 10 h. The surface morphology of the samples was investigated by Scanning Electron Microscopy (EOL JSM-5600 LV scanning electron microscope). The microstructure and particle size of the material were analyzed by Transmission Electron Microscopy together with a Selected Area Electron Diffraction Pattern (FEI, TECNAI S twin microscope with an accelerating voltage of 100 kV).

2.3.3. Preparation of electrodes and electrochemical characterizations

Electrochemical performances of the fabricated electrodes were analyzed in a symmetric two-electrode configuration using VMP3 bio-logic electrochemical workstation. The carbon cloth coated with $Mn(OH)_2/Co(OH)_2$ nanoparticles (1 cm ×1 cm) was used as the electrodes. The electrodes were separated by a polypropylene separator (Celgard 3400), which was previously dipped in a 2 M KOH, and the assembly was sandwiched in a supercapacitor test cell (ECC-std, EL-Cell GmbH). The electrochemical performance of the electrode materials was measured in the symmetric two-electrode configuration by cyclic voltammetry (CV), galvanostatic charge-discharge (GCD), and electrochemical impedance spectroscopy (EIS) techniques. The CV curves were recorded for a range of 0 - 1 V at different scan rates, (5-200 mV/s). The GCDs were measured for the same range of voltage, under different current densities, from 0.25 mA/g to 2 mA/g. The EIS was performed in the frequency range from 100 kHz to 10 MHz at open-circuit voltage by applying a 5 mV signal.

2.4. Results and Discussion

2.4.1. Structural and morphological characterization

X-ray diffraction pattern (XRD) of the as-synthesized binary metal hydroxide nanocomposite electrode material is shown in **Figure 2.2 (a)** The main mineralogical phases obtained in the synthesized nanoparticles are $Co(OH)_2$ and $Mn(OH)_2$. The precipitated manganese and cobalt were oxidized to Mn^{2+} and Co^{2+} ions (Ilton et al. 2016; Pattanayak et al. 1989). The precipitations of Mn^{2+} and Co^{2+} respectively undergo the formation of $Mn(OH)_2$ and $Co(OH)_2$ nanoparticles (Ilton et al. 2016; Pattanayak et al. 1989; Yang et al. 2010). Cobalt hydroxides crystallize in two polymorphs, α-$Co(OH)_2$ and β-$Co(OH)_2$. The α-$Co(OH)_2$ is isostructural, and it consists of hydrotalcite-like compounds with positively charged $Co(OH)_{2-x}$ layers (Yang et al. 2010). On the other hand, β-cobalt hydroxide is a stoichiometric phase of the composition $Co(OH)_2$ containing a brucite-like structure with a hexagonal packing of hydroxyl ions having Co(II) occupying alternate rows of octahedral sites (Yang et al. 2010). The XRD spectra of the as-prepared sample (**Figure 2.2 (a)**) consist of peaks from both β-cobalt hydroxide and manganese hydroxide phases. The diffraction peaks situated at 2θ values 19^o, 32.42^o, 37.87^o, 38.66^o, 51.32^o, 57.83^o, and 59.55^o are respectively indexed to (001), (100), (011),

(002), (012), (110), and (003) planes of hexagonal $Co(OH)_2$ having space group P-3m1 (164) (JCPDS card no. 089-8616, $\alpha=\beta=90^o$ and $\gamma=120^o$). The lattice parameter values are obtained as, a = b = 3.13 Å, and c = 4.61 Å from the XRD data. Diffraction peaks observed at 2θ values 18.72^o, 31^o, 36.51^o, 37.98^o, 49.84^o, 55.25^o, 58.87^o, and 64.75^o are readily indexed to the lattice reflections from (001), (100), (011), (002), (012), (110), (111) and (200) planes of hexagonal $Mn(OH)_2$ having space group P-3m1 (164) (JCPDS file no.073-1133, $\alpha=\beta=90^o$ and $\gamma=120^o$). The lattice parameter values are obtained as, a = b = 3.21 Å, and c = 4.62 Å from the XRD data. The absence of any other oxide peaks in the diffraction pattern confirms that all the Co and Mn particles are formed into hydroxide forms (Anandan et al. 2013; Yang et al. 2010). The peaks obtained for $Co(OH)_2$ and $Mn(OH)_2$, were sharp and highly intense, indicating the crystalline nature of the as-prepared $Mn(OH)_2/Co(OH)_2$ nanocomposite.

FTIR spectra of the $Mn(OH)_2/Co(OH)_2$ nanoparticles were studied to determine the surface functional group of the sample and are shown in **Figure 2.2 (b)**. The peak at 1630 cm^{-1} originates from the O-H stretching modes of water molecules and the hydrogen bonding among the hydroxyl groups in the hydroxide sample, which shows the highly hydroxylated nature of the synthesized sample (Barzegar et al. 2015; Laheäär et al. 2015). The broad peaks at around 3200-3600 cm^{-1} can be attributed to the symmetric stretching vibrational modes of surface-adsorbed H_2O molecules. The peak at 1608 cm^{-1} indicates the C=O stretching vibration of the carboxyl groups. The peak occurring at about 636 cm^{-1} is attributed to the stretching and bending modes of metal-hydroxide (M-OH) functional group in the sample (Anandan et al. 2013; Nakamoto 2006). The bands observed at 510 cm^{-1} may be due to the C-C stretching (Su et al. 2008). The absence of a metal-oxygen functional group indicates that the synthesized samples are in the pure metal hydroxide form.

To identify the oxidation state of the Co and Mn in the $Mn(OH)_2/Co\ (OH)_2$ nanocomposite, XPS studies were carried out. The survey XPS spectrum in **Figure 2.3 (a)** confirms the presence of manganese and cobalt elements. XPS survey spectra show peaks due to Mn ($2p_{3/2}$, $2p_{1/2}$), Co ($2p_{3/2}$, $2p_{1/2}$), O1s and C1s, indicating that no other impurities are present. **Figure 2.3 (b)** shows the high - resolution Mn 2p spectrum of the sample. The spectrum consists of two main broad peaks at 653.0 and 641.2 eV, which

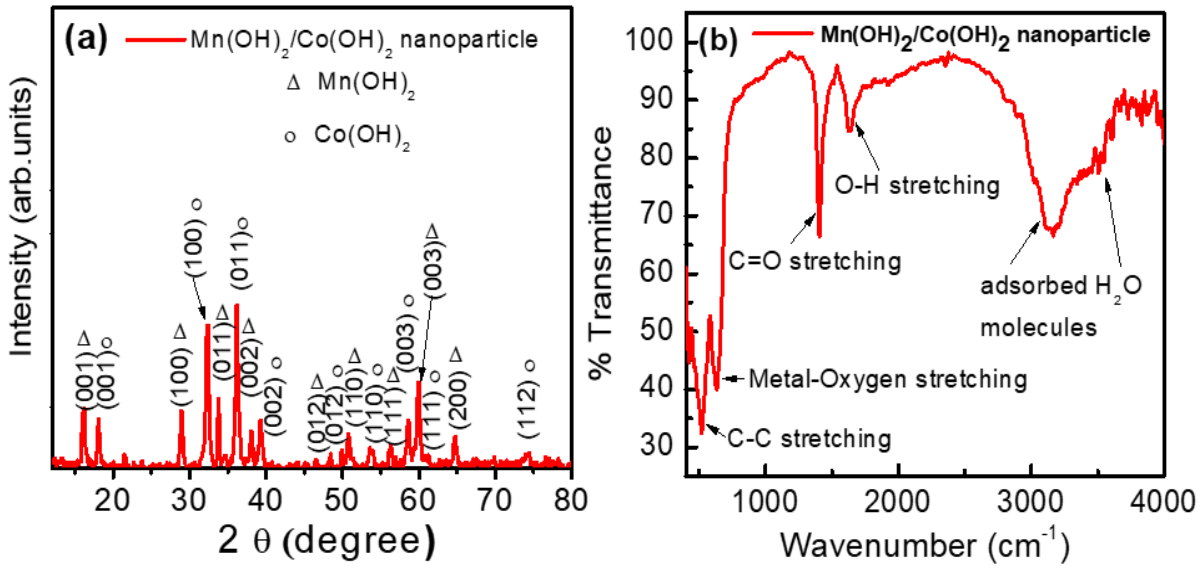

Figure 2.2. (a) XRD pattern and (b) FTIR spectra of $Mn(OH)_2/Co(OH)_2$ nanoparticles.

can be ascribed to Mn $2p_{1/2}$, and Mn $2p_{3/2}$ spin-orbit lines, respectively. The peak value of 643 eV in high-resolution XPS spectra agrees well with those reported for $Mn(OH)_2$ corresponding to the 2^+ oxidation state of Mn (Mn^{2+}) (Biesinger et al. 2011; Ramírez et al. 2014). **Figure 2.3 (c)** shows the high-resolution Co 2p spectrum of the sample. The spectrum consists of two broad peaks, corresponding to $2p_{1/2}$ and $2p_{3/2}$ spin-orbit lines. The sample shows two prominent peaks at binding energies of 795.3 and 780.0 eV, corresponding to Co $2p_{1/2}$ and Co $2p_{3/2}$ respectively, which assigns to the presence of Co^{2+} chemical state (Yang et al. 2010). The spectrum also contains two weak satellite structures at the high binding energy side of $2p_{1/2}$ and $2p_{3/2}$ main peaks, which is either due to the coupling between unpaired electrons in the atom (multiplet splitting) or a multiple electron excitation (McIntyre and Cook 1975; Younis et al. 2013). The O1s spectrum of the material was analyzed to check the presence of hydroxide **Figure 2.3 (d)**. The O1s spectrum of the as-prepared material shows the main peak at 529.3 eV, which can be assigned to the hydroxide group (OH^-) (McIntyre and Cook 1975). According to previous studies on metal hydroxides, O1s peak indirectly indicates the presence of Mn-OH and Co-OH bonding (Yang et al. 2010). In addition, two low intensity peaks are observed at binding energies of 530.3 eV and 532 eV due to the presence of O=C and structural water (McIntyre and Cook 1975; Xu et al. 2015). This means oxygen helps to enhance the binding power of Co and Mn atoms in $Co(OH)_2$ and $Mn(OH)_2$. C1s peak **Figure 2.3 (e)** is originated due to the carbon cloth substrate used in the fabrication of electrode material. It is observed that the C1s spectrum of the as-synthesized binary metal

hydroxide nanocomposite can be decomposed into three major components, corresponds to different functional groups of the carbon atom. Peaks at 284.2 eV, 285.7 eV, and 288.2 eV can be respectively assigned to Sp2 hybridized carbon, Sp3 hybridized carbon, and C=O group (Kundu et al. 2008; Yan et al. 2010). The XPS spectral analysis confirms that the as-synthesised material contains $Mn(OH)_2$ and Co $(OH)_2$.

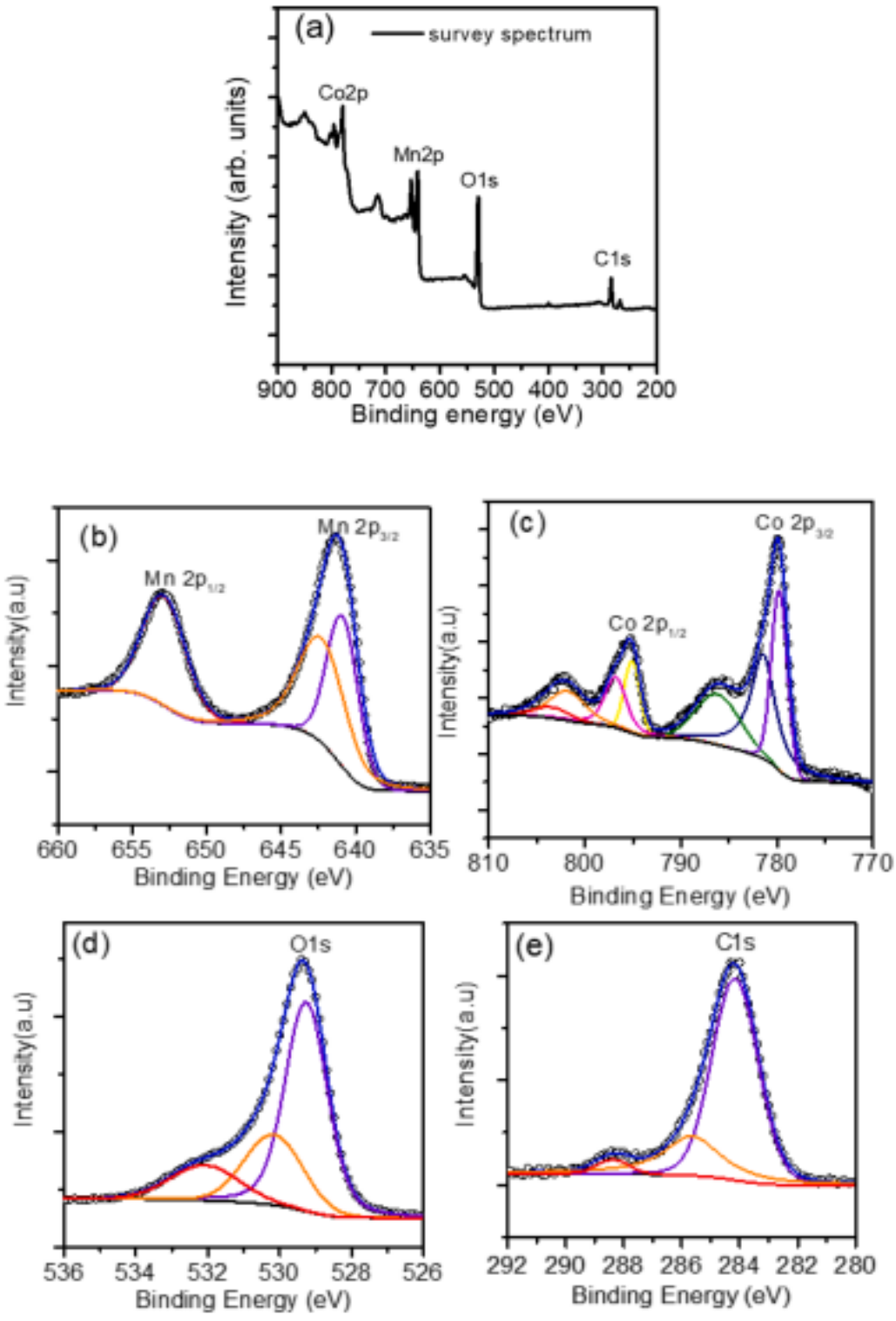

Figure 2.3. XPS spectra of synthesized $Mn(OH)_2/Co(OH)_2$ nanoparticles: (a) The whole survey spectrum, (b) Mn2p spectra, (c) Co2p spectra, (d) O1s spectra, (e) C1s spectra.

Nitrogen adsorption-desorption isotherms of as-synthesized binary metal hydroxide nanoparticles over carbon cloth electrodes are given in **Figure 2.4 (a).** The pore density and surface area of the nanoparticles were analyzed using nitrogen physisorption measurements. BET surface area values of binary metal hydroxide nanocomposites are calculated as 31 m^2 g^{-1}, using the isotherms. The pore size distributions of the samples calculated from adsorption isotherms using the Barret-Joyner-Halenda (BJH) method are shown in **Figure 2.4 (b)**. BJH Desorption cumulative volume of pores between 1.7 nm and 300 nm diameter for $Mn(OH)_2/Co(OH)_2$ nanocomposite is 0.21 cm^3 g^{-1}. The high surface area and pore volume possessed by the nanocomposite facilitate effective interaction with a high density of electrolyte ions, resulting in enhanced electrode-electrolyte accessibility and hence improved electrochemical performance.

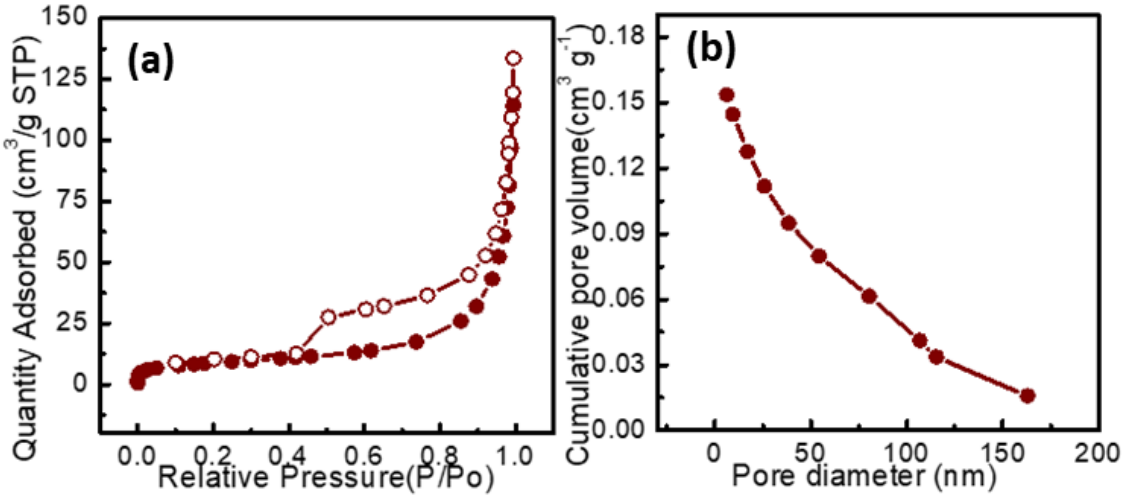

Figure 2.4. (a) Nitrogen-adsorption and desorption isotherms and (b) Pore-size distribution of the $Mn(OH)_2/Co(OH)_2$ nanoparticles.

The surface morphology of the sample, $Mn(OH)_2/Co(OH)_2$ nanoparticles grown over carbon cloth substrate, was analyzed using the SEM images represented in **Figure 2.5**. The SEM image in **Figure 2.5 (a)** represents the high-resolution image of the bare carbon cloth substrate before the chemical reaction. The SEM images (**Figure 2.5 (b, c, and d)**) indicate the uniform distribution of nanoflake-like morphology of binary metal hydroxide nanocomposite. From **Figure 2.5 (d)**, a thick deposition of the material over carbon cloth with porous nature is observed. The electrochemical performance of the electrode

material greatly depends on its morphology (Reghu Nath et al. 2019; Su et al. 2019; Tang et al. 2019). Direct deposition of $Mn(OH)_2/Co(OH)_2$ nanocomposite over carbon cloth substrate can increase the capacitance property by delivering essential usage of material, great electrode contact, fast ion diffusion, more electroactive sites, rapid transfer of electrons, and large conductivity. In addition, the porous nanoflake-type morphology of binary metal hydroxide nanocomposite highly improves the specific surface area of the electrode which is evident from BET results. This will increase the redox reaction rate and lead to improving the kinetics of charge transfer (Selvaraj et al. 2020). Utilizing these advantages in morphology, the as-grown binary metal hydroxide nanocomposite enhances the electrochemical properties of the material.

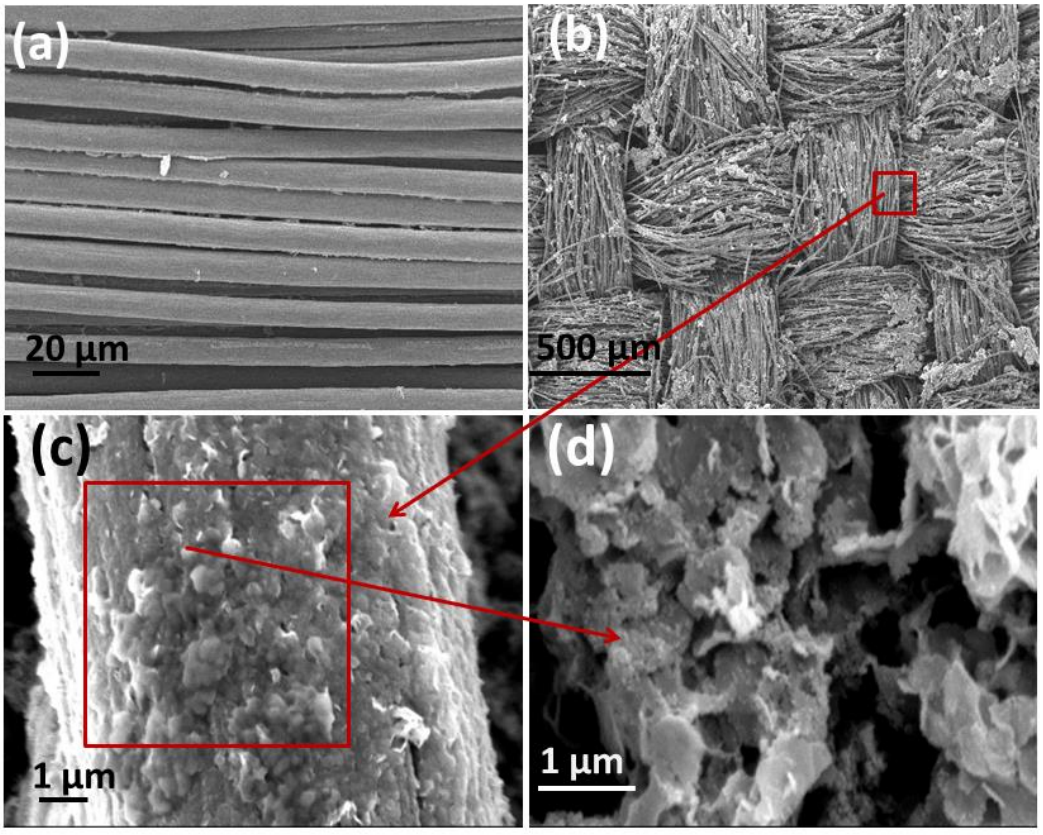

Figure 2.5. SEM images of (a) bare carbon cloth and (b), (c), and (d) $Mn(OH)_2/Co(OH)_2$ nanoparticles grown over carbon cloth.

The microstructure of the as-synthesized binary metal hydroxide nanocomposite was further confirmed by transmission electron microscopy (TEM). **Figure 2.6 (a, b, and c)** show the TEM images of the deposited nanocomposite, which indicates that individual flakes are composed of spherical nanoparticle aggregates having an average particle size

of 14 nm. The nanostructure of the synthesized material can increase the specific surface area and decrease the diffusion path for charge transfer (Barzegar et al. 2015; Sheng et al. 2005). The selected area electron diffraction (SAED) pattern is shown in **Figure 2.6 (d)**, which shows diffraction rings revealing the polycrystalline nature of the material. The microstructure of the electrode material with porous nature is expected to offer more electrolyte accessible surface area and hence is suitable for the supercapacitor application (Gomez and Kalu 2013; Han et al. 2018).

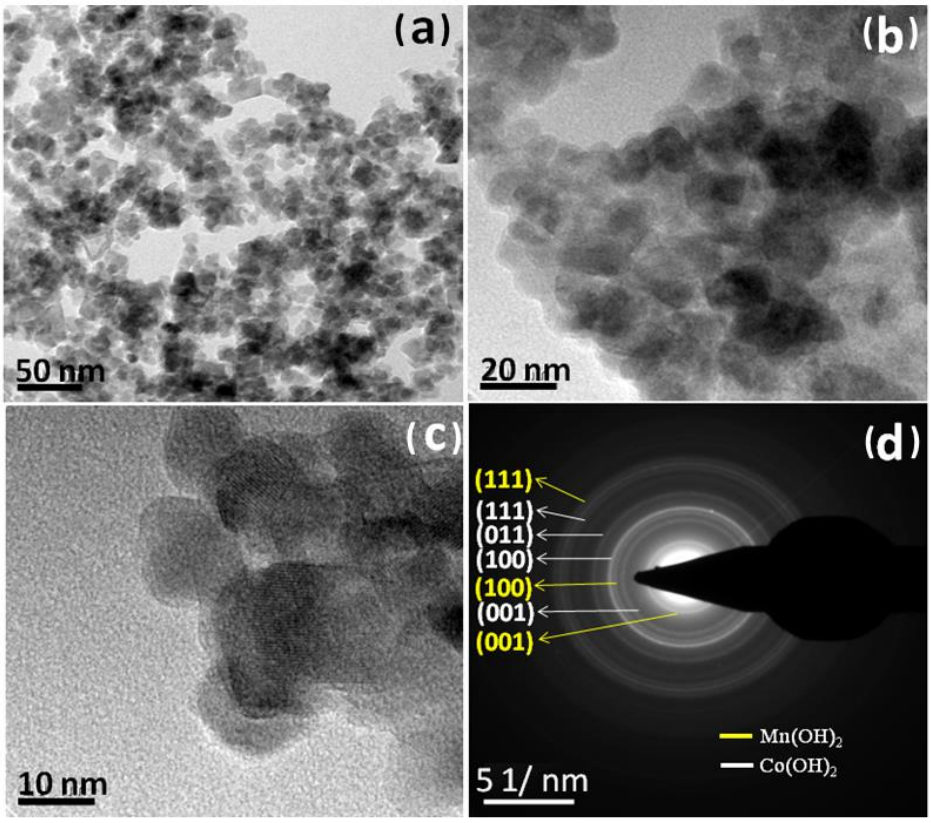

Figure 2.6. (a) TEM image (b) and (c) HRTEM images and (d) SAED pattern of $Mn(OH)_2/Co(OH)_2$ nanoparticles

2.4.2 Electrochemical characterization

The electrochemical characterizations of the as-synthesized binary metal hydroxide nanoparticles over carbon cloth substrate were carried out in the symmetric two-electrode configuration. The electrochemical measurements were conducted using a 2M KOH electrolyte. For comparison, symmetric supercapacitors were fabricated based on individual hydroxide-coated carbon fabric ($Co(OH)_2$/carbon cloth, $Mn(OH)_2$ /carbon cloth) electrodes as well and the electrochemical performance measurements were also

carried out. The results are shown in **Figure 2.7**. Cyclic voltammograms of symmetric supercapacitors based on $Mn(OH)_2$ nanoparticles, $Co(OH)_2$ nanoparticles, and $Mn(OH)_2/Co(OH)_2$ nanoparticles electrodes measured in a potential range of 0-1 V at different scan rates of 5, 10, 20, 50, 100, and 200 mVs^{-1} are shown in **Figure 2.7 (a), (c), and (e)** respectively. The shape of the CV curves is quite different from the rectangular shape expected for ideal double-layer capacitors (Rakhi et al. 2016a; Su et al. 2019). The CV loop reveals its expected pseudocapacitive nature. The current response value of the CV curve increases with an increase in the scan rates, indicating a capacitive behavior. In addition, the CV shape does not alter consequently, implying outstanding reversibility for the binary metal hydroxide nanoparticles (Elkholy et al. 2019). For the symmetric capacitor based on the nanocomposite, the Faradaic redox peaks arise from the reversible valance state changes between Mn^{2+} and Co^{2+} ions in the electrode with OH^- ions in the KOH electrolyte. The probable electrochemical reactions are represented using the following equations (Jagadale et al. 2016; Wu et al. 2011):

$$Co(OH)_2 + OH^- \leftrightarrow CoOOH + H_2O + e^- \quad (2.1)$$

$$CoOOH + OH^- \leftrightarrow CoO_2 + H_2O + e^- \quad (2.2)$$

$$Mn(OH)_2 + OH^- \leftrightarrow MnOOH + H_2O + e^- \quad (2.3)$$

The mass loading of the binary metal hydroxide nanocomposite in our case was 1 mg. The greater area of the CV loop indicates that $Mn(OH)_2/Co(OH)_2$ nanoparticles contained larger specific capacitance values, this may be due to the enhanced synergy between $Mn(OH)_2$ and Co $(OH)_2$ materials. The Csp values of the electrodes from CVs and GCDs are calculated using **equations 1.4 and 1.6** respectively. A maximum Csp value of 385 Fg^{-1} was obtained for the as-synthesized binary metal hydroxide nanocomposite at a $5mVs^{-1}$ scan rate. Galvanostatic charge-discharge curves of symmetric supercapacitors based on $Mn(OH)_2$ hydroxide, $Co(OH)_2$ hydroxide, and $Mn(OH)_2/Co(OH)_2$ nanoparticle electrodes at different current densities in a potential range of 0 - 1 V are shown in **Figure 2.7 (b), (d), and (f)**, respectively. The nearly triangular shape of the CD curves indicates the reduced internal resistance of the supercapacitor. The direct contact of the active electrode materials on conducting carbon cloth substrate helps in improving the electrode conductivity. From the CD curves, the Csp values for symmetric supercapacitors based on $Mn(OH)_2/Co(OH)_2$ nanoparticle electrodes are evaluated as, 160, 193, 234, 293, and 402 Fg^{-1} at current densities of 2, 1, 0.75, 0.50, and 0.25 Ag^{-1} respectively and the values are

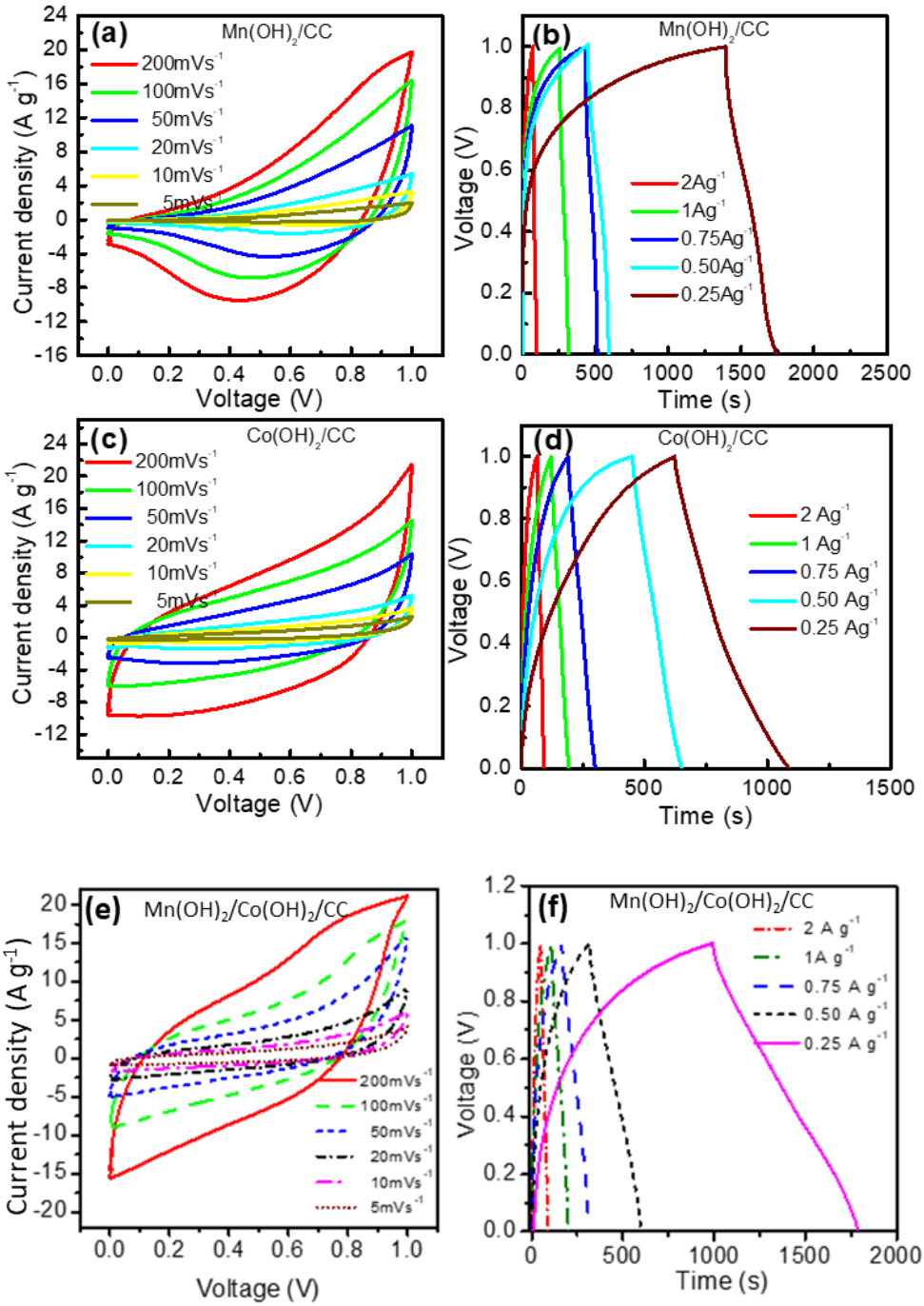

Figure 2.7. Cyclic voltammograms of symmetric supercapacitors based on (a) $Mn(OH)_2/CC$, (c) $Co(OH)_2/CC$, and (e) $Mn(OH)_2/Co(OH)_2/CC$ electrodes at different scan rates. Galvanostatic charge-discharge curves of (b) $Mn(OH)_2/CC$, (d) $Co(OH)_2/CC$, and (f) $Mn(OH)_2/Co(OH)_2/CC$ electrodes at different current densities.

consistent with the values obtained from the CV measurements. The specific energy and specific power values for the device are calculated using the **equations 1.7 and 1.8** respectively. At a specific power of 1 kW kg^{-1}, the specific energy obtained for a

supercapacitor based on $Mn(OH)_2/Co(OH)_2$ nanoparticle material is 27 Wh kg^{-1}. The maximum specific energy obtained for the symmetric supercapacitor electrode is 53 Wh kg^{-1}. The Comparison of the electrochemical performance (cyclic voltammograms at a constant scan rate of 20 mVs^{-1}, and the Galvanostatic charge-discharge curves at a current density of 0.25 A g^{-1}) of the symmetric supercapacitors based on the three different types of electrodes $Co(OH)_2$/carbon cloth, $Mn(OH)_2$ /carbon cloth, and $Mn(OH)_2/Co(OH)_2$/carbon cloth are shown in **Figure 2.8 (a) and (b)**, respectively.

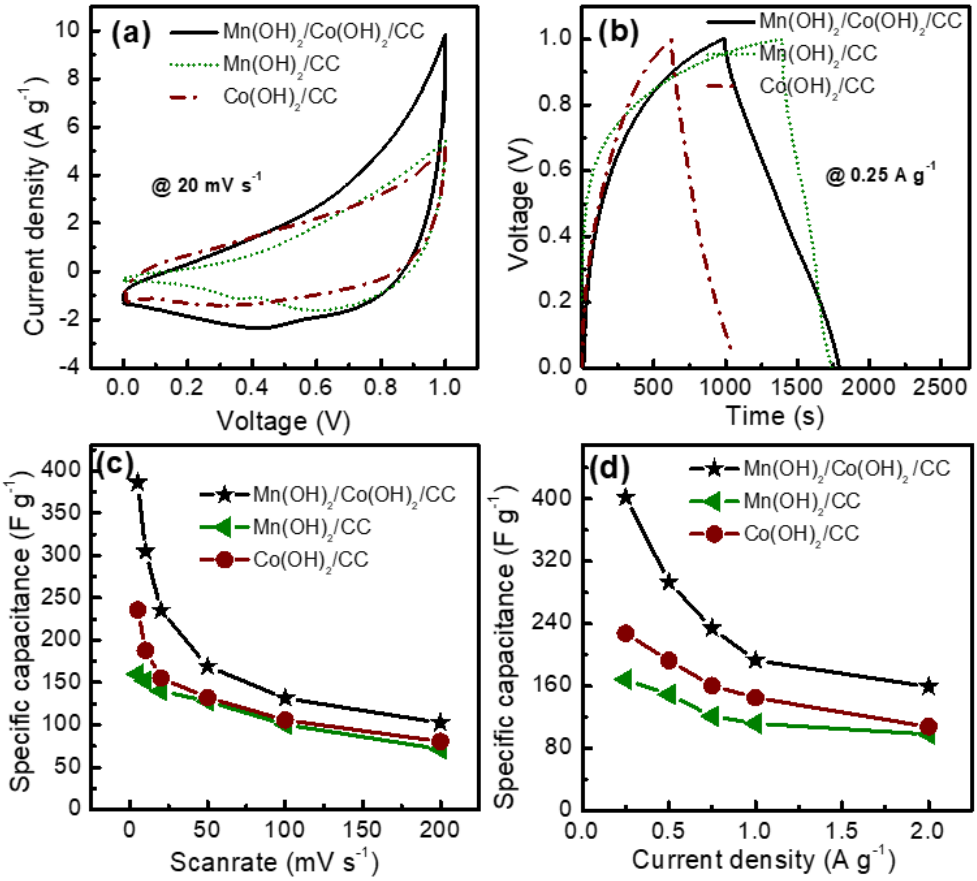

Figure 2.8. Comparison of the electrochemical performance of symmetric supercapacitors: (a) cyclic voltammograms at a constant scan rate of 20 mV s^{-1}, (b) Galvanostatic charge-discharge curves at a current density of 0.25 A g^{-1}, Variation of specific capacitance as a function of (c) scan rates, and (d) current densities.

Results indicate that the binary metal-based supercapacitor exhibits a better energy storage performance as compared to the individual hydroxides. The superior performance of the $Mn(OH)_2/Co(OH)_2$ nanoparticles can be attributed to the synergistic effect of the

component hydroxides. The presence of Mn from $Mn(OH)_2$ incorporation may support the fast transportation of electrons and better penetration of ions (Zhao et al. 2020). The change in oxidation states of Mn and Co can deliver outstanding redox performance during charging and discharging (Chen et al. 2019a; Jagadale et al. 2016). This provides excellent structural stability and superior electrochemical performance to the $Mn(OH)_2/Co(OH)_2$ nanoparticle. Variations of Csp as a function of scan rates and current densities for the devices are shown in **Figure 2.8 (c) and (d)**, respectively. The decrease in the Csp value at high scan rates and higher current densities is due to the limitation in the ion transfer of electrolytes.

The cycling stability test of the electrode was carried out by recording the CD measurements for 6000 repeated cycles at 2 Ag^{-1}. The cyclic performance of the fabricated supercapacitors is shown in **Figure 2.9 (a)**. The $Mn(OH)_2$/CC, $Co(OH)_2$/CC, and $Mn(OH)_2/Co(OH)_2$/CC nanoparticle electrodes retains respectively, 90 %, 92 %, and 94 % of their maximum Csp after 6000 cycles, showing that the electrode exhibits long term cyclic stability. The direct growth of the

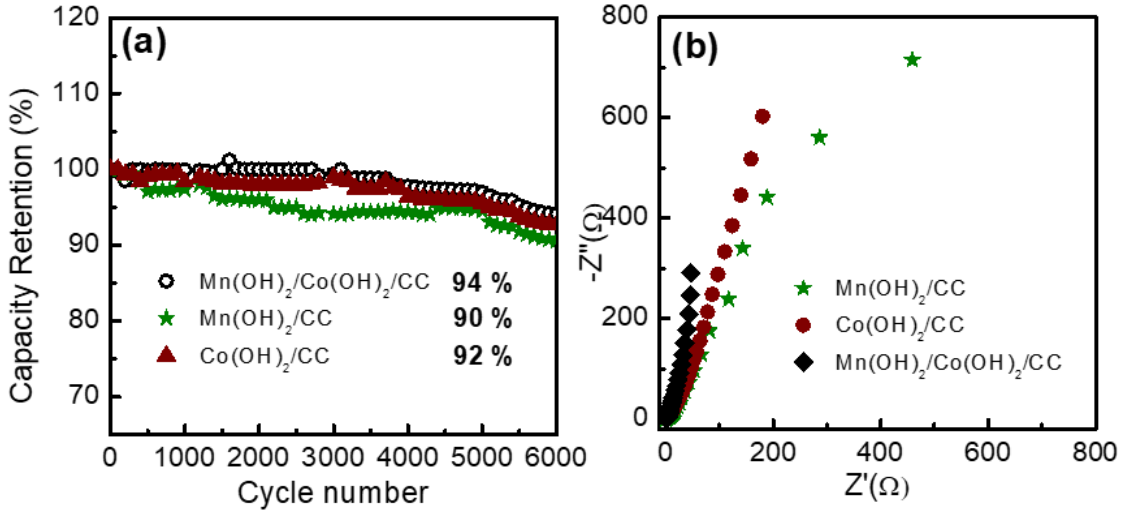

Figure 2.9. Comparison of (a) cycling performance of $Co(OH)_2$/CC, $Mn(OH)_2$/CC, and $Mn(OH)_2/Co(OH)_2$/CC at a current density of 2 A g^{-1} and (b) Nyquist plots of $Co(OH)_2$/CC, $Mn(OH)_2$/CC, and $Mn(OH)_2/Co(OH)_2$/CC based electrodes.

nanoparticles on the surface of conducting carbon cloth substrate provides greater stability to the electrode (Salunkhe et al. 2014). The EIS technique was used to analyze the electrode/electrolyte interfacial performance (Stoller and Ruoff 2010). The Nyquist plot for the as-synthesized nanoparticles over carbon cloth is presented in **Figure 2.9 (b)**.

The X-intercept of the spectra reveals the value of bulk electrolyte solution resistance (Rs). The Rs values obtained for the $Mn(OH)_2$/CC, $Co(OH)_2$/CC, and $Mn(OH)_2/Co(OH)_2$/CC electrodes are 0.92, 0.90, and 0.89 Ω respectively. The charge transfer resistance (Rct) of the fabricated supercapacitor, which is a property of the electrode conductivity and the electroactive surface area, can be calculated from the diameter of the semicircle arc in the high-frequency region of the Nyquist plot. The very low Rct value of the supercapacitor indicates that the electrodes possess a large electroactive surface area and excellent electronic conductivity at the interface of electrode and electrolyte (Deng et al. 2020; Rakhi et al. 2014). The straight line or Warburg line is a result of the diffusion of electrolyte ions within the porous electrodes. The nearly vertical Warburg line parallel to the Y- axis at the low-frequency region of the Nyquist plot indicates ideal capacitive behaviour for the binary metal hydroxide nanoparticles. Moreover, the shorter length of the Warburg line of $Mn(OH)_2/Co(OH)_2$ nanoparticles implies fast ion diffusion processes in the porous metal hydroxide electrode (Jagadale et al. 2016; Rakhi et al. 2014). Herein, the symmetric supercapacitor based on the $Mn(OH)_2/Co(OH)_2$ nanoparticles exhibits superior performance as compared to the supercapacitors based on $Mn(OH)_2$ and $Co(OH)_2$ as electrode materials. The present study demonstrates that the direct growth of $Mn(OH)_2/Co(OH)_2$ nanoparticles over flexible carbon cloth substrate has an exciting impact on supercapacitor performance. The improved performance can be attributed to the direct growth of $Mn(OH)_2/Co(OH)_2$ nanoparticles over the conducting fabric, which provides excellent flexibility and sufficient mechanical strength. The carbon fabric provides a large surface area for active material loading, and a three-dimensional porous network for effective electrolyte diffusion (Wang et al. 2016). The significant effects of each component in the $Mn(OH)_2/Co(OH)_2$ based nanoparticle electrode contribute to its efficient electrochemical performance.

To further improve the electrochemical performance of $Mn(OH)_2/Co(OH)_2$ nanoparticles, we directly deposited them over a 3D nickel foam substrate. Synthesis of $Mn(OH)_2/Co(OH)_2$ nanoparticles over nickel foam substrate ($Mn(OH)_2/Co(OH)_2$/NF) was carried out by following the similar procedure that was used for $Mn(OH)_2/Co(OH)_2$ nanoparticles over carbon cloth ($Mn(OH)_2/Co(OH)_2$/CC). The only difference is that, herein nickel foam is used instead of carbon cloth. **Figure 2.10**. shows the schematic of the preparation of the $Mn(OH)_2/Co(OH)_2$/NF.

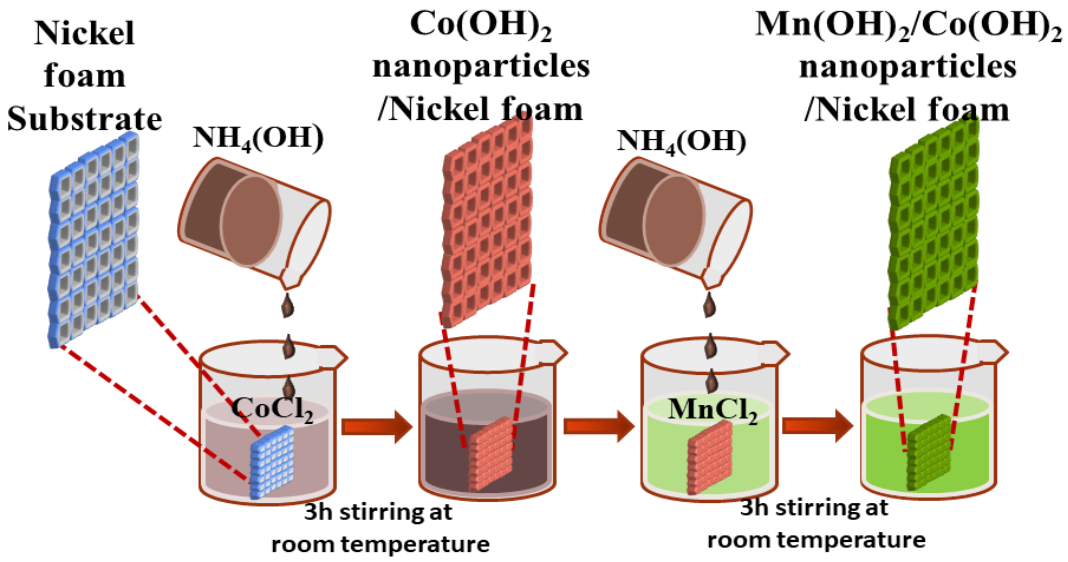

Figure 2.10. The schematic of the preparation of nickel foam supported $Mn(OH)_2/Co(OH)_2$ nanoparticles electrode.

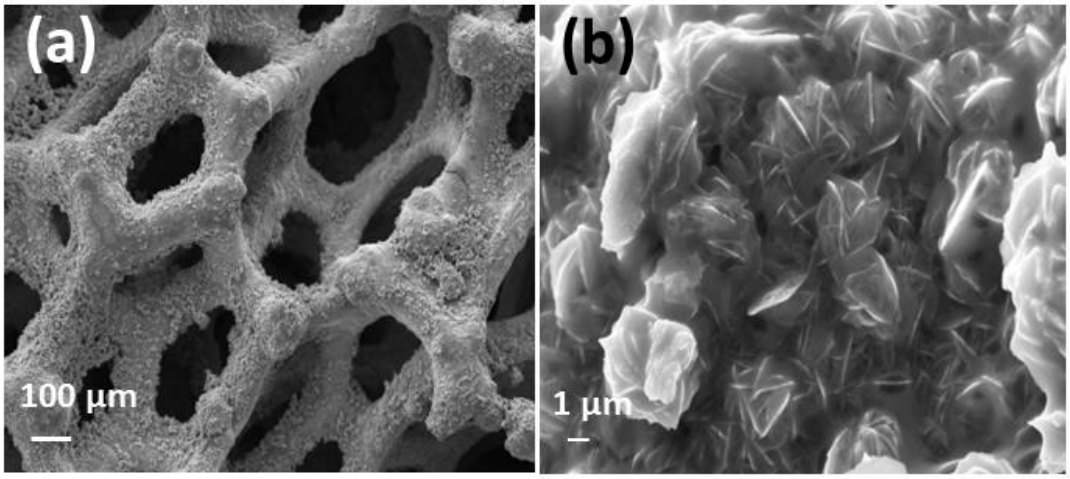

Figure 2.11. (a) SEM and (b) FESEM images of $Mn(OH)_2/Co(OH)_2$/NF.

The surface morphology of the $Mn(OH)_2/Co(OH)_2$/NF was analyzed using the SEM images represented in **Figure 2.11 (a) and (b)**. The nanostructures grown over the nickel foam substrate are given in **Figure 2.11 (a)**. The FESEM image in **Figure 2.11 (b)** shows the homogeneous distribution of nanoflake-like morphology of binary metal hydroxides. The material directly grown over nickel foam substrate can enhance the capacitance property through the crucial usage of active material, increased electrode contact, fast transfer of electrons, and greater conductivity (Salunkhe et al. 2014; Sharifi et al. 2021). In addition, the nanoflake-like morphology of $Mn(OH)_2/Co(OH)_2$/NF highly boosts the

active surface area of the electrode. EDX spectra and EDX elemental mapping images for $Mn(OH)_2/Co(OH)_2$/NF based electrode are presented in **Figure 2.12 (a–f)**. EDX spectra **(Figure 2.12 (b))** exhibit peaks corresponding to the elements cobalt (Co), manganese (Mn), and oxygen (O). The peaks of Ni are observed due to the utilization of NF substrate (Chen et al. 2017a). The elemental mapping images once again confirm the presence of manganese, cobalt, oxygen, and nickel elements in the $Mn(OH)_2/Co(OH)_2$/NF electrode. In addition, it can also be observed that all the elements are uniformly distributed over the nickel foam substrate.

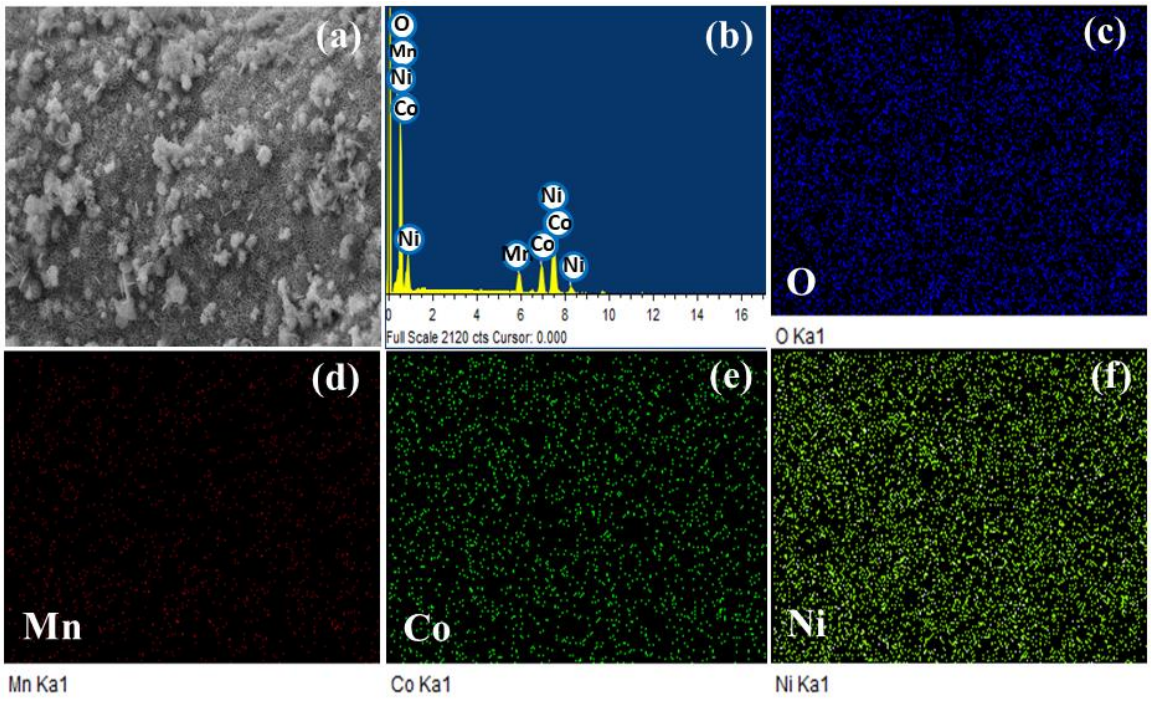

Figure 2.12. EDX spectra (b) and EDX elemental mapping images (c-f) for $Mn(OH)_2/Co(OH)_2$/NF based electrode.

The electrochemical properties of the $Mn(OH)_2/Co(OH)_2$/NF electrode were carried out in the symmetric two-electrode configuration using a 2M KOH electrolyte. The results are shown in **Figure 2.13 (a-f)**. Cyclic voltammograms of symmetric supercapacitors based on $Mn(OH)_2/Co(OH)_2$/NF electrodes measured in a potential range of 0-1 V at different scan rates of 5, 10, 20, 50, 100, and 200 mVs^{-1} are shown in **Figure 2.13 (a)**. The shape of the CV curves is quite different from the ideal rectangular nature which shows a pseudocapacitive behaviour (Castro-Gutiérrez et al. 2020). In addition, the shape of the CV curve does not change consequently, showing outstanding reversibility for the $Mn(OH)_2/Co(OH)_2$/NF electrode (Bai et al. 2020; Barik et al. 2020).

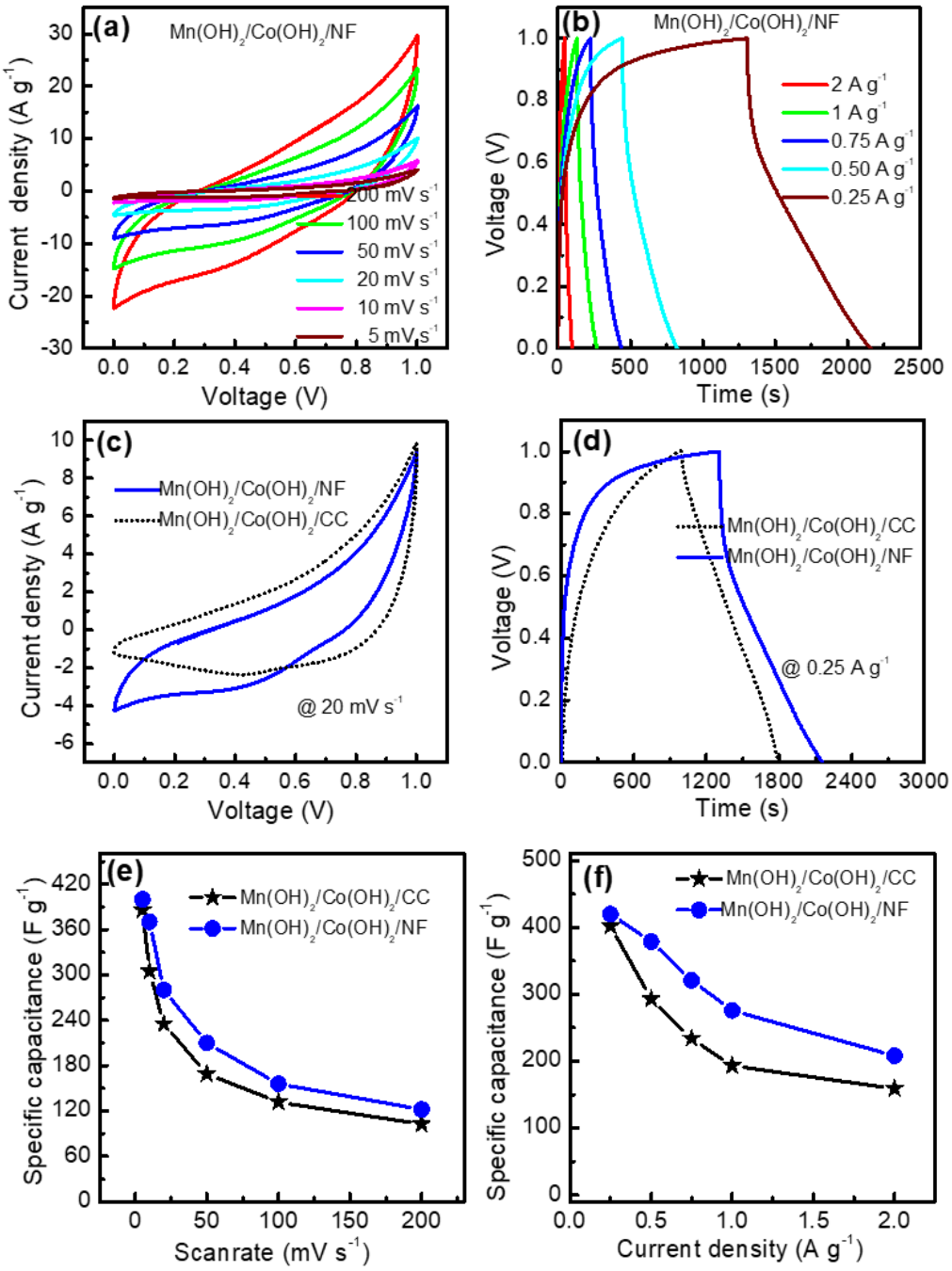

Figure 2.13. (a) Cyclic voltammograms of $Mn(OH)_2/Co(OH)_2$/NF electrodes at different scan rates, (b) Galvanostatic charge-discharge curves of $Mn(OH)_2/Co(OH)_2$/NF electrodes at different current densities, Comparison of (c) cyclic voltammograms at a constant scan rate of 20 mV s^{-1}, (d) GCD curves at a current density of 0.25 A g^{-1}, variation of specific capacitance as a function of (e) scan rates, and (f) current densities.

A maximum Csp value of 400 F g^{-1} was obtained for the $Mn(OH)_2/Co(OH)_2$/NF electrode at a 5mV s^{-1} scan rate. Galvanostatic charge-discharge curves of symmetric supercapacitors based on $Mn(OH)_2/Co(OH)_2$/NF electrodes at different current densities

in a potential range of 0 - 1 V are shown in **Figure 2.13 (b)**. The GCD curves also deviated from the ideal triangular shape, indicating the pseudocapacitive nature of the electrode material (Castro-Gutiérrez et al. 2020). From the GCD curves, the Csp values for $Mn(OH)_2/Co(OH)_2$/NF based electrodes are evaluated as, 208, 276, 321, 379, and 420 F g^{-1} at current densities of 2, 1, 0.75, 0.50, and 0.25 A g^{-1} respectively and the values are compatible with the values obtained from the CV analysis. The greater Csp value of the $Mn(OH)_2/Co(OH)_2$/NF electrodes compared to $Mn(OH)_2/Co(OH)_2$/CC electrodes can be attributed to the direct contact of the active materials on conducting 3D nickel foam substrate. At a specific power of 1 kW kg^{-1}, the $Mn(OH)_2/Co(OH)_2$/NF based electrodes exhibit a specific energy of 29 Wh kg^{-1}. A comparison of the cyclic voltammograms at a constant scan rate of 20 mVs^{-1}, and the Galvanostatic charge-discharge curves at a current density of 0.25 A g^{-1} of the $Mn(OH)_2/Co(OH)_2$/CC and $Mn(OH)_2/Co(OH)_2$/NF based electrodes are shown in **Figure 2.13 (c) and (d)**, respectively. A comparison of variation of Csp as a function of scan rates and current densities for the $Mn(OH)_2/Co(OH)_2$/CC and $Mn(OH)_2/Co(OH)_2$/NF electrodes are shown in **Figure 2.13 (e) and (f)**, respectively. The results show that the $Mn(OH)_2/Co(OH)_2$/NF based electrodes exhibit a better energy storage performance as compared to the $Mn(OH)_2/Co(OH)_2$/CC based electrodes. The superior performance of the $Mn(OH)_2/Co(OH)_2$/NF based electrodes can be attributed to the 3D open porous structure of nickel foam substrate with increased electroactive surface area. This can access more ions during the chemical reaction and enhances the overall performance of the electrode.

The EDLC and pseudocapacitive contribution of $Mn(OH)_2/Co(OH)_2$/CC, $Mn(OH)_2$/CC, $Co(OH)_2$/CC, and $Mn(OH)_2/Co(OH)_2$/NF electrodes are calculated using Trasatti's analysis method (Liu 2018; Mathis et al. 2019). The pseudocapacitive contribution is dominating for all the electrode materials as observed from CV and GCD curves. The following equations are used to calculate the contributions, (Mathis et al. 2019)

$$C_{SP} = \frac{A}{f \times V \times m} \text{ F g}^{-1} \tag{2.4}$$

$$C = constant * v^{-0.5} + C_{EDLC} \tag{2.5}$$

$$C^{-1} = constant * v^{0.5} + C_T^{-1} \tag{2.6}$$

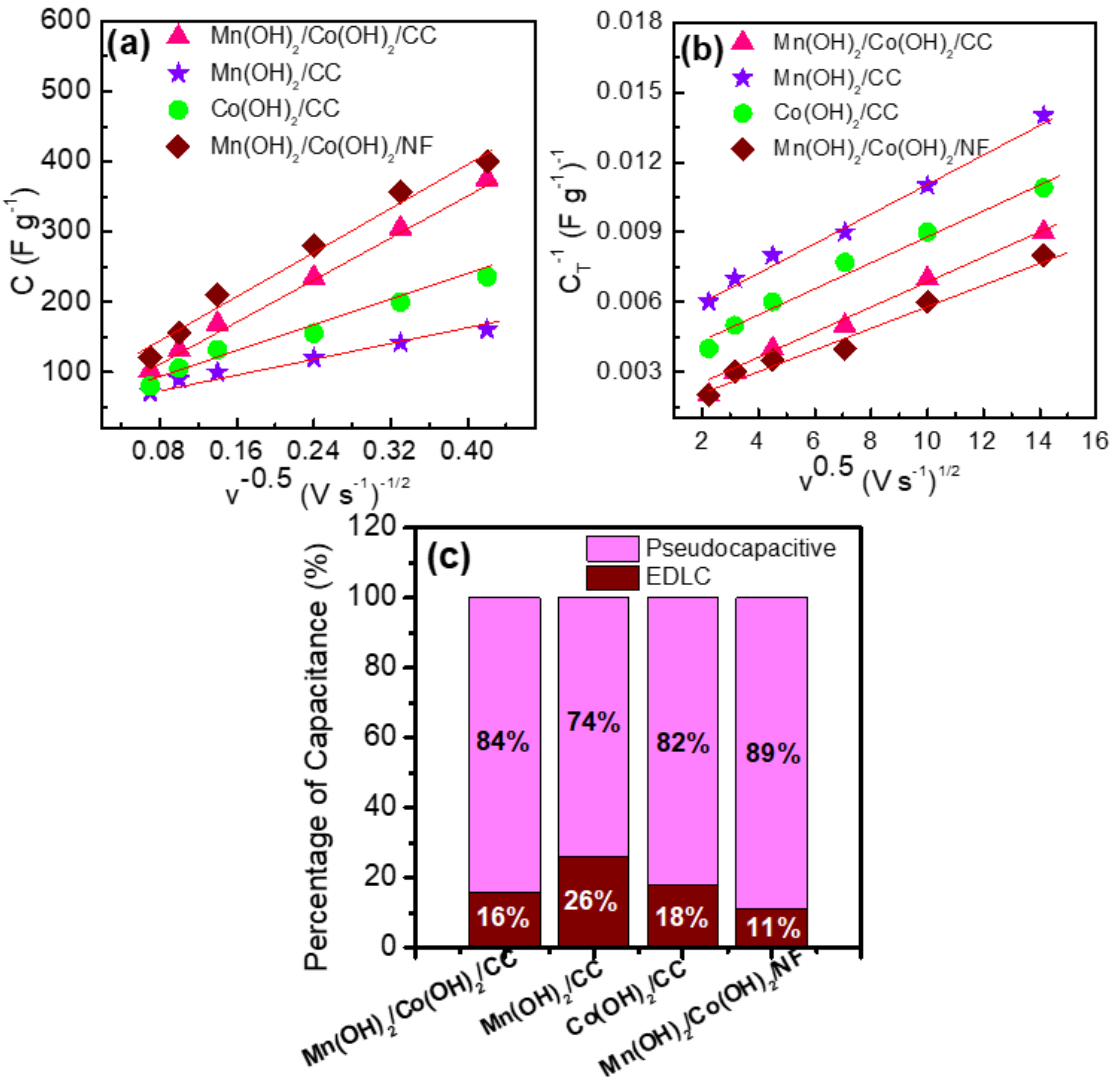

Figure 2.14. (a) linear fit of specific capacitance (Csp) vs. reciprocal of the square root of scan rate ($v^{-0.5}$) (b) a linear fit of reciprocal of specific capacitance (Csp^{-1}) vs. square root of scan rate ($v^{0.5}$) (c) a percentage of capacitance contribution calculated for different electrodes from Trasatti's analysis.

Here, A stands for the integral area of current and potential charge obtained from the CV curve, the 'm' is the mass loading of the active material per electrode, and 'f' is the scan rate.

$$C_T = C_{Pseudo} + C_{EDLC} \tag{2.7}$$

$$\%\, C_{EDLC} = \frac{C_{EDLC}}{C_T} * 100 \tag{2.8}$$

$$\%C_{Pseudo} = \frac{C_{Pseudo}}{C_T} * 100 \quad (2.9)$$

% C_{EDLC} and % C_{Pseudo} stand for the capacitance percentage of electric double layer and pseudocapacitance. Using Trasatti's method *C* vs ($V^{1/2}$) and (*1/C*) Vs ($V^{1/2}$) were plotted for electrodes and the results are shown in **Figure 2.14 (a and b).** The percentage of capacitance contribution measured for the sample based on Trasatti's analysis is presented in **Figure 2.14 (c).**

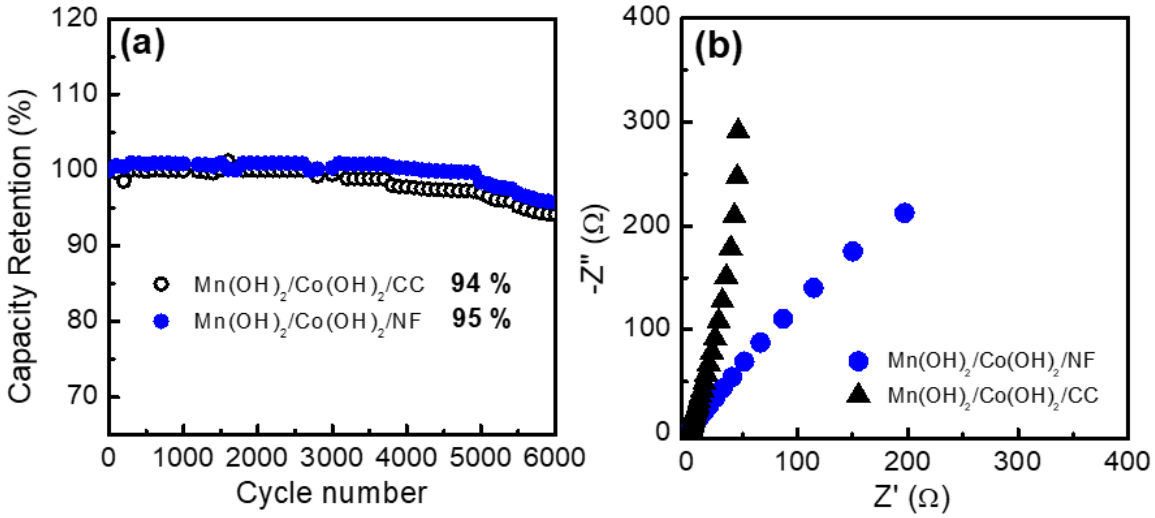

Figure 2.15. Comparison of (a) cycling performance of $Mn(OH)_2/Co(OH)_2$/CC, and $Mn(OH)_2/Co(OH)_2$/NF at a current density of 2 A g^{-1}, and (b) Nyquist plots of $Mn(OH)_2/Co(OH)_2$/CC, and $Mn(OH)_2/Co(OH)_2$/NF based electrodes.

The comparison of the cycling stability test of the $Mn(OH)_2/Co(OH)_2$/CC, and $Mn(OH)_2/Co(OH)_2$/NF electrodes is shown in **Figure 2.15 (a)**. The $Mn(OH)_2/Co(OH)_2$/NF retains 95 % of their maximum Csp after 6000 GCD cycles, showing that the electrode exhibits long-term cyclic stability. The increased cycle life can be assigned to the direct contact of the nanostructures over the nickel foam substrate. The Nyquist plot comparison for the $Mn(OH)_2/Co(OH)_2$/CC, and $Mn(OH)_2/Co(OH)_2$/NF electrodes is presented in **Figure 2.15 (b)**. The R_s values obtained for the $Mn(OH)_2/Co(OH)_2$/NF electrode is 0.76 Ω. Also, a low R_{ct} value of the $Mn(OH)_2/Co(OH)_2$/NF suggests that the electrodes hold a large electroactive surface area and good electronic conductivity at the interface of the electrode and electrolyte. Moreover, the shorter Warburg line of $Mn(OH)_2/Co(OH)_2$/ NF shows fast diffusion of electrolyte ions towards the porous electrode. The present study focuses on the variation

in supercapacitor performance of $Mn(OH)_2/Co(OH)_2$ nanoparticles grown over different current collectors. Herein, the symmetric supercapacitor based on the $Mn(OH)_2/Co(OH)_2$/NF exhibits superior performance as compared to the supercapacitors based on $Mn(OH)_2/Co(OH)_2$/CC electrode materials. The improved performance can be attributed to the more open porous structure of nickel foam compared to the carbon fabric which has a closed porous structure. Thus, nickel foam provides a large electroactive surface area during the chemical reaction and enhances the overall electrode performance.

2.5. Conclusion

In conclusion, we prepared $Mn(OH)_2/Co(OH)_2$ nanostructures over different current collectors, and their supercapacitor performance was studied. The symmetric supercapacitor fabricated by the $Mn(OH)_2/Co(OH)_2$/CC, and $Mn(OH)_2/Co(OH)_2$/NF based electrodes respectively exhibit a maximum specific capacitance of 385 F g^{-1} and 400 F g^{-1} at 5 mV s^{-1}. Furthermore, the supercapacitor electrodes exhibit remarkable cyclic stability. The $Mn(OH)_2/Co(OH)_2$/CC electrode delivers 94% and $Mn(OH)_2/Co(OH)_2$/NF electrode delivers 95% capacitance retention at 2 A g^{-1} after 6000 continuous GCD cycles. The superior electrochemical performance of $Mn(OH)_2/Co(OH)_2$/NF electrode is due to the highly porous structure that provides a large area for active material growth, excellent mechanical strength, and good electrical conductivity. The study proves that the direct growth of active materials over conducting substrate is a promising approach for the fabrication of high-performance supercapacitor electrode

Chapter 3

Electrochemical energy storage properties of $MnCo_2O_4$ nanoneedles

3.1. Outline of the chapter

The chapter deals with the application Mn-Co oxides for electrochemical energy storage. $MnCo_2O_4$ nanoneedles self-organized into urchin-like morphology have been directly grown over conducting nickel foam (NF) substrate by hydrothermal method for supercapacitor application. An aqueous symmetric supercapacitor fabricated with binder-free $MnCo_2O_4$ electrodes exhibits a maximum specific capacitance of 420 F g^{-1} at 5 mV s^{-1}. At a specific power of 1 kW kg^{-1}, the supercapacitor device based on $MnCo_2O_4$ nanoneedle delivers a specific energy of 39 Wh kg^{-1}. The electrode also offers outstanding cyclic stability, which retains 96 % of its initial discharge capacitance after 10000 continuous charge-discharge cycles at a constant high current density of 5 A g^{-1}.

3.2. Introduction

Among the different pseudocapacitive materials, transition metal oxides have great demand as they can exist in variable oxidation states, and thus can contribute to enhanced surface redox reactions. A growing interest in this direction has been recently concentrated on binary metal oxides having two different metal cations such as $NiCo_2O_4$ (Li et al. 2019), $ZnCo_2O_4$ (Sim et al. 2019; Xiao et al. 2018), $ZnMn_2O_4$ (Sim et al. 2019), $MnCo_2O_4$ (BoopathiRaja and Parthibavarman 2019), etc. The occurrence of two independent cations delivers more active sites for redox reactions, enhances the conductivity of electrons, increases structural stability, and enhances the physical and chemical properties of the material for pseudocapacitor electrodes (Xu et al. 2014). Among different binary metal oxides, spinel $MnCo_2O_4$ attracted great interest due to its low cost, great availability, high value of capacitance, superior electrochemical properties, and eco-friendly nature (BoopathiRaja and Parthibavarman 2019; Gonçalves et al. 2021; Zhu et al. 2021). Manganese transports more electrons and cobalt exhibits higher oxidation potential (Wang and Wu 2017). Thus, spinel $MnCo_2O_4$ can be used as a promising electrode material for energy storage applications.

Reports are available for the synthesis of spinel $MnCo_2O_4$ and their application as electrode material for supercapacitors. Kong et al. demonstrated spinel $MnCo_2O_4$ electrode through a simple sol-gel process, and its capacitive properties were tested using 2 M KOH aqueous electrolyte, which exhibited a large specific capacitance (C_{sp}) value of 405 F g^{-1} at 5 mA cm^{-2} current density along with a cyclic stability of 95.1% over 1000 cycles, in three-electrode configuration (Kong et al. 2014a). Hui et al. synthesized manganese cobalt oxide ($MnCo_2O_4$) having hierarchical chestnut-like nanoneedle (NN) morphology via a simple and affordable hydrothermal process, with a C_{sp} of 1535 F g^{-1} at 1 A g^{-1} in three-electrode configuration (Hui et al. 2016). Lei et al. fabricated microspherical-shaped cobalt-manganese oxide as electrode materials with a C_{sp} value of 348 F g^{-1} at 0.5 A g^{-1} in three-electrode technique for energy storage application (Lei et al. 2014). The reports on supercapacitor performance studies available so far for $MnCo_2O_4$ nanostructures are in three electrode configurations (half-cell measurement). The present study is an attempt to evaluate the performance of a real device in a two-electrode configuration (full-cell measurement). The specific capacitance calculation based on the

three electrode configuration results in an exaggerated specific capacitance value as compared to the corresponding value from the two electrode technique (Kong et al. 2014a; Rakhi et al. 2016a; Rakhi et al. 2014; Stoller and Ruoff 2010). As compared to the three-electrode measurement, two electrode measurements are more appropriate as they mimic all evaluation processes carried out in a real supercapacitor cell.

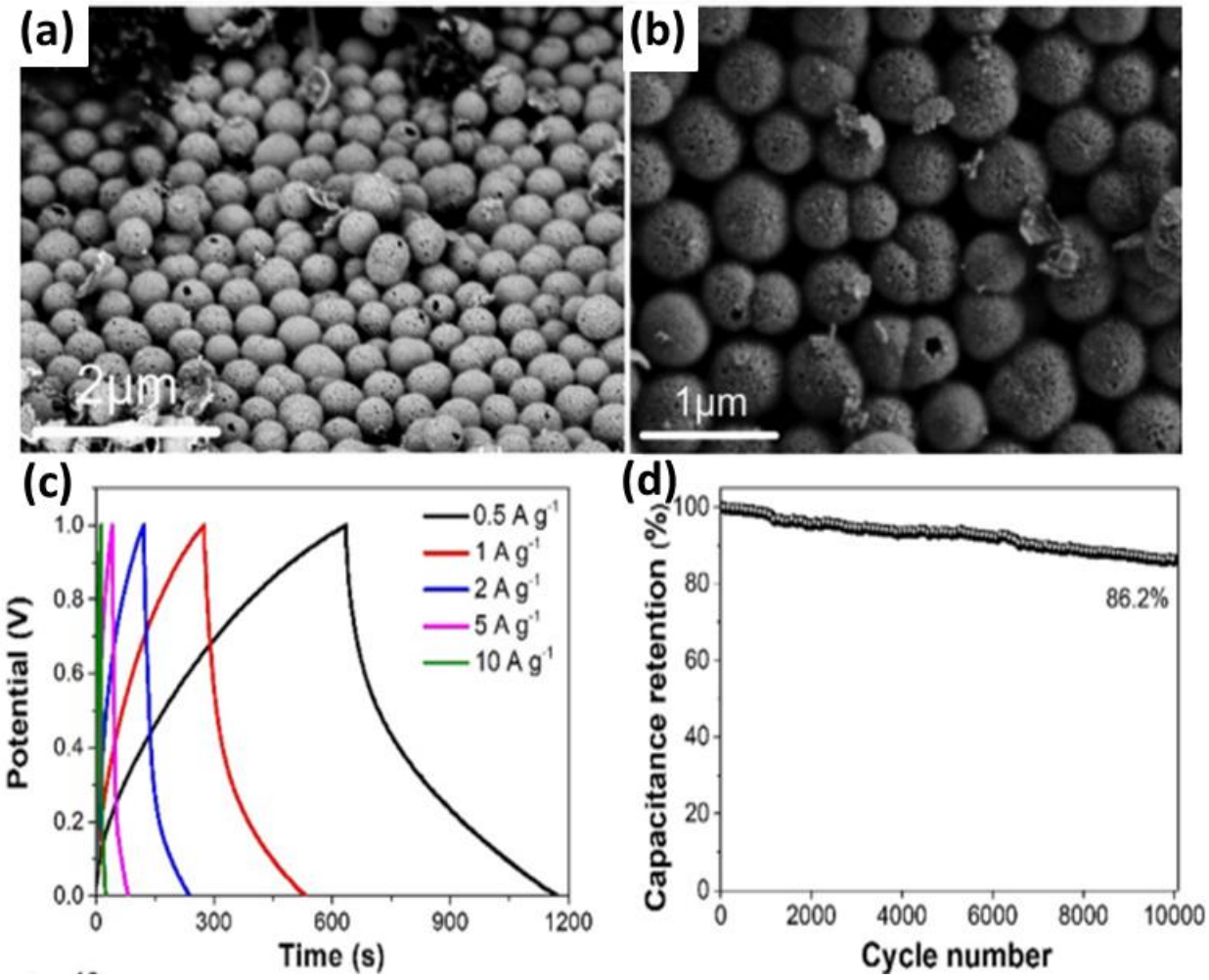

Figure 3.1. (a) and (b) SEM images, (c) GCD, and (d) stability performance of the $MnCo_2O_4$ hollow spheres directly grown on a nickel foam substrate as pseudocapacitive electrodes (Adapted from the reference (Zhu et al. 2021)).

Recently, 3D nickel foam, which has a high specific surface area, great conductivity, and large macropores, has been widely employed as the current collector material for the fabrication of pseudocapacitors (Anil Kumar et al. 2022; Meng et al. 2022). The nickel foam with a uniform macropore network structure provides more active sites for electrochemical reactions and shortens the ion diffusion path (Meng et al. 2022). Zhu et

al. synthesized spinel $MnCo_2O_4$ hollow spheres ($MnCo_2O_4$ HSs) on nickel foam as pseudocapacitive electrodes for supercapacitor application via a two-step solvothermal process. The support of nickel foam and the hollow structure of $MnCo_2O_4$ HSs greatly enhance the ion and charge transport rates. The resultant $MnCo_2O_4$ HSs/NF electrode exhibits a superior specific capacitance value of 489 F g^{-1} at 1 A g^{-1} (Zhu et al. 2021). In addition, the combination of $MnCo_2O_4$ with a conductive matrix-type nickel foam can increase the cyclic stability and rate capabilities of materials (Chen et al. 2017a).

In the present study, we discuss the electrochemical performance of $MnCo_2O_4$ nanoneedles that is self-organized into flower-like morphology over Ni foam substrates prepared using a simple hydrothermal process. The nanostructured $MnCo_2O_4$ directly grown over a conducting three-dimensional (3D) nickel foam substrate can be used as a binder-free electrode material for supercapacitor measurement. The direct growth of $MnCo_2O_4$ nanoneedles over the conductive nickel foam will increase the electroactive surface area and enhance the chemical reaction. Upon its evaluation as a supercapacitor electrode, the as-synthesized $MnCo_2O_4$ nanoneedle electrode exhibits a high value of C_{sp} along with superior cyclic performance.

3.3. Experimental Section

3.3.1. Synthesis of $MnCo_2O_4$ nanoneedles over nickel foam

In a typical synthesis method, 0.03 molar manganese nitrate hexahydrate ($Mn(NO_3)_2{\cdot}6H_2O$), 0.06 molar cobalt nitrate hexahydrate ($Co(NO_3)_2{\cdot}6H_2O$), and 0.3 molar urea $CO(NH_2)_2$ were transferred to a Teflon-lined stainless autoclave containing 15 ml DI water and 15 ml ethanol. A nickel foam (NF) substrate containing 1 × 1 cm^2 in size was cleaned consecutively with acetone, 2 M HCl, distilled water, and ethanol for 10 min each to provide a clear surface. The pretreated NF substrate was then added to the above solution. The autoclave was sealed and heated to 90 ^oC for 8 h and then cooled down to room temperature. The final products were collected, washed, dried, and annealed at 280 ^oC for 3 h to attain $MnCo_2O_4$ nanoneedles. The mass of the NF substrate was calculated before and after the deposition of the active materials using a METTLER TOLEDO XP6 ultra microbalance. The mass loading of the $MnCo_2O_4$ nanoneedles on NF was approximately 1 mg/electrode. The preparation of $MnCo_2O_4$ nanoneedles on NF was schematically illustrated in **Figure 3.2**.

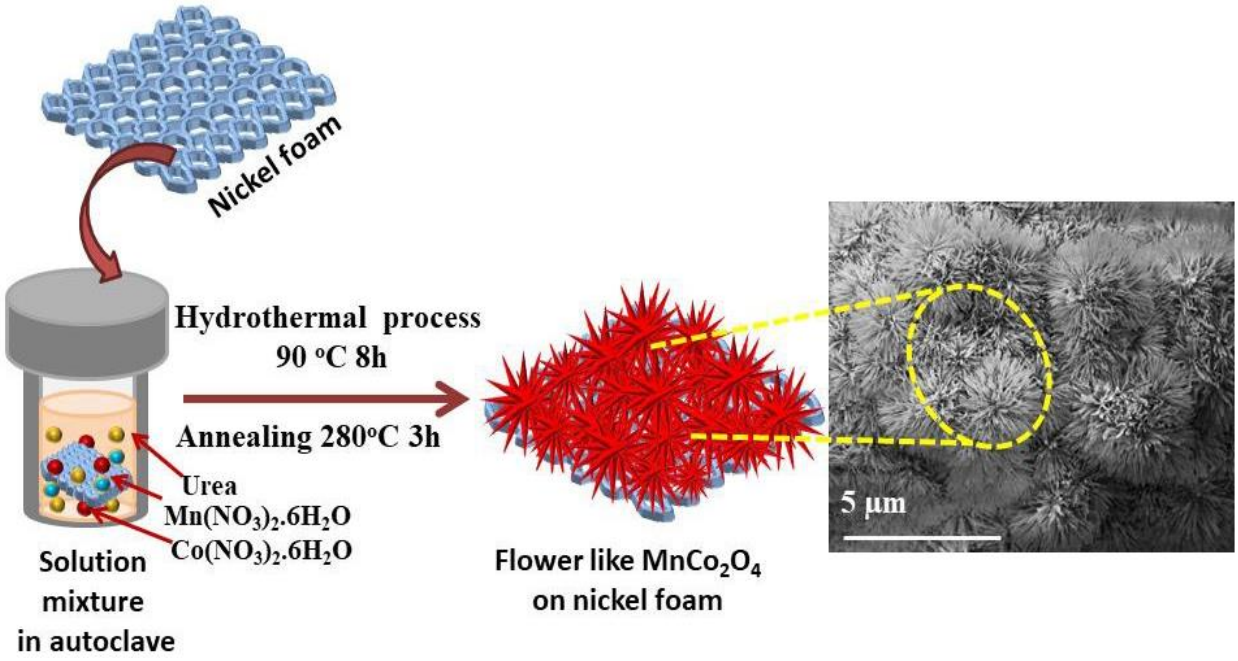

Figure 3.2. Schematic illustration of the preparation of $MnCo_2O_4$ nanoneedles over nickel foam as electrode material for supercapacitor application.

Experimental details of the general characterization of the as-prepared electrode materials, the fabrication of symmetric supercapacitor, and electrochemical performance analysis are given in **Chapter 2, Section 2.3**

3.4. Results and Discussion

3.4.1. Structural and morphological characterization

The XRD spectra of the fabricated $MnCo_2O_4$ nanoparticle are shown in **Figure 3.3 (a)** All the major peaks obtained in the spectrum can be readily indexed to the standard JCPDS card no. 023-1237 corresponding to spinel $MnCo_2O_4$. The XRD pattern of the as-synthesized sample exhibits peaks situated at 2θ values 17.41°, 30.84 °, 35.98°, 37.98°, 43.98°, 54.99°, 58.31°, 64.43°, 72.04° and 76.86° are respectively indexed to (111), (220), (311), (222), (400), (422), (511), (440), (620), and (622) planes of cubic $MnCo_2O_4$ having spinel structure and space group Fdз m (227) (JCPDS card no. 023-1237, $\alpha=\beta=\gamma=90^o$). The lattice parameter values (a,b,c) of the sample calculated from the XRD results (a = b = c = 8.29 Å) are well agree with the standard values (a = b = c = 8.26 Å). The observed broadening of the peaks in the spectrum is due to the nanostructured nature of the synthesized sample. The HRTEM analysis of the as prepared sample further confirmed

that the $MnCo_2O_4$ nanoneedles are composed of a large number of interconnected spherical nanocrystallites of $MnCo_2O_4$. Hence, the average crystallite size of the as-synthesized $MnCo_2O_4$ nanostructure was calculated using the Scherrer's equation from the XRD data. The average crystallite size of the sample is 11 nm. The atomic structure of the spinel $MnCo_2O_4$ is presented in **Figure 3.3 (b).**

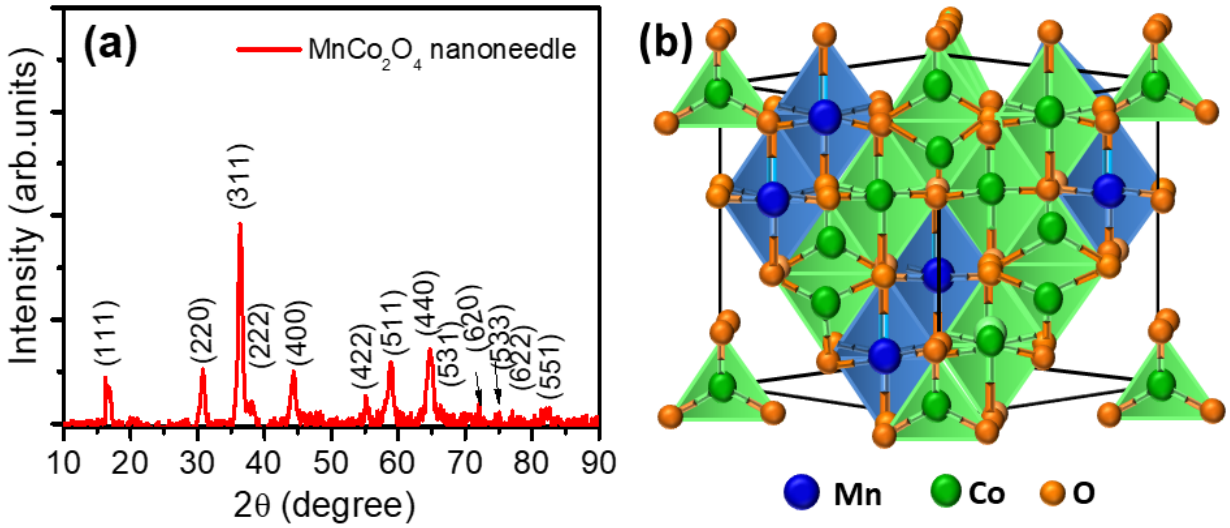

Figure 3.3. (a) XRD pattern of $MnCo_2O_4$ nanoneedles, and (b) The atomic structure of the spinel $MnCo_2O_4$

XPS analysis was adopted (**Figure 3.4**) to analyze the oxidation states of the cobalt and manganese in the $MnCo_2O_4$ nanoneedles. The XPS survey spectrum (**Figure 3.4 (a)**) proves the existence of elements such as cobalt, manganese, and oxygen. The high resolution XPS spectra of Co2p show two major peaks corresponding to the spin orbit splitting of Co ($2p_{3/2}$ and $2p_{1/2}$) and the associated characteristic satellite peaks, which could be deconvoluted as shown in **Figure 3.4 (b)**. The deconvolution of $2p_{3/2}$ and the $2p_{1/2}$ peaks reveal the presence of mixed oxidation states for Co ions. The peaks at 796.90 eV and 781.77 eV are attributed to the $2P_{1/2}$ and $2P_{3/2}$ states of Co^{2+} ions (Dong et al. 2017; Wang et al. 2015b), while the peaks at 795.36 eV and 780.34 eV are attributed to the $2P_{1/2}$ and $2P_{3/2}$ states of Co^{3+} ions (Wang et al. 2015b). The difference in energy of the $2P_{1/2}$ and $2P_{3/2}$ levels of Co ions is ~15 eV. The presence of the four characteristic satellite peaks at 805.70 and 790.10 eV (corresponding to Co^{3+} ions) and 803.60 and 786.62 eV (corresponding to Co^{2+} ions) further validates the presence of these ions in the sample

(Wang et al. 2015b). The mixed valance states of Co ions favour the electrochemical properties of the sample. The high resolution XPS spectra of Mn2p show two major peaks corresponding to the spin orbit splitting of Mn ions (2p3/2 and 2p1/2) as shown in **Figure 3.4 (c)**. The deconvolution of 2p3/2 and the 2p1/2 peaks reveal the presence of mixed oxidation states of Mn ions in the sample. The peaks at 653.50 eV and 641.96 eV are attributed to the 2p1/2 and 2p3/2 states of Mn2+ ions (Ashok et al. 2020), while the peaks

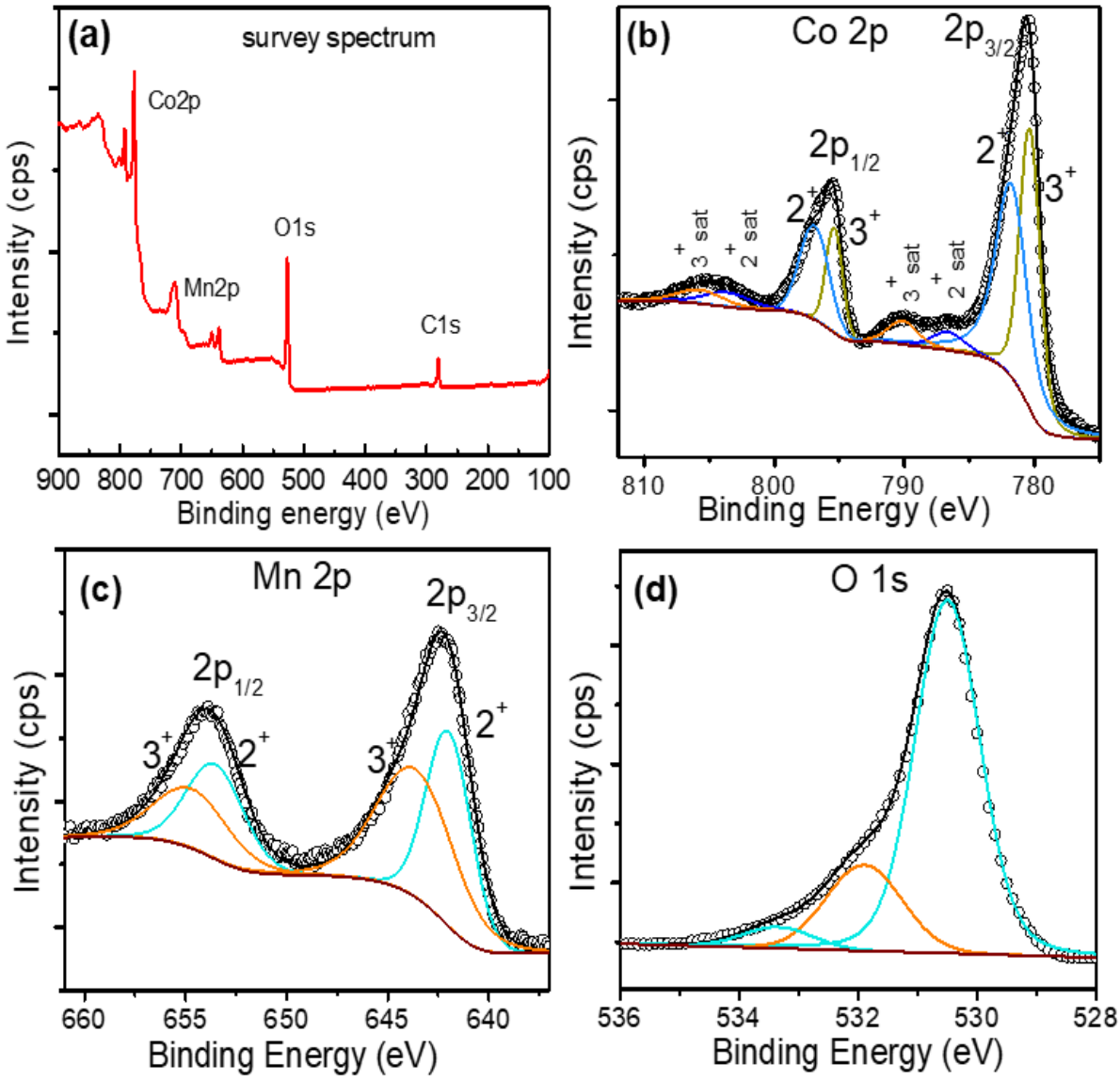

Figure 3.4. XPS spectra of synthesized $MnCo_2O_4$ nanoneedle: (a) The survey spectrum, (b) Co2p spectra, (c) Mn2p spectra, and (d) O1s spectra.

at 654.68 eV and 643.60 eV are attributed to the 2p1/2 and 2p3/2 states of Mn3+ ions (Ashok et al. 2020; Wang et al. 2015b). The mixed valance states of Mn ions also favour

the electrochemical properties of the sample. The high resolution XPS spectra of O1s shown in **Figure 3.4 (d)** could be deconvoluted into three peaks corresponding to the oxygen in the spinel structure of the $MnCo_2O_4$ sample (peak at 530.50 eV) and two small peaks at 533.35 eV and 531.90 eV respectively due to presence of small amount of hydroxide functional groups attached to the sample surface and physically adsorbed water molecules.

BET measurements of as-synthesized $MnCo_2O_4$ nanoneedles were conducted to measure the specific surface area and porous nature of the electrodes. Nitrogen adsorption-desorption isotherms of $MnCo_2O_4$ nanoneedles are presented in **Figure 3.5 (a)**, with a hysteresis loop revealing a porous behavior of the sample. The specific surface area value calculated for $MnCo_2O_4$ electrode material from BET measurements is 35 m^2 g^{-1}. **Figure 3.5 (b)** shows the distribution of pore size of the product measured using the BJH method (Barrett-Joyner-Halenda) from adsorption isotherms. The BJH desorption cumulative pore volume of $MnCo_2O_4$ electrode material from 1.7 nm to 300 nm diameter is 0.12 cm^3 g^{-1}. The increased specific surface area value and porous structure enhance the capacitance property of the $MnCo_2O_4$ by increasing the ion transport and reversible redox process (Liu et al. 2020b).

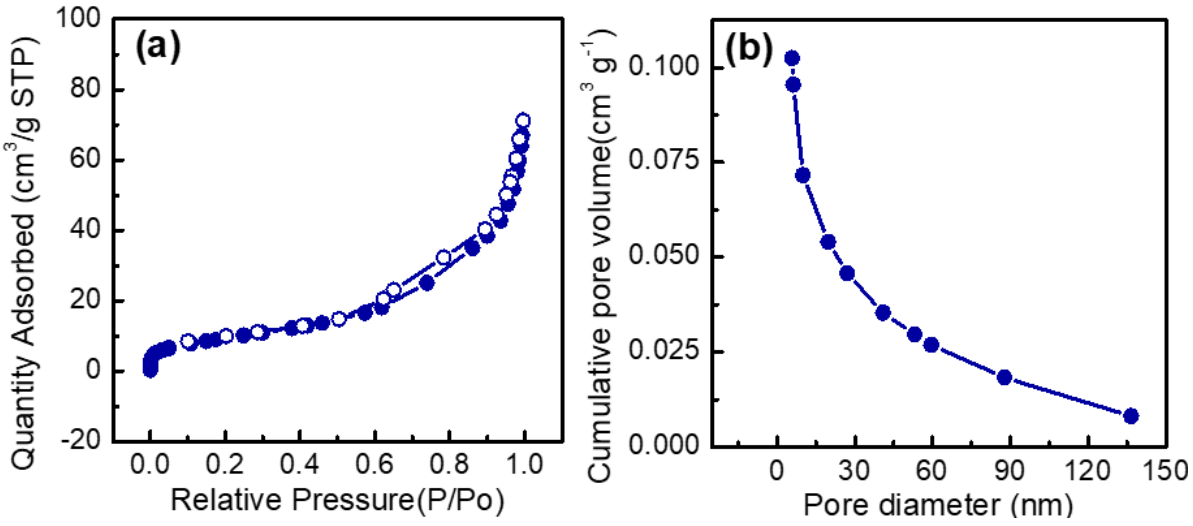

Figure 3.5. (a) Nitrogen-adsorption and desorption isotherms and (b) Pore-size distribution of the $MnCo_2O_4$ nanoneedles.

SEM was carried out to analyze the surface morphology of the synthesized material. **Figure 3.6 (a-c)** shows the SEM images of the $MnCo_2O_4$ nanoneedles grown on NF.

Figure 3.6 (a and b) shows a sea urchin-like surface morphology of the sample with a mean diameter of 2 µm that is entirely covering the conductive NF substrate. The FESEM image (**Figure. 3.6 (c)**) reveals that, the samples consist of so many long and fine nanoneedles grown vertically from the center into outward direction. This type of open porous structure can provide large electroactive surface area to the $MnCo_2O_4$ nanoneedle based electrode material, which is also noticeable from the BET analysis. In addition, the

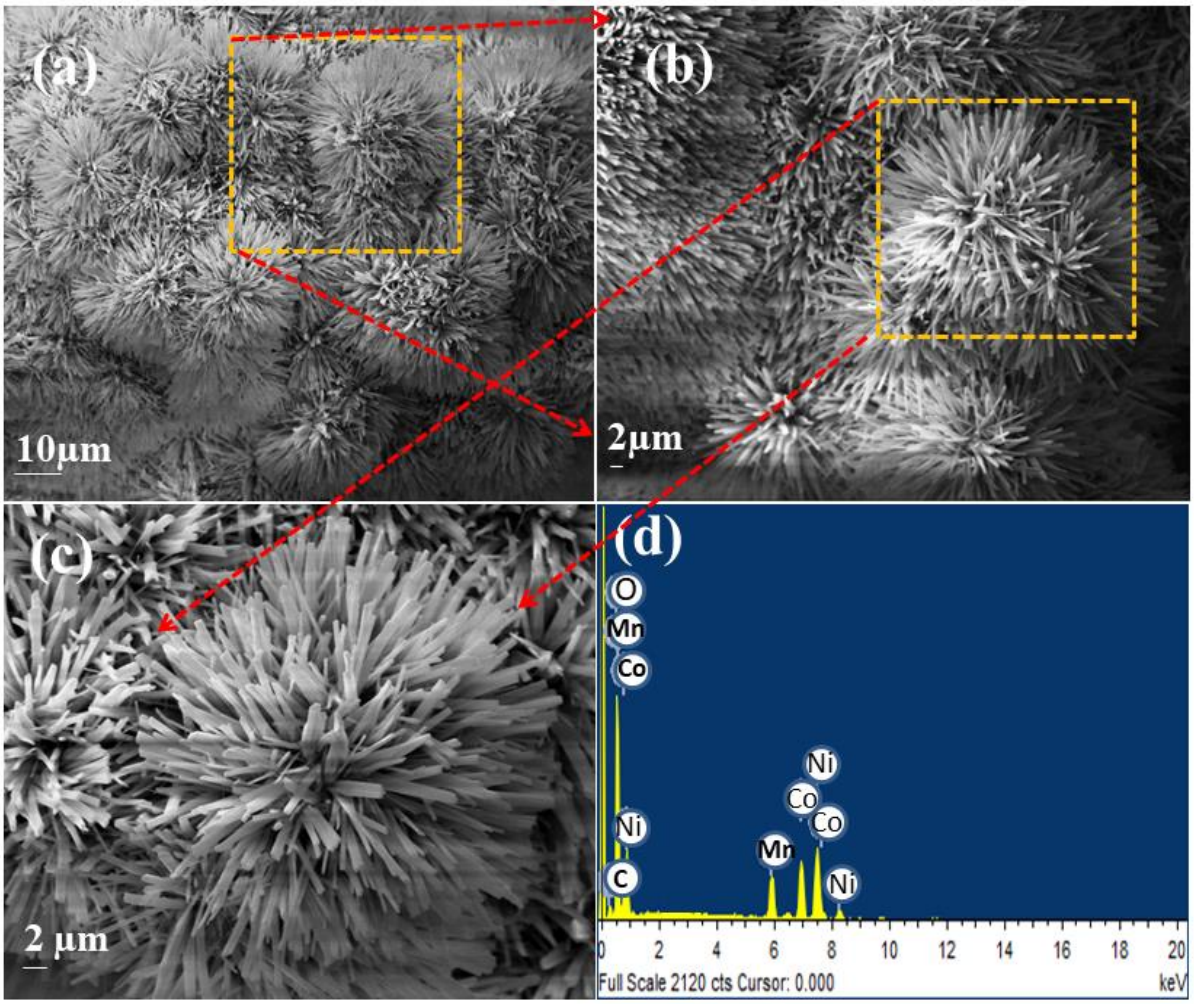

Figure 3.6. FESEM images (a), (b), and (c) of $MnCo_2O_4$ nanoneedles grown over NF substrate and (d) EDX spectra of $MnCo_2O_4$ nanoneedles.

direct growth of nanoparticles on NF can enhance the C_{sp} value by providing necessary utilization of the products, excellent contact with the electrode, and high conductivity. Also, the round-shaped nanoneedles have a mean tip diameter of 30 nm and a bottom width of 70 nm. These different nanoneedle structures provide rapid ion diffusion and ion

transport, which greatly enhance the electrode performance as a supercapacitor device. The elemental composition of the synthesized material was carried out using EDX spectroscopy technique and is presented in **Figure 3.6 (d)**. EDX spectra exhibit peaks

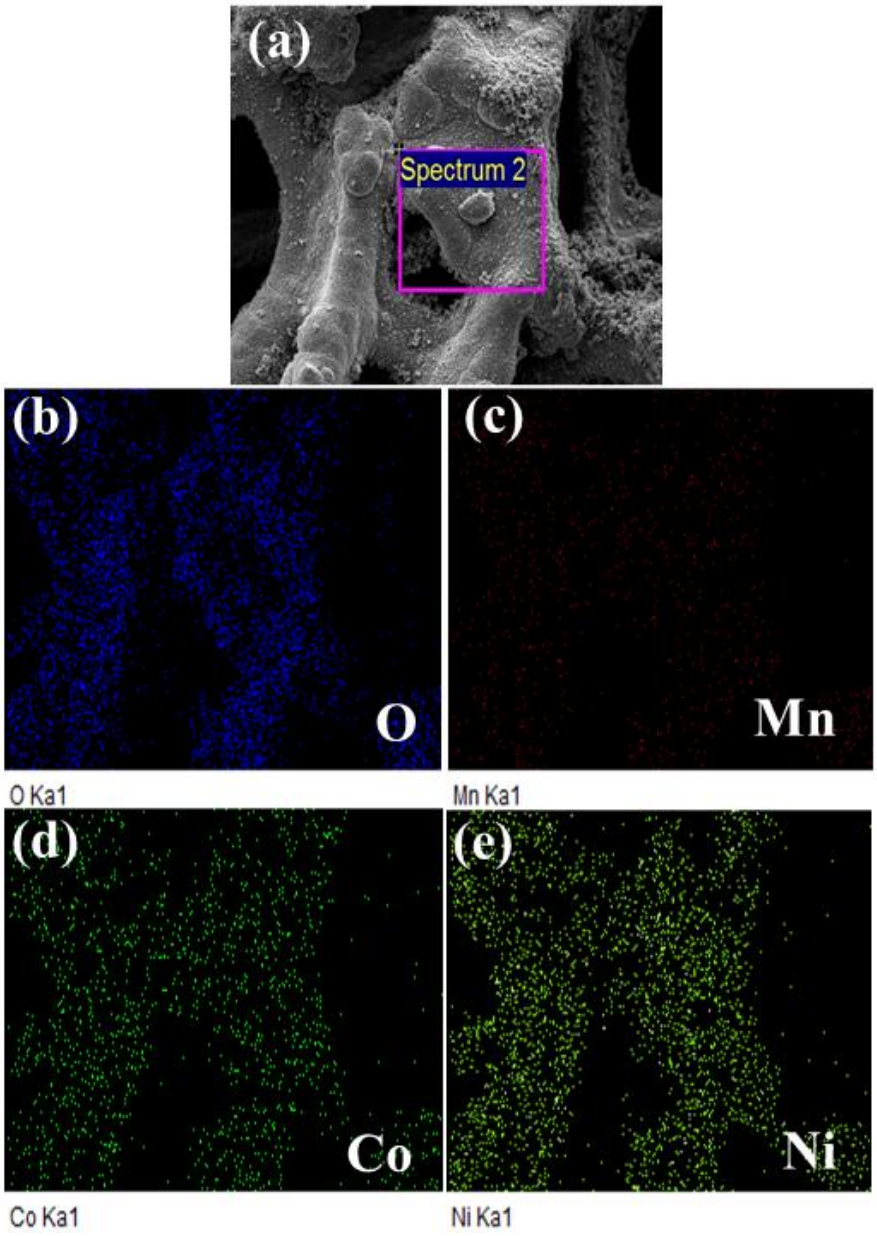

Figure 3.7. (a-e) EDX elemental mapping images for $MnCo_2O_4$ nanoneedles

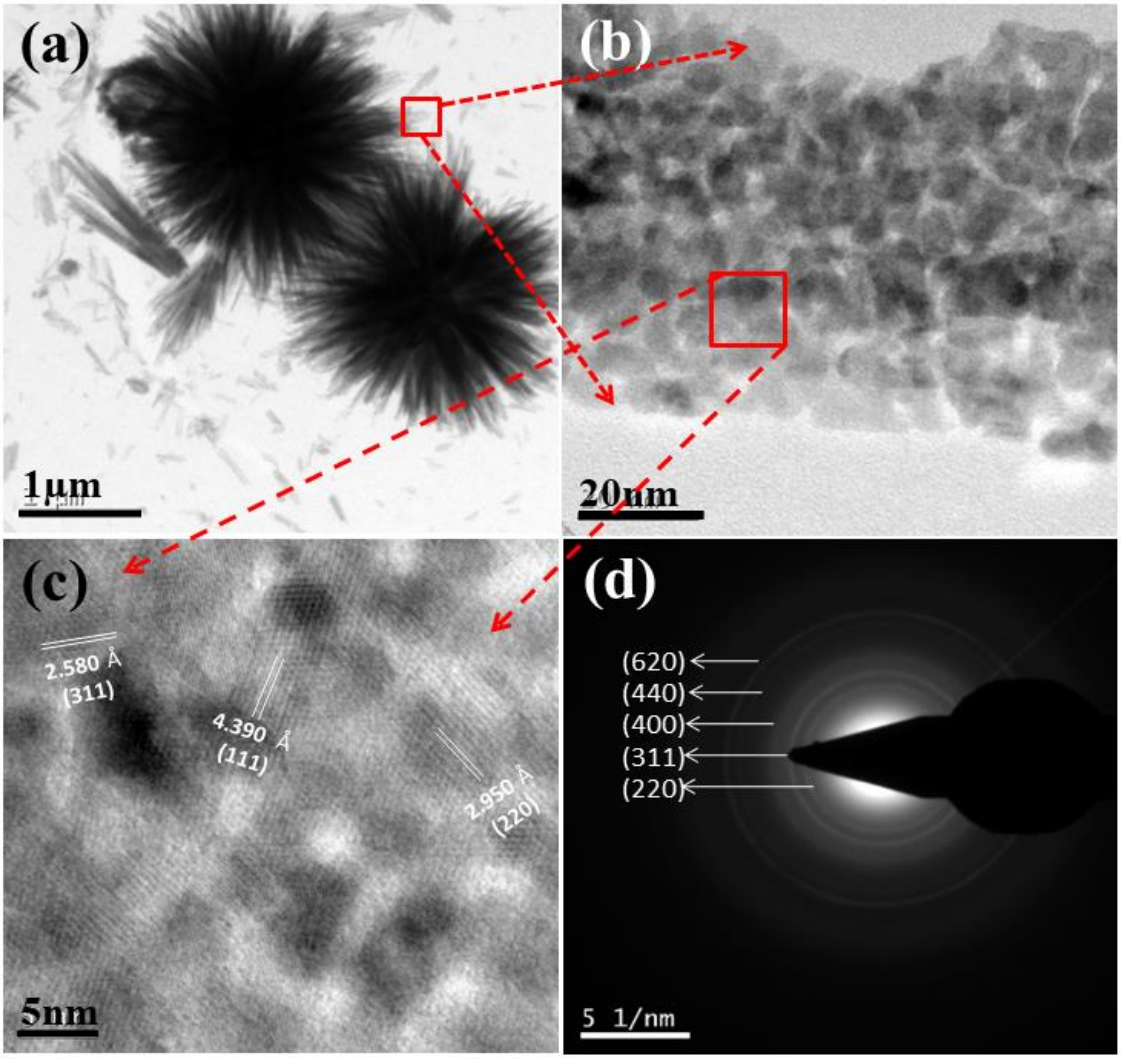

Figure 3.8. (a) TEM image (b) and (c) HRTEM images and (d) SAED pattern of $MnCo_2O_4$ nanoneedle.

corresponding to the elements manganese (Mn), cobalt (Co), and oxygen (O) in the as-prepared $MnCo_2O_4$ nanoneedles. The peaks of Ni observed may be due to the presence of NF substrate. EDX elemental mapping images for $MnCo_2O_4$ nanoneedle-based electrodes are presented in **Figure 3.7 (a-e)**. The elemental mapping images confirm the presence of manganese, cobalt, and oxygen elements in the $MnCo_2O_4$ nanoneedle electrode. The presence of nickel (**Figure 3.7(e)**) is due to the nickel foam substrate used. In addition, it can also be observed that manganese, cobalt, and oxygen are homogeneously distributed over the nickel foam substrate. The detailed morphology of the electrode material was further investigated using TEM (**Figure 3.8 (a-c)**). The TEM image shown in **Figure 3.8 (a)** shows sea urchin like morphology of the sample and are assembled by various 1D nanoneedles. The HRTEM images shown in **Figure 3.8 (b and c)** further reveal that

nanoneedle-like structures are formed by large number of interconnected nanoparticles of $MnCo_2O_4$. The average particle size of $MnCo_2O_4$ nanoparticles is calculated as 13 nm with a 5 - 15 nm range of size distribution. These unique porous nanoparticles assembled nanoneedle structure gives outstanding Faradaic performance due to the fast ion diffusion, leading to a large specific capacitance value. The HRTEM images presented in **Figure 3.8 (c)** show that the equal inter-planar distances of 4.390, 2.950, and 2.580 Å are consistent with the standard inter-planar distances of 4.780, 2.925, and 2.493 Å, which respectively correspond to the (111), (220), and (311) crystal planes, confirming the well-crystalline structure of cubic $MnCo_2O_4$. The SAED pattern of $MnCo_2O_4$ nanoparticles are shown in **Figure 3.8 (d)**. The rings of the SAED pattern can be readily indexed to the planes of the $MnCo_2O_4$ crystal structure, in good agreement with the XRD data.

3.4.2 Electrochemical characterization

Electrochemical tests were carried out to investigate the electrode behavior and evaluate the specific capacitance value of the assynthesized $MnCo_2O_4$ electrode. **Figure 3.9 (a)** displays cyclic voltammetric (CV) curves of $MnCo_2O_4$ at various scan rates between 5 and 200 mV s^{-1} in the voltage range of 0-1 V. The CV loops are observed to be deviate from the ideal rectangular type behavior, ensuring that, the C_{sp} contribution is mainly due to the pseudocapacitive nature of the $MnCo_2O_4$ electrode (Rakhi et al. 2016a; Stoller and Ruoff 2010). From the CV loop, current response enhances as scan rate increases showing the excellent rate capability of the electrode. Moreover, the CV curves retain the quasi-rectangular shape even at 200 mV s^{-1} scan rate, which indicates high electronic conductivity and great reversibility for the $MnCo_2O_4$ based electrode material [28]. The highly reversible Faradaic reactions occur due to the changes in valance states of Co^{2+}/Co^{3+} and Mn^{2+}/Mn^{3+} ions (electrode) with OH^- ions (KOH electrolyte). The possible redox reaction for $MnCo_2O_4$ is explained by the following Equations. (1-3) (BoopathiRaja and Parthibavarman 2019; Li et al. 2014a).

$$MnCo_2O_4 + H_2O + OH^- \rightarrow MnOOH + CoOOH + e^- \quad (3.1)$$

$$MnOOH + OH^- \rightarrow MnO_2 + H_2O + e^- \quad (3.2)$$

$$CoOOH + OH^- \leftrightarrow CoO_2 + H_2O + e^- \quad (3.3)$$

The large area of the CV curve reveals that the symmetric supercapacitor based on $MnCo_2O_4$ nanoneedles poses high charge storage capacity, which may be attributed to the high specific surface area of the unique nanoneedle-like morphology, as evident from BET result. A maximum Csp value of 420 F g^{-1} was attained for the $MnCo_2O_4$ electrodes at 5 mV s^{-1}. The galvanostatic charge-discharge (GCD) curves of $MnCo_2O_4$ nanoneedle-based electrodes at various current densities from 1 to 5 A g^{-1} are shown in **Figure 3.9 (b)**. The triangular shape of the GCD curve designates lower internal resistance of the

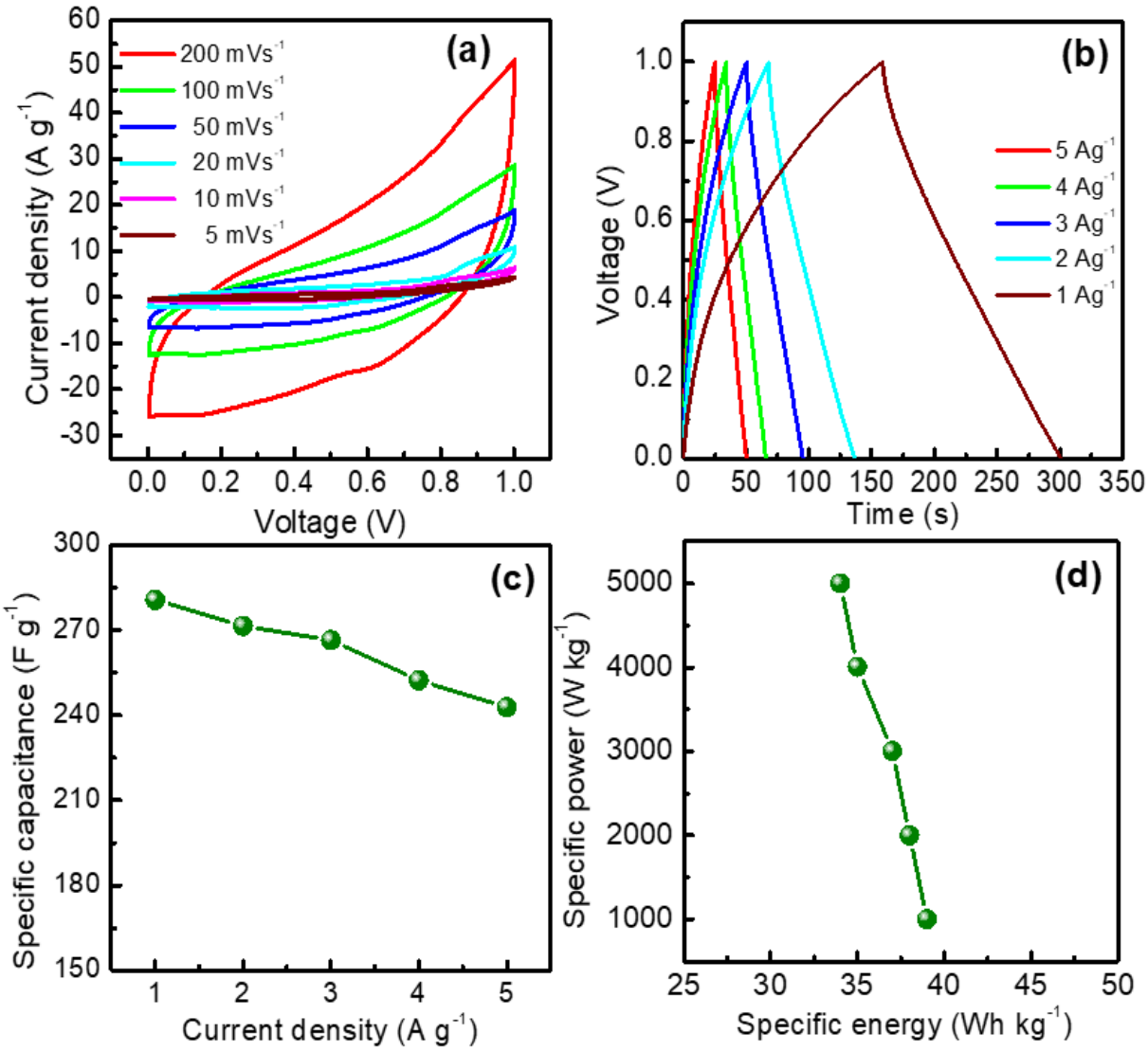

Figure 3.9. (a) Cyclic voltammograms at different scan rates, (b) Galvanostatic charge-discharge curves at different current densities for supercapacitors based on $MnCo_2O_4$ nanoneedles (c) Variation of Csp as a function of current densities, and (d) Ragone plot.

supercapacitor electrodes. In addition, the symmetrical shapes of the GCD curve demonstrate the highly reversible reaction of the electrode materials (Xiao et al. 2020a). The direct growth of $MnCo_2O_4$ nanoneedle materials on nickel foam substrates helps in enhance the conductivity of electrode materials (Chebil et al. 2020). The direct growth of $MnCo_2O_4$ nanoneedles over NF eliminates the use of binders used in conventional electrode preparation (Zhu et al. 2021). The porous structure of the $MnCo_2O_4$ nanoneedle is favourable to increasing the electro-active surface area and thus improving the electrode performance of the sample (Hao et al. 2015; Kuang et al. 2017). In addition, an urchin-like 3D porous structure established by the self-organization of $MnCo_2O_4$ nanoneedles on NF substrate is useful to elevate the reaction area at the interface between electrode and electrolyte and improve the speed of electrolyte ions in the electroactive sites (Chen et al. 2019b; Zhao et al. 2016). The changes in C_{sp} values of the electrode material as a function of current densities are shown in **Figure 3.9 (c)**. At a current density of 1 A g^{-1}, the supercapacitor exhibits a C_{sp} value of 280 F g^{-1}. The C_{sp} decreases at larger current densities, this may due to the lower ion transfer rate of electrolytes. The Ragone plot (specific energy vs specific power) for the $MnCo_2O_4$ nanoneedle based symmetric supercapacitor is presented in **Figure 3.9 (d)**. At a specific power of 1 kW kg^{-1}, the specific energy achieved for $MnCo_2O_4$ nanoneedle based supercapacitor material is 39 Wh kg^{-1}.

The percentage of capacitance contribution measured for the sample based on Trasatti's analysis is presented in **Figure 3.10 (c).** The EDLC and pseudocapacitive contribution of $MnCo_2O_4$ nanoneedle-based electrode are 5 % and 95 % respectively.

Long-term cyclic performance at higher current density is an essential requirement for the practical application of supercapacitor electrode materials. Hence, the cyclic stability measurement of the supercapacitor was performed by conducting GCD tests for 10,000 continuous cycles at 5 A g^{-1}, and the result is shown in **Figure 3.11 (a)**. The device retains 96 % of its maximum Csp value after 10,000 cycles, indicating that the electrode material has outstanding cycle life.

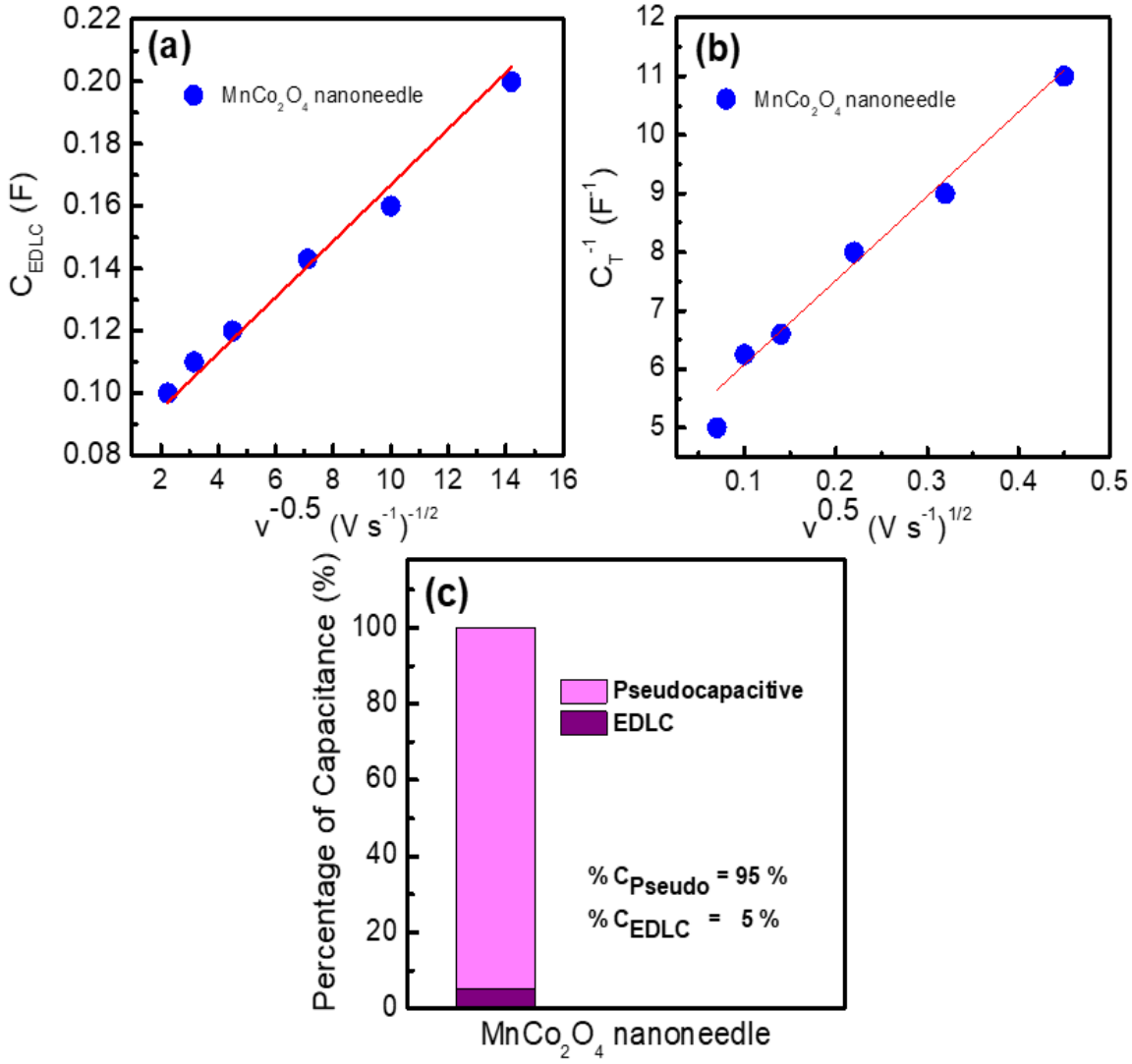

Figure 3.10. (a) linear fit of specific capacitance (Csp) vs. reciprocal of square root of scan rate ($v^{-0.5}$) (b) a linear fit of reciprocal of specific capacitance (Csp^{-1}) vs. square root of scan rate ($v^{0.5}$) (c) percentage of capacitance contribution calculated for $MnCo_2O_4$ nanoneedle electrode from Trasatti's analysis.

The $MnCo_2O_4$ nanoneedle directly grown on the NF substrate gives excellent cyclic stability to the electrode. The Csp value and cycle life performance in the present study are dramatically high compared with the same compound reported by Sahoo et al. (Sahoo et al. 2015a) and Li et al. (Li et al. 2014c). Sahoo et al. reported the fabrication of spinel $MnCo_2O_4$ nanosheets on nickel foam via electrodeposition, and the electrode delivered a specific capacitance value of 95.6 F g^{-1} at 1 mV s^{-1} along with a cycle life of 80 % at the end of 1000 cycles (Sahoo et al. 2015a). Li et al. reported urchin-like $MnCo_2O_4$ and

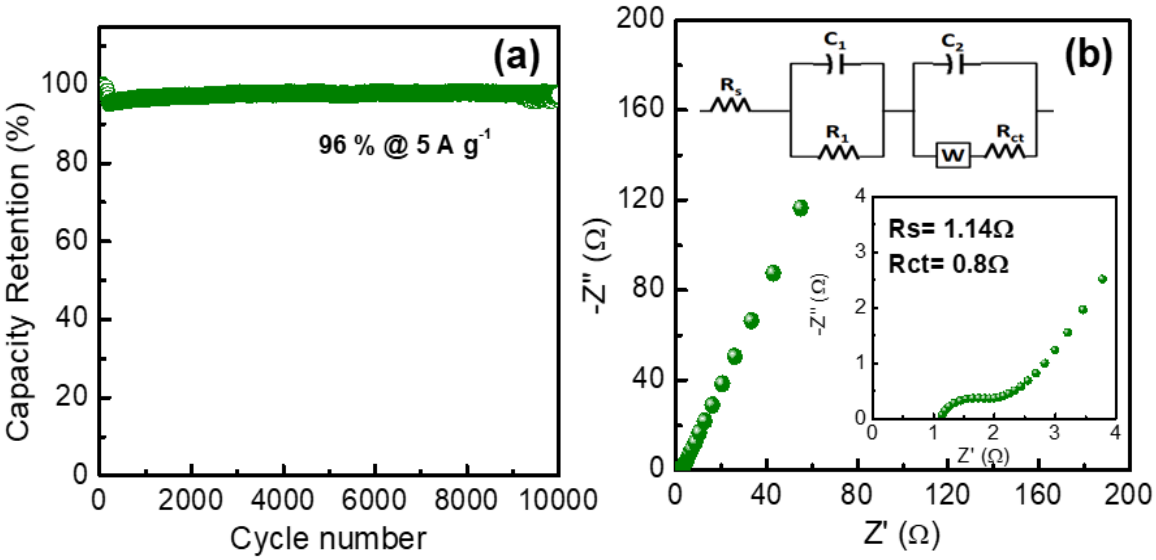

Figure 3.11. (a) Cycling performance of supercapacitor based on $MnCo_2O_4$ nanoneedle electrodes at a current density of 5 A g^{-1} and (b) Nyquist plot.

retained 151.2 F g^{-1} C_{sp} at 5 mV s^{-1} along with a cyclic stability of 83.6 % after 2200 cycles (Li et al. 2014c). Padmanathan et al. reported mesoporous $MnCo_2O_4$ via a solvothermal approach, which delivers 189 F g^{-1} at 1 A g^{-1} with a cyclic stability of 88 % at the end of 2500 CD loops (Padmanathan and Selladurai 2014a). All these works are based on three electrode measurements, and it is known that three electrode techniques deliver an exaggerated C_{sp} value as compared to two electrode measurements. A comparison of performance of $MnCo_2O_4$ nanoneedle as supercapacitor electrode with literature data is presented in **Table 3.1**. The electrochemical impedance spectroscopy (EIS) measurement was conducted to study the properties of charge transfer in the electrode material. **Figure 3.11 (b)** shows the Nyquist plot obtained for the as-prepared electrode material. The high frequency region of the Nyquist plot consists of a semicircle part, and the lower frequency region consists of a linear part. The X – intercept of the semicircle part gives the total solution resistance (R_s) value of the electrolyte for the $MnCo_2O_4$ nanoparticle electrode as 1.14 Ω. The charge- transfer resistance (R_{ct}) value is measured from the diameter of the semicircle part in the middle frequency region. The lower R_{ct} value for the electrode material indicates an effectively high charge transfer rate between the nanoneedle electrode and electrolyte interface. The shorter inclined line in

Electrode material	**Voltage window**	**Electrolyte**	**Specific capacitance ($F\ g^{-1}$)**	**Cyclic stability**	**Reference**
$MnCo_2O_4$ Nanosheet	-0.1 to 0.4 V	6 M KOH	189 F g^{-1} at 1 A g^{-1} (Half cell)	88% (2500 cycles)	(Padmanathan and Selladurai 2014b)
$MnCo_2O_4$ nanosheet/ nickel foam	-0.1 to 0.4 V	2 M KOH	95.6 F g^{-1} at 1 mV s^{-1} (Half cell)	80% (1000 cycles)	(Sahoo et al. 2015a)
Urchin-like $MnCo_2O_4$	-0.35 to 0.55 V	1M KOH	151.2 F g^{-1} at 5 mV s^{-1} (Half cell)	83.6% (2200 cycles)	(Li et al. 2014b)
spinel $MnCo_2O_4$	-0.2 to 0.6 V	2M KOH	405 F g^{-1} at 5 mA cm^{-2} (Half cell)	95.1% (1000 cyces)	(Kong et al. 2014b)
$MnCo_2O_4$ nanoneedle	**0 to 1 V**	**2M KOH**	**420 F g^{-1} at 5 mV s^{-1} (Full cell)**	**96% (10000 cycles)**	**Present work**

Table 3.1. Comparative study of supercapacitor performance of $MnCo_2O_4$ nanoneedle with literature data

the low frequency part represents the rapid diffusion of electrolyte ions in the electrode material. The remarkable electrochemical performance may be attributed to the unique one-dimensional porous nanoneedle structure of $MnCo_2O_4$ and the direct growth of the material over the NF current collector, resulting in the self-organization of the

nanoneedles in to 3D urchin-like microstructure, which provides maximum electrolyte accessibility and low internal resistance (Miao et al. 2019; Wang et al. 2014). These results validate that $MnCo_2O_4$ nanoneedles grown on NF substrates are outstanding electrode materials for supercapacitor device applications.

3.5. Conclusion

One-dimensional $MnCo_2O_4$ nanoneedles were directly grown over a conducting NF substrate using a facile hydrothermal process. The nanoneedles were self-organized into 3D urchin-like microstructures, which were capable of providing maximum electrolyte accessibility. The $MnCo_2O_4$ nanoneedles were composed of a large number of $MnCo_2O_4$ nanoparticles, which greatly increased the device properties by boosting the electro active surface sites, and thereby promoting fast diffusion of ions at the electrode-electrolyte interface. The $MnCo_2O_4$ nanoneedle-based supercapacitor device delivered a maximum C_{sp} of 420 F g^{-1} at 5 mV s^{-1}. The device exhibited a specific energy of 39 Wh kg^{-1}, at 1 kW kg^{-1}. In addition, it demonstrated a cycling stability of 96 % at 5 A g^{-1}, even after 10,000 GCD cycles. The results indicate that $MnCo_2O_4$ nanoneedle based electrodes can play a potential role in future energy storage applications.

Chapter 4

$MnCo_2S_4$ nanoflowers directly grown over Nickel foam for high-performance supercapacitor applications

4.1. Outline of the chapter

The chapter deals with the application of the Mn-Co sulfide system for electrochemical energy storage. $MnCo_2S_4$ nanoflowers have been directly grown over nickel foam (NF) substrate via a simple hydrothermal process for electrochemical energy storage. A symmetric supercapacitor assembled using $MnCo_2S_4$ nanoflower electrode delivers an impressive specific capacitance of 1243 F g^{-1} at 1 A g^{-1} along with a cyclic performance of 97 % and a coulombic efficiency of 98 % at 5 A g^{-1} after 10000 charge-discharge cycles. Furthermore, at a specific power of 1 kW kg^{-1}, the $MnCo_2S_4$ nanoflower-based symmetric supercapacitor exhibits superior performance with an increased specific energy of 170 Wh kg^{-1}, and a gravimetric energy density of 42 Wh kg^{-1} at a gravimetric power density of 250 W kg^{-1}. The present study demonstrates the potential of $MnCo_2S_4$ nanoflower-based electrodes for electrochemical energy storage applications.

4.2. Introduction

Nowadays, supercapacitors are successfully applied in hybrid electric vehicles, electronic devices, volatile memory backups in PCs, and uninterrupted power supplies (UPS) (González et al. 2016; Xiao et al. 2020b). However, the widespread application of supercapacitors is still hindered by their very low energy density values (Gogotsi and Simon 2011). Hence, research in the area of supercapacitors is focused on improving the energy density of these devices without losing their power density. The lower electrical conductivity of transition metal oxides and hydroxides inhibits the ion diffusion rate, resulting in poor capacitance values and cyclic performance (Gonçalves et al. 2021). Therefore, producing an excellent active electrode material with increased electrical conductivity and a good nanostructure is necessary to elevate the electrochemical properties of the supercapacitors.

Recently, monometallic sulfides such as CoS_2 (Gao et al. 2019), MnS (Li et al. 2015a), NiS (Hu et al. 2020), MoS_2 (Feng et al. 2019), WS_2 (Sambath Kumar et al. 2020), etc. have been broadly utilized as pseudocapacitor electrode materials. Employing their high energy density, electrochemical activity, stability, and enhanced conductivity, binary metal sulfides such as $CuCo_2S_4$ (Sonia et al. 2021), $NiCo_2S_4$ (Chen et al. 2020), $ZnCo_2S_4$ (Yi et al. 2021), and $MnCo_2S_4$ (Hsu et al. 2021) are considered as superior electrode materials compared to monometallic sulfides. Among them, limited studies are available for $MnCo_2S_4$ as an electrode material for supercapacitors. $MnCo_2S_4$ can deliver superior conductivity due to the synergy between cobalt and manganese (Hsu et al. 2021; Nasrin et al. 2021). In addition, cobalt delivers a higher oxidation potential, and manganese can transport more electrons, generating a higher rate capacity. As a result, metal sulfide incorporating both cobalt and manganese can favour fast electron and ion transport rates to provide an outstanding electrochemical performance (Wang et al. 2019b). Different types of simple and low-cost synthesis techniques are employed to produce $MnCo_2S_4$ nanostructures. Rout *et al*. reported manganese cobalt sulfide nanosheets on nickel foam via a simple electrodeposition method, which delivers a greater specific capacitance of 2421 F g^{-1} at 1 A g^{-1} in three-electrode format (Sahoo and Rout 2016). The schematic illustration of the preparation of nanoparticles via electrodeposition technique is presented in **Figure 4.1**. However, for high mass loading application electrodeposition process takes much time. Wie *et al*. fabricated $MnCo_2S_4$ nanotubes by self-template method and shows

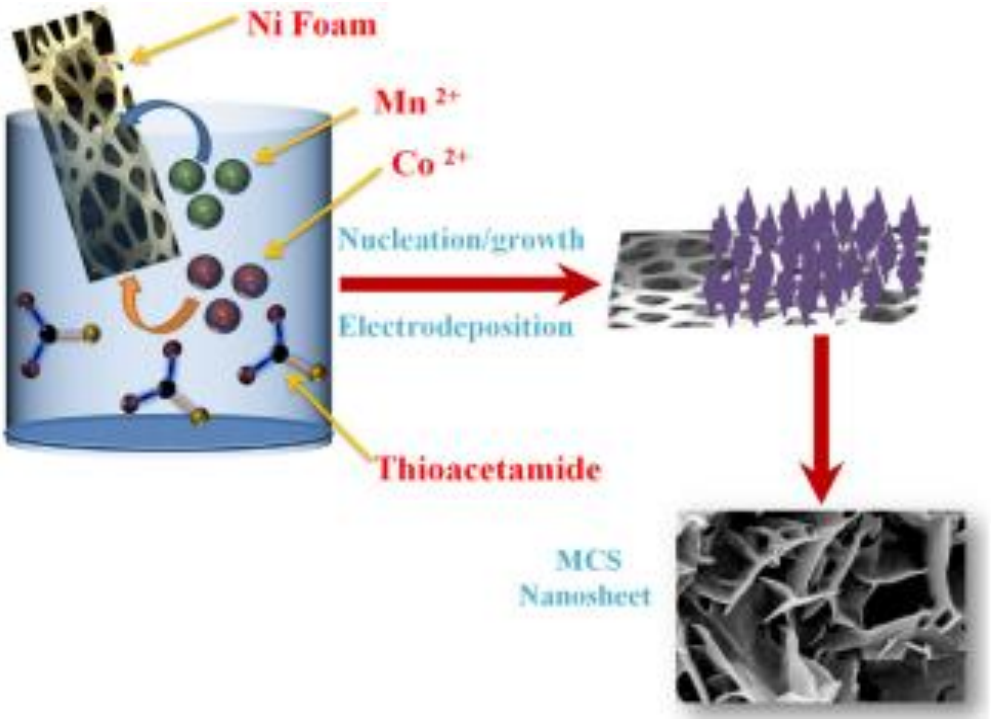

Figure 4.1. Schematic of the synthesis of $MnCo_2S_4$ nanosheet (Adapted from the reference (Sahoo and Rout 2016))

a specific capacitance of 705.2 F g^{-1} at 0.5 A g^{-1} in three-electrode format (Wie et al. 2017). Wang *et al*. reported manganese cobalt sulfide on Ni foam by a rapid microwave technique which exhibits a superior value of capacitance of 2084 F g^{-1} at 1 A g^{-1} in the three-electrode form (Wang et al. 2019a). Hydrothermal synthesis received great attention during recent times due to so many advantages such as moderate operating conditions, one-step synthesis method, good dispersion in solution, and eco-friendly nature (Abdel-Salam et al. 2022; Lama Tamang et al. 2022). Recently, Zhang *et al*. reported $MnCo_2S_4$ nanoparticles via a hydrothermal method and gives a specific capacitance of 1150 F g^{-1} at 1 A g^{-1} in three-electrode arrangements (Zhang et al. 2019). However, it is a known fact that three-electrode measurement yields an exaggerated capacitive performance value due to heightened sensitivity (Stoller and Ruoff 2010). Reports suggest that the electrochemical measurements in two electrode cell configuration provide the clear indication of the actual electrochemical performance of the active electrode material of a supercapacitor (Augustyn et al. 2014b; Simon and Gogotsi 2008a; Stoller and Ruoff 2010).

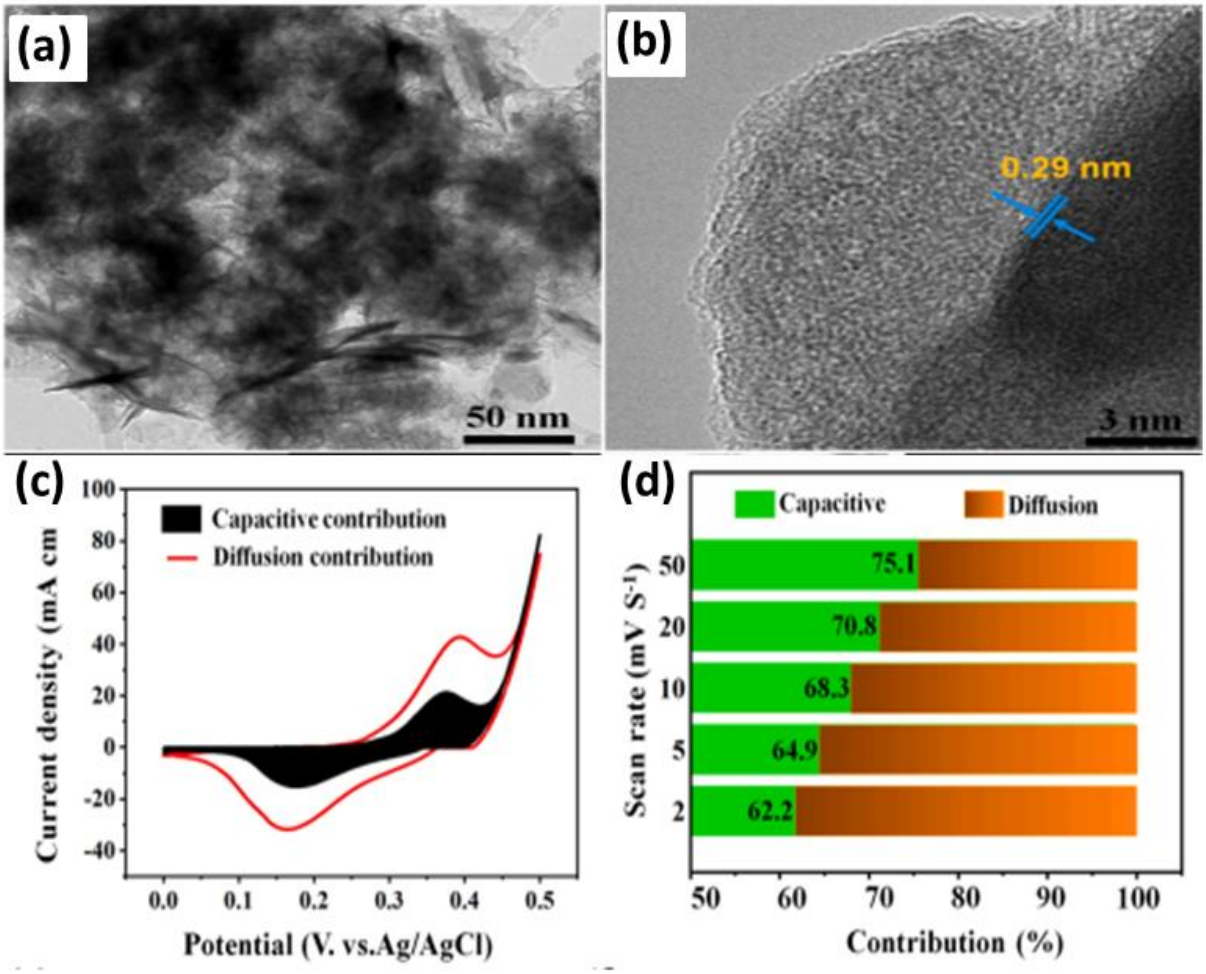

Figure 4.2. (a) and (b) TEM images of $MnCo_2S_4$ nanoflowers, and (c) and (d) Electrochemical characterization of $MnCo_2S_4$ nanoflowers (Adapted from the reference (Mola et al. 2021))

In this work, a simple, low-cost hydrothermal technique has been utilized for the direct growth of $MnCo_2S_4$ nanoflowers over a Ni foam substrate. The electrochemical energy storage performance of the as-grown electrodes is evaluated using symmetric two-electrode configurations in 2 M KOH electrolyte. The structural and morphological characterizations of the electrode materials and the electrochemical performance of the fabricated device are carried out using various techniques, and the results are discussed. The outstanding electrochemical performance of the $MnCo_2S_4$ nanoflowers can be attributed to the direct growth of the nanoparticles over the 3D conducting nickel foam. The porous nickel foam support improves the electrode/electrolyte contact area and decreases the ion diffusion paths.

4.3 Experimental Section

4.3.1 Synthesis of $MnCo_2S_4$ nanoflowers over nickel foam

$MnCo_2S_4$ nanoflowers were synthesized using a low-cost hydrothermal technique. In a typical process, $Mn(NO_3)_2.6H_2O$ (0.02 M), $Co(NO_3)_2.6H_2O$ (0.04 M), urea $CO(NH_2)_2$ (0.1 M), and NH_4F (0.08 M) were added to a Teflon-lined stainless steel autoclave containing a mixture of 20 mL of DI water and ethanol (1;1 ratio). Ni foam substrate (1x2 cm^2) is immersed in the above solution mixture after thorough repeated cleaning using 2 M HCl, acetone, and deionized water to remove all the surface impurities. The sealed autoclave was kept at 90^o C for 10 h and then cooled down to room temperature. The product was collected. It was then mixed with 0.2 g of $Na_2S.9H_2O$ and once again transferred to the autoclave containing 20 ml of DI water. The sealed autoclave was then heated to 160 ^oC for 6 h. The final product was collected, washed 2-3 times with DI water, and then dried at 60 ^oC in a vacuum oven for 12 h. The mass loading of the active material was calculated from the mass difference of Ni foam substrate before and after deposition. The synthesis of $MnCo_2S_4$ nanoflowers on NF was schematically shown in **Figure 4.3.** Herein, urea acts as a template and forms the precipitates of carbonates of Mn^{2+} and Co^{2+}. NH_4F delivers more active sites for nucleation and produces more precipitation of Mn^{2+} and Co^{2+}. The calcination process generates $MnCo_2S_4$. The hydrothermal sulfurization using aqueous Na_2S solution replaces oxygen with sulfur and forms $MnCo_2S_4$ nanoflower. The probable mechanism of formation of $MnCo_2S_4$ nanoflowers is represented using the following chemical equations (Mola et al. 2021).

$$CO(NH_2)_2 + 2H_2O \rightarrow 2NH_4^+ + CO_3^{2-} \quad (4.1)$$

$$Mn + CO_3^{2-} \rightarrow MnCO_3 \downarrow \quad (4.2)$$

$$Co + CO_3^{2-} \rightarrow CoCO_3 \downarrow \quad (4.3)$$

$$O_2 + 2MnCO_3 + 4CoCO_3 \rightarrow 2MnCo_2O_4 + 6CO_2 \uparrow \quad (4.4)$$

$$MnCo_2O_4 + 4Na_2S + 4H_2O \rightarrow MnCo_2S_4 + 8NaOH \quad (4.5)$$

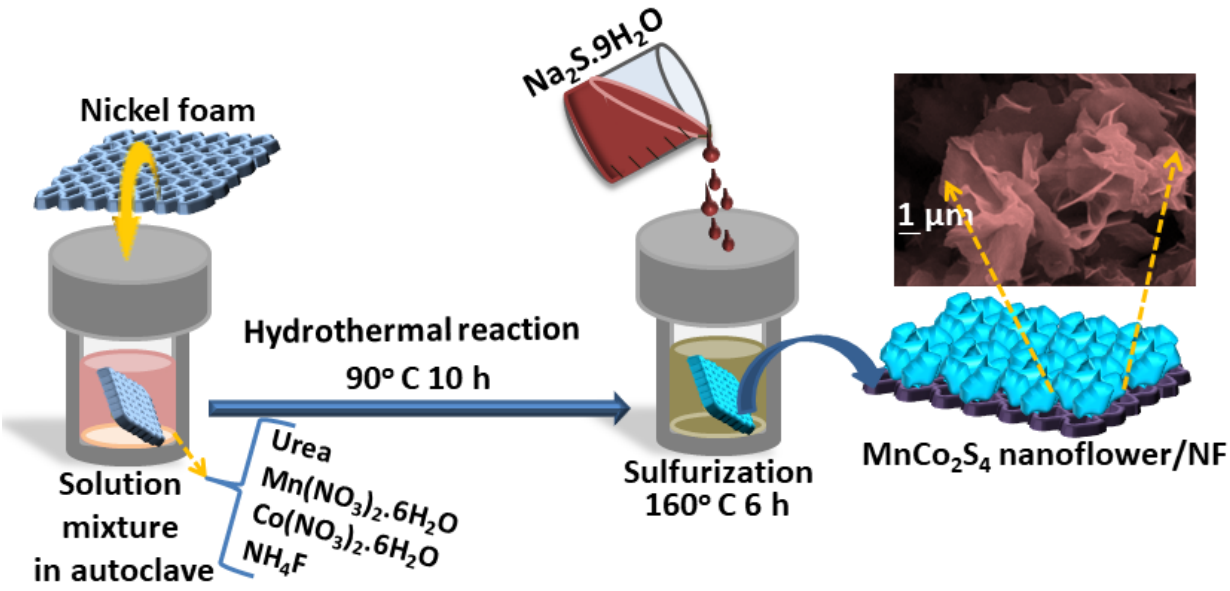

Figure 4.3. The schematic of the preparation of $MnCo_2S_4$ nanoflower-based electrode material for supercapacitor application.

Experimental details of the general characterization of the as-prepared electrode materials and the fabrication of Symmetric supercapacitor and electrochemical performance analysis are given in **chapter 2 section 2.3**

4.4 Results and Discussion

4.4.1 Structural and morphological characterization

The crystal structure of the as-synthesized nanomaterial is determined by powder X-ray diffraction (XRD) and the results are presented in **Figure 4.4 (a)**. The XRD pattern of $MnCo_2S_4$ nanoflowers shows peaks at 2θ values of 17.89°, 24.0°, 27.0°, 28.76°, 35.67 °, 40.80°, 44.63°, 50.41°, 54.74°, 57.79°, 61.58°, 63.96°, and 68.90° corresponding to reflections from (111), (220), (311), (222), (400), (331), (422), (511), (440), (531), (442), (620), and (444) planes respectively, which is similar to the diffraction peaks of cubic Co_3S_4 having space group Fdϊ m (227) (JCPDS card no. 73-1703, $\alpha=\beta=\gamma=90^o$). The lattice parameter values are obtained as, a = b = c = 9.52 Å from the XRD data. In $MnCo_2S_4$, Mn gets substituted at the Co site of Co_3S_4. Hence, the incorporation of the Mn element does not alter the crystal structure of $MnCo_2S_4$, but only alters its crystal parameter (Wang et al. 2019b). The schematic of the primitive cell of $MnCo_2S_4$ nanoflower is represented in **Figure 4.4 (b)**. The largest blue, middle sized maroon and smallest yellow-colored spheres are Mn, Co and S atoms, respectively. The average

crystallite size of $MnCo_2S_4$ nanoflowers was calculated as 12 nm from Scherrer's equation ($D=0.9\lambda/(\beta\cos\theta)$). The absence of other impurity peaks in the XRD pattern indicates the high purity of the synthesized sample.

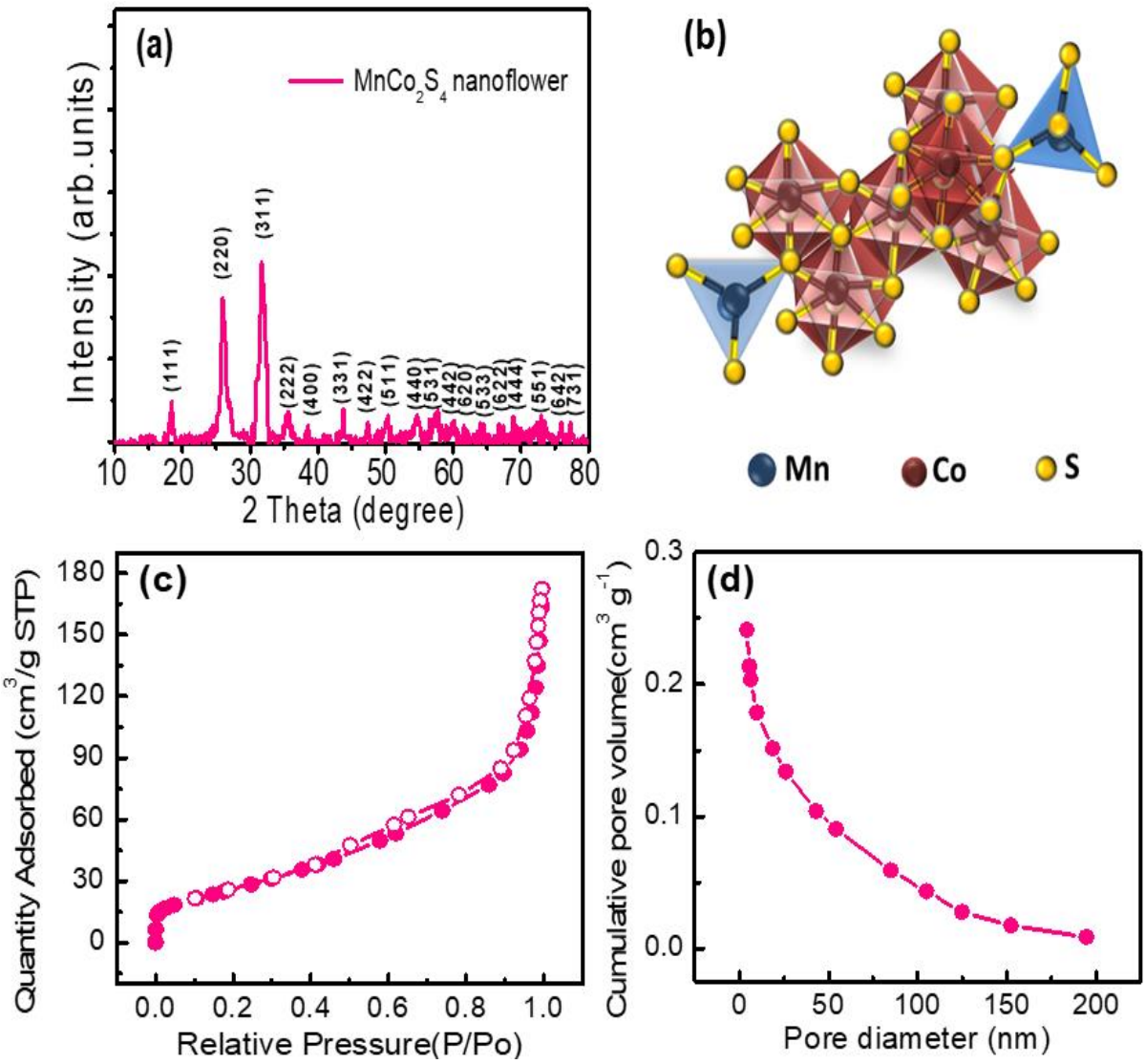

Figure 4.4. (a) Powder XRD patterns and (b) Schematic of primitive cell of $MnCo_2S_4$ nanoflower (c) Nitrogen-adsorption and desorption isotherms of the $MnCo_2S_4$ nanoflower, and (d) pore-size distribution of the $MnCo_2S_4$ nanoflower

Surface area and porosity are two crucial parameters, determining the suitability of the supercapacitor electrode materials. The nitrogen adsorption-desorption isotherms of as-synthesized nanomaterials were conducted to obtain the specific surface area and porosity of the electrodes. The Brunauer–Emmett–Teller (BET) surface area measurement results are presented in **Figure 4.4 (c)**. The sample exhibits type IV isothermal behavior (**Figure**

4.4 (c)), indicating the mesoporous structures of the material. The BET surface area values calculated for as-grown material are 98 m^2 g^{-1}. **Figure 4.4 (d)** shows the pore size distribution of the sample from the BJH method (Barret-Joyner-Halenda). The BJH analysis desorption cumulative pore volume of as-grown material from 1.70 nm to 300 nm diameter is 0.29 cm^3 g^{-1}. The high specific surface area and mesoporous structure are expected to deliver more active sites for the redox reaction and increase the electrochemical performance of the electrode material (Elshahawy et al. 2017a; Zhang et al. 2013).

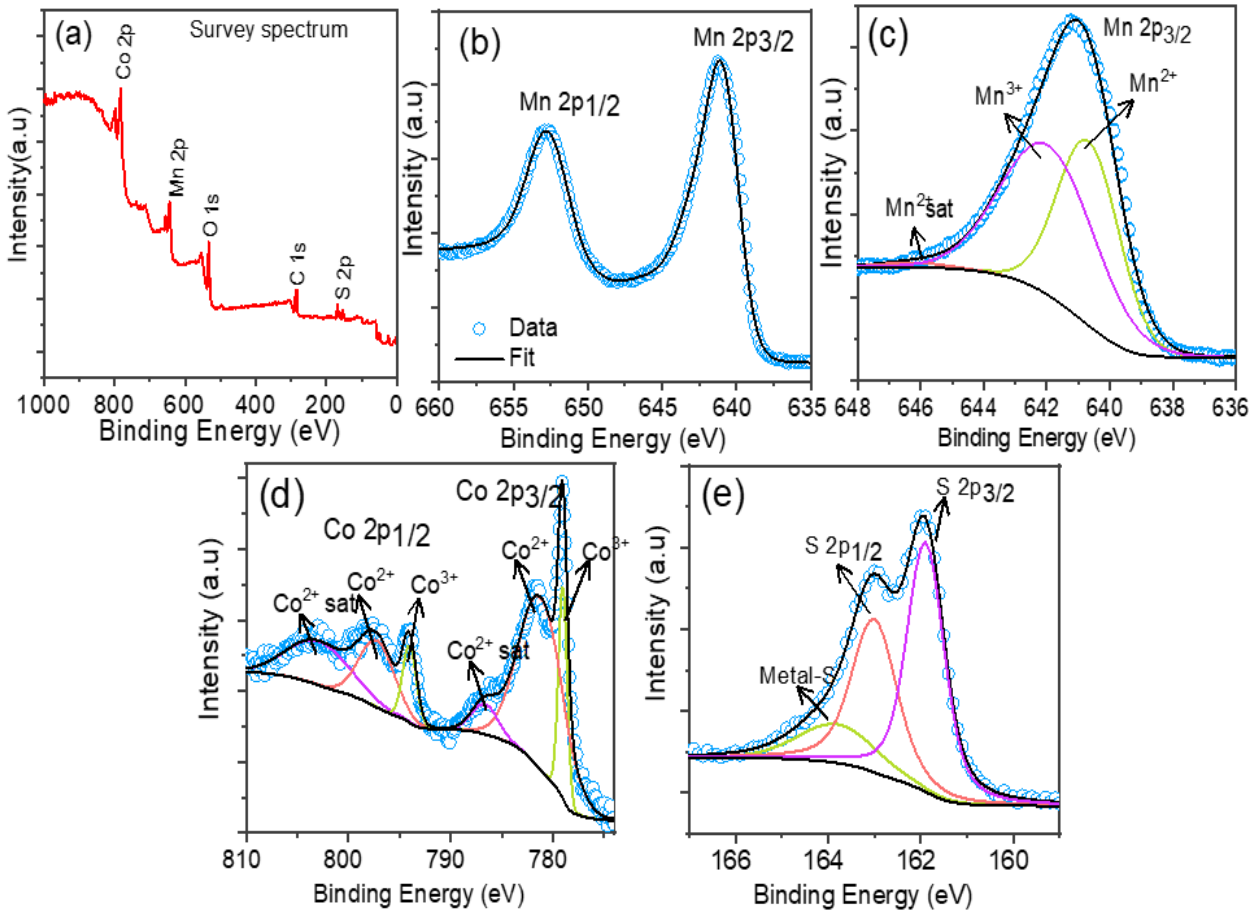

Figure 4.5. XPS spectra of synthesized $MnCo_2S_4$ nanoflower: (a) the survey spectrum, (b) Mn2p spectra, (c) deconvoluted Mn $2p_{3/2}$ spectra, (d) Co2p spectra, and (e) S2p spectra

To evaluate the near-surface oxidation states of the prepared as-grown nanomaterials, X-ray photoelectron spectroscopy (XPS) measurements were carryout and the results are presented in **Figure 4.5 (a-e)**. Deconvolution of all high-resolution XPS spectra was carried out using the software AAnalyzer. Shirley backgrounds were used and a GL-20 (Gaussian with 20% Lorentian) function was used to represent the individual peaks.

Figure 4.5 (a) shows the survey spectra which confirm the existence of Mn, Co, S, O, and C elements in the synthesized product. The Mn $2p_{3/2}$ high resolution spectra (**Figure 4.5 (c))** could be deconvoluted into three peaks: One centered at 640.7 eV corresponding to Mn^{2+}, the second one centered at 641.9 eV corresponding to Mn^{3+} and a small satellite peak at 646.2 eV corresponding to the Mn^{2+} satellite. The satellite peak is shifted by 5.5 eV from the main Mn^{2+} peak. From the ratio of the areas under Mn^{2+} and Mn^{3+} peaks, it is estimated that the ratio of Mn^{2+} to Mn^{3+} in the sample is 0.83, indicating that the predominant charge state is Mn^{3+}.

The Co 2p spectra (**Figure 4.5 (d))** is composed of six peaks: four main and two satellite peaks. The main peaks at 779.0 and 794.0 eV suggest the presence of Co^{3+}, and the presence of peaks at 781.2 and 797.2 eV suggest the presence of Co^{2+}. The two satellite peaks are located at 786.6 and 802.9 eV. The energy difference between the satellite and main peaks determines the oxidation state of Co. The formal valency is likely to be +2 if the energy difference is about 6.0 eV, and +3 if the difference is about 9 − 10 eV. Since the energy differences between the main and satellite peaks are 5.4 and 5.7 eV, the satellite peaks are predominantly due to Co^{2+}. From the areas under the individual peaks, it is seen that the ratio of Co^{2+} to Co^{3+} in the sample is 4.61, indicating that the predominant charge state is Co^{2+}. The S 2p spectra (**Figure 4.5 (e))** could be fitted with three peaks, one at 161.9 eV (due to S $2p_{3/2}$) and the second at 163.0 eV (indexed to S $2p_{1/2}$), indicating the presence of S^{2-} species, and the third peak at 163.8 eV, attributed to the metal-sulfur bonds in the compound (Hua et al. 2019; Mola et al. 2021) (Zhang et al. 2019). XPS analysis confirms the substitution of the Mn element at the Co site of Co_3S_4 leading to the formation of $MnCo_2S_4$.

The surface morphology of the $MnCo_2S_4$ nanomaterials is characterized by scanning electron microscopy (SEM). The SEM images (**Figures 4.6 (a and b)**) show a flower-like surface morphology of the sample, and the FESEM image (**Figure 4.6 (c)**) confirms that the $MnCo_2S_4$ nanoflowers are composed of several nanosheets. The nanoflower-like surface morphology provides maximum electrochemically active sites to the electrode material, enhances the electrolyte accessible surface area, and increases the electrochemical property of the $MnCo_2S_4$ nanoflowers (Rohith et al. 2021). The unique structure of the sample not only increases the redox reaction, but also provides a path for electron/ion transportation, which is useful for the better usage of active material (Zhao et

al. 2020). The EDX spectra and EDX elemental mapping images of $MnCo_2S_4$ nanoflower are included in **Figure 4.7 (a-f)**. The EDX spectra confirm the presents of manganese, cobalt, sulfur, oxygen, and nickel element (due to the usage of Ni-foam substrate) **(Figure 4.7 (b))**. From the EDX elemental mapping images **(Figure 4.7 (c-f)**) the presence of manganese, cobalt, and sulfur in the $MnCo_2S_4$ nanoflower electrode can be confirmed once again. The figure also depicts the homogeneous spreading of elements over the NF substrate.

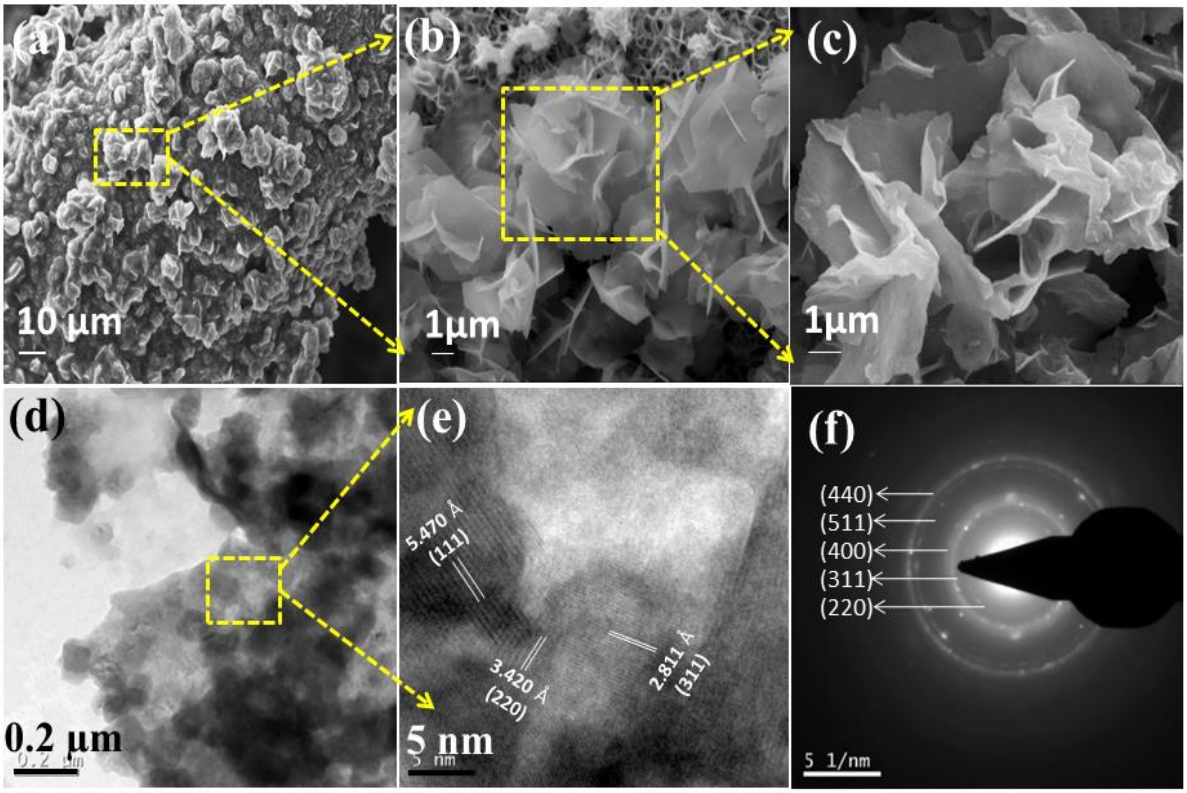

Figure 4.6. FESEM images (a), (b), and (c), and TEM (d) and HRTEM (e) images of $MnCo_2S_4$ nanoflower grown over NF substrate, (f) SAED pattern of $MnCo_2S_4$ nanoflower.

The transmission electron microscopy (TEM) and high-resolution TEM (HRTEM) images are used to study the microstructure of the $MnCo_2S_4$ nanoflowers (**Figure 4.6 (d and e)**). TEM image (**Figure 4.6 (d)**) reveals that the individual nanosheets are composed of several small nanoparticles. The average particle size of $MnCo_2S_4$ nanoparticles is obtained as 14 nm with a size distribution of 7 nm to 16 nm. Clearly, nanostructured particles enhance the electroactive surface area and thereby increase the capacitive performance (Yi et al. 2021). The HRTEM image (**Figure 4.6 (e)**) denotes the inter-

planar distances of 5.470, 3.420, and 2.811 Å corresponding to the (111), (220), and (311) crystal planes, which confirms the highly crystalline nature of the $MnCo_2S_4$ nanoflower. The morphology and microstructure of $MnCo_2S_4$ nanoflower provides maximum electroactive surface area and boosts the redox reaction, which increases the specific capacitance and cyclic stability of the electrode material (Li et al. 2015a). The selected area electron diffraction (SAED) pattern of $MnCo_2S_4$ nanoflower represented in **Figure 4.6 (f)** indicates the polycrystalline nature of the material. The SAED pattern rings can be readily indexed to the planes of the obtained crystal structure of the samples and the results match very well with the XRD data.

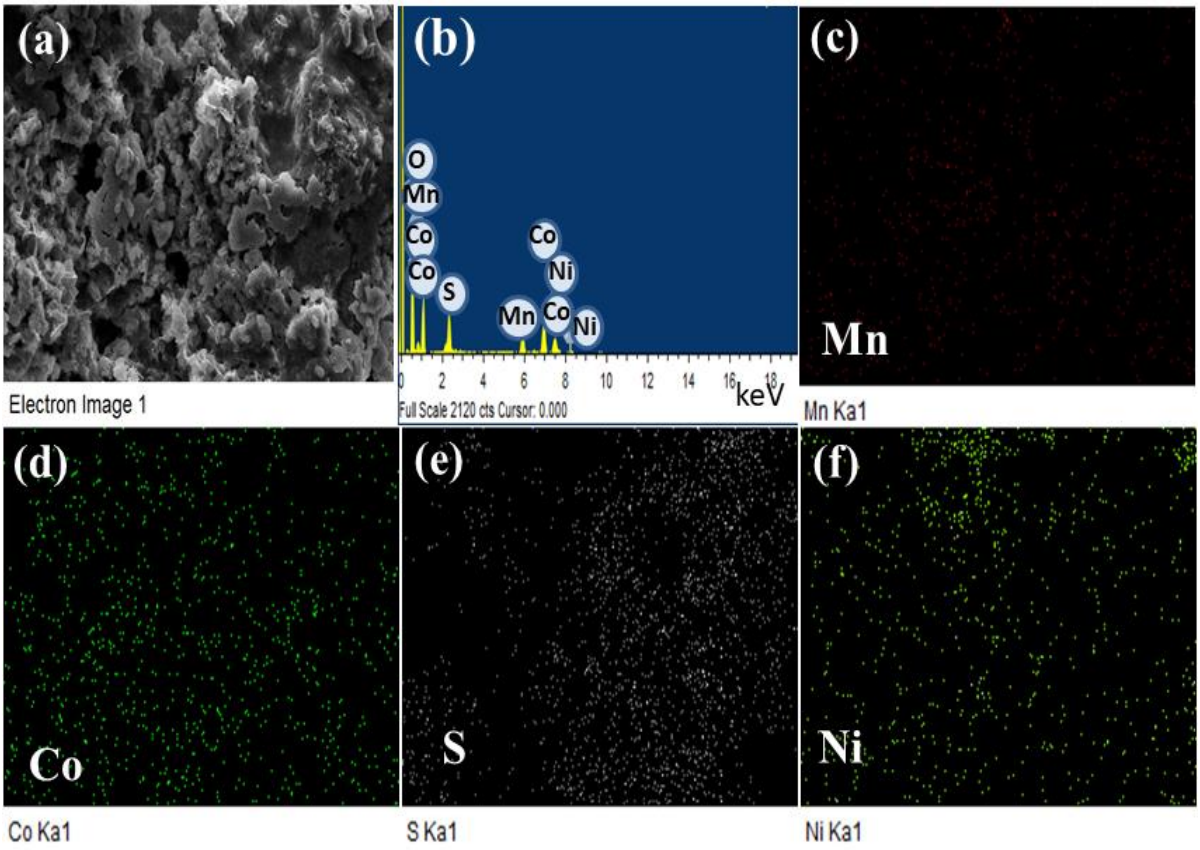

Figure 4.7. (a) SEM image, (b) EDX spectra, and (c, d, e, and f) EDX elemental mapping images for $MnCo_2S_4$ nanoflower based electrode.

4.4.2 Electrochemical characterization

To evaluate the energy storage performance of the $MnCo_2S_4$ nanoflower electrodes in real supercapacitor devices, a symmetric supercapacitor is fabricated, and the electrochemical performance measurements were carried out in a two-electrode configuration. **Figure 4.8 (a)** shows the CV loops of the fabricated symmetric supercapacitor at various scan rates

(5 – 200 mV s^{-1}). The CV curves exhibit a Faradaic type nature, indicating the presence of redox reactions during the electrochemical process (Gogotsi and Simon 2011). The shape of the CV loops does not change even at higher scan rates, signifying the stable redox process of the $MnCo_2S_4$ nanoflower electrodes (Murugan et al. 2006; Simon et al. 2014). Moreover, the current response increases with an increase in scan rate,

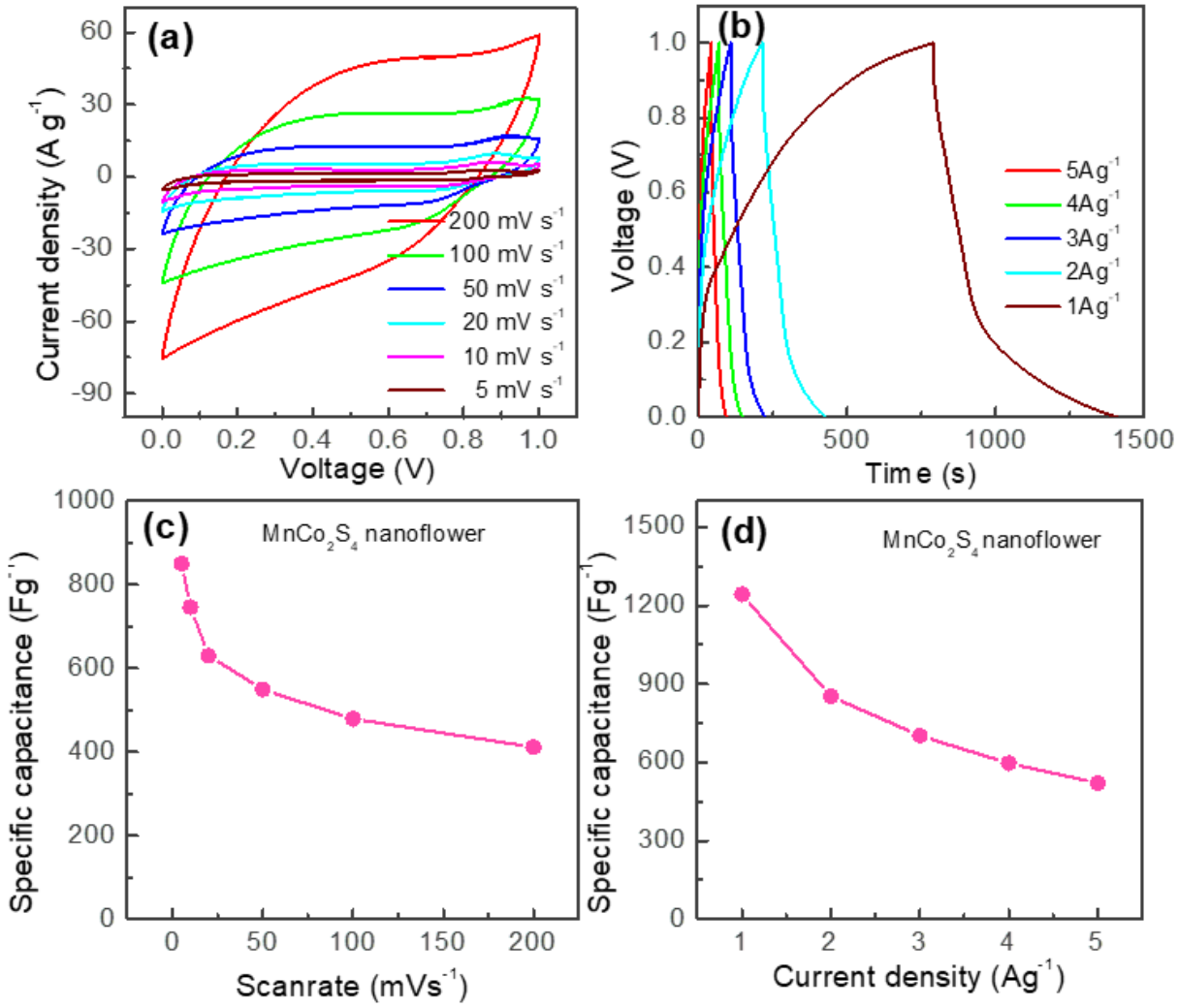

Figure 4.8. (a) Cyclic voltammograms at different scan rates, (b) Galvanostatic charge-discharge curves at different current densities, Variation of Csp as a function of scanrate (c), and current densities (d) of $MnCo_2S_4$ nanoflowers in symmetric two-electrode configuration.

representing the outstanding rate capability of the electrode (Augustyn et al. 2014a). The CV loop displays a wide area, revealing the superior charge storage capability of the

$MnCo_2S_4$ nanoflower-based electrode, which may be due to the large specific surface area of the unique nanoflower-like morphology. A maximum Csp value of 850 F g^{-1} was reached for the $MnCo_2S_4$ nanoflower electrodes at 5mV s^{-1}. The GCD curves of $MnCo_2S_4$ nanoflower-based electrodes at different current densities (1- 5 A g^{-1}) are depicted in **Figure 4.8 (b)**. The GCD curves deliver an elevated discharge time, showing the superior electrochemical performance of the material, as evident from the CV results. The specific capacitance of the $MnCo_2S_4$ nanoflower-based electrode is obtained as 520, 597, 702, 853, and 1243 F g^{-1} corresponding to the current densities of 5, 4, 3, 2, and 1 A g^{-1} respectively. The highest specific capacitance value of the material can be ascribed to the unique 2D nanosheet-like morphology and smallest ion diffusion path (Hua et al. 2019). The gravimetric capacitance values of the device at current densities of 5, 4, 3, 2, and 1 A g^{-1} are 130, 149, 175, 213, and 310 F g^{-1} respectively. The variation of specific capacitance value as a function of scanrate, and current densities of $MnCo_2S_4$ nanoflower electrode is depicted in **Figure 4.8 (c)** and **(d)** respectively. The direct growth of $MnCo_2S_4$ nanoflower on NF substrate is favorable to boosting the electrode conductivity and electroactive surface area, which helps in increasing the overall device performance (Han et al. 2018). The EDLC and pseudocapacitive contribution of $MnCo_2S_4$ nanoflower-based electrode are calculated using Trasatti's analysis method (Mathis et al. 2019). The pseudocapacitive contribution is dominating for the $MnCo_2S_4$ nanoflower-based electrode materials as evident from CV and GCD profiles. Using Trasatti's method C vs ($V^{1/2}$) and ($1/C$) Vs ($V^{1/2}$) were plotted for $MnCo_2S_4$ nanoflower-based devices and the results are shown in **Figure 4.9 (a and b).** The percentage of capacitance contribution measured for the sample based on Trasatti's analysis is presented in **Figure 4.9 (c)**. **Equations 2.4 to 2.9** are used to calculate the contributions. The EDLC and pseudocapacitive contribution of $MnCo_2S_4$ nanoflower-based electrode are 40 % and 60 % respectively. At higher current densities, the capacitance value decreases, due to the shorter electrolyte ion transport rate (Gogotsi and Simon 2011).

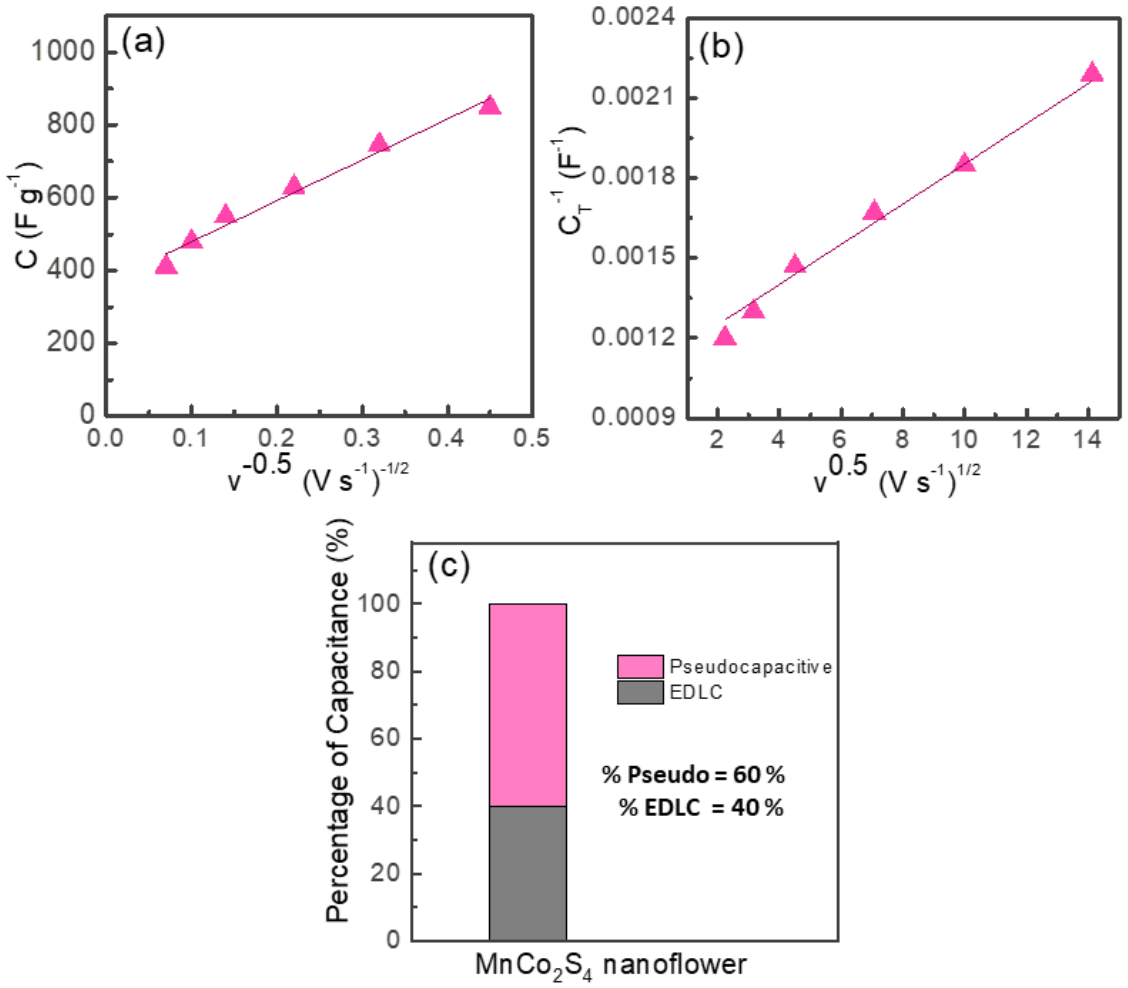

Figure 4.9. (a) linear fit of specific capacitance (Csp) vs. reciprocal of square root of scan rate ($v^{-0.5}$) (b) a linear fit of reciprocal of specific capacitance (Csp^{-1}) vs. square root of scan rate ($v^{0.5}$) (c) percentage of capacitance contribution calculated for $MnCo_2S_4$ nanoflower electrode from Trasatti's analysis.

The Ragone plot (specific energy vs specific power) for the $MnCo_2S_4$ nanoflower-based symmetric supercapacitor is given in **Figure 4.10 (a)**. At a specific power of 1 kW kg^{-1}, the $MnCo_2S_4$ nanoflower-based symmetric supercapacitor device delivers specific energy of 170 Wh kg^{-1}, and a gravimetric energy density of 42 Wh kg^{-1} at a gravimetric power density of 250 W kg^{-1}. Electrochemical impedance spectroscopy was conducted on $MnCo_2S_4$ nanoflower for the analysis of the charge transfer mechanism, and the results are presented in **Figure 4.10 (b)**. The Nyquist plot contains a semicircle at the high frequency part, and a vertical line at the low frequency part.

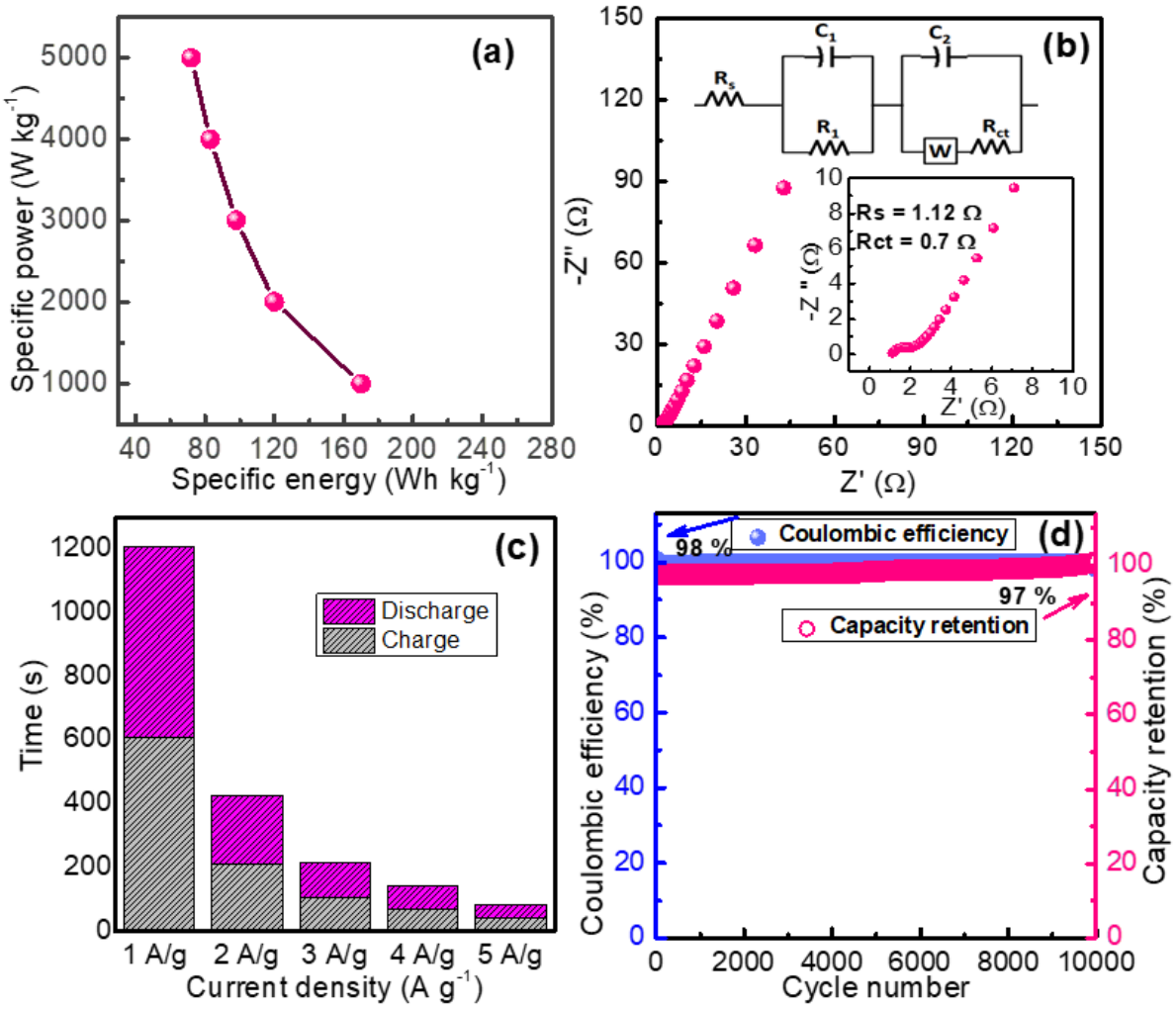

Figure 4.10. (a) Ragone plot, (b) Nyquist plots, (c) Charge-discharge time taken for $MnCo_2S_4$ nanoflower at varying current densities and (d) Cycling performance and Coulombic efficiency of $MnCo_2S_4$ nanoflower at 5 A g^{-1} of $MnCo_2S_4$ nanoflower based symmetric supercapacitor.

The X intercept of the spectra gives equivalent series resistance (R_s) of the electrode material and is obtained as 1.12 Ω only, which indicates increased conductivity of the electrode material. The radius of the semicircle part gives the charge transfer resistance (R_{ct}) at the electrode/electrolyte interface, which is very low for the synthesized electrode material, indicating the $MnCo_2S_4$ nanoflower connected to the NF substrate can reduce the path of ion diffusion and decreases the R_{ct} value (Hua et al. 2019). At the low-frequency part, the 45^o slope line (Warburg line) is observed associated with the real axis, which arises due to the diffusion resistance of ions in electrolyte (Stoller and Ruoff 2010). The slope line at 45^o reveals that the charge transfer mechanism in the electrode is not

purely based on capacitive nature but is under a diffusion-controlled process (Nilson et al. 2011). The charge-discharge time taken for the material at varying current densities was presented at a constant voltage window (0.0 to 1.0 V) in **Figure 4.10 (c)**. The coulombic efficiency and cyclic stability test of $MnCo_2S_4$ nanoflower-based electrodes were conducted at 5 A g^{-1}, and presented in **Figure 4.10 (d)**. The material exhibits 97 % capacitance retention at the end of 10000 cycles at 5 A g^{-1}. The coulombic efficiency of the $MnCo_2S_4$ nanoflower can be measured from the charge-discharge ratio of the capacitance value. The material delivers a coulombic efficiency of 98 % for 10000 cycles, which indicates excellent charge-discharge reversibility of the $MnCo_2S_4$ nanoflower. The electrode performance of $MnCo_2S_4$ nanoflower is extremely high compared with the available reports on $MnCo_2S_4$. Zhang *et al*. reported the synthesis of $MnCo_2S_4$ nanoparticles via the hydrothermal method and the $MnCo_2S_4$ NP-based electrode exhibits

Electrode material	**Voltage window**	**Electrolyte**	**Specific capacitance (F g^{-1})**	**Cyclic stability**	**Reference**
$MnCo_2S_4$ Nanostructures /NF	0 to 0.5 V	2 M KOH	779 F g^{-1} @ 1 A g^{-1} (Half cell)	96.5% (3000 cycles)	(Mola et al. 2021)
$MnCo_2S_4$ Spherical nanoparticles	0 to 0.5 V	2 M KOH	707 F g^{-1} @ 2 A g^{-1} (Half cell)	95.15% (10000 cycles)	(Dakshana et al. 2020)
$MnCo_2S_4$ core-shell nanostructures	-0.1 to 0.5 V	3 M KOH	2067 F g^{-1} @ 1A g^{-1} (Half cell)	80.2% (6000 cycles)	(Liu and Jun 2017)
$MnCo_2S_4$ nanoparticles	0 to 0.6 V	3 M KOH	1150 F g^{-1} @ 1A g^{-1} (Half cell)	88.2% (5000 cycles)	(Zhang et al. 2019)
$MnCo_2S_4$ nanoflower	**0 to 1 V**	**2 M KOH**	**1980 F g^{-1} @ 1 A g^{-1} (Half cell) 1243 F g^{-1} @ 1 A g^{-1} (Full cell)**	**97% (10000 cycles)**	**Present work**

Table 4.1. Comparative study of electrochemical performance of $MnCo_2S_4$ nanoflower electrodes with literature data

a specific capacitance value of 1150 F g^{-1} at 1 A g^{-1} and cyclic stability retention of 88.2 % after 5000 cycles in the three-electrode system (Zhang et al. 2019). Mola *et al*. reported $MnCo_2S_4$ nanoflower using a hydrothermal approach and the electrode deliver 779 F g^{-1} at a current density of 1 A g^{-1} along with a cycle life of 96.5 % after 3000 cycles in the three-electrode system (Mola et al. 2021). The unique nanoflower structure of the electrode material delivers large electroactive sites for the electrochemical process, which is useful for excellent cycle life. The direct growth of $MnCo_2S_4$ nanoflowers over the NF substrate will improve the contact between the active electrode materials and the current collector, which will decrease the contact resistance, and effectively increase the electrode conductivity (Lama Tamang et al. 2022). In addition, the 3D open porous back born of nickel foam delivers outstanding mechanical strength and easy access to electrolyte ions for charge transfer. A comparison of performance of $MnCo_2S_4$ nanoflower as supercapacitor electrode with literature data is presented in **Table 4.1**. The superior performance of the $MnCo_2S_4$ nanoflower-based electrode can be attributed to the individual nanostructure, excellent diffusion rate, good conductivity, and outstanding cyclic stability.

4.5 Conclusion

In summary, an efficient binder-free $MnCo_2S_4$ nanoflower supercapacitor electrode was fabricated using a facile hydrothermal method. The unique nanostructure and chemical properties of the material helped to elevate the capacitive property of the electrode. In a symmetric two-electrode configuration, the as-grown electrode delivered an excellent specific capacitance of 1243 F g-1 at 1 A g-1, outstanding cyclic stability of 97% and greater coulombic efficiency of 98 % at 5 A g-1 after 10000 charge-discharge cycles. The fabrication of the electrode used in the present work allows each $MnCo_2S_4$ nanoflower to have its own electrical contact with the nickel foam substrate and elevate the electrochemical reaction. These outstanding electrochemical results indicates the importance of the $MnCo_2S_4$ nanoflower supercapacitor electrode for electrochemical energy storage applications.

Chapter 5

Direct growth of $MnCoSe_2$ nanoneedles on 3D nickel foam for supercapacitor application

5.1 Outline of the chapter

The present chapter deals with the synthesis of $MnCoSe_2$ nanoneedles on 3D nickel foam substrate for electrochemical energy storage. Symmetric supercapacitors are fabricated using $MnCoSe_2$ nanoneedle electrodes. The electrochemical performance analysis reveals that $MnCoSe_2$ nanoneedle-based supercapacitor electrode exhibits a specific capacitance of 384 F g^{-1} at 1 A g^{-1}. The $MnCoSe_2$ nanoneedle-based supercapacitor device has a specific energy of 53 Wh kg^{-1} at a specific power of 1 kW kg^{-1} and a superior cyclic stability of 95% retention after 10000 charge-discharge cycles at 5 A g^{-1}. The increased electrochemical performance can be ascribed to the three-dimensional nanowire-like surface morphology with a large electroactive site for enhanced redox reaction. Furthermore, high conductivity due to the presence of selenium provides rapid electron transfer and thereby improves the electrochemical properties of supercapacitors.

5.2 Introduction

Selenium (Se), a group 16 element, (chalcogen family) is considered a favorable candidate for many applications such as; solar cells, electrocatalysis, batteries, fuel cells, and metallic alloys due to its greater electrical conductivity and superior chemical properties (Chen et al. 2022; Khalafallah et al. 2022). Resides in the same group, Se shares a similar chemical property with the elements oxygen (O) and sulfur (S). But the metallic property of Se is superior to that of S and O and therefore exhibits an increased electronic conductivity, which is extremely useful for electrochemical applications. Accordingly, Se-based material has received great interest in supercapacitor applications because of its innumerable qualities, such as superior energy density, high redox potential, and large theoretical capacitance (Barik et al. 2021; Liu et al. 2020a). Supercapacitors exhibit outstanding properties among various electrochemical energy resources due to their capability of fast charge/discharge, enhanced power density, and long cyclic stability (Mathis et al. 2019; Xiao et al. 2020a). According to the charge storage mechanism, supercapacitors are categorized into electric double-layer capacitors (EDLC) where the adsorption/desorption process takes place physically and pseudocapacitors where redox reactions take place on the active material surface (Liu et al. 2022; Mathis et al. 2019). Carbon-type materials (eg. graphene, activated carbon, CNTs, etc.) are widely utilized as active electrodes in EDLCs with low specific capacitance and energy density (Bai et al. 2020). Pseudocapacitors generally use transition metal oxides or hydroxides (eg. Co_3O_4, $Mn(OH)_2$, $Co(OH)_2$, etc.) and conducting polymers (eg. PANI, PPy, etc.) as electrode materials to increase the capacitance bearing low cycle life and poor conductivity (Cui and Meng 2020). Hence, it is necessary to establish a unique electrode material with exceptional electrical conductivity and improved structural properties.

Recently, selenium-based transition metal dichalcogenides (TMDs) (MSe_2, where, M = Co, Mn, Ni, Mo or W) have attracted significant scientific interest as electrode materials for super capacitors because of their increased redox performance, larger conductivity, great availability, and electrochemical activity (Cherusseri et al. 2019; Joseph et al. 2020; Pathak et al. 2020). Reports are available on the supercapacitor performance of different transition metal selenides such as,- $NiSe_2$ (Vidhya et al. 2021b), $CoSe_2$ (Chen et al. 2018),

$MnSe_2$ (Sajjad et al. 2021), $MoSe_2$ (Rajput and Arora 2021), WSe_2 (Iamprasertkun et al. 2021), etc. Rahul *et al*. report the synthesis of few-layer $MoSe_2$ nanosheets for supercapacitor application by liquid exfoliation method and at 0.1 A g^{-1} the manufactured electrode delivers 15 F g^{-1} of specific capacitance in the three-electrode setup. (Rajput and Arora 2021). Disha *et al*. report that WSe_2 micro/nanorods for supercapacitor application and the fabricated transition metal selenide deliver better performance in three-electrode configuration (Chakravarty and Late 2015). In particular, $CoSe_2$ achieved great attention because of its large availability, greater capacitance, environment-friendly nature, fast charge transfer rate at the electrode-electrolyte interface, and enhanced electrochemical properties. Mansi *et al*. studied a comparative electrochemical energy storage performance of $CoSe_2$, $NiSe_2$, and $MnSe_2$. The result shows that $CoSe_2$ retains a superior specific capacitance of 148 F g^{-1}, along with a better cycle life with capacitance retention of 98.46%, over 3000 cycles compared to $NiSe_2$ (139 F g^{-1} along with 59.44% capacitance retention) and $MnSe_2$ (50 F g^{-1} along with 86.70% capacitance retention) in two-electrode configuration (Pathak et al. 2020). Very recently, the binary transition metal selenides are greatly employed as supercapacitor electrodes due to their high specific capacitance and increased rate capability (Jiang et al. 2022; Mohamed and Allam 2022). Therefore, the incorporation of other transition metals with $CoSe_2$ provides multiple oxidation states for redox reaction (Mohamed and Allam 2022). Recent reports indicate the enhanced electrochemical performance of Mn and Co-based binary transition metal selenides (Miao et al. 2019). The presence of the Mn element, with multiple oxidation states, large abundance, non-toxicity, environment friendly, and great stability enhance the supercapacitor property of the electrode(Sakib et al. 2021). As a result, binary transition metal selenide, such as $MnCoSe_2$, is expected to perform as an improved electrode material for supercapacitor applications. In a $MnCoSe_2$ system, manganese (Mn) delivers noticeable carrier mobility, cobalt (Co) increases the capacitance value due to its higher oxidation potential, and selenium (Se) incorporation results in fast electron transfer and good rate capability (Chebil et al. 2020; Zhang et al. 2020). Reports on the electrochemical energy storage capability of $MnCoSe_2$-based electrodes are available. Vidhya *et al*. report the fabrication of $MnSe_2$-$CoSe_2$ metal composite and in a three-electrode design, the material has a maximum specific capacitance of 373 F g^{-1} and a cyclic stability of 95.86% over 5000 GCD cycles. (Vidhya et al. 2021a). Miao *et al*. fabricated $MnCoSe_2$ nanoneedle on nickel foam substrate by the simple hydrothermal

method as electrode material for supercapacitors and at 1 A g^{-1} the composite retains 1656 F g^{-1} of specific capacitance along with enhanced cycle life of 91.8 % over 8000 cycles in a half cell configuration (Miao et al. 2019). But it is widely accepted that the three-electrode strategy invariably results in a higher capacitance number than the two-electrode approach. (Augustyn et al. 2014a; Gogotsi and Simon 2011). The electrochemical performance of $MnCoSe_2$ electrodes in symmetric two-electrode arrangement will be important to analyse because it offers the true device performance and very limited reports are only available in such configuration.

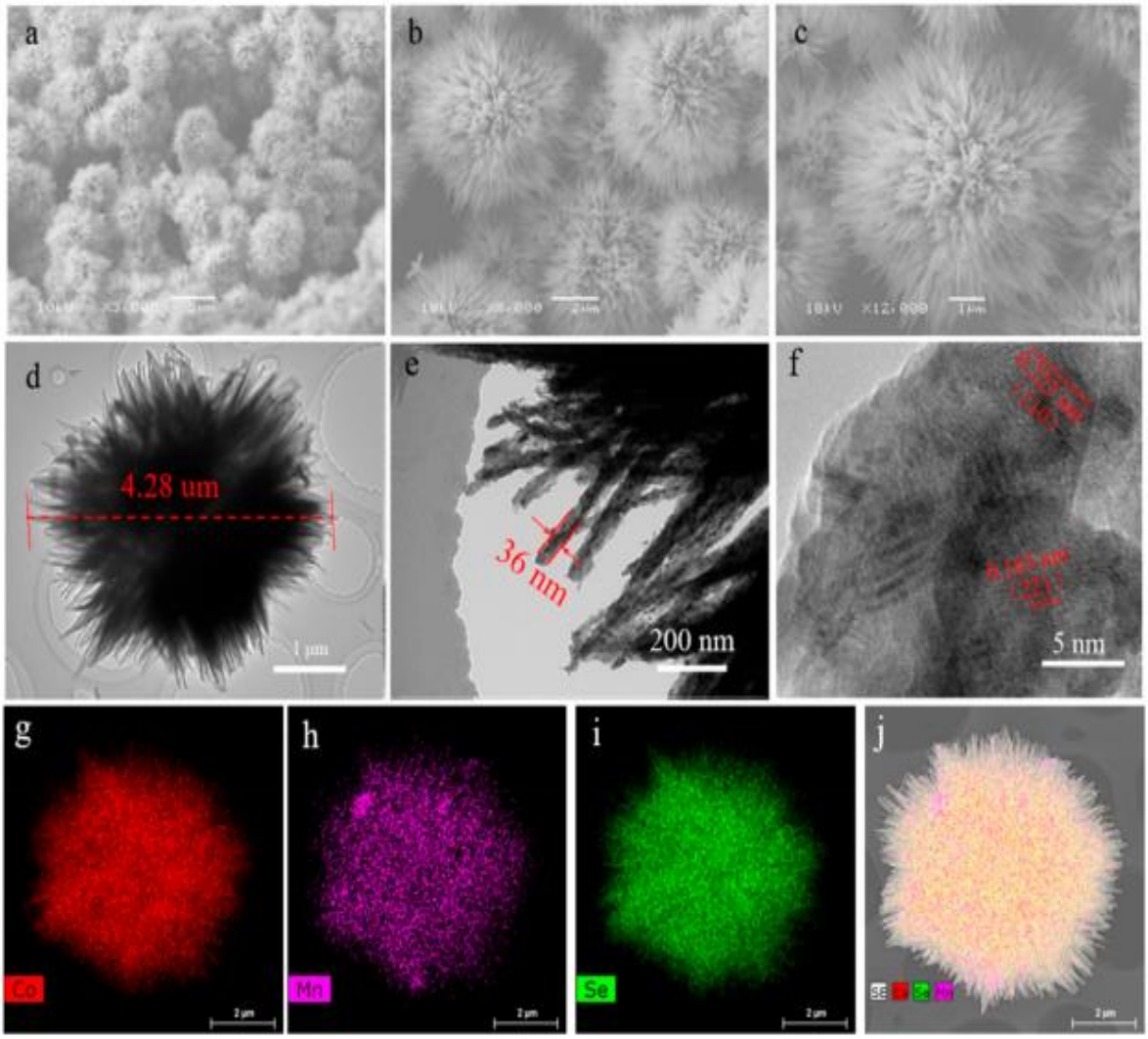

Figure 5.1. SEM (a-c), TEM (d-f), and elemental mapping images (g-j) of MnCo-selenide (Adapted from the reference (Miao et al. 2019))

In the present study, $MnCoSe_2$ nanoneedles are grown directly on a nickel foam via a simple hydrothermal approach. The performance of the material was examined in a symmetric two-electrode setup, and the results are described.

5.3 Experimental Section

5.3.1 Synthesis of $MnCoSe_2$ nanoneedle on nickel foam

A simple and inexpensive hydrothermal process was used to produce $MnCoSe_2$ nanoneedles. cobalt nitrate hexahydrate ($Co(NO_3)_2.6H_2O$) (0.04 M), Manganese nitrate hexahydrate ($Mn(NO_3)_2.6H_2O$) (0.02 M), and urea $CO(NH_2)_2$ (0.2 M) were placed in an autoclave including 30 mL of a 1:1 combination of deionized water and ethanol. Cleaned nickel foam of area 1x1 cm^2 is added to the above solution mixture. To eliminate contaminants, Ni foam is rinsed with 2 M HCl, acetone, and deionized water before deposition. Before cooling to ambient temperature, the autoclave was tightly sealed and preheated to 100^o C for 6 h. After adding 0.2 g of Se powder to the resulting product, it was transported to an autoclave including 20 ml of deionized H_2O. The autoclave was closed and again kept at 180 ^oC for 12 h. The resultant material was taken out, rinsed multiple times using deionized H_2O, and dried for 12 h at 60 ^oC. A microbalance is used to calculate the loaded mass of electroactive material by determining the change in mass of nickel foam prior to and afterwards deposit. The mass loading of the $MnCoSe_2$ nanoneedle over nickel foam was around 1mg/electrode. The synthesis of $MnCoSe_2$ nanoneedle over nickel foam was depicted in **Figure 5.2.**

Experimental details of the general characterization of the as-prepared electrode materials and the fabrication of Symmetric supercapacitor and electrochemical performance analysis are given in **chapter 2 section 2.3.**

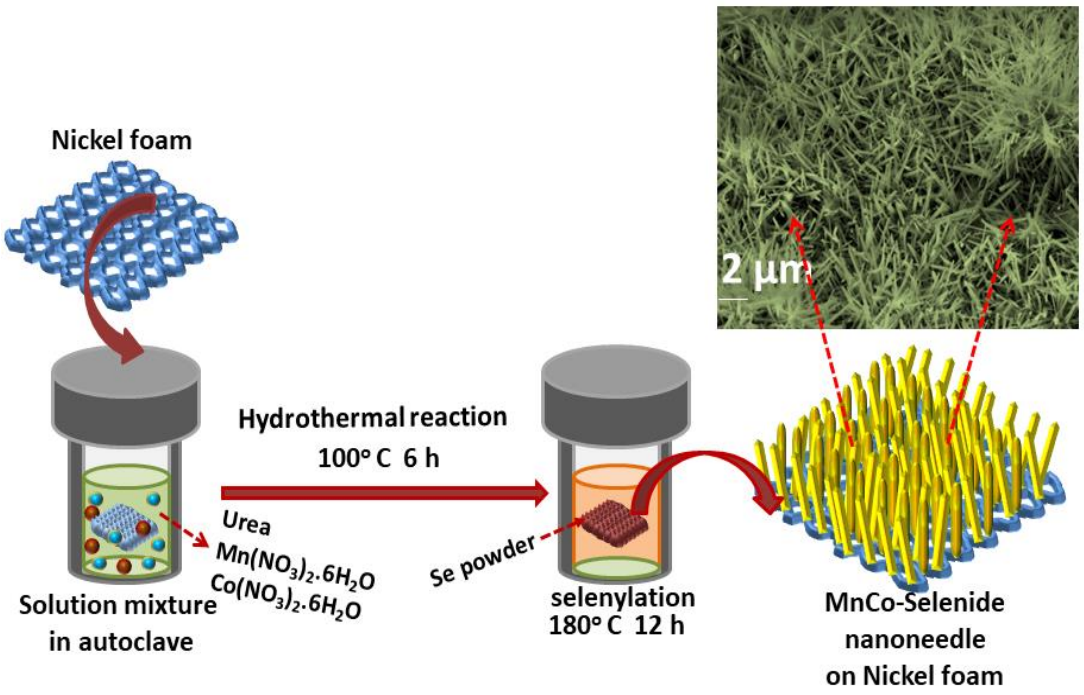

Figure 5.2. The schematic of the synthesis of $MnCoSe_2$ nanoneedle.

5.4. Results and Discussion

5.4.1. Structural and morphological characterization

X-ray diffraction (XRD) patterns were used to examine the crystal structure of the synthesized material. The recorded XRD pattern of the $MnCoSe_2$ nanoneedle is shown in **Figure 5.3**. The diffraction peaks observed at 2θ values of 24.42°, 29.06°, 31.42°, 34.47°, 35.47°, 37.46°, 40.52°, 43.35°, 47.21°, 48.47°, 49.88°, 50.73°, 53.89°, 55.29°, 56.43°, 59.54°, 60.42°, 61.46°, 62.76°, 63.63°, 64.45°, 65.24°, 66.16°, and 67.21° can be attributed to the reflections from (110), (011), (101), (111), (120), (220), (210), (121), (211), (220), (002), (130), (031), (221), (131), (310), (022), (230), (301), (040), (202), (311), (320), and (231) planes of orthorhombic $CoSe_2$ having space group Pnnm(58) (JCPDS, card no. 053-0449, $\alpha=\beta=\gamma=90^o$), respectively. The lattice parameter values are obtained as, a = 4.94 Å, b = 5.98 Å, and c = 3.82 Å from the XRD data. It is quite difficult to find out the presence of Mn element through the XRD analysis, because of the small amount of replacement of Mn^{2+} with Co^{2+} ion (Miao et al. 2019). But the orthorhombic structure of $CoSe_2$ is not altered by the substitution (Miao et al. 2019). According to Scherrer's equation ($D=0.9\lambda/(\beta\cos\theta)$), the average crystallite size of $MnCoSe_2$ nanoneedle is 14 nm. There were no further impurity peaks found, revealing the high product purity of the prepared $MnCoSe_2$ nanoneedles.

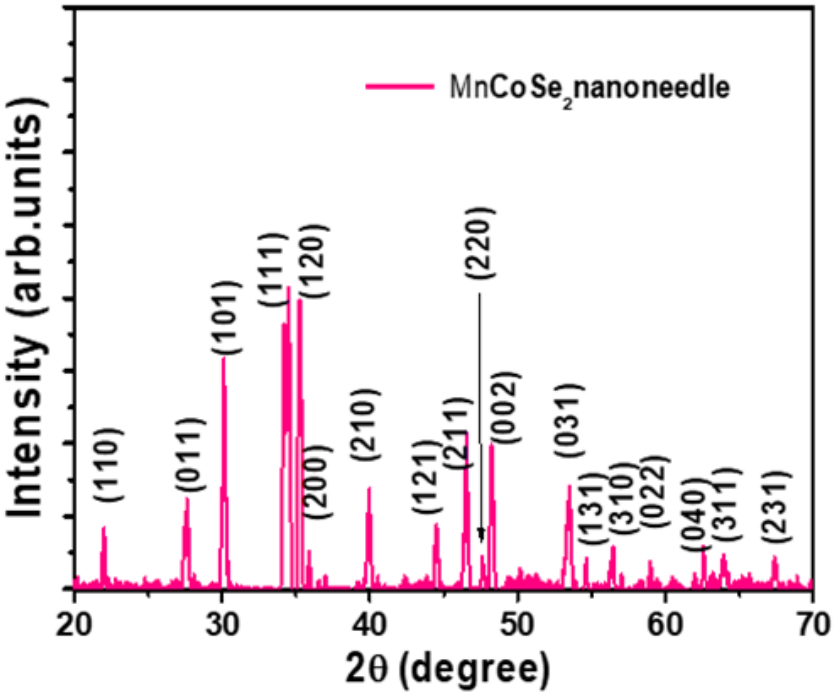

Figure 5.3. Powder XRD spectra of $MnCoSe_2$ nanoneedle

Nitrogen adsorption/desorption isotherms were used to determine the specific surface area and porosity of $MnCoSe_2$ nanoneedle. **Figure 5.4 (a) and (b)** show the BET results. The $MnCoSe_2$ nanoneedle shows a type IV isotherm (**Figure 5.4 (a)**), specifying the mesoporous structures of the sample. The $MnCoSe_2$ nanoneedle-based electrodes deliver a BET surface area value of 50 $m^2 g^{-1}$. **Figure 5.4 (b)** depicts the pore size distribution of the material as determined by the BJH (Barret-Joyner-Halenda) method. The pore volume of $MnCoSe_2$ nanoneedle is obtained as 0.25 $cm^3 g^{-1}$. The greater specific surface area and mesoporous nature can improve the redox active sites thereby enhance the electrode performance of $MnCoSe_2$ nanoneedle.

XPS analysis were performed to analyse the oxidation states of the synthesized $MnCoSe_2$ nanoneedle, and the findings are shown in Figure 4 (a-d). The software AAnalyzer was used to deconvolve all high quality XPS spectra. Shirley backdrops were utilised, and the

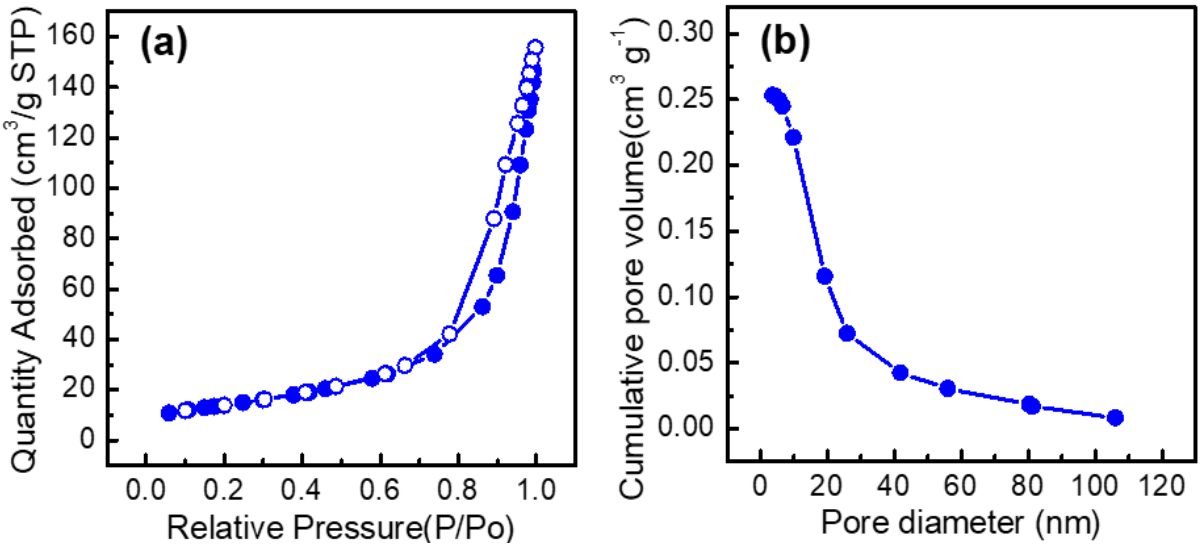

Figure 5.4. (a) Nitrogen-adsorption and desorption isotherms, and (b) pore-size distribution of the $MnCoSe_2$ nanoneedle

individual peaks were mainly represented by a GL-20 (Gaussian with 20% Lorentian) function. The survey spectrum of the sample is presented in **Figure 5.5 (a).** The high-resolution Mn 2p spectra (**Figure 5.5 (b)**) has two major peaks corresponding to the $2p_{3/2}$ and $2p_{1/2}$ regions. The Mn $2p_{3/2}$ spectra may be subdivided into three peaks: one at 640.3 eV associated to Mn^{2+}, another at 641.6 eV related to Mn^{3+}, and a satellite peak at 644.6 eV referring to the Mn^{2+} satellite. The mixed charge state of Mn is beneficial for the charge transfer mechanisms, thereby directly contributing to enhanced performance of the fabricated electrodes for supercapacitor application. The ratio of the area that lies beneath the Mn^{3+} and Mn^{2+} peaks is calculated to be 2.2, indicating that Mn^{3+} is the predominant charge state in the sample. Similarly, the Mn $2p_{1/2}$ spectra could also be devided into three peaks: one at 651.8 eV belonging to Mn^{2+}, one at 653.0 eV referring to Mn^{3+}, and one at 655.9 eV representing the Mn^{2+} satellite.

The Co 2p spectra (**Figure 5.5 (c)**) has two major regions corresponding to the Co $2p_{3/2}$ and the Co $2p_{1/2}$ regions, each having a satellite component. Peaks at 778.5 and 793.8 eV indicate the existence of Co^{3+}, while peaks at 779.7 and 795.3 eV indicate the presence of Co^{2+}. Two satellite peaks of the Co^{2+} ions are located at 784.6 and 801.0 eV. The oxidation state that leads to the satellite component is determined by the energy gap among the main and satellite peaks. If the energy gap is around 6.0 eV, the valence state is probably to be +2, and +3 if the difference is around 9 to 10 eV. Based on our observations of the energy gap among the main and satellite peaks, it appears that the

Co^{2+} ion is the primary contributor to the satellite peaks, differing by only 0.2 eV from the main peak. Our analysis of the discrete peak areas suggests that the sample has a Co^{2+} to Co^{3+} ratio of 1.5, indicating that Co^{2+} ions are the most prevalent charge state in the sample. The detailed Se 3d spectra, shown in **Figure 5.5 (d)**, can be divided into three peaks. The first peak, located at 54.5 eV, is identified as Se $3d_{5/2}$. The second peak,

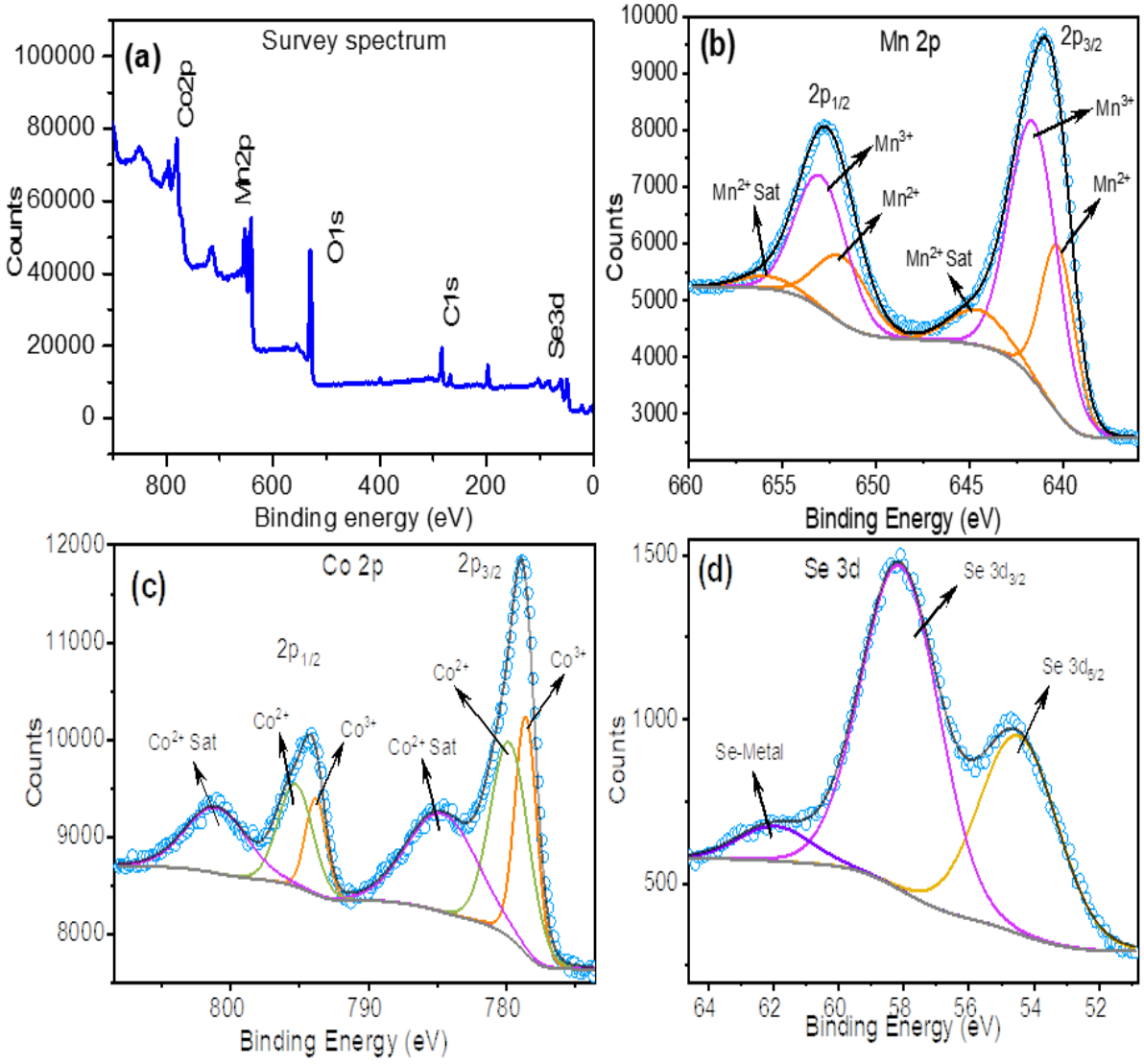

Figure 5.5. XPS spectra of $MnCoSe_2$ nanoneedle: (a) the survey spectrum, (b) Mn2p spectra, (c) Co2p spectra, and (d) Se3d spectra

at 58.1 eV, is indexed to Se $3d_{3/2}$, representing the existence of S2. The final peak, observed at 61.9 eV, is due to Se- metal bonds (such as Se-surface oxygen and Se-adventitious carbon) in the compound (Vidhya et al. 2021a; Xuan et al. 2021).

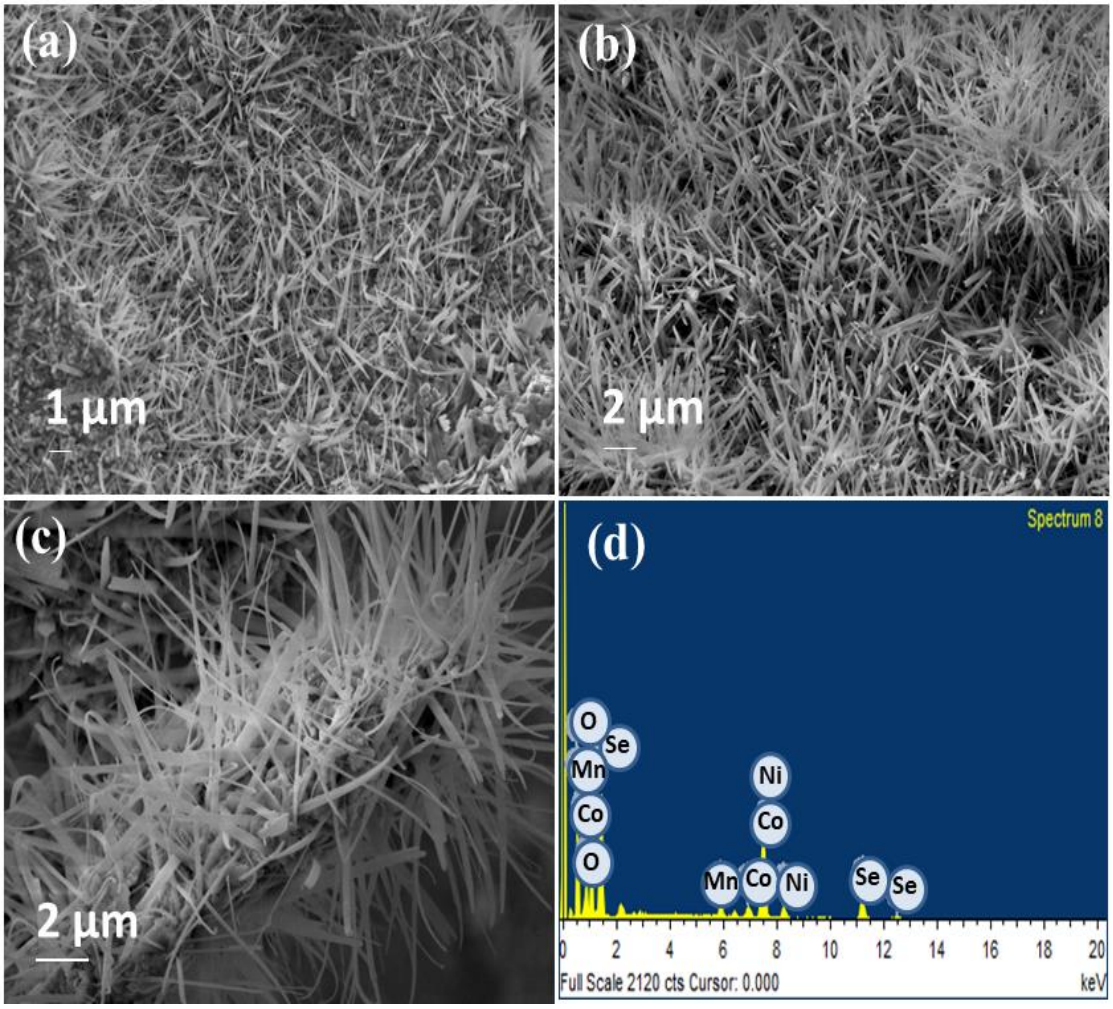

Figure 5.6. FESEM images (a), (b), and (c) of $MnCoSe_2$ nanoneedle and (d) EDX spectra of $MnCoSe_2$ nanoneedle-based electrode material.

FESEM and EDS techniques were conducted to analyse the detailed surface morphology and elemental composition of the $MnCoSe_2$ nanoneedles. The SEM images at different magnifications are represented in **Figure 5.6**. SEM images of the $MnCoSe_2$ nanoneedles over the nickel foam substrate (**Figure 5.6 (a and b)**) exhibits a nanoneedle-like surface profile. FESEM image (**Figure 5.6 (c)**) gives an average diameter of 56 nm. The nanoneedle-like surface morphology delivers a superior electrochemical property that enhances the active sites of the electrode material and increases the capacitive performance (Chakravarty and Late 2015). **Figure 5.6 (d)** depicts the EDX spectrum.

The spectra shows peaks from Mn, Co, O, Ni, and Se. The signals of Ni are obtained because of the usage of nickel foam in the preparation method. **Figure 5.7 (a-f)** shows EDX elemental mapping images for the $MnCoSe_2$ nanoneedle. The elemental mapping images of $MnCoSe_2$ nanoneedle (**Figure 5.7 (a-f)**) further confirm the existence of cobalt, manganese, oxygen, and selenium components in the sample. Aadditionally, the elements are uniformly distributed over the conductive NF substrate, which is very useful for the superior electrochemical process.

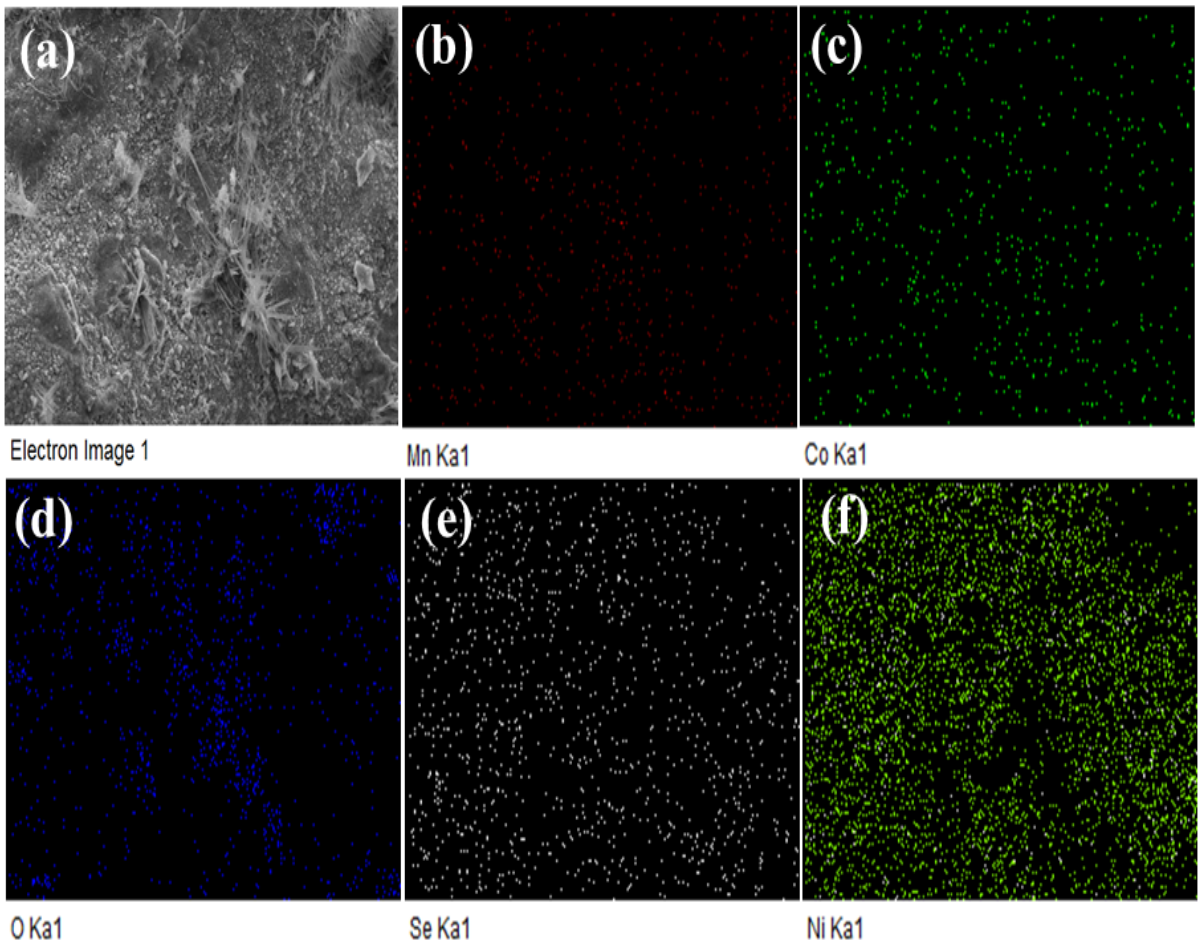

Figure 5.7 (a-f). EDX elemental mapping images of $MnCoSe_2$ nanoneedle

The microstructure of the $MnCoSe_2$ nanoneedle was further explored via TEM (**Figure 5.8 (a-d)**). The TEM image of the sample (**Figure 5.8 (a)**) shows a nanoneedle-like structure. These TEM results matches well with the morphology of the sample from the SEM images. In **Figure 5.8 (b)**, one can see that each nanoneedle is made up of many tiny nanoparticles having an average particle size of 15 nm. The unique microstructure

will increase the active surface area for electrochemical reactions and thus enhance the capacitive property (Selvaraj et al. 2020). The HRTEM image (**Figure 5.8 (c)**) shows the fringe spacing of 2.592, 2.491, and 1.901 Å are well identified as the (111), (120), and (211) crystal planes of $CoSe_2$, which match very well with the XRD results. The SAED pattern of $MnCoSe_2$ nanoneedle is shown in **Figure 5.8 (d)**. The SAED pattern rings correlate to the planes of the $CoSe_2$ crystal structure and are in accordance with the XRD results.

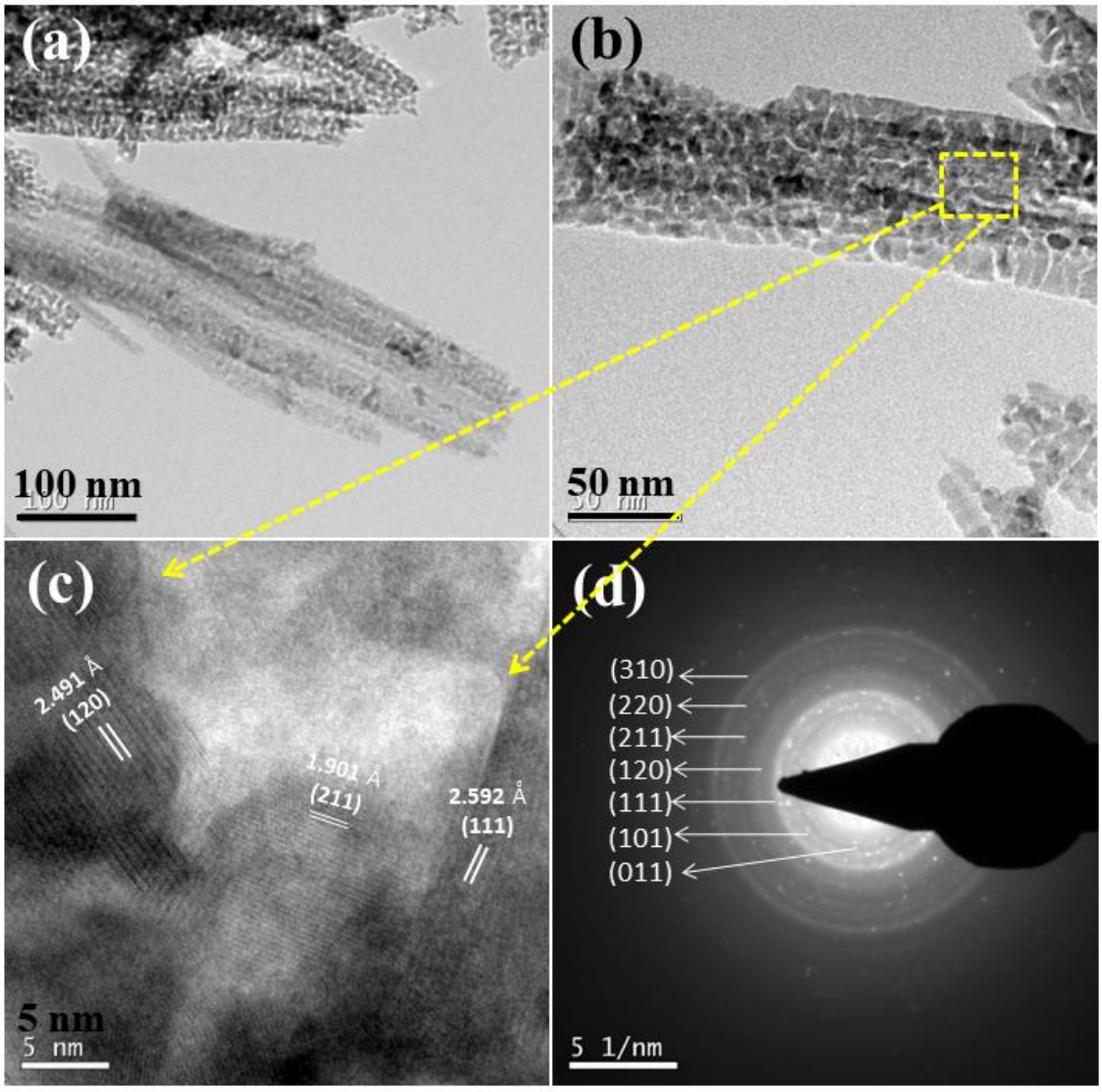

Figure 5.8. (a) TEM image (b) and (c) HRTEM images and (d) SAED pattern of $MnCoSe_2$ nanoneedle.

5.4.2. Electrochemical characterization

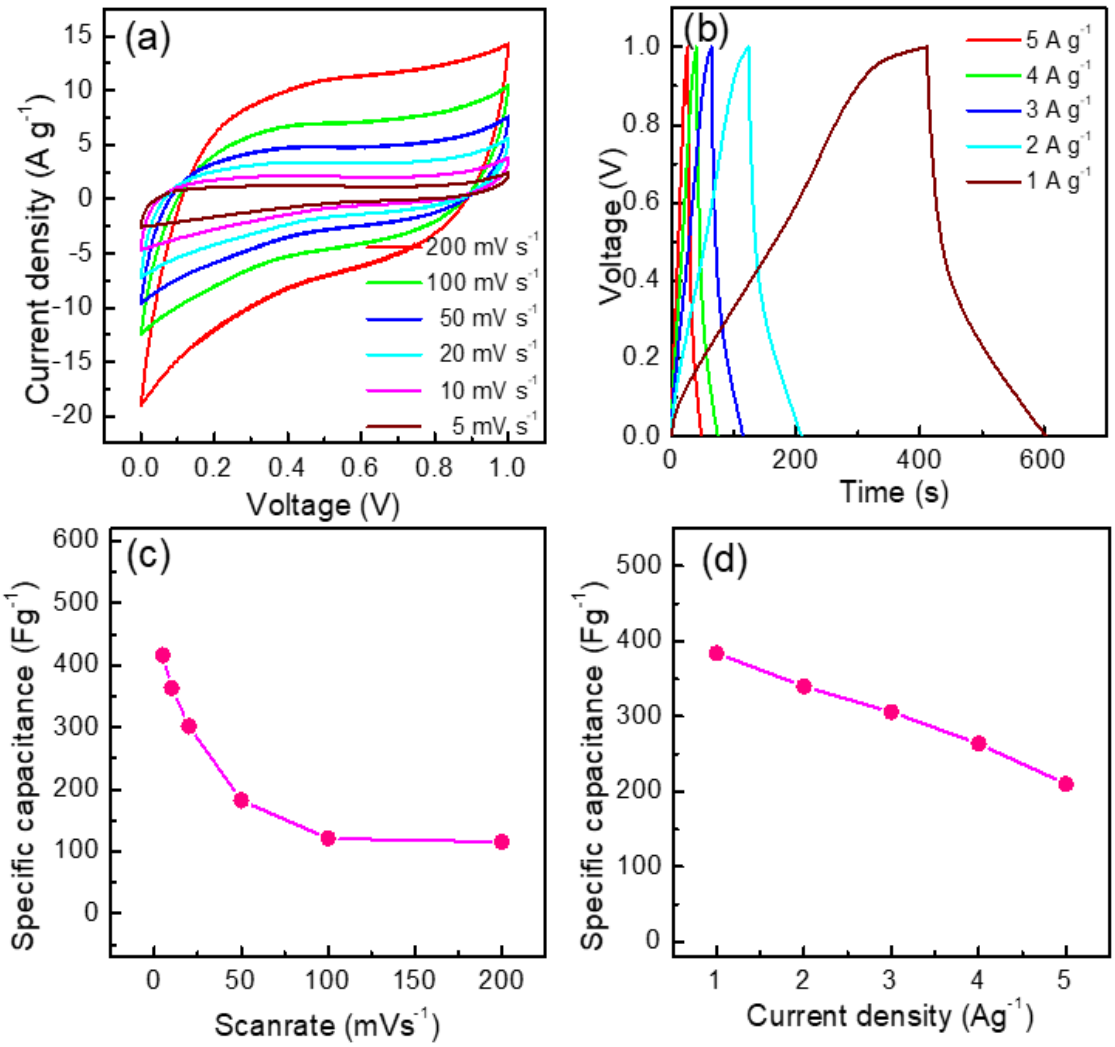

Figure 5.9. (a) Cyclic voltammograms of $MnCoSe_2$ nanoneedle at different scan rates, (b) Galvanostatic charge-discharge curves of $MnCoSe_2$ nanoneedle at different current densities, (c) Variation of specific capacitance as a function of scan rate and, (d) current densities of $MnCoSe_2$ nanoneedle

The supercapacitor tests of $MnCoSe_2$ nanoneedle were conducted in two electrode arrangement with a 2 M KOH. The CV curves of $MnCoSe_2$ nanoneedle recorded in a potential range of 0 to 1 V at different scan rates are shown in **Figure 5.9 (a)**. The CV loops show that the faradaic redox processes are primarily responsible for the charge storage process. With increasing scan rate, the area of the CV curve also grows, revealing

a superior reverse faradaic reaction. The redox reactions between Se^{2-}, $Co^{2+}/Co^{3+}/Co^{4+}$, and Mn^{2+}/Mn^{3+} are described by the equations below (Xuan et al. 2021).

$$MnSe + OH^- \leftrightarrow MnSeOH + e^- \quad (5.1)$$

$$CoSe + OH^- \leftrightarrow CoSeOH + e^- \quad (5.2)$$

$$CoSeOH + OH^- \leftrightarrow CoSeO + H_2O + e^- \quad (5.3)$$

The large area of the CV loops suggest that the $MnCoSe_2$ nanoneedle has a high capacitance value. At a scan rate of 5mV s^{-1}, the $MnCoSe_2$ nanoneedle-based electrodes give an ultimate C_{sp} of 416 F g^{-1}.

The GCD measurements were conducted at different current densities within the potential ranges of 0 to 1 V at current ranges from 1 to 5 A g^{-1} and are presented in **Figure 5.9 (b).** The GCD profiles of $MnCoSe_2$ nanoneedle (**Figure 5.9 (b)**) deviate from the perfect triangular shape EDLC behavior, which shows the pseudocapacitive property of the nanocomposite. The duration for charging/discharging decreases with the increase in current density values from 1 to 5 A g^{-1}. The specific capacitance value of $MnCoSe_2$ nanoneedle electrode is calculated using the GCD loops as 210, 264, 306, 340, and 384 F g^{-1} respectively according to the current density values 5, 4, 3, 2, and 1 A g^{-1}. The outstanding value of specific capacitance of $MnCoSe_2$ nanoneedle could be assigned to the distinctive 1D nanoneedle-like structure grown directly over the NF substrate (Gogotsi and Simon 2011; Xu et al. 2018). The different C_{sp} values of $MnCoSe_2$ nanoneedle electrodes at different scan rate and current densities are respectively shown in **Figure 5.9 (c) and (d)**. It is observed that, $MnCoSe_2$ nanoneedle maintains a specific capacitance of 210 F g^{-1} even at a higher current density of 5 A g^{-1}, suggesting its superior rate capability.

Trasatti's analysis approach is used to determine the contribution of EDLC and the pseudocapacitive nature of $MnCoSe_2$ nanoneedle-based electrodes. From Trasatti's analysis *C* vs ($V^{1/2}$) and (*1/C*) Vs ($V^{1/2}$) were arranged for $MnCoSe_2$ nanoneedle electrode and the findings are represented in **Figure 5.10 (a) and (b).** The capacitance in percentage were calculated using Trasatti's method and is depicted in **Figure 5.10 (c).** The $MnCoSe_2$ nanoneedle-based device exhibits 13 % EDLC and 87 % pseudocapacitive type of charge storage as evidenced by the CV and GCD loops.

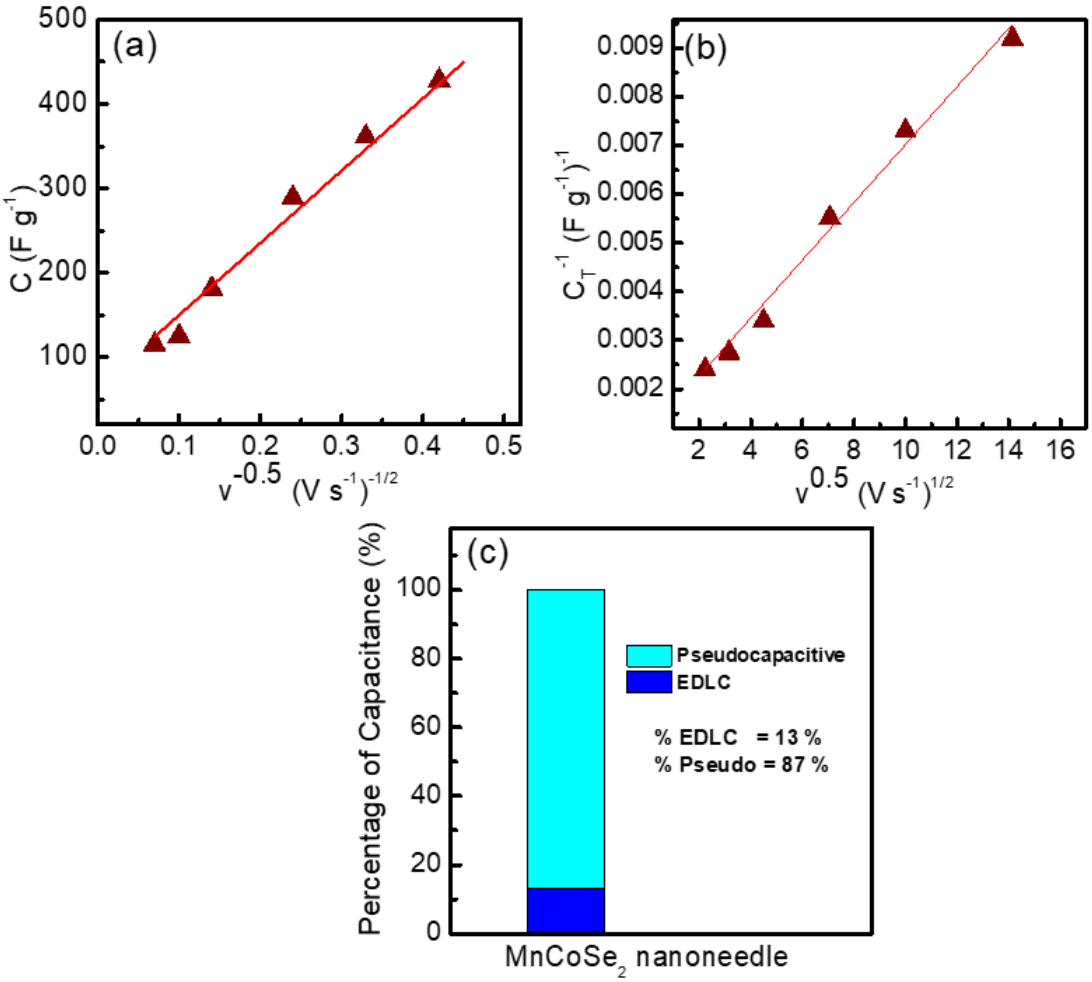

Figure 5.10. (a) linear fit of specific capacitance (Csp) vs. reciprocal of the square root of scan rate ($v^{-0.5}$) (b) a linear fit of reciprocal of specific capacitance (Csp^{-1}) vs. square root of scan rate ($v^{0.5}$) (c) percentage of capacitance contribution calculated for $MnCoSe_2$ nanoneedle based on Trasatti's analysis.

Figure 5.11 (a) depicts the specific energy versus specific power value (Ragone plot) associated with the $MnCoSe_2$ nanoneedle-based symmetric supercapacitor. The $MnCoSe_2$ nanoneedle-based supercapacitor device has a specific energy of 53 Wh kg^{-1} at a specific power of 1 kW kg^{-1}. Nyquist plot of $MnCoSe_2$ nanoneedle was taken and the results are shown in **Figure 5.11 (b)**. The EIS spectra mainly contain a semicircle at the higher frequency region and a vertical line (Warburg line) at the lower frequency region (Conway et al. 1997; Dakshana et al. 2020). The charge-transfer resistance (R*ct*) between active electrode material and electrolyte is obtained from the diameter of the semicircle region. The $MnCoSe_2$ nanoneedle delivers lower R*ct*, indicating that the material grown directly on nickel foam substrate can lower the ion diffusion path and reduce the R*ct* rate

(Jiang et al. 2014). Intercept in the higher-frequency region of the Nyquist plot gives the solution resistance (R*s*). The solution resistance (R*s*) value of the $MnCoSe_2$ nanoneedle is only 1.86 Ω, which demonstrates the higher conductivity of the synthesized material. Finally, the shorter Warburg line is observed at the lower frequency, which results from the rapid diffusion of electrolyte ions (Xiao et al. 2020b). **Figure 5.11 (c)** represents the cyclic stability performance of $MnCoSe_2$ nanoneedle electrodes at 5 A g^{-1} current density. The $MnCoSe_2$ nanoneedle delivers a cyclic stability of 95 % after 10000 cycles at 5 A g^{-1} showing its extremely high cycle life. The unique nanoneedle assembly over the 3D NF substrate is responsible for the exceptional electrochemical performance of $MnCoSe_2$ nanoneedle-based electrode.

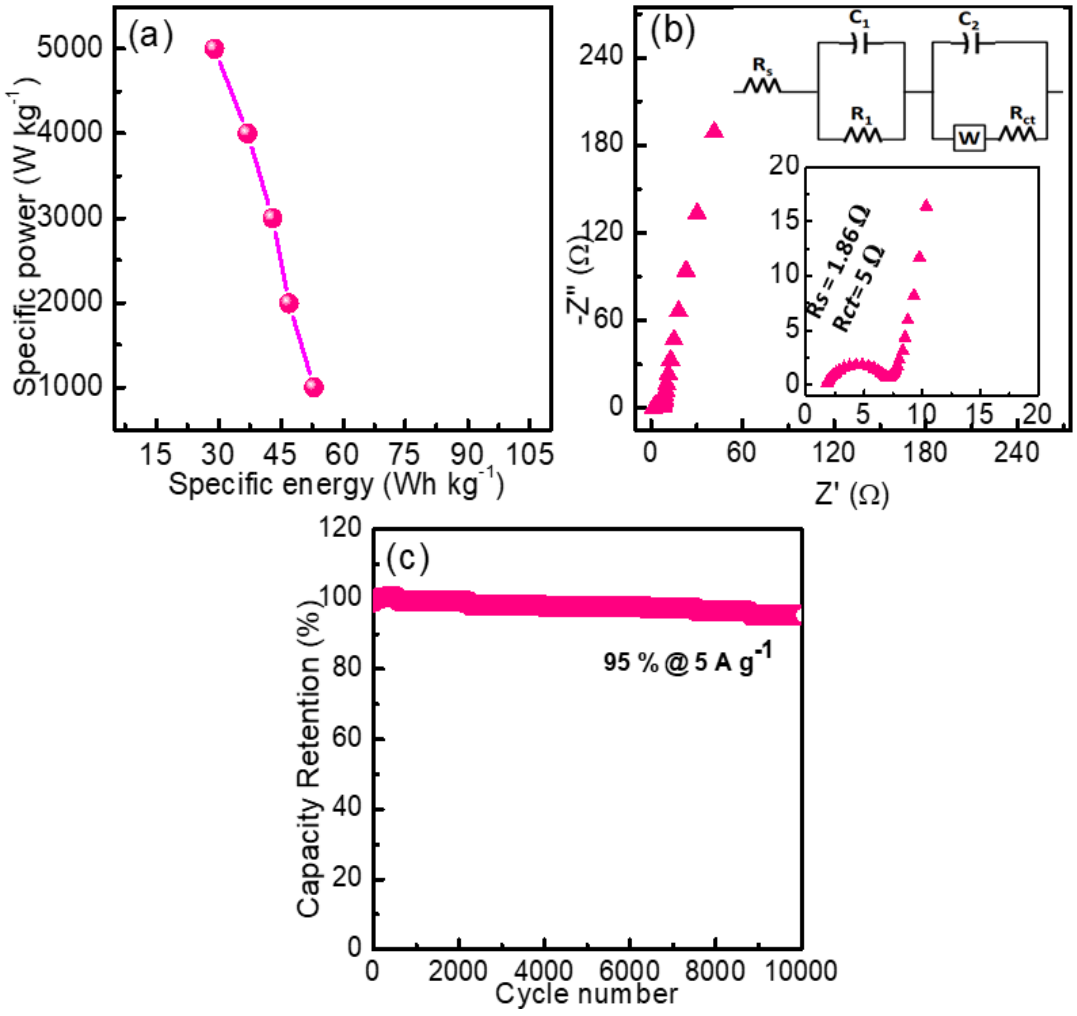

Figure 5.11. (a) Ragone plot of $MnCoSe_2$ nanoneedle, (b) Nyquist plots of $MnCoSe_2$ nanoneedle and, (c) Cycling performance of $MnCoSe_2$ nanoneedle based electrodes at a current density of 5 A g^{-1}.

A comparison of performance of $MnCoSe_2$ nanoneedle as supercapacitor electrode with literature data is presented in **Table 5.1**.

Electrode material	**Voltage window**	**Electrolyte**	**Specific capacitance ($F\ g^{-1}$)**	**Cyclic stability**	**Reference**
$MnSe_2/CoSe_2$/ rGO composite	0 to 0.7 V	2 M KOH	1138 C g^{-1} at 1 A g^{-1} (Half cell)	98.5 % (5000 cycles)	(Xuan et al. 2021)
urchin-like $MnCoSe_2$	0 to 0.4 V	6 M KOH	1656 F g^{-1} at 1 A g^{-1} (Half cell)	91.8 % (8000 cycles)	(Miao et al. 2019)
$MnSe_2$-$CoSe_2$ composite	0 to 0.6 V	1 M KOH	373 F g^{-1} at 1 A g^{-1} (Half cell)	95.86 % (5000 cycles)	(Vidhya et al. 2021a)
$MnCoSe_2$ nanoneedle	**0 to 1 V**	**2 M KOH**	**384 F g^{-1} at 1 A g^{-1} (Full cell)**	**95% (10000 cycles)**	**Present work**

Table 5.1. Comparative study of supercapacitor performance of $MnCoSe_2$ nanoneedle with literature data

5.5 Conclusion

In summary, $MnCoSe_2$ nanoneedle were directly grown over Ni foam substrate and a symmetric supercapacitor device based on the freestanding $MnCoSe_2$ nanoneedle electrodes was constructed. The unique nanoneedle-like structure grown directly over a conductive 3-D nickel foam substrate dramatically enhances the electrochemical performance by increasing the active surface area and electrical conductivity. Over 10000 charge-discharge cycles, the supercapacitor has an amazing specific capacitance value of 384 F g^{-1} at 1 A g^{-1} and an outstanding cyclic stability of 95% at 5 A g^{-1}. Moreover, the $MnCoSe_2$ nanoneedle-based symmetric supercapacitor exhibits a higher specific energy value of 53 Wh kg^{-1}, at a specific power of 1 kW kg^{-1}, showing its potential application in advanced electrochemical energy-storage devices.

Chapter 6

$MnCo_2S_4$ nanoflower as efficient cathode materials for asymmetric supercapacitors

6.1 Outline of the chapter

The chapter deals with the application of $MnCo_2S_4$ nanoflower as effective cathode materials for asymmetric supercapacitors. Considering the outstanding electrochemical performance of $MnCo_2S_4$ nanoflowers-based system, an asymmetric supercapacitor (ASC) device has been developed using $MnCo_2S_4$ nanoflower as the cathode and rGO as the anode. The asymmetric supercapacitor exhibits superior performance with an increased gravimetric capacitance of 162 F g^{-1} at 1 A g^{-1}, an excellent cycle life of 99% along with a high coulombic efficiency of 99.5% after 10000 cycles. The device delivers a gravimetric energy density of 73 W h kg^{-1} at a gravimetric power density of 151 W kg^{-1}. This asymmetric supercapacitor technology has the potential to greatly advance high-energy storage applications thanks to its exceptional electrochemical performance.

6.2 Introduction

Asymmetric supercapacitors (ASCs) are a new class of supercapacitors that have been gaining popularity in recent years. ASCs are made up of two electrodes, one of which is a pseudocapacitive electrode and the other of which is an electrochemical double-layer capacitor (EDLC) electrode. The pseudocapacitive electrode stores energy through faradaic reactions, while the EDLC electrode stores energy through electrostatic double-layer formation. This combination of storage mechanisms gives ASCs a number of advantages over traditional supercapacitors, including higher energy density, higher power density, and longer cycle life. As a result of these advantages, ASCs are being considered for a variety of applications, including Portable electronics, Electric vehicles, and Grid storage. ASCs are a promising new technology that has the potential to revolutionize the way we store energy. As research and development in this area continues, it is likely that ASCs will become even more widespread and affordable in the future.

The energy density (E) greatly depends on the capacity of the device (C) and the operating potential (V) (Gogotsi and Simon 2011). Thus, to increase the energy density, a device needs to be fabricated with high capacitance electrode materials with a wide operating potential window. The limitation of the available electrochemical potential window of aqueous supercapacitors (1.2 V) can be enhanced by the asymmetric combination of electrode materials. The construction of an asymmetric hybrid supercapacitor with $MnCo_2S_4$ electrode and other carbon-based electrodes such as activated carbon, CNTs, and reduced graphene oxide (rGO) can deliver better outcomes (Hua et al. 2019; Muzaffar et al. 2019). rGO is most popular among the nanocarbons because of its outstanding conductivity, extremely small structure, large specific surface area, and desirable mechanical properties (Dubal et al. 2017; Khasim et al. 2020). Hence, the combination of $MnCo_2S_4$ cathode and rGO anode is expected to maximize the electrode performance by escalating the electrochemical potential window, capacitance value, and cycle life. Reports are available for hybrid supercapacitors that make use of the combination of $MnCo_2S_4$ and rGO as electrode materials. Jun *et al*. synthesized $MnCo_2S_4$ nanowire by a simple hydrothermal technique and the device fabricated using $MnCo_2S_4$ and rGO as electrodes deliver a large energy density of 31.3 W h kg^{-1} at a power density of 800 W kg^{-1} (Liu and Jun 2017). Han et al. reported manganese cobalt sulfide sheet

bound onto reduced graphene oxide and nickel foam (MCS/rGO/NF) via a time-controlled sulfurization method (Han et al. 2018). The hybrid supercapacitor fabricated using MCS/rGO/NF-3h as positive electrode and rGO as negative electrode shows a greater energy density value of 45.4 W h kg^{-1} at 850.2 W kg^{-1} power density. Hua et al. synthesized three-dimensional nitrogen doped carbon matrix (3DNC) over $MnCo_2S_4$ nanosheet. The hybrid supercapacitor assembled using 3DNC@$MnCo_2S_4$//AC gives a high energy density of 68.8 Wh kg^{-1} at the power density of 800 W kg^{-1} along with a cyclic stability of 82% retention after 5000 cycles (Hua et al. 2019). All these results indicate that $MnCo_2S_4$ based hybrid supercapacitor exhibit an outstanding capacitance value and long cycle life.

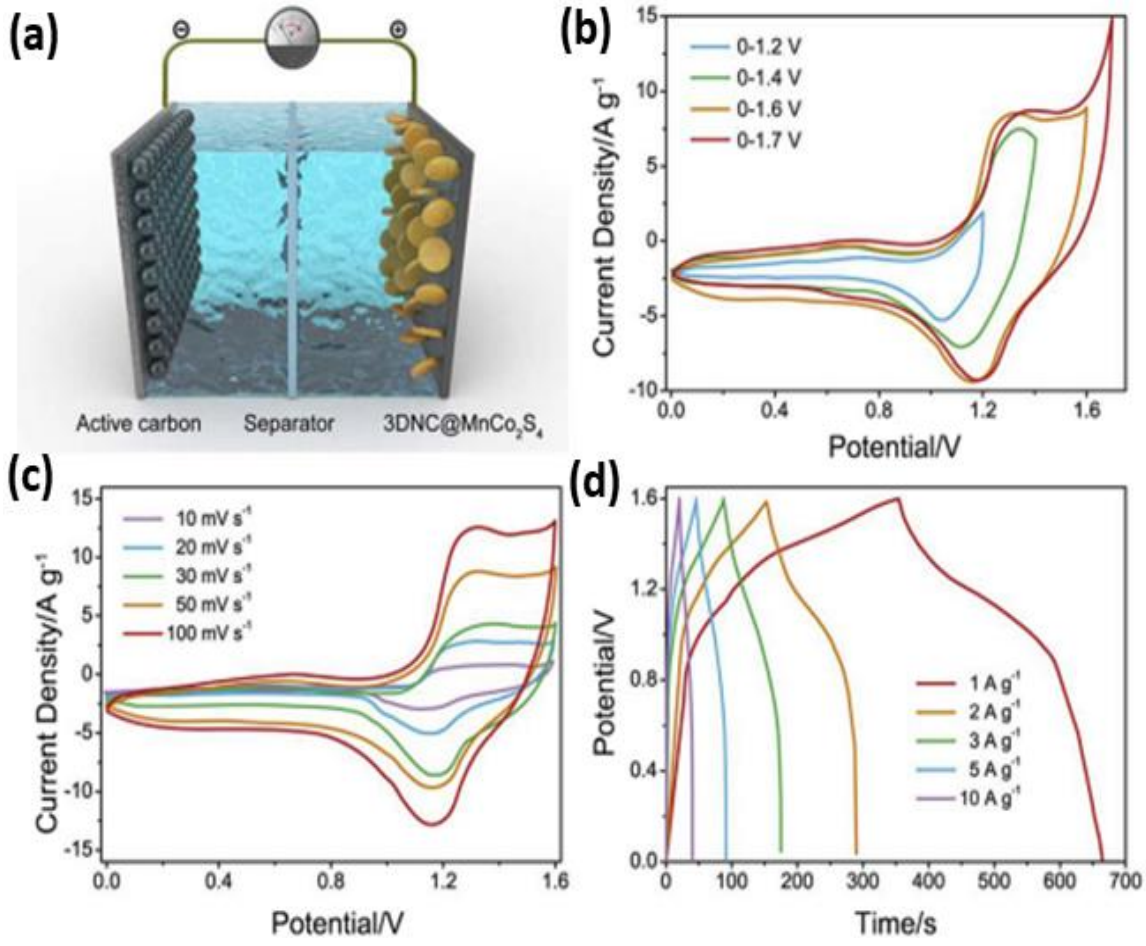

Figure 6.1. (a) Schematic illustration for the synthesis of 3DNC@$MnCo_2S_4$//AC HSC. (b) CV curves of the HSC device at different voltages. (c,d) CV curves and GCD curves of the HSC at various scan rates and current densities (Adapted from the reference(Hua et al. 2019)).

Herein, an asymmetric supercapacitor (ASC) has been built employing reduced graphene oxide (rGO) as the negative electrode and $MnCo_2S_4$ nanoflower as the positive electrode to increase the energy density of the device. Using various techniques, the electrochemical performance of the constructed device as well as the structural and morphological characterizations of the rGO based negative electrode material is carried out and the results are discussed.

6.3. Experimental Section

6.3.1. Fabrication and performance studies of asymmetric supercapacitors

The electrochemical performance of $MnCo_2S_4$ nanoflowers and rGO were taken in three electrode configurations, in which Ag/AgCl and platinum were used respectively as the reference and counter electrode and 2M KOH as the electrolyte. For the study of $MnCo_2S_4$ nanoflowers in three electrode configurations, $MnCo_2S_4$ nanoflowers directly grown over nickel foam substrate was taken as the working electrode. The nickel foam (NF) substrate was cleaned previously using 2M HCl by 20 minutes of ultrasonication followed by washing with ethanol and DI water. rGO electrodes were fabricated via coating the rGO slurry on nickel foam substrate using the traditional drop casting method. The coated electrodes were dried at 60 ^{o} C for 12 h in a vacuum oven. The loaded mass of the active material was measured from the weight difference of the nickel foam substrates before and after the deposition using a microbalance (XP26, METTLER TOLEDO). The mass loading of $MnCo_2S_4$ nanoflower and rGO electrodes was calculated as ~1 mg/electrode.

To measure the $MnCo_2S_4$ nanoflowers//rGO asymmetric hybrid supercapacitor device which assembled with $MnCo_2S_4$ nanoflowers as the positive electrode and rGO as the negative electrode. 1M KOH is used as the electrolyte for the electrochemical study of the hybrid system. The mass loading of positive and negative electrodes was calculated from the charge-balancing equation given below.

$$\frac{m_+}{m_-} = \frac{C_- \times V_-}{C_+ \times V_+} \tag{6.1}$$

where, C_+ and C_- represent the specific capacitance of positive and negative electrodes respectively, m_+ and m_- are the mass of the electrodes, and V_+ and V_- attribute to the potential window of the positive and negative electrode in three-electrode configuration.

Experimental details of the general characterization of the as-prepared electrode materials and the electrochemical performance analysis are given in **chapter 2 section 2.3**

The gravimetric capacitance (C_g) values were calculated from the charge-discharge technique using the following equation:

$$C_g = \frac{i}{M}\left(\frac{dv}{dt}\right)^{-1} \quad (6.2)$$

Where 'i' is the constant current for charge-discharge, M is the total mass of the active materials in both the electrodes ($M = m_1 + m_2$), and $\left(\frac{dv}{dt}\right)$ is the slope of the discharge curve.

The gravimetric energy density (E_g) and gravimetric power density (P_g) values were also calculated from CD curves using equations 8 and 9, respectively.

$$E_g = \frac{1}{2} C_g \Delta V^2 \quad (6.3)$$

Where ΔV is the potential window of discharge process, C_g is the gravimetric capacitance (Fg^{-1}) and E_g (W h kg^{-1}) is the gravimetric energy density.

$$P_g = \frac{Eg}{\Delta t} \quad (6.4)$$

Where Δt is the discharge time and P_g (k W kg^{-1}) is the gravimetric power density.

6.4 Results and Discussion

Reduced graphene oxide (rGO) is an ideal candidate for the negative electrode in hybrid supercapacitors (Baby et al. 2010; Bai et al. 2013; Liu and Jun 2017; Pettong et al. 2016; Zhao et al. 2022). Synthesis of rGO via a modified Hummer's method and their structural and morphological characterizations are represented in **Figure 6.2**. The XRD pattern of the rGO sample (**Figure 6.2 (a)**) exhibits a peak at 22^o and 44^o corresponding to the (002) and (101) plane of rGO (Tang et al. 2015). The SEM image of rGO is presented in **Figure 6.2 (b). Figure 6.2 (b)** shows a three-dimensional interconnected network of rGO. The porous network of rGO is really helpful to enhance the active surface area. The combination of $MnCo_2S_4$ nanoflower and rGO as the hybrid supercapacitor will reduce the volume expansion and shrinkage of the electrodes throughout the charge- discharge

measurement, thereby increasing the cycle life of the electrodes (Dutta and De 2018). The TEM images of rGO (**Figure 6.2 (c and d)**) represent wrinkled sheet like morphology which is identical to the SEM image. The SAED pattern of rGO is represented in **Figure 6.2 (e).**

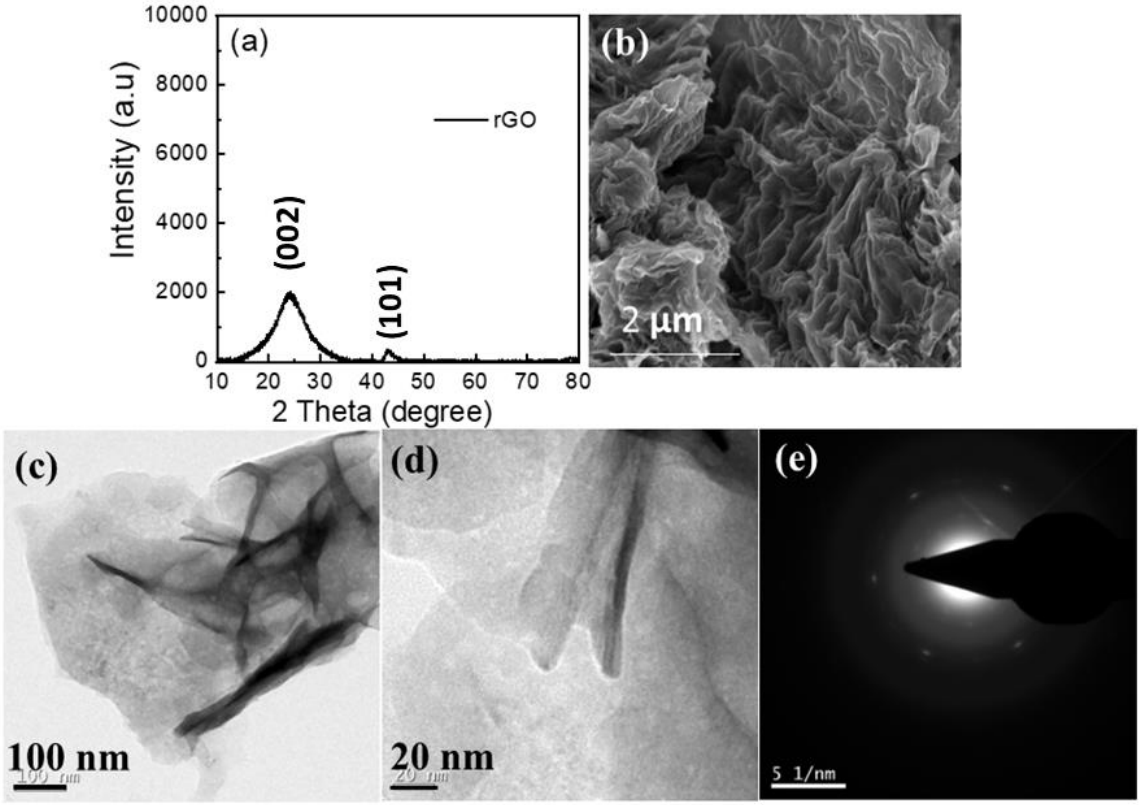

Figure 6.2. (a) XRD, (b) SEM, (c), and (d) HRTEM images of rGO, and (e) SAED pattern of rGO.

The electrochemical behavior of $MnCo_2S_4$ nanoflower electrode is first evaluated in three-electrode configurations using a 1 M KOH electrolyte. The CV loops of $MnCo_2S_4$ nanoflower measured in a voltage window of 0 to 1 V (*vs.* Ag/AgCl) at various scan rates in three-electrode techniques are presented in **Figure 6.3 (a)**. The CV curves exhibit a Faradaic behavior. The area under the CV loop increases with an increase in scan rate without any change in the CV curve, specifying a highly reversible Faradaic reaction. **Figure 6.3 (a)** reveals a cathodic peak at about 0.4 V for $MnCo_2S_4$ nanoflower electrode. The shape of the CV loops is well agreed with the earlier reports on the electrochemical measurements of $MnCo_2S_4$ in KOH electrolyte (Lee et al. 2021). The $MnCo_2S_4$ nanoflower electrodes show a maximum Csp value of 2000 F g^{-1} at 5 mV s^{-1}. The GCD curves of $MnCo_2S_4$ nanoflower in a three-electrode configuration were taken at various current densities in the voltage range of 0 to 1 V and are presented in **Figure 6.3 (b)**. The

GCD curves of $MnCo_2S_4$ nanoflower are not exhibiting any ideal triangular shape, which is due to the pseudocapacitive contribution from the material. The specific capacitance of $MnCo_2S_4$ nanoflower electrode is obtained from GCD curves as 1615, 1720, 1791, 1844, and 1980 F g^{-1} corresponding to the current densities 5, 4, 3, 2, and 1 A g^{-1} respectively. The electrode performance of rGO was also conducted in a three-electrode configuration. The CV loops of rGO measured in a voltage window of -1.0 to 0 V (*vs.* Ag/AgCl) at various scan rates are presented in **Figure 6.3 (c)**. The mass loading of rGO for the three electrode measurements was taken as 1 mg/electrode. The CV loops of rGO show typical EDLC behavior. The GCD curves of rGO (**Figure 6.3 (d)**) are observed to be a triangular shape, which represents the EDLC behavior.

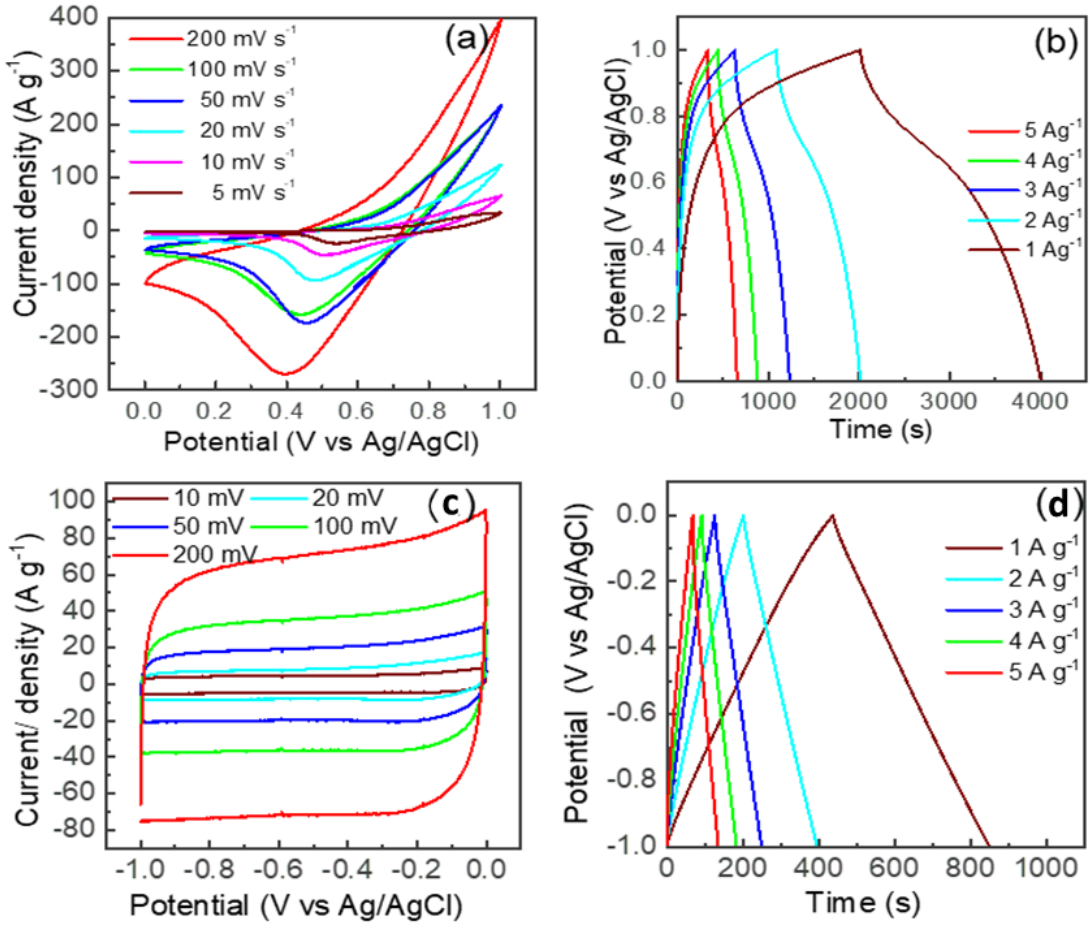

Figure 6.3. (a) and (b) Cyclic voltammograms at different scan rates and Galvanostatic charge-discharge curves at different current densities of $MnCo_2S_4$ nanoflowers, (c) and (d) Cyclic voltammograms at different scan rates and Galvanostatic charge-discharge curves at different current densities of rGO in three-electrode configurations.

To enhance the gravimetric energy density, an asymmetric supercapacitor device (ASC) was fabricated using $MnCo_2S_4$ nanoflower as the positive electrode and rGO as the negative electrode in 2 M KOH electrolyte. The schematic diagram of $MnCo_2S_4$ nanoflower//rGO is shown in **Figure 6.4 (a)**. A comparative study of CV curves of positive and negative electrodes is taken in a three-electrode set up to measure the possible potential windows of $MnCo_2S_4$ nanoflower//rGO based asymmetric supercapacitor and the result is shown in **Figure 6.4 (b)**. It is observed that $MnCo_2S_4$ nanoflower and rGO based electrodes maintain potential widows between 0.0 and 1.0 V and between -1.0 and 0.0 V respectively (*vs.* Ag/AgCl). In order to achieve reliable asymmetric supercapacitor performance working in an elevated voltage window, it is mandatory to balance the charge (Q) between positive and negative electrodes. The mass ratios of $MnCo_2S_4$ nanoflower and rGO have been determined 1:5 using the charge-balancing equation (**equation 6.1**). The mass loading of $MnCo_2S_4$ nanoflower was kept as 1 mg/electrode and that of rGO as 5 mg/electrode.

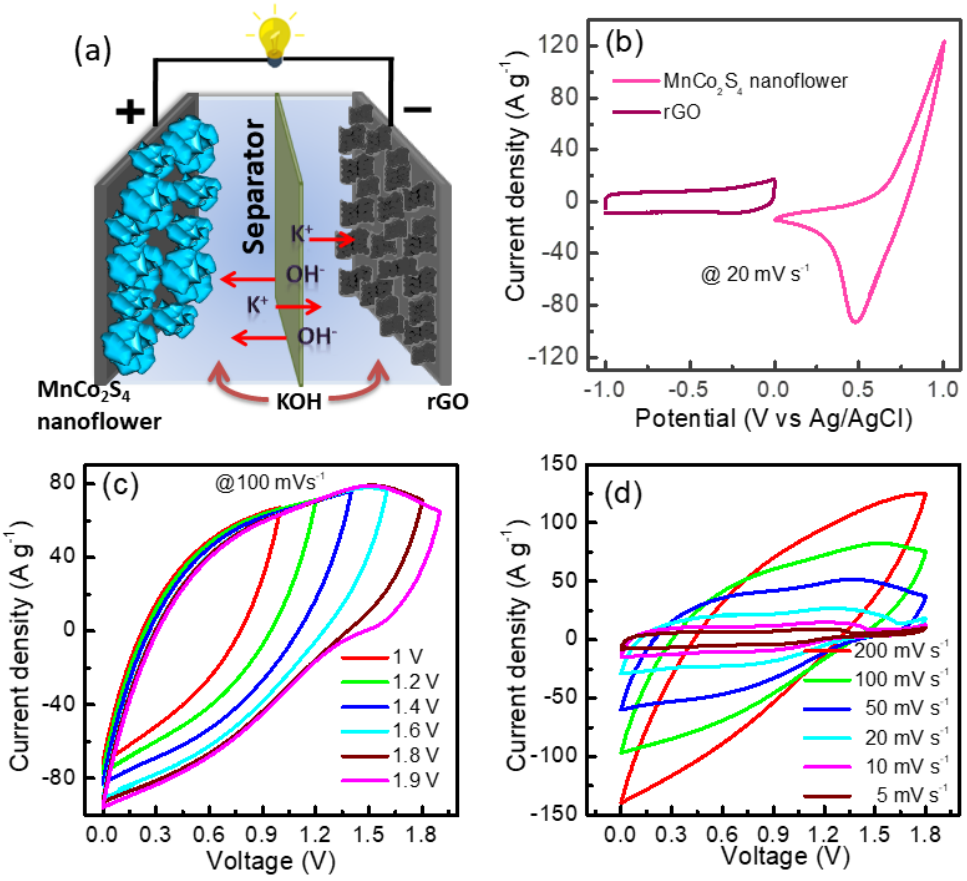

Figure 6.4. (a) Schematic illustration of the fabricated $MnCo_2S_4$ nanoflower//rGO based ASC device, (b) comparison of CV loops of positive ($MnCo_2S_4$ nanoflower) and negative

(rGO) electrode at a scan rate of 20 mV s^{-1} in three-electrode configurations, (c) Cyclic voltammograms of $MnCo_2S_4$ nanoflower//rGO at different voltage windows, (d) Cyclic voltammograms of $MnCo_2S_4$ nanoflower//rGO at different scan rates.

To optimize the operational potential window of $MnCo_2S_4$ nanoflower//rGO, the CV loops at various potential ranges are carried out at 100 mV s^{-1} scan rate and the results are presented in **Figure 6.4 (c)**. The device exhibits the maximum performance within the potential window of 0-1.8 V. The CV curves of $MnCo_2S_4$ nanoflower//rGO at various scan rates are given in **Figure 6.4 (d)**. As shown in **Figure 6.4 (d)**, the ASC device exhibits a combination of pseudocapacitive and EDLC behaviour due to the effect of $MnCo_2S_4$ nanoflower and rGO, respectively. The CV loops retain their initial shape even at a larger scan rate of 200 mV s^{-1} suggesting excellent rate performance of the electrode.

The GCD curves of the $MnCo_2S_4$ nanoflower//rGO device with a voltage range of 0 to 1.8 V are conducted (**Figure 6.5 (a)**). The nearly symmetrical shape of the GCD curve reveals the superior electrochemical reversibility of the device. The gravimetric device capacitance values calculated from the GCD curves are 121, 127, 135, 140, 146, 153, and 162 F g^{-1} respectively at 10, 7, 5, 4, 3, 2, and 1 A g^{-1}. The gravimetric device capacitance values of the ASC device as a function of current densities are presented in **Figure 6.5 (b)**. The Ragone plot (**Figure 6.5 (c)**) of the ASC gives a high gravimetric energy density value of 73 Wh kg^{-1}, at a gravimetric power density of 151 W kg^{-1}. Even at 1.7 kW kg^{-1}, the device still delivers gravimetric energy density of 55 W h kg^{-1}, demonstrating good rate performance. The energy and power density values of the $MnCo_2S_4$ nanoflower//rGO device are superior to the previous reports on the same type of electrode materials (Han et al. 2018; Hua et al. 2019; Jia et al. 2018; Laleh 2020; Lee et al. 2021; Li et al. 2021; Yi et al. 2021). The cyclic test along with the coulombic efficiency of the $MnCo_2S_4$ nanoflower//rGO device (**Figure 6.5 (d)**) reveals extremely high cycle life as well as coulombic efficiency for the electrode. The fabricated device exhibit 99 % of capacitance retention after 10000 cycles at 5 A g^{-1}. In addition, the ASC device exhibits an outstanding coulombic efficiency of above 99.5 % after 10000 continuous cycles, which denotes superior charge-discharge reversibility.

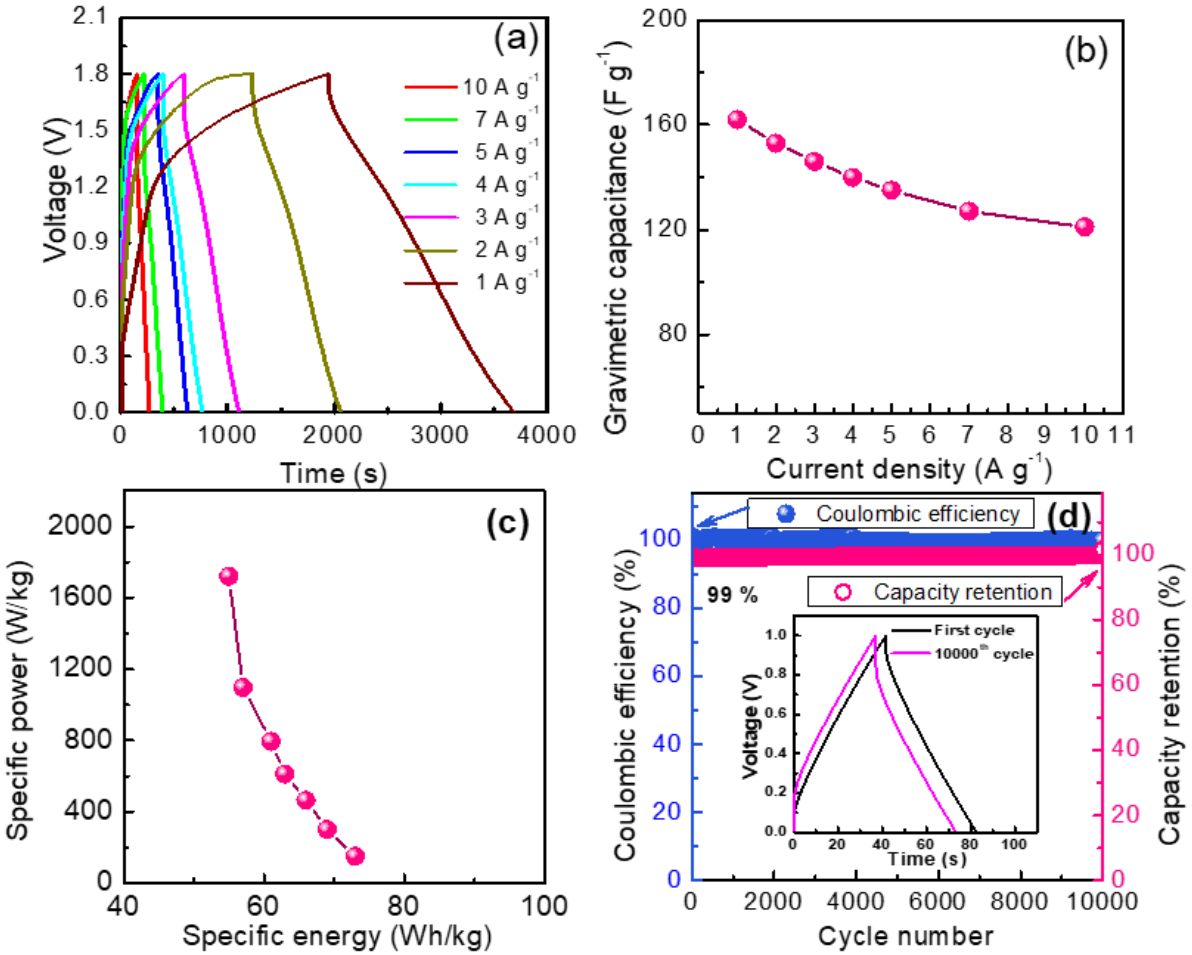

Figure 6.5. (a) Galvanostatic charge-discharge curves of $MnCo_2S_4$ nanoflower//rGO recorded at different current densities, (b) Variation of gravimetric capacitance value of $MnCo_2S_4$ nanoflower//rGO as a function of current densities, (c) Ragone plot, and (d) Cycling performance and Coulombic efficiency of ASC device at 5 A g^{-1} and the inset figure shows GCD profiles of first cycle and 10000^{th} cycle.

Figure 6.6 (a) shows the Nyquist plot for the $MnCo_2S_4$ nanoflower//rGO based ASC device. The EIS spectra were fitted using ZSimpWIN3.21 software to find out the charge transfer mechanism. **Figure 6.6 (b)** shows the equivalent circuit model to measure the EIS data. The Nyquist plot reveals a small semicircle in the high frequency region and a vertical line in the low frequency region. The intercept of the real axis at the high frequency range gives the solution resistance, R_s which is also known as equivalent series resistance (ESR). The R_s value of the ASC device is obtained as 1.3 Ω. The semicircle

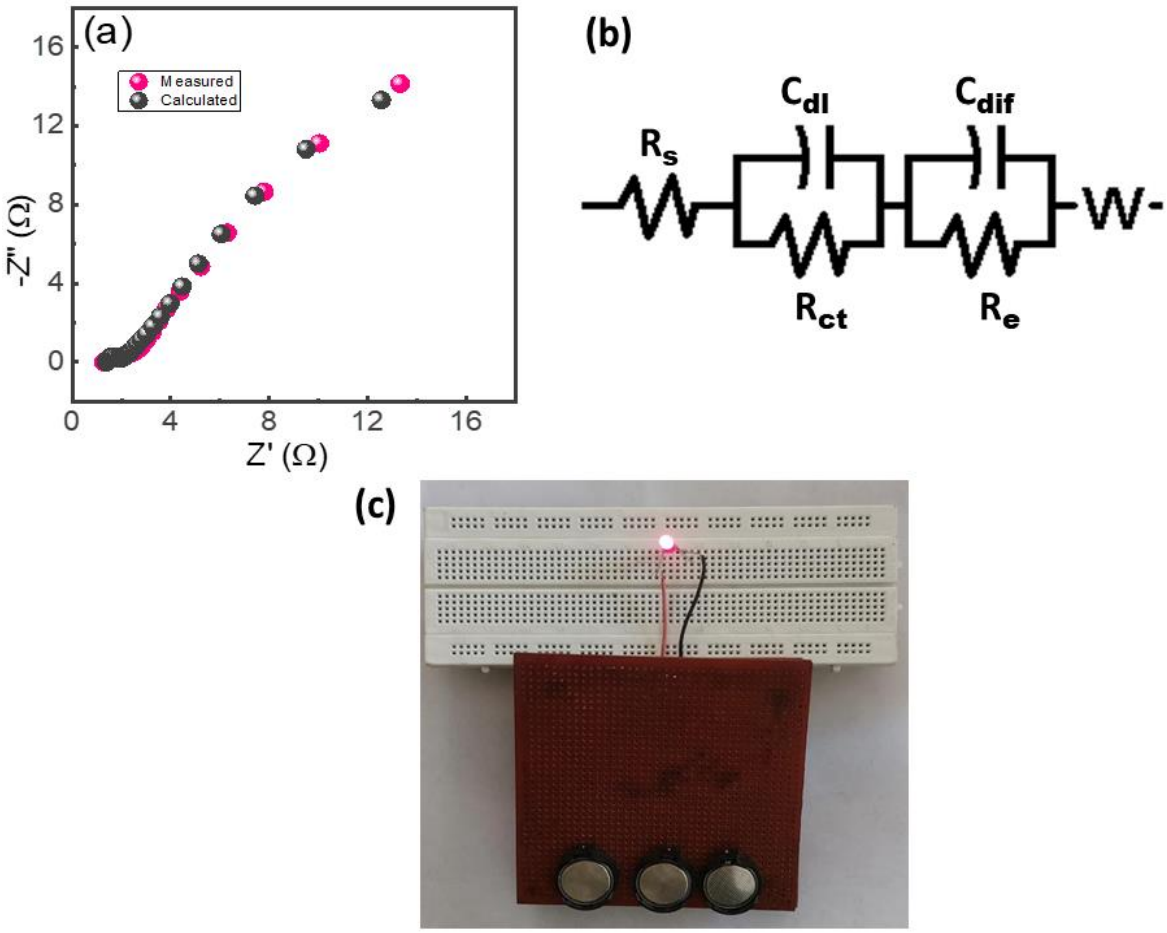

Figure 6.6. (a) Nyquist plot, (b) Equivalent circuit used for fitting nyquist plot, and (c) a red LED lighted by three series-connected ASC devices

region at the high and intermediate frequency range emerged due to the electrochemical process in between the electrode and electrolyte, which can be represented using the circuit element, C_{dl} (double layer capacitor). A charge transfer resistance (R_{ct}) is connected in parallel to C_{dl}. The Faradaic redox reaction between the $MnCo_2S_4$ nanoflower and OH^- ions in the KOH electrolyte may supposed to contain a capacitor (C_{dif}). An electron-transfer resistor (R_e) is connected in parallel with C_{dif}. The R_{ct} and R_e values for the $MnCo_2S_4$ nanoflower//rGO ASC device are 0.4 and 15 Ω, respectively. So, the first part of the circuit (C_{dl}, R_{ct}) illustrates the double layer formation and the second part (C_{dif}, R_e) illustrates the diffusion-controlled process. The last part (W) indicates the Warburg impedance. The lower R_s and R_{ct} values signify the strong contact between the active electrode materials and Ni foam substrate (Dubal et al. 2015). Three ASC devices were connected in series and were used to power a red LED. The devices were charged

for 5 seconds, and they were able to power the LED for more than 10 minutes (**Figure 6.6 (c)**. This experiment shows that the $MnCo_2S_4$ nanoflower//rGO ASC device has the potential to be a very practical and efficient energy storage device. The electrochemical performance of the ASC device is much better than the previous reports as presented in **Table 6.1.**

Electrode material	**Voltage window**	**Specific capacitance ($F\ g^{-1}$)**	**Energy Density ($W\ h\ k\ g^{-1}$)**	**Cyclic stability**	**Ref**
$MnCo_2S_4$ //graphene	0 to 1.5 V (1 M KOH)	132.2 F g^{-1} at 2 A g^{-1}	32.9 W h kg^{-1} at 295.2 W kg^{-1}	87.7% (5000 cycles)	(Lee et al. 2021)
$MnCo_2S_4$/NSG //NSG	0 to 1.5 V (1 M KOH)	204.6 F g^{-1} at 1 A g^{-1}	62.9 W h kg^{-1} at 740 W kg^{-1}	90.9% (5000 cycles)	(Wang et al. 2019b)
$MnCo_2S_4$//AC	0 to 1.6 V (1 M KOH)	52.3 F g^{-1} at 1 A g^{-1}	20.8 W h kg^{-1} at 400 W kg^{-1}	91.1% (5000 cycles)	(Jia et al. 2018)
$MnCo_2S_4$//rGO/Ni	0 to 1.6 V (3M KOH)	88 F g^{-1} at 1 A g^{-1}	31.3 W h kg^{-1} at 800 W kg^{-1}	89% (5000 cycles)	(Liu and Jun 2017)
$MnCo_2S_4$ Nanoflower //rGO	**0 to 1.8 V (2 M KOH)**	**162 F g^{-1} at 1 A g^{-1}**	**55 W h kg^{-1} at 1.7 kW kg^{-1}**	**99% (10000 cycles)**	**Present work**

Table 6.1. Comparative study of $MnCo_2S_4$ nanoflower//rGO based asymmetric supercapacitor (ASC) with literature data

6.5 Conclusion

In summary, an efficient asymmetric supercapacitor (ASC) device was fabricated using $MnCo_2S_4$ nanoflower as the cathode and rGO as the anode. The assembled $MnCo_2S_4$ nanoflower//rGO ASC device exhibited a large gravimetric device specific capacitance of 162 F g^{-1} at 1 A g^{-1} and a remarkable cyclic performance of 99 % at 5 A g^{-1} along with a high coulombic efficiency of 99.5% after 10000 cycles. The ASC device delivered a gravimetric energy density of 73 Wh kg^{-1}, at a gravimetric power density of 151.2 W kg^{-1}, indicating the great potential of $MnCo_2S_4$ nanoflower electrode for electrochemical energy storage.

Chapter 7

Summary and Future Scope

The thesis entitled "Nanostructured materials for electrochemical energy storage" results from research on supercapacitor electrode materials that have greater capacitance and stability for high-power applications. The main topic of the thesis is the electrochemical characteristics of nanomaterials based on binary Mn-Co systems. The seven chapters that comprise the thesis present extensive detail on Mn-Co-based binary transition metal oxides, hydroxides, sulfides, and selenides.

$Mn(OH)_2/Co(OH)_2$ nanoparticles were synthesized via the chemical bath deposition method over different current collectors, carbon cloth, and nickel foam. The $Mn(OH)_2/Co(OH)_2$ over nickel foam exhibited a superior electrochemical performance due to the highly porous structure that provides a large area for active material growth, excellent mechanical strength, and good electrical conductivity. The symmetric supercapacitor with $MnCo_2O_4$ nanoneedle directly grown on nickel foam via hydrothermal method further enhanced the specific capacitance and cycle life. When $MnCo_2S_4$ based system was explored, the electrochemical performance was found to be significantly enhanced. The metallic property of Se is superior to that of S and O and therefore Se based systems exhibit an increased electronic conductivity, which is extremely useful for electrochemical applications. Keeping this in mind, $MnCoSe_2$ nanoneedles were fabricated, and electrochemical performance was studied. In the last chapter, an asymmetric supercapacitor device was fabricated using $MnCo_2S_4$ nanoflower as the positive electrode and rGO as the negative electrode to increase the energy density for potential applications.

The results of this work indicate that $Mn(OH)_2/Co(OH)_2$ nanoparticles, $MnCo_2O_4$ nanoneedles, $MnCoSe_2$ nanoneedles, and $MnCo_2S_4$ nanoflowers are potential candidates for supercapacitor electrodes because they have electrochemical charge storage properties in increasing order. Further studies are needed to optimize the synthesis conditions and to explore the use of these materials in real-world applications.

As a future study, the performance of $MnCo_2S_4$ can be studied using organic and ionic liquid-based electrolytes for real-time applications. Moreover, the performance of the asymmetric supercapacitor described in the last chapter can be modified by changing the anode material to MXenes.

BIBLIOGRAPHY

Abdel-Salam, A.I., Attia, S.Y., El-Hosiny, F.I., Sadek, M.A., Mohamed, S.G., Rashad, M.M., 2022. Facile one-step hydrothermal method for $NiCo_2S_4$/rGO nanocomposite synthesis for efficient hybrid supercapacitor electrodes. Materials Chemistry and Physics 277, 125554.

Aghazadeh, M., Ganjali, M.R., 2017. Starch-assisted electrochemical fabrication of high surface area cobalt hydroxide nanosheets for high performance supercapacitors. Journal of Materials Science: Materials in Electronics 28(15), 11406-11414.

Akhtar, M.A., Sharma, V., Biswas, S., Chandra, A., 2016. Tuning porous nanostructures of $MnCo_2O_4$ for application in supercapacitors and catalysis. RSC Advances 6(98), 96296-96305.

Anandan, S., Gnana Sundara Raj, B., Lee, G.-J., Wu, J.J., 2013. Sonochemical synthesis of manganese (II) hydroxide for supercapacitor applications. Materials Research Bulletin 48(9), 3357-3361.

Anil Kumar, Y., Yadav, A.A., Al-Asbahi, B.A., Kang, S.-W., Moniruzzaman, M., 2022. Sulfur Nanoparticle-Decorated Nickel Cobalt Sulfide Hetero-Nanostructures with Enhanced Energy Storage for High-Performance Supercapacitors. Molecules 27(21), 7458.

Anjana, P.M., Sarath Kumar, S.R., Rakhi, R.B., 2021. Direct growth of $Mn(OH)_2$/$Co(OH)_2$ nanocomposite on carbon cloth for flexible supercapacitor electrodes. Journal of Energy Storage 33, 102151.

Ashok, A., Kumar, A., Ponraj, J., Mansour, S.A., 2020. Preparation of Mesoporous/Microporous $MnCo_2O_4$ and Nanocubic $MnCr_2O_4$ Using a Single Step Solution Combustion Synthesis for Bifunction Oxygen Electrocatalysis. Journal of The Electrochemical Society 167(5), 054507.

Atram, R.R., Bhuse, V.M., Atram, R.G., Wu, C.-M., Koinkar, P., Kondawar, S.B., 2021. Novel carbon nanofibers/thionickel ferrite/polyaniline (CNF/$NiFe_2S_4$/PANI) ternary nanocomposite for high performance supercapacitor. Materials Chemistry and Physics 262, 124253.

Augustyn, V., Simon, P., Dunn, B., 2014a. Pseudocapacitive oxide materials for high-rate electrochemical energy storage. Energy & Environmental Science 7, 1597.

Augustyn, V., Simon, P., Dunn, B., 2014b. Pseudocapacitive oxide materials for high-rate electrochemical energy storage. Energy & Environmental Science 7(5), 1597-1614.

Bai, X., Cao, D., Zhang, H., 2020. Simultaneously morphology and phase controlled synthesis of cobalt manganese hydroxides/reduced graphene oxide for high performance supercapacitor electrodes. Ceramics International 46(11, Part B), 19135-19145.

Barik, R., Tanwar, V., Kumar, R., Ingole, P.P., 2020. A high energy density and high rate capability flexible supercapacitor based on electro-spun highly porous SnO_2@ carbon nanofibers. Journal of Materials Chemistry A 8(30), 15110-15121.

Barik, R., Yadav, A.K., Jha, S.N., Bhattacharyya, D., Ingole, P.P., 2021. Two-Dimensional Tungsten Oxide/Selenium Nanocomposite Fabricated for Flexible Supercapacitors with Higher Operational Voltage and Their Charge Storage Mechanism. ACS Applied Materials & Interfaces 13(7), 8102-8119.

Barzegar, F., Bello, A., Momodu, D.Y., Dangbegnon, J.K., Taghizadeh, F., Madito, M.J., Masikhwa, T.M., Manyala, N., 2015. Asymmetric supercapacitor based on an α-MoO_3 cathode and porous activated carbon anode materials. RSC Advances 5(47), 37462-37468.

Biesinger, M.C., Payne, B.P., Grosvenor, A.P., Lau, L.W.M., Gerson, A.R., Smart, R.S.C., 2011. Resolving surface chemical states in XPS analysis of first row transition metals, oxides and hydroxides: Cr, Mn, Fe, Co and Ni. Applied Surface Science 257(7), 2717-2730.

BoopathiRaja, R., Parthibavarman, M., 2019. Hetero-structure arrays of $MnCo_2O_4$ nanoflakes@nanowires grown on Ni foam: Design, fabrication and applications in electrochemical energy storage. Journal of Alloys and Compounds 811, 152084.

Castro-Gutiérrez, J., Celzard, A., Fierro, V., 2020. Energy Storage in Supercapacitors: Focus on Tannin-Derived Carbon Electrodes. Frontiers in Materials 7.

Chakravarty, D., Late, D.J., 2015. Microwave and hydrothermal syntheses of WSe_2 micro/nanorods and their application in supercapacitors. RSC Advances 5(28), 21700-21709.

Chebil, A., Kuzgun, O., Dridi, C., Ates, M., 2020. High power density supercapacitor devices based on nickel foam–coated rGO/$MnCo_2O_4$ nanocomposites. Ionics 26(11), 5725-5735.

Chen, D., Chen, H., Chang, X., Liu, P., Zhao, Z., Zhou, J., Xu, G., Lin, H., Han, S., 2017a. Hierarchical CoMn-layered double hydroxide nanowires on nickel foam as electrode material for high-capacitance supercapacitor. Journal of Alloys and Compounds 729, 866-873.

Chen, H.C., Qin, Y., Cao, H., Song, X., Huang, C., Feng, H., Zhao, X.S., 2019a. Synthesis of amorphous nickel–cobalt–manganese hydroxides for supercapacitor-battery hybrid energy storage system. Energy Storage Materials 17, 194-203.

Chen, T., Li, S., Wen, J., Gui, P., Guo, Y., Guan, C., Liu, J., Fang, G., 2018. Rational Construction of Hollow Core-Branch CoSe2 Nanoarrays for High-Performance Asymmetric Supercapacitor and Efficient Oxygen Evolution. Small 14(5), 1700979.

Chen, T., Shi, R., Zhang, Y., Wang, Z., 2019b. A $MnCo_2O_4$@$NiMoO_4$ Core-Shell Composite Supported on Nickel Foam as a Supercapacitor Electrode for Energy Storage. ChemPlusChem 84 1, 69-77.

Chen, T., Wei, S., Wang, Z., 2020. $NiCo_2S_4$-Based Composite Materials for Supercapacitors. ChemPlusChem 85(1), 43-56.

Chen, X., Paul, R., Dai, L., 2017b. Carbon-based supercapacitors for efficient energy storage. National Science Review 4, 1-37.

Chen, Y., Wang, N., Tang, X., Pillai, S.C., Hu, W., 2022. High performance supercapacitors using selenium partially reduced Co_3O_4 on carbon cloth electrode with 3D interconnected architecture nanowires. Applied Surface Science 605, 154785.

Cherusseri, J., Choudhary, N., Sambath Kumar, K., Jung, Y., Thomas, J., 2019. Recent trends in transition metal dichalcogenide based supercapacitor electrodes. Nanoscale Horizons 4(4), 840-858.

Conway, B.E., Birss, V., Wojtowicz, J., 1997. The role and utilization of pseudocapacitance for energy storage by supercapacitors. Journal of Power Sources 66(1), 1-14.

Cui, M., Meng, X., 2020. Overview of transition metal-based composite materials for supercapacitor electrodes. Nanoscale Advances 2(12), 5516-5528.

Dakshana, M., Meyvel, S., Malarvizhi, M., Sathya, P., 2020. Electrochemical investigation of hydrothermally induced MnCo2S4 nanoparticles as an electrode material for high performance supercapacitors. Nanosystems: Physics, Chemistry, Mathematics 11, 230-236.

Deng, X., Li, J., Shan, Z., Sha, J., Ma, L., Zhao, N., 2020. A N, O co-doped hierarchical carbon cathode for high-performance Zn-ion hybrid supercapacitors with enhanced pseudocapacitance. Journal of Materials Chemistry A 8(23), 11617-11625.

Dong, Y., Wang, Y., Xu, Y., Chen, C., Wang, Y., Jiao, L., Yuan, H., 2017. Facile synthesis of hierarchical nanocage $MnCo_2O_4$ for high performance supercapacitor. Electrochimica Acta 225, 39-46.

Elkholy, A.E., El-Taib Heakal, F., Allam, N.K., 2019. A facile electrosynthesis approach of amorphous Mn-Co-Fe ternary hydroxides as binder-free active electrode materials for high-performance supercapacitors. Electrochimica Acta 296, 59-68.

Elshahawy, A., Li, X., Zhang, H., Hu, Y., Ho, K., Guan, C., Wang, J., 2017a. Controllable $MnCo_2S_4$ Nanostructure for high performance hybrid supercapacitor. J. Mater. Chem. A 5.

Elshahawy, A.M., Li, X., Zhang, H., Hu, Y., Ho, K.H., Guan, C., Wang, J., 2017b. Controllable $MnCo_2S_4$ nanostructures for high performance hybrid supercapacitors. Journal of Materials Chemistry A 5(16), 7494-7506.

Feng, N., Meng, R., Zu, L., Feng, Y., Peng, C., Huang, J., Liu, G., Chen, B., Yang, J., 2019. A polymer-direct-intercalation strategy for MoS_2/carbon-derived heteroaerogels with ultrahigh pseudocapacitance. Nature Communications 10(1), 1372.

Gao, M., Le, K., Wang, G., Wang, Z., Wang, F., Liu, W., Liu, J., 2019. Core-shell Cu_2-xS @ CoS_2 heterogeneous nanowire array with superior electrochemical performance for supercapacitor application. Electrochimica Acta 323, 134839.

Gogotsi, Y., Simon, P., 2011. True Performance Metrics in Electrochemical Energy Storage. Science 334(6058), 917-918.

Gomez, J., Kalu, E.E., 2013. High-performance binder-free Co–Mn composite oxide supercapacitor electrode. Journal of Power Sources 230, 218-224.

Gonçalves, J.M., Silva, M.N.T., Naik, K.K., Martins, P.R., Rocha, D.P., Nossol, E., Munoz, R.A.A., Angnes, L., Rout, C.S., 2021. Multifunctional spinel $MnCo_2O_4$ based materials for energy storage and conversion: a review on emerging trends, recent developments and future perspectives. Journal of Materials Chemistry A 9(6), 3095-3124.

González, A., Goikolea, E., Barrena, J.A., Mysyk, R., 2016. Review on supercapacitors: Technologies and materials. Renewable and Sustainable Energy Reviews 58, 1189-1206.

Halper, S., M., Ellenbogen, C., J., 2006. Supercapacitors: A Brief Overview.

Han, X., Xuan, H., Gao, J., Liang, T., Yang, J., Xu, Y., Han, P., Du, Y., 2018. Construction of manganese-cobalt-sulfide anchored onto rGO/Ni foam with a high capacity for hybrid supercapacitors. Electrochimica Acta 288, 31-41.

Hao, P., Zhao, Z., Li, L., Tuan, C.-C., Li, H., Sang, Y., Jiang, H., Wong, C.P., Liu, H., 2015. The hybrid nanostructure of $MnCo_2O_{4.5}$ nanoneedle/carbon aerogel for symmetric supercapacitors with high energy density. Nanoscale 7(34), 14401-14412.

He, Y., Chen, W., Gao, C., Zhou, J., Li, X., Xie, E., 2013. An overview of carbon materials for flexible electrochemical capacitors. Nanoscale 5(19), 8799-8820.

Hsu, S.-Y., Hsu, F.-H., Chen, J.-L., Cheng, Y.-S., Chen, J.-M., Lu, K.-T., 2021. The supercapacitor electrode properties and energy storage mechanism of binary transition metal sulfide $MnCo_2S_4$ compared with oxide $MnCo_2O_4$ studied using in situ quick X-ray absorption spectroscopy. Materials Chemistry Frontiers 5(13), 4937-4949.

Hu, Q., Zou, X., Huang, Y., Wei, Y., YaWang, Chen, F., Xiang, B., Wu, Q., Li, W., 2020. Graphene oxide-drove transformation of NiS/Ni(3)S(4) microbars towards Ni(3)S(4) polyhedrons for supercapacitor. Journal of colloid and interface science 559, 115-123.

Hua, M., Cui, F., Huang, Y., Zhao, Y., Lian, J., Bao, J., Zhang, B., Yuan, S., Li, H., 2019. Crafting nanosheet-built $MnCo_2S_4$ disks on robust N-doped carbon matrix for hybrid supercapacitors. Electrochimica Acta 323, 134770.

Hui, K.N., Hui, K.S., Tang, Z., Jadhav, V.V., Xia, Q.X., 2016. Hierarchical chestnut-like $MnCo_2O_4$ nanoneedles grown on nickel foam as binder-free electrode for high

energy density asymmetric supercapacitors. Journal of Power Sources 330, 195-203.

Iamprasertkun, P., Hirunpinyopas, W., Deerattrakul, V., Sawangphruk, M., Nualchimplee, C., 2021. Controlling the flake size of bifunctional 2D WSe_2 nanosheets as flexible binders and supercapacitor materials. Nanoscale Advances 3(3), 653-660.

Ilton, E.S., Post, J.E., Heaney, P.J., Ling, F.T., Kerisit, S.N., 2016. XPS determination of Mn oxidation states in Mn (hydr)oxides. Applied Surface Science 366, 475-485.

Jagadale, A.D., Guan, G., Li, X., Du, X., Ma, X., Hao, X., Abudula, A., 2016. Ultrathin nanoflakes of cobalt–manganese layered double hydroxide with high reversibility for asymmetric supercapacitor. Journal of Power Sources 306, 526-534.

Jia, H., Song, Y., Wu, J., Fu, W., Zhao, J., Liu, X., 2018. A novel P-doped $MnCo_2S_4$ nanoneedles assembled dandelion-like structure for high performance hybrid supercapacitors. Materials Letters 233, 55-58.

Jiang, B., Liu, Y., Zhang, J., Wang, Y., Zhang, X., Zhang, R., Huang, L.-L., Zhang, D., 2022. Synthesis of bimetallic nickel cobalt selenide particles for high-performance hybrid supercapacitors. RSC Advances 12(3), 1471-1478.

Jiang, S.L., Shi, T.L., Long, H., Sun, Y.M., Zhou, W., Tang, Z.R., 2014. High-performance binder-free supercapacitor electrode by direct growth of cobalt-manganese composite oxide nansostructures on nickel foam. Nanoscale Research Letters 9.

Joseph, N., Shafi, P.M., Bose, A.C., 2020. Recent Advances in 2D-MoS_2 and its Composite Nanostructures for Supercapacitor Electrode Application. Energy & Fuels 34(6), 6558-6597.

Khalafallah, D., Huang, W., Wunn, M., Zhi, M., Hong, Z., 2022. Promoting the energy storage capability via selenium-enriched nickel bismuth selenide/graphite composites as the positive and negative electrodes. Journal of Energy Storage 45, 103716.

Khan, M.S., Asif, A., Khawaldeh, S., Tekin, A., 2018. Dopamine Detection using Mercaptopropionic Acid and Cysteamine for Electrodes Surface Modification. J Electr Bioimpedance, pp. 3-9.

Khomenko, V., Frackowiak, E., Béguin, F., 2005. Determination of the specific capacitance of conducting polymer/nanotubes composite electrodes using different cell configurations. Electrochimica Acta 50(12), 2499-2506.

Kim, B.K., Sy, S., Yu, A., Zhang, J., 2015. Electrochemical Supercapacitors for Energy Storage and Conversion. Handbook of Clean Energy Systems, pp. 1-25.

Kim, H., Cho, M.-Y., Kim, M.-H., Park, K.-Y., Gwon, H., Lee, Y., Roh, K.C., Kang, K., 2013. A Novel High-Energy Hybrid Supercapacitor with an Anatase TiO_2–Reduced Graphene Oxide Anode and an Activated Carbon Cathode. Advanced Energy Materials 3(11), 1500-1506.

Kong, L.-B., Lu, C., Liu, M.-C., Luo, Y.-C., Kang, L., Li, X., Walsh, F.C., 2014a. The specific capacitance of sol–gel synthesised spinel $MnCo_2O_4$ in an alkaline electrolyte. Electrochimica Acta 115, 22-27.

Kong, L.B., Lu, C., Liu, M.C., Luo, Y.C., Kang, L., Li, X.H., Walsh, F.C., 2014b. The specific capacitance of sol-gel synthesised spinel $MnCo_2O_4$ in an alkaline electrolyte. Electrochimica Acta 115, 22-27.

Kuang, L., Ji, F., Pan, X., Wang, D., Chen, X., Jiang, D., Zhang, Y., Ding, B., 2017. Mesoporous $MnCo_2O_{4.5}$ nanoneedle arrays electrode for high-performance asymmetric supercapacitor application. Chemical Engineering Journal 315, 491-499.

Kumar, L., Boruah, P.K., Borthakur, S., Saikia, L., Das, M.R., Deka, S., 2021. CuCo-Layered Double Hydroxide Nanosheet-Based Polyhedrons for Flexible Supercapacitor Cells. ACS Applied Nano Materials 4(5), 5250-5262.

Kundu, S., Wang, Y., Xia, W., Muhler, M., 2008. Thermal Stability and Reducibility of Oxygen-Containing Functional Groups on Multiwalled Carbon Nanotube Surfaces: A Quantitative High-Resolution XPS and TPD/TPR Study. The Journal of Physical Chemistry C 112(43), 16869-16878.

Laheäär, A., Przygocki, P., Abbas, Q., Béguin, F., 2015. Appropriate methods for evaluating the efficiency and capacitive behavior of different types of supercapacitors. Electrochemistry Communications 60, 21-25.

Lama Tamang, T., Mohamed, S.G., Dhakal, G., Shim, J.-J., 2022. Morphology controlling of manganese-cobalt-sulfide nanoflake arrays using polyvinylpyrrolidone capping agent to enhance the performance of hybrid supercapacitors. Journal of Colloid and Interface Science 624, 494-504.

Lee, D., Lee, H.W., Mathur, S., Kim, K.H., 2021. Influence of cycling stability on structure and properties of $MnCo_2S_4$ nanocomposite for high-performance supercapacitors. Journal of Alloys and Compounds 868, 158850.

Lei, W., He, P., Wang, Y., Zhang, X., Xia, A., Dong, F., 2014. Solvothermal preparation of microspherical shaped cobalt–manganese oxide as electrode materials for supercapacitors. Composites Science and Technology 102, 82-86.

Li, L., Zhang, Y.Q., Liu, X.Y., Shi, S.J., Zhao, X.Y., Zhang, H., Ge, X., Cai, G.F., Gu, C.D., Wang, X.L., Tu, J.P., 2014a. One-dimension $MnCo_2O_4$ nanowire arrays for electrochemical energy storage. Electrochimica Acta 116, 467-474.

Li, M., Cheng, J.P., Wang, J., Liu, F., Zhang, X.B., 2016. The growth of nickel-manganese and cobalt-manganese layered double hydroxides on reduced graphene oxide for supercapacitor. Electrochimica Acta 206, 108-115.

Li, W., Xu, K., Song, G., Zhou, X., Zou, R., Yang, J., Chen, Z., Hu, J., 2014b. Facile synthesis of porous $MnCo_2O_{4.5}$ hierarchical architectures for high-rate supercapacitors. CrystEngComm 16, 2335-2339.

Li, W., Xu, K., Song, G., Zhou, X., Zou, R., Yang, J., Chen, Z., Hu, J., 2014c. Facile synthesis of porous $MnCo_2O_{4.5}$ hierarchical architectures for high-rate supercapacitors. CrystEngComm 16(12), 2335-2339.

Li, X., Shen, J., Li, N., Ye, M., 2015a. Fabrication of γ-MnS/rGO composite by facile one-pot solvothermal approach for supercapacitor applications. Journal of Power Sources 282, 194.

Li, Y., Han, X., Yi, T., He, Y., Li, X., 2019. Review and prospect of $NiCo_2O_4$-based composite materials for supercapacitor electrodes. Journal of Energy Chemistry 31, 54-78.

Li, Y., Wu, M.S., Ouyang, C.Y., 2015b. The structural and electronic properties of spinel $MnCo_2O_4$ bulk and low-index surfaces: From first principles studies. Applied Surface Science 349, 510-515.

Liu, D., Li, S., He, Y., Liu, C., Li, Q., Sui, Y., Qi, J., Zhang, P., Chen, C., Chen, Z., Liu, S., 2022. Co(OH)F@CoP/CC core-shell nanoarrays for high-performance supercapacitors. Journal of Energy Storage 55, 105417.

Liu, S., Jun, S.C., 2017. Hierarchical manganese cobalt sulfide core–shell nanostructures for high-performance asymmetric supercapacitors. Journal of Power Sources 342, 629-637.

Liu, T., 2018. How to Differentiate Capacitances using Trasatti and Dunn Methods.

Liu, Y.-L., Yan, C., Wang, G.-G., Li, F., Kang, Q., Zhang, H.-Y., Han, J.-C., 2020a. Selenium-rich nickel cobalt bimetallic selenides with core–shell architecture enable superior hybrid energy storage devices. Nanoscale 12(6), 4040-4050.

Liu, Y., Liu, Q., Wang, L., Yang, X., Yang, W., Zheng, J., Hou, H., 2020b. Advanced Supercapacitors Based on Porous Hollow Carbon Nanofiber Electrodes with High Specific Capacitance and Large Energy Density. ACS Applied Materials & Interfaces 12(4), 4777-4786.

Maile, N., Fulari, V., Ghongade, S., Khare, S., Kamble, H., 2018. Electrochemical synthesis of $Mn(OH)_2$ and $Co(OH)_2$ thin films for supercapacitor electrode application.

Mathis, T.S., Kurra, N., Wang, X., Pinto, D., Simon, P., Gogotsi, Y., 2019. Energy Storage Data Reporting in Perspective—Guidelines for Interpreting the Performance of Electrochemical Energy Storage Systems. Advanced Energy Materials 9(39), 1902007.

McIntyre, N.S., Cook, M.G., 1975. X-ray photoelectron studies on some oxides and hydroxides of cobalt, nickel, and copper. Analytical Chemistry 47(13), 2208-2213.

Melkiyur, I., Yuvakkumar, R., Ravi, G., Balasubramaniam, S., Pannipara, M., Al-sehemi, A., Velauthapillai, D., 2021. Quaternary Cu_2FeSnS_4 /PVP/rGO Composite for Supercapacitor Applications. ACS Omega XXXX.

Meng, J., Lu, S., Xu, W., Li, S., Dong, X., 2022. Fabrication of composite material of $RuCo_2O_4$ and graphene on nickel foam for supercapacitor electrodes. RSC Advances 12(24), 15508-15516.

Miao, C., Xu, P., Zhao, J., Zhu, K., Cheng, K., Ye, K., Yan, J., Cao, D., Wang, G., Zhang, X., 2019. Binder-Free Hierarchical Urchin-like Manganese–Cobalt Selenide with High Electrochemical Energy Storage Performance. ACS Applied Energy Materials 2(5), 3595-3604.

Mohamed, A.M., Allam, N.K., 2022. Transition Metal Selenide (TMSe) electrodes for electrochemical capacitor devices: A critical review. Journal of Energy Storage 47, 103565.

Mola, B.A., Mani, G., Sambasivam, S., Pallavolu, M.R., Ghfar, A.A., Ouladsmane, M., Alsawat, M., Reddy, N.R., Noh, Y., Jilcha, S.K., Kim, H.-J., Obaidat, I.M.,

Kumar, Y.A., 2021. Crafting nanoflower-built $MnCo_2S_4$ anchored to Ni foam as a prominent energy conversion and energy storage electrode for high-performance supercapacitor applications. Journal of Energy Storage 43, 103155.

Murugan, A.V., Viswanath, A.K., Gopinath, C.S., Vijayamohanan, K., 2006. Highly efficient organic-inorganic poly(3,4-ethylenedioxythiophene)-molybdenum trioxide nanocomposite electrodes for electrochemical supercapacitor. Journal of Applied Physics 100(7), 074319.

Muzaffar, A., Ahamed, M.B., Deshmukh, K., Thirumalai, J., 2019. A review on recent advances in hybrid supercapacitors: Design, fabrication and applications. Renewable and Sustainable Energy Reviews 101, 123-145.

Nakamoto, K., 2006. Handbook o Vibrational Spectroscopy/In rared and Raman Spectra o Inorganic and Coordination Compounds. John Wiley & Sons, Ltd.

Nasrin, K., Subramani, K., Karnan, M., Sathish, M., 2021. $MnCo_2S_4$ – MXene: A novel hybrid electrode material for high performance long-life asymmetric supercapattery. Journal of colloid and interface science 600, 264-277.

Nguyet, H.M., Tam, L.T.T., Tung, D.T., Yen, N.T., Dung, H.T., Dung, N.T., Phan N, H., Tuan, L.A., Minh, P.N., Lu, L.T., 2022. Facile synthesis of $MnCo_2S_4$ nanosheets as a binder-free electrode material for high performance supercapacitor applications. New Journal of Chemistry 46(29), 13996-14003.

Nilson, R., Brumbach, M., Bunker, B., 2011. Modeling the Electrochemical Impedance Spectra of Electroactive Pseudocapacitor Materials. Journal of The Electrochemical Society 158, A678-A688.

Nissinen, T.A., Kiros, Y., Gasik, M., Leskelä, M., 2003. $MnCo_2O_4$ Preparation by Microwave-Assisted Route Synthesis (MARS) and the Effect of Carbon Admixture. Chemistry of Materials 15(26), 4974-4979.

Padmanathan, N., Selladurai, S., 2014a. Mesoporous $MnCo_2O_4$ spinel oxide nanostructure synthesized by solvothermal technique for supercapacitor. Ionics 20(4), 479-487.

Padmanathan, N., Selladurai, S., 2014b. Mesoporous $MnCo_2O_4$ spinel oxide nanostructure synthesized by solvothermal technique for supercapacitor. Ionics 20(4), 479-487.

Pal, B., Yang, S., Ramesh, S., Thangadurai, V., Jose, R., 2019. Electrolyte selection for supercapacitive devices: a critical review. Nanoscale Advances 1(10), 3807-3835.

Pathak, M., Tamang, D., Kandasamy, M., Chakraborty, B., Rout, C.S., 2020. A comparative experimental and theoretical investigation on energy storage performance of $CoSe_2$, $NiSe_2$ and $MnSe_2$ nanostructures. Applied Materials Today 19, 100568.

Pattanayak, J., Rao, V.S., Maiti, H.S., 1989. Preparation and thermal stability of manganese oxides obtained by precipitation from aqueous manganese sulphate solution. Thermochimica Acta 153, 193-204.

Raicopol, M., Pruna, A., Pilan, L., 2013. Supercapacitance of Single-Walled Carbon Nanotubes-Polypyrrole Composites. Journal of Chemistry 2013, 367473.

Rajput, R., Arora, S., 2021. MoSe2 nanosheets as an efficient electrode material for supercapacitors. Materials Today: Proceedings 54, 728-732.

Rakhi, R.B., Ahmed, B., Anjum, D., Alshareef, H.N., 2016a. Direct Chemical Synthesis of MnO_2 Nanowhiskers on Transition-Metal Carbide Surfaces for Supercapacitor Applications. ACS Applied Materials & Interfaces 8(29), 18806-18814.

Rakhi, R.B., Chen, W., Hedhili, M.N., Cha, D., Alshareef, H.N., 2014. Enhanced Rate Performance of Mesoporous Co_3O_4 Nanosheet Supercapacitor Electrodes by Hydrous RuO_2 Nanoparticle Decoration. ACS Applied Materials & Interfaces 6(6), 4196-4206.

Rakhi, R.B., Nagaraju, D.H., Beaujuge, P., Alshareef, H.N., 2016b. Supercapacitors based on two dimensional VO_2 nanosheet electrodes in organic gel electrolyte. Electrochimica Acta 220, 601-608.

Ramírez, A., Hillebrand, P., Stellmach, D., May, M.M., Bogdanoff, P., Fiechter, S., 2014. Evaluation of MnOx, Mn_2O_3, and Mn_3O_4 Electrodeposited Films for the Oxygen Evolution Reaction of Water. The Journal of Physical Chemistry C 118(26), 14073-14081.

Reghu Nath, A., Jayachandran, A., Sandhyarani, N., 2019. Nanosheets of nickel, cobalt and manganese triple hydroxides/oxyhydroxides as efficient electrode materials for asymmetrical supercapacitors. Dalton Transactions 48(13), 4211-4217.

Rendale, S.S., Bhat, T.S., Patil, P.S., 2022. $MnCo_2O_4$ nanomaterials based electrodes for supercapacitors. Inorganic Chemistry Communications 145, 109945.

Rohith, R., Manuraj, M., Jafri, R.I., Rakhi, R.B., 2021. Co-MoS_2 nanoflower coated carbon fabric as a flexible electrode for supercapacitor. Materials Today: Proceedings.

Sadighi, Z., Liu, J., Ciucci, F., Kim, J.-K., 2018. Mesoporous $MnCo_2S_4$ nanosheet arrays as an efficient catalyst for Li–O_2 batteries. Nanoscale 10(33), 15588-15599.

Sahoo, S., Naik, K.K., Rout, C.S., 2015b. Electrodeposition of spinel $MnCo_2O_4$ nanosheets for supercapacitor applications. Nanotechnology 26(45), 455401.

Sahoo, S., Rout, C.S., 2016. Facile Electrochemical Synthesis of Porous Manganese-Cobalt-Sulfide Based Ternary Transition Metal Sulfide Nanosheets Architectures for High Performance Energy Storage Applications. Electrochimica Acta 220, 57-66.

Sajjad, M., Ismail, J., Shah, A., Mahmood, A., Shah, M., Rahman, S., Lu, W., 2021. Fabrication of 1.6V hybrid supercapacitor developed using $MnSe_2$/rGO positive electrode and phosphine based covalent organic frameworks as a negative electrode enables superb stability up to 28,000 cycles. The Journal of Energy Storage 44, 103318.

Sakib, M.N., Ahmed, S., Rahat, S.M.S.M., Shuchi, S.B., 2021. A review of recent advances in manganese-based supercapacitors. Journal of Energy Storage 44, 103322.

Salunkhe, R.R., Bastakoti, B.P., Hsu, C.-T., Suzuki, N., Kim, J.H., Dou, S.X., Hu, C.-C., Yamauchi, Y., 2014. Direct Growth of Cobalt Hydroxide Rods on Nickel Foam and Its Application for Energy Storage. Chemistry – A European Journal 20(11), 3084-3088.

Sambath Kumar, K., Choudhary, N., Pandey, D., Ding, Y., Hurtado, L., Chung, H.-S., Tetard, L., Jung, Y., Thomas, J., 2020. Investigating 2D WS_2 supercapacitor electrode performance by Kelvin probe force microscopy. Journal of Materials Chemistry A 8(25), 12699-12704.

Sankar, K.V., Selvan, R.K., Meyrick, D., 2015. Electrochemical performances of $CoFe_2O_4$ nanoparticles and a rGO based asymmetric supercapacitor. RSC Advances 5(121), 99959-99967.

Sannasi, V., Subbian, K., 2019. Preparation of $MnCo_2O_4$ by microwave assisted method for supercapacitor applications.

Saravanakumar, B., Ravi, G., Ganesh, V., Guduru, R.K., Yuvakkumar, R., 2019. $MnCo_2O_4$ nanosphere synthesis for electrochemical applications. Materials Science for Energy Technologies 2(1), 130-138.

Sari, F.N.I., Lin, K.-C., Ting, J.-M., 2022. Mn(OH)2-containing $Co(OH)_2$/$Ni(OH)_2$ Core-shelled structure for ultrahigh energy density asymmetric supercapacitor. Applied Surface Science 576, 151805.

Selvaraj, A.R., Kim, H.-J., Senthil, K., Prabakar, K., 2020. Cation intercalated one-dimensional manganese hydroxide nanorods and hierarchical mesoporous activated carbon nanosheets with ultrahigh capacitance retention asymmetric supercapacitors. Journal of Colloid and Interface Science 566, 485-494.

Sharifi, S., Rahimi, K., Yazdani, A., 2021. Highly improved supercapacitance properties of $MnFe_2O_4$ nanoparticles by MoS_2 nanosheets. Scientific Reports 11(1), 8378.

Sharma, P., Bhatti, T.S., 2010. A review on electrochemical double-layer capacitors. Energy Conversion and Management 51(12), 2901-2912.

Sheng, H., Zhang, X., Ma, Y., Wang, P., Zhou, J., Su, Q., Lan, W., Xie, E., Zhang, C.J., 2019. Ultrathin, Wrinkled, Vertically Aligned $Co(OH)_2$ Nanosheets/Ag Nanowires Hybrid Network for Flexible Transparent Supercapacitor with High Performance. ACS Applied Materials & Interfaces 11(9), 8992-9001.

Sheng, L.M., Liu, M., Liu, P., Wei, Y., Liu, L., Fan, S.S., 2005. Field emission from self-assembly structure of carbon-nanotube films. Applied Surface Science 250(1), 9-13.

Shinde, S.K., Ramesh, S., Bathula, C., Ghodake, G.S., Kim, D.Y., Jagadale, A.D., Kadam, A.A., Waghmode, D.P., Sreekanth, T.V.M., Kim, H.S., Nagajyothi, P.C., Yadav, H.M., 2019. Novel approach to synthesize $NiCo_2S_4$ composite for high-performance supercapacitor application with different molar ratio of Ni and Co. Scientific Reports 9(1), 13717.

Sim, C.-K., Majid, S.R., Mahmood, N.Z., 2019. Durable porous carbon/$ZnMn_2O_4$ composite electrode material for supercapacitor. Journal of Alloys and Compounds 803, 424-433.

Simon, P., Gogotsi, Y., 2008b. Materials for electrochemical capacitors. Nature Materials 7(11), 845-854.

Simon, P., Gogotsi, Y., Dunn, B., 2014. Where Do Batteries End and Supercapacitors Begin? Science 343(6176), 1210-1211.

Sonia, Y.K., Paliwal, M.K., Meher, S.K., 2021. The rational design of hierarchical CoS_2/$CuCo_2S_4$ for three-dimensional all-solid-state hybrid supercapacitors with

high energy density, rate efficiency, and operational stability. Sustainable Energy & Fuels 5(4), 973-985.

Stoller, M.D., Ruoff, R.S., 2010. Best practice methods for determining an electrode material's performance for ultracapacitors. Energy & Environmental Science 3(9), 1294-1301.

Su, D., Tang, Z., Xie, J., Bian, Z., Zhang, J., Yang, D., Zhang, D., Wang, J., Liu, Y., Yuan, A., Kong, Q., 2019. Co, Mn-LDH nanoneedle arrays grown on Ni foam for high performance supercapacitors. Applied Surface Science 469, 487-494.

Su, L.-H., Zhang, X.-G., Liu, Y., 2008. Electrochemical performance of Co–Al layered double hydroxide nanosheets mixed with multiwall carbon nanotubes. Journal of Solid State Electrochemistry 12(9), 1129-1134.

Tang, N., Wang, W., You, H., Zhai, Z., Hilario, J., Zeng, L., Zhang, L., 2019. Morphology tuning of porous CoO nanowall towards enhanced electrochemical performance as supercapacitors electrodes. Catalysis Today 330, 240-245.

Vidhya, M.S., Yuvakkumar, R., Ravi, G., Babu, E.S., Saravanakumar, B., Nasif, O., Alharbi, S.A., Velauthapillai, D., 2021a. Demonstration of 1.5 V asymmetric supercapacitor developed using $MnSe_2$-$CoSe_2$ metal composite. Ceramics International 47(8), 11786-11792.

Vidhya, M.S., Yuvakkumar, R., Ravi, G., Saravanakumar, B., Velauthapillai, D., 2021b. Asymmetric polyhedron structured $NiSe_2$@$MoSe_2$ device for use as a supercapacitor. Nanoscale Advances 3(14), 4207-4215.

Wang, D., Li, J., Zhang, D., Liu, T., Zhang, N., Chen, L., Liu, X., Ma, R., Qiu, G., 2016. Layered Co–Mn hydroxide nanoflakes grown on carbon cloth as binder-free flexible electrodes for supercapacitors. Journal of Materials Science 51(8), 3784-3792.

Wang, F., Zhou, K., Zheng, J., Ma, J., 2019a. Rapid synthesis of porous manganese cobalt sulfide grown on Ni foam by microwave method for high performance supercapacitors. Synthetic Metals 256, 116113.

Wang, G., Zhang, L., Zhang, J., 2012. A review of electrode materials for electrochemical supercapacitors. Chemical Society Reviews 41(2), 797-828.

Wang, H., Zhang, K., Song, Y., Qiu, J., Wu, J., Yan, L., 2019b. $MnCo_2S_4$ nanoparticles anchored to N- and S-codoped 3D graphene as a prominent electrode for asymmetric supercapacitors. Carbon 146, 420-429.

Wang, J.-G., Kang, F., Wei, B., 2015a. Engineering of MnO_2-based nanocomposites for high-performance supercapacitors. Progress in Materials Science 74, 51-124.

Wang, R., Wu, J., 2017. 5 - Structure and Basic Properties of Ternary Metal Oxides and Their Prospects for Application in Supercapacitors. In: Dubal, D.P., Gomez-Romero, P. (Eds.), Metal Oxides in Supercapacitors, pp. 99-132. Elsevier.

Wang, R., Yan, X., Lang, J., Zheng, Z., Zhang, P., 2014. A hybrid supercapacitor based on flower-like $Co(OH)_2$ and urchin-like VN electrode materials. Journal of Materials Chemistry A 2(32), 12724-12732.

Wang, S., Hou, Y., Wang, X., 2015b. Development of a Stable $MnCo_2O_4$ Cocatalyst for Photocatalytic CO_2 Reduction with Visible Light. ACS Applied Materials & Interfaces 7(7), 4327-4335.

Wang, T., Yu, F., Wang, X., Xi, S., Chen, K.-J., Wang, H., 2020a. Enhancing cycling stability of transition metal-based layered double hydroxides through a self-sacrificial strategy for hybrid supercapacitors. Electrochimica Acta 334, 135586.

Wang, Y., Lv, C., Ji, G., Hu, R., Zheng, J., 2020b. An all-in-one supercapacitor with high stretchability via a facile strategy. Journal of Materials Chemistry A 8(17), 8255-8261.

Wie, C., Sun, Y., Zhan, N., Liu, M., Zhao, L., Cheng, C., Zhang, D., 2017. Preparation of Hierarchical $MnCo_2S_4$ Nanotubes for High-Performance Supercapacitors and Non-Enzymatic Glucose Sensors. ChemistrySelect 2(34), 11154-11159.

Wu, C.-M., Fan, C.-Y., Sun, I.W., Tsai, W.-T., Chang, J.-K., 2011. Improved pseudocapacitive performance and cycle life of cobalt hydroxide on an electrochemically derived nano-porous Ni framework. Journal of Power Sources 196(18), 7828-7834.

Wu, Z., Zhu, Y., Ji, X., 2014. $NiCo_2O_4$-based materials for electrochemical supercapacitors. Journal of Materials Chemistry A 2(36), 14759-14772.

Xiao, J., Zhan, H., Wang, X., Xu, Z.-Q., Xiong, Z., Zhang, K., Simon, G.P., Liu, J.Z., Li, D., 2020a. Electrolyte gating in graphene-based supercapacitors and its use for probing nanoconfined charging dynamics. Nature nanotechnology 15(8), 683-689.

Xiao, J., Zhan, H., Wang, X., Xu, Z.-Q., Xiong, Z., Zhang, K., Simon, G.P., Liu, J.Z., Li, D., 2020b. Electrolyte gating in graphene-based supercapacitors and its use for probing nanoconfined charging dynamics. Nature Nanotechnology.

Xiao, X., Wang, G., Zhang, M., Wang, Z., Zhao, R., Wang, Y., 2018. Electrochemical performance of mesoporous $ZnCo_2O_4$ nanosheets as an electrode material for supercapacitor. Ionics 24(8), 2435-2443.

Xie, L., Su, F., Xie, L., Guo, X., Kong, Q.-Q., Sun, G., Ahmad, A., Li, X., Yi, z., Wang, Z., Chen, C.-M., 2020. Review: Effect of pore structure and doping species on charge storage mechanisms in porous carbon-based supercapacitor. Materials Chemistry Frontiers 4.

Xu, J., Sun, Y., Lu, M., Wang, L., Zhang, J., Tao, E., Qian, J., Liu, X., 2018. Fabrication of the porous $MnCo_2O_4$ nanorod arrays on Ni foam as an advanced electrode for asymmetric supercapacitors. Acta Materialia 152, 162-174.

Xu, J., Wu, J., Luo, L., Chen, X., Qin, H., Dravid, V., Mi, S., Jia, C., 2015. Co_3O_4 nanocubes homogeneously assembled on few-layer graphene for high energy density lithium-ion batteries. Journal of Power Sources 274, 816-822.

Xu, Y., Lu, W., Xu, G., Chou, T.-W., 2021. Structural supercapacitor composites: A review. Composites Science and Technology 204, 108636.

Xu, Y., Wang, X., An, C., Wang, Y., Jiao, L., Yuan, H., 2014. Facile synthesis route of porous $MnCo_2O_4$ and $CoMn_2O_4$ nanowires and their excellent electrochemical properties in supercapacitors. Journal of Materials Chemistry A 2(39), 16480-16488.

Xuan, H., Zhang, G., Han, X., Wang, R., Liang, X., Li, Y., Han, P., 2021. Construction of $MnSe_2$/$CoSe_2$/reduced graphene oxide composites with enhanced electrochemical performance as the battery-like electrode for hybrid supercapacitors. Journal of Alloys and Compounds 863, 158751.

Yan, D., Li, Y., Liu, Y., Zhuo, R., Wu, Z., Geng, B., Wang, J., Ren, P., Yan, P., Geng, Z., 2014. Synthesis and electrochemical properties of multilayered porous hexagonal $Mn(OH)_2$ nanoplates as supercapacitor electrode material. Materials Letters 136, 7-10.

Yan, J., Wei, T., Shao, B., Ma, F., Fan, Z., Zhang, M., Zheng, C., Shang, Y., Qian, W., Wei, F., 2010. Electrochemical properties of graphene nanosheet/carbon black composites as electrodes for supercapacitors. Carbon 48(6), 1731-1737.

Yang, J., Liu, H., Martens, W.N., Frost, R.L., 2010. Synthesis and Characterization of Cobalt Hydroxide, Cobalt Oxyhydroxide, and Cobalt Oxide Nanodiscs. The Journal of Physical Chemistry C 114(1), 111-119.

Yang, Y., Zhu, P., Zhang, L., Zhou, F., Li, T., Bai, R., Sun, R., Wong, C., 2019. Electrodeposition of $Co(OH)_2$ Improving Carbonized Melamine Foam Performance for Compressible Supercapacitor Application. ACS Sustainable Chemistry & Engineering 7(19), 16803-16813.

Yi, T.-F., Chang, H., Wei, T.-T., Qi, S.-Y., Li, Y., Zhu, Y.-R., 2021. Approaching high-performance electrode materials of $ZnCo_2S_4$ nanoparticle wrapped carbon nanotubes for supercapacitors. Journal of Materiomics 7(3), 563-576.

Younis, A., Chu, D., Lin, X., Lee, J., Li, S., 2013. Bipolar resistive switching in p-type Co_3O_4 nanosheets prepared by electrochemical deposition. Nanoscale Research Letters 8(1), 36.

Yu, M., Zeng, Y., Zhang, C., Lu, X., Zeng, C., Yao, C., Yang, Y., Tong, Y., 2013. Titanium dioxide@polypyrrole core–shell nanowires for all solid-state flexible supercapacitors. Nanoscale 5(22), 10806-10810.

Yu, Z., Cheng, Z., Wang, X., Dou, S.X., Kong, X., 2017. High area-specific capacitance of $Co(OH)_2$/hierarchical nickel/nickel foam supercapacitors and its increase with cycling. Journal of Materials Chemistry A 5(17), 7968-7978.

Zhang, F., Cho, M., Eom, T., Kang, C., Lee, H., 2019. Facile synthesis of manganese cobalt sulfide nanoparticles as high-performance supercapacitor electrode. Ceramics International 45(16), 20972-20976.

Zhang, L., Yang, X., Zhang, F., Long, G., Zhang, T., Leng, K., Zhang, Y., Huang, Y., Ma, Y., Zhang, M., Chen, Y., 2013. Controlling the Effective Surface Area and Pore Size Distribution of sp2 Carbon Materials and Their Impact on the Capacitance Performance of These Materials. Journal of the American Chemical Society 135(15), 5921-5929.

Zhang, Z., Huang, Y., Liu, X., Wang, X., Liu, P., 2020. Core–Shell Co, Zn Bimetallic Selenide Embedded Nitrogen-Doped Carbon Polyhedral Frameworks Assist in Sodium-Ion Battery Ultralong Cycle. ACS Sustainable Chemistry & Engineering 8(22), 8381-8390.

Zhao, C., Liang, S., Jiang, Y., Gao, F., Xie, L., Chen, L., 2020. Mn doped $Co(OH)_2$ nanosheets as electrode materials for high performance supercapacitors. Materials Letters 270, 127751.

Zhao, Y., Hu, L., Zhao, S., Wu, L., 2016. Preparation of $MnCo_2O_4$@$Ni(OH)_2$ Core–Shell Flowers for Asymmetric Supercapacitor Materials with Ultrahigh Specific Capacitance. Advanced Functional Materials 26(23), 4085-4093.

Zhong, C., Deng, Y., Hu, W., Qiao, J., Zhang, L., Zhang, J., 2015. A review of electrolyte materials and compositions for electrochemical supercapacitors. Chemical Society Reviews 44(21), 7484-7539.

Zhu, Z., Gao, F., Zhang, Z., Zhuang, Q., Liu, Q., Yu, H., Fu, M., 2021. In-situ growth of $MnCo_2O_4$ hollow spheres on nickel foam as pseudocapacitive electrodes for supercapacitors. Journal of Colloid and Interface Science 587, 56-63.

LIST OF PUBLICATIONS

From the thesis

1. **P.M. Anjana**, S.R. Sarath Kumar, R.B. Rakhi, $MnCo_2S_4$ nanoflowers directly grown over nickel foam as cathode for high-performance asymmetric hybrid supercapacitors, Journal of Energy Storage 61 (2023) 106672, DOI: https://doi.org/10.1016/j.est.2023.106672

2. **P.M. Anjana**, S.R. Sarath Kumar, R.B. Rakhi, Manganese cobalt oxide nanoflakes for electrochemical energy storage, Journal of Materials Science: Materials in Electronics 33 (2022) 8484-8492, DOI: 10.1007/s10854-021-06377-5

3. **P.M. Anjana**, S.R. Sarath Kumar, R.B. Rakhi, $MnCo_2O_4$ nanoneedles self-organized microstructures for supercapacitors, Materials Today Communications 28 (2021) 102720, DOI: https://doi.org/10.1016/j.mtcomm.2021.102720

4. **P.M. Anjana**, S.R. Sarath Kumar, R.B. Rakhi, Direct growth of $Mn(OH)_2/Co(OH)_2$ nanocomposite on carbon cloth for flexible supercapacitor electrodes, Journal of Energy Storage 33 (2021) 102151, DOI: https://doi.org/10.1016/j.est.2020.102151

5. **P.M. Anjana**, S.R. Sarath Kumar, R.B. Rakhi, Direct growth of $MnCoSe_2$ nanoneedles on 3D nickel foam for supercapacitor application, Surfaces and Interfaces (Under Review)

Not from the part of Thesis

1. **P.M. Anjana**, J.F. Joe Sherin, C. Vijayakumar, S.R. Sarath Kumar, M.R. Bindhu, R.B. Rakhi, Role of reduced graphene oxide-Co-double-doped Fe3O4 nanocomposites for photocatalytic and supercapacitor applications, Materials Science and Engineering: B, 290, (2023) 116313, DOI: https://doi.org/10.1016/j.mseb.2023.116313

2. **P.M. Anjana**, P.R. Ranjani, R.B. Rakhi, Cu-Fe based oxides and selenides as advanced electrode materials for high performance symmetric supercapacitors,

Materials Letters 296 (2021) 129827, DOI: https://doi.org/10.1016/j.matlet.2021.129827

3. **P.M. Anjana**, M.R. Bindhu, R.B. Rakhi, Green synthesized gold nanoparticle dispersed porous carbon composites for electrochemical energy storage, Materials Science for Energy Technologies 2 (2019) 389-395, DOI: https://doi.org/10.1016/j.mset.2019.03.006
4. **P.M. Anjana**, M.R. Bindhu, M. Umadevi, R.B. Rakhi, Antibacterial and electrochemical activities of silver, gold, and palladium nanoparticles dispersed amorphous carbon composites, Applied Surface Science 479 (2019) 96-104, DOI: https://doi.org/10.1016/j.apsusc.2019.02.057
5. **P.M. Anjana**, M.R. Bindhu, M. Umadevi, R.B. Rakhi, Antimicrobial, electrochemical and photocatalytic activities of Zn doped Fe_3O_4 nanoparticles, Journal of Materials Science: Materials in Electronics 29 (2018) 6040-6050, DOI: https://link.springer.com/article/10.1007/s10854-018-8578-2
6. I. Mukkatt, **A.P. Mohanachandran**, A. Nirmala, D. Patra, P.A. Sukumaran, R.S. Pillai, R.B. Rakhi, S. Shankar, A. Ajayaghosh, Tunable Capacitive Behavior in Metallopolymer-based Electrochromic Thin Film Supercapacitors, ACS Applied Materials & Interfaces 14 (2022) 31900-31910, DOI: https://doi.org/10.1021/acsami.2c05744
7. V.V. Mohan, **P.M. Anjana**, R.B. Rakhi, A study on the effect of phase conversion of tungsten nanostructures on their electrochemical energy storage performance, Materials Advances 3 (2022) 5900-5910, DOI: https://doi.org/10.1039/D2MA00475E
8. V.V. Mohan, M. Manuraj, **P.M. Anjana**, R.B. Rakhi, WS_2 Nanoflowers as Efficient Electrode Materials for Supercapacitors, Energy Technology 10 (2022) 2100976, DOI: https://doi.org/10.1002/ente.202100976
9. V.V. Mohan, **P.M. Anjana**, R.B. Rakhi, One pot synthesis of tungsten oxide nanomaterial and application in the field of flexible symmetric supercapacitor energy storage device, Materials Today: Proceedings 62 (2022) 848-851, DOI: http://dx.doi.org/10.1016/j.matpr.2022.04.046
10. P. Rupa Ranjani, **P.M. Anjana**, R.B. Rakhi, Solvothermal synthesis of $CuFeS_2$ nanoflakes as a promising electrode material for supercapacitors, Journal of Energy Storage 33 (2021) 102063, DOI: https://doi.org/10.1016/j.est.2020.102063

11. I. Mukkatt, **P.M. Anjana**, A. Nirmala, R.B. Rakhi, S. Shankar, A. Ajayaghosh, Metal ion-induced capacitance modulation in near-isostructural complexes-derived electrochromic coordination polymers, Materials Today Chemistry 16 (2020) 100260, DOI: https://doi.org/10.1016/j.mtchem.2020.100260
12. J. Kavil, **P.M. Anjana**, D. Joshy, A. Babu, G. Raj, P. Periyat, R.B. Rakhi, g-C_3N_4/CuO and g-C_3N_4/Co_3O_4 nanohybrid structures as efficient electrode materials in symmetric supercapacitors, RSC Advances 9 (2019) 38430-38437, DOI: https://doi.org/10.1039/C9RA08979A
13. J. Kavil, **P.M. Anjana**, C.P. Roshni, P. Periyat, K.G. Raj, R.B. Rakhi, Multifunctional nanohybrid material from discarded razor blades as cost-effective supercapacitor electrodes and oil-spill cleaners, Applied Surface Science 487 (2019) 109-115, DOI: https://doi.org/10.1016/j.apsusc.2019.05.055
14. J. Kavil, **P.M. Anjana**, P. Periyat, R.B. Rakhi, One-pot synthesis of g-C_3N_4/MnO_2 and g-C_3N_4/SnO_2 hybrid nanocomposites for supercapacitor applications, Sustainable Energy & Fuels 2 (2018) 2244-2251, DOI: https://doi.org/10.1039/C8SE00279G
15. J. Kavil, **P.M. Anjana**, P. Periyat, R.B. Rakhi, Titania nanotubes dispersed graphitic carbon nitride nanosheets as efficient electrode materials for supercapacitors, Journal of Materials Science: Materials in Electronics 29 (2018) 16598-16608,DOI:10.1007/s10854-018-9753-1
16. M.P. Kumar, L.M. Lathika, **P.M. Anjana**, R.B. Rakhi, A High-Performance Flexible Supercapacitor Anode Based on Polyaniline/Fe_3O_4 Composite@Carbon Cloth, ChemistrySelect 3 (2018) 3234-3240, DOI: https://doi.org/10.1002/slct.201800305

LIST OF CONFERENCES/WORKSHOPS ATTENDED

1. **P.M.Anjana**, and R.B.Rakhi, "Direct growth of Manganese Cobalt - Double hydroxide on flexible carbon cloth for supercapacitor application", Third International Conference on Nanomaterials: Synthesis, Characterization, and Applications (ICN-2018) held at Mahatma Gandhi University, Kottayam, Kerala, India on May 11-13, 2018
2. **P.M.Anjana**, and R.B.Rakhi, "Direct growth of polyaniline/Fe_3O_4 composite on flexible carbon cloth for supercapacitor application", Polymer Conference for Young Researchers (PCYR-18) held at CSIR-NIIST, Trivandrum on November 17, 2018
3. **P.M.Anjana**, M.R. Bindhu, and R.B.Rakhi, "Preparation and characterization of Zn doped Fe_3O_4 nanoparticles and its supercapacitor application", International Conference on Energy Materials (ICEM-2019) organized by Department of Physics, Mother Teresa Women's University, Kodaikanal, India, held on January 9, 2019 (**Best Oral Presentation Award**)
4. **P.M.Anjana**, M.R. Bindhu, M. Umadevi, R.B. Rakhi, "Antibacterial and electrochemical activities of silver, gold, and palladium nanoparticles dispersed amorphous carbon composites", 5th International Conference on Nanoscience and Nanotechnology (ICONN-2019), held at SRM Institute of Science And Technology (SRM IST), Chennai, India on January 28-30, 2019
5. **P.M.Anjana**, and R.B.Rakhi," Preparation and characterization of Mixed Co-Mn Double hydroxide and its supercapacitor application", National Workshop on Advanced Analytical Techniques in Materials Science (WAATMS 2020) organized by Department of Nanoscience and Technology, University of Calicut during January 20-23, 2020
6. **P.M.Anjana**, and R.B.Rakhi," 2D flexible graphite oxide sheets for supercapacitor application", International Virtual Conference on Advanced Nanomaterials Appications (VCAN 2020), organized by Centre for Nanotechnology Research (CNR), Vellore Institute of Technology, Vellore, India during June 17-19, 2020
7. **P.M.Anjana**, S.R. Sarath Kumar and R.B.Rakhi, "$MnCo_2O_4$ nanowires self-organized microflowers as electrode materials for supercapacitors", International

Conference on Nanoscience and Nanotechnology (ICONN 2021) organized by Department of Physics and Nanotechnology, SRM IST, India during February 01 - 03, 2021.

8. **P.M.Anjana**, and R.B.Rakhi," Direct growth of $Mn(OH)_2/Co(OH)_2$ nanocomposite on carbon cloth as flexible supercapacitor electrodes", International Conference on Multifunctional Electronic Materials and Processing (MEMP-2021) organized by Centre for Materials for Electronics Technology (C-MET), Pune during March 8-10, 2021
9. **P.M.Anjana**, and R.B.Rakhi, "Two-dimensional flexible graphite oxide sheets for electrochemical energy storage application", Sustainable Materials and Technologies for Bio and Energy Applications (SMTBEA-2021) organized by the Department of Electronics & Communication Engineering, SSN College of Engineering, Kalavakkam, Chennai, 603110, India during May19-21, 2021
10. **P.M.Anjana**, S.R. Sarath Kumar and R.B.Rakhi, "$MnCo_2O_4$ nanoneedles self-organized microstructures for supercapacitors", International e-Conference on Advanced Materials (ICOAM 2021) organized by Department of Physics, JP College of Arts & Science, Agarakattu, Tenkasi-627851, Tamil Nadu, India held on 24th & 25th Septemper 2021.
11. **P.M.Anjana**, S.R. Sarath Kumar and R.B.Rakhi, "Fabrication and supercapacitor performance study of MnCo2S4 nanoflower on 3D conducting Nickel foam", Recent Trends in Energy and Environment (SNREE 2022) organized by The Department of Physics, SN College, Varkala-695145, Kerala, India held on 8-9 December 2022.
12. **P.M.Anjana**, S.R. Sarath Kumar and R.B.Rakhi, "Facile hydrothermal synthesis of $MnCo_2S_4$ nanoflower on Nickel foam substrate for supercapacitor application", National Conference on Recent Trends in Material Science and Technology (NCMST 2022) organized by The Department of Chemistry, Indian Institute of Space Science and Technology (IIST), Valiamala-695547, Thiruvananthapuram, Kerala, India held on 28-30 December 2022.
13. **P.M. Anjana**, S.R. Sarath Kumar and R.B. Rakhi, "Hydrothermal Synthesis of $MnCo_2S_4$ nanoflower for Electrochemical Energy storage" National Conference on Advanced Materials and Manufacturing Technologies (AMMT 2023) organized by CSIR-NIIST, Trivandrum, held on 23-24 February 2023